UNIVERSITY OF CALIFORNIA,
IRVINE

Temporal analysis of planar liquid-jet atomization

DISSERTATION

submitted in partial satisfaction of the requirements
for the degree of

DOCTOR OF PHILOSOPHY

in Mechanical and Aerospace Enigneering

by

Arash Zandian

Dissertation Committee:
Professor William A. Sirignano, Chair
Professor Said E. Elghobashi
Professor Roger H. Rangel

2018

DEDICATION

To my lovely parents ...

TABLE OF CONTENTS

LIST OF FIGURES

LIST OF TABLES

ACKNOWLEDGMENTS

I would like to thank Professor William A. Sirignano, the chair of my committee, for his endless support, patience, and unique perspectives towards my research.

Besides my advisor, I would like to thank the rest of my thesis committee, Professor Said E. Elghobashi and Professor Roger A. Rangel, for their encouragement and insightful comments.

I would like to acknowledge Professor Fazle Hussain at Texas Tech University, who was always very insightful and supportive during my Ph.D. research. His comments have highly enhanced my research output and I have learned a lot from him and enjoyed his companion throughout my Ph.D. pursuit.

I gratefully acknowledge the access to the XSEDE supercomputer under Allocation TG-ASC150024, and to the UCI HPC cluster which made it possible to perform our high resolution computations.

The support from Professor Said E. Elghobashi, especially at the very beginning of my Ph.D. path, is greatly appreciated. His insightful comments in numerical methods and computational coding paved my path towards computational modeling.

I would also like to acknowledge the valuable contribution of Dr. Dorrin Jarrahbashi at the Texas A&M University in developing the three-dimensional CFD code with level-set method used in this work. Dr. Pavel Popov at University of Illinois Urbana-Champaign is thanked for his mentorship in parallelizing the CFD code. I would also like to thank my labmates, for their scientific advice and many insightful discussions and suggestions.

My endless gratitude goes to my brother and parents for their unconditional love, support, and encouragement.

CURRICULUM VITAE

Arash Zandian

EDUCATION:

Doctor of Philosophy in Mechanical and Aerospace Engineering **2018**
University of California, Irvine *Irvine, USA*

Master of Science in Mechanical and Aerospace Engineering **2014**
University of California, Irvine *Irvine, USA*

Bachelor of Science in Mechanical Engineering **2012**
University of Tehran *Tehran, Iran*

PUBLICATIONS:

Refereed journal publications

Zandian, A., Sirignano, W. A., Hussain, F., "Understanding liquid-jet atomization cascades via vortex dynamics", *Journal of Fluid Mechanics*, Vol. 843, 2018, pp. 293–354.

Zandian, A., Sirignano, W. A., Hussain, F., "Planar liquid jet: Early deformation and atomization cascades", *Physics of Fluids*, Vol. 29 (6), 2017, 062109.

Zandian, A., Ashjaee, M., "The thermal efficiency improvement of a steam Rankine cycle by innovative design of a hybrid cooling tower and a solar chimney concept", *Renewable Energy*, Vol. 51, 2013, pp. 465–473.

Peer-reviewed conference proceedings

Zandian, A., Sirignano, W. A., Hussain, F., "Dynamics of a spatially developing liquid jet with slower coaxial gas flow", to be presented at *14th ICLASS*, 2018, Chicago, IL.

Zandian, A., Sirignano, W. A., Hussain, F., "Mechanisms of liquid stream breakup: Vorticity and time and length scales", *28th ILASS-Europe*, 2017, Valencia, Spain.

Zandian, A., Sirignano, W. A., Hussain, F., "Explaining the planar liquid jet atomization via vortex dynamics", *29th ILASS-Americas*, 2017, Atlanta, GA.

Zandian, A., Sirignano, W. A., Hussain, F., "Planar liquid sheet breakup mechanisms, time scales, and length scale cascade", *29th ILASS-Americas*, 2017, Atlanta, GA.

Zandian, A., Sirignano, W. A., Hussain, F., "Three-dimensional liquid sheet breakup: Vorticity dynamics", *54th AIAA-ASM*, 2016, San Diego, CA.

Contributed Conference Presentations

Zandian, A., Sirignano, W. A., Hussain, F., "Mechanisms, role of vorticity, and time scales for planar liquid sheet breakup", *69th APS Division of Fluid Dynamics*, 2016, Portland, OR.

Zandian, A., Sirignano, W. A., Hussain, F., 'Temporal length-scale cascade and expansion rate on planar liquid jet instability", *69th APS Division of Fluid Dynamics*, 2016, Portland, OR.

Published thesis

Zandian, A., "Numerical analysis of the temporal and spatial instabilities on an annular liquid jet", M.S. thesis, University of California, Irvine, June 2014.

Zandian, A., "Numerical simulation and geometrical optimization of heat transfer off a vehicle windshield subject to defrosting and demisting airflow", B.S. thesis, University of Tehran, February 2012.

RESEARCH EXPERIENCE:

Graduate Research Assistant **2012–2018**
University of California, Irvine *Irvine, California*

TEACHING ASSISTANT:

Viscous and Compressible Flows **Spring 2014, Spring 2018**
University of California, Irvine *Irvine, California*

Introduction to Fluid Mechanics **Winter 2013, Fall 2016, Fall 2017**
University of California, Irvine *Irvine, California*

Introduction to Thermodynamics **Spring 2016, Spring 2017**
University of California, Irvine *Irvine, California*

Engineering Analysis II **Winter 2015, Winter 2016**
University of California, Irvine *Irvine, California*

Introduction to Engineering Computations **Fall 2013**
University of California, Irvine *Irvine, California*

Linear Control Systems **Spring 2012**
University of Tehran *Tehran, Iran*

Thermal Power-Plants Technology **Winter 2011**
University of Tehran *Tehran, Iran*

HONORS AND AWARDS:

Mechanical and Aerospace Engineering Graduate Student of the Year **2018**
School of Engineering, UC-Irvine

XSEDE super-computer allocation award **August 2017**
National Science Foundation

Vakhshoori Scholarship **September 2014**
The Vakhshoori Foundation, San Jose, CA

Donald K. Edwards Endowed Fellowship **2012–2013**
Mechanical & Aerospace Engineering Department, UC-Irvine

ABSTRACT OF THE DISSERTATION

Temporal analysis of planar liquid-jet atomization

By

Arash Zandian

Doctor of Philosophy in Mechanical and Aerospace Enigneering

University of California, Irvine, 2018

Professor William A. Sirignano, Chair

The temporal evolution of three-dimensional instabilities on an incompressible planar liquid sheet segment is studied using direct numerical simulation (DNS), and the level-set and volume-of-fluid methods for the liquid-gas interface tracking. The purpose of this study is to reveal new crucial insights into the development of three-dimensional instabilities on liquid sheets, which result in formation of lobes, bridges and ligaments, and eventually break into droplets. Three atomization cascades are distinguished at early breakup, which are well categorized on a gas Weber number (We_g) versus liquid Reynolds number (Re_l) map. Each atomization domain has a distinct breakup mechanism with its own characteristic time and length scales in the cascade process. λ_2 method is used to identify the vortices near the liquid-gas interface and relate the vortex interactions to the surface dynamics at different stages of the jet breakup – namely, lobe formation, lobe perforation, ligament formation, stretching and tearing. Vortex dynamics explains the hairpin formation, and the interaction between the hairpins and the Kelvin-Helmholtz (KH) roller explains the perforation of the lobes at high We_g, the formation of corrugations on the lobe front edge at high Re_l, and the stretching of lobes into ligaments at low Re_l and low We_g. Streamwise vorticity generation – resulting in three-dimensional instabilities – is mainly caused by vortex stretching and baroclinic torque at high and low density ratios, respectively. Generation of streamwise vortices and their interaction with spanwise vortices produce the liquid structures seen at various flow

conditions, understanding of which is crucial for controlling the droplet-size distribution and jet spread rate in primary atomization. Probability density functions (PDFs) of the local radius of curvature and the local cross-flow displacement of the liquid-gas interface are evaluated over wide ranges of Re_l, We_g, gas-to-liquid density ratio and viscosity ratio, and wavelength-to-sheet thickness ratio. A novel analysis enables us to show the temporal cascade of liquid-structure length scales as well as quantify the spread rate of the liquid jet during primary atomization. The spray angle and the mean surface length scale are evaluated from the PDFs and are compared for wide ranges of dimensionless parameters. The validity and usefulness of the temporal analysis is established by a comparison with dynamics of a spatially developing liquid jet with slower coaxial gas flow. It is shown that the deformations in the upstream region of the jet cap follow a periodic behavior that can be well portrayed in a frame moving with the convective velocity of the liquid jet, as is implemented in our temporal model.

Chapter 1

Introduction

Transient nonlinear behavior and high-pressure conditions relevant to Diesel-engine operation are the main themes of the proposed research. The focus of the research is in the identification of the major physical mechanisms in the conversion of the planar liquid jet into droplets during primary atomization. The breakup mechanisms are to be analyzed and the causes of distinct liquid structure cascades are to be understood and related to the flow properties and vortex interactions. The time and length scales associated with each breakup mechanism are to be defined to help us evaluate the cascade rate and spread rate of the liquid jet during primary atomization. The outcome of this study is essentially useful for designing potential control mechanisms for the droplet size.

1.1 Background and Motivation

Atomization generally refers to the disintegration of a bulk liquid material into droplets in a surrounding gas. Atomizers are utilized in spraying liquids in many industrial and household applications. Gas-liquid two-phase jet flows are encountered in a variety of engineering

applications such as fuel injection, propulsion and combustion systems, agricultural sprays and chemical reactors. The atomizers could be categorized into planar sheets, cylindrical jets, or annular jets, based on the cross-sectional geometry of the injecting liquid jet. Either one of these jets could be accompanied by a coflowing high-speed gas stream, as in air-blasted and air-assisted atomizers, which are integral parts in both aircraft propulsion systems and internal combustion engines.

The unified design approach of atomizers in different fields requires the interrelations between different spray characteristics of the atomizers with the pertinent input parameters such as liquid fuel properties, injection conditions and atomizer geometries. This requires a physical understanding of the flow field inside the atomizer and of the mechanism of spray formation outside the atomizer. The modeling of the atomization process is a very challenging task as it is affected by variety of factors such as the nozzle geometry, the thermo-physical properties of the liquid, and the aerodynamic liquid-gas interaction. The initial breakup of a liquid jet is often referred to as primary breakup or primary atomization. A population of larger droplets produced in the primary atomization may be unstable at some critical flow conditions and thus may undergo further disruption into smaller droplets. This process is usually termed as secondary atomization. Many reasons can be given to explain why primary atomization remains such a challenging topic. First, the complex flows associated with liquid breakup involve turbulence, surface tension effects, and potentially large density and viscosity gradients. Then, the difficulty associated with modeling is due to the importance of small liquid scales in combustion systems, in which the interest is mostly in the size distribution of small liquid scales which determine the evaporation rate.

Liquid-fuel injection systems operate under conditions of high Weber numbers (We) induced by the large velocity of the jet and high Reynolds numbers (Re). Our purpose is to understand the mechanisms of jet flow under these extreme conditions which lead to the formation of small drops and mist. The disintegration of liquid jets can be framed in terms of insta-

bilities. The instabilities are well known to be critical in the distortion of the liquid/gas interface and in the process by which ligaments of liquid are torn from the jet core. Three kinds of instabilities that can lead to breakup are capillary instability, Kelvin-Hemholtz (KH) instability, and Rayleigh-Taylor (RT) instability. These instabilities can take a symmetric/axisymmetric form at the early stages; however, three-dimensional (3D) instabilities can also occur and prevail later in time. Various parameters affecting the liquid-gas interface instabilities at the early stages of jet injection are to be investigated and compared in this study.

The main focus of this research is on three-dimensional, transient computations of planar liquid streams subject to atomization in a gaseous medium. A temporal analysis is performed on a liquid segment with combined Navier-Stokes and level-set or volume-of-fluid calculations. Vortices are determined via post-processing the data for more detailed study of the effects of vortex dynamics on the jet instabilities. The main objectives are to (i) detail and explain cascade of structures on the liquid surface with time, including lobe, ligament, and droplet formations; (ii) investigate the causes of different breakup mechanisms and relate the surface dynamics to vortex dynamics; (iii) explain the roles different breakup regimes play in the cascade of length scales and spray development during primary atomization; and (iv) study the effects of the key non-dimensional parameters – i.e. Re, We, gas-to-liquid density ratio and viscosity ratio, and the wavelength-to-sheet-thickness ratio – on the atomization process and on the temporal variation of the spray width and the liquid-structures length scale.

1.2 Literature review

In this section, the most important instabilities involved in liquid jet breakup are introduced; then, the works and contributions of the previous researchers on the field of liquid-jet in-

stability and atomization are presented in four different categories – liquid jet instability development, breakup regimes, droplet-size distribution, and spray angle. The assumptions made in each section, the key findings, and the remaining questions to be answered are mentioned in the corresponding sections. Next, the vortex dynamics studies in homogeneous flows are presented and their relevance to the non-homogeneous (two-phase) flows is established.

1.2.1 Capillary instability

The Plateau-Rayleigh instability, often just called the Rayleigh instability or the capillary instability, explains why and how a falling stream of fluid breaks up into smaller packets with the same volume but less surface area. In 1873, Plateau experimentally found that a vertically falling stream of water will breakup into drops if its wavelength is greater than about 3.13 to 3.18 times the stream diameter; i.e. $\lambda \geq \pi D$. Later, Rayleigh [69] showed theoretically that a vertically falling column of non-viscous liquid with a circular cross-section should breakup into drops if the wavelength of the instabilities on the surface of the column exceeded the circumference of the column cross-section.

Studies of capillary instability revealed that a liquid jet is unstable for axial disturbances with wave numbers less than a cut-off wave number k_c, but stable otherwise. For each wavelength of an unstable disturbance one main drop and one or more usually smaller drop(s), referred to as the satellite or spherous drop(s), are formed. Figure 1.1 shows image of a typical liquid

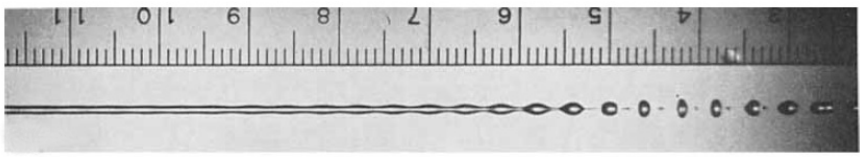

Figure 1.1: Typical photograph of a liquid jet, showing the formation of main and satellite drops from capillary instabilities.

jet becoming unstable when it is subject to small perturbation. The instabilities grow and cause the liquid jet to finally breakup into the main and satellite droplets. The capillary instability plays the most significant role in breakup of liquid ligaments during atomization.

The classical study of the capillary instability of liquid jets was published in the seminal work of Lord Rayleigh [69]. With the assumption of an inviscid liquid, he obtained an equation for the growth rate of a given axisymmetric surface disturbance by equating the potential and kinetic energies computed for the flow. Further, with the hypothesis that the disturbance with the maximum growth rate would lead to the breakup of the jet, he obtained an expression for the resulting droplet size assuming that it would be of the order of the wavelength of this disturbance. Later, Weber [90] included the effect of viscosity in his analysis of the jet breakup based on the 3D partial differential equations of hydrodynamics of Newtonian viscous liquids. He found that the effect of the liquid viscosity is to shift the fastest growing waves to longer wavelengths and to slow down their growth rate, without, however, altering the value of the cut-off wave-number.

The explanation of capillary instability begins with the existence of tiny perturbations in the stream. These are always present, no matter how smooth the stream is. These disturbances may be in the form of surface displacement, pressure or velocity fluctuations in the supply system or on the jet surface, as well as fluctuations in liquid properties such as temperature, viscosity, or surface tension coefficient. If the perturbations are resolved into sinusoidal components, we find that some components grow with time while others decay. Among those that grow with time, some grow at faster rates than the others. Whether a component decays or grows, and how fast it grows is entirely a function of its wave-number and the radius of the original cylindrical stream.

When a liquid-gas interface is deformed, as shown in Figure 1.2, the surface tension forces may tend to bring it back to its equilibrium shape. The equilibrium shape of the interface is defined based on all the forces that may act on it, including the gravitational and pressure

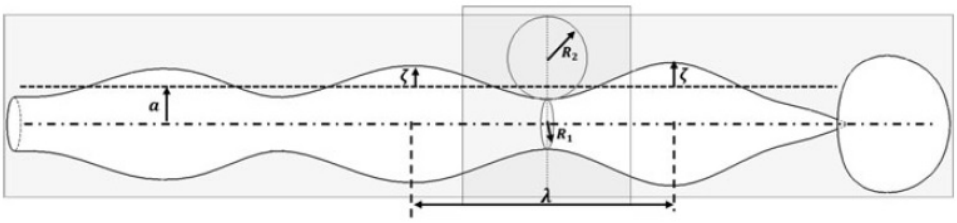

Figure 1.2: Schematic of an unstable liquid jet or ligament.

forces. On a flat interface, as the disturbed interface tends to move to its equilibrium shape, a wave-like propagation appears. If the forces that are acting on the disturbed interface are the surface tension or the capillary forces, the waves are referred to as the capillary waves.

Although a thorough understanding of how this happens requires a mathematical development, Figure 1.2 can provide a conceptual understanding. At the trough, the radius of the stream R_1 is smaller. Hence according to the Young-Laplace equation, the pressure due to surface tension is increased. Likewise, the radius of the stream is greater at the peak and, by the same reasoning, pressure due to surface tension is reduced. If this were the only effect, we would expect that the higher pressure in the trough would squeeze liquid into the lower pressure region in the peak. Therefore, the wave grows in amplitude over time. However, the Young-Laplace equation is influenced by two separate radius components: one is the radius R_1, already discussed, of the stream itself, and the other is the radius of curvature of the wave itself, R_2. The fitted arc in the figure shows this radius at a trough. The radius of curvature at the trough is in fact negative, meaning that, according to Young-Laplace, it actually decreases the pressure in the trough. The radius of curvature at the peak, on the other hand, is positive and increases the pressure in that region. The effect of these components is opposite to the effects of the radius of the stream itself.

The two effects, in general, do not exactly cancel. One of them will have greater magnitude than the other, depending upon wave-number and the initial radius of the stream. When the wave-number is such that the radius of curvature of the wave dominates that of the radius

of the stream, those waves decay over time. When the effect of the radius of the stream dominates that of the curvature of the wave, such instabilities grow exponentially in time.

Provided that the wavelength of surface deformation is long, the curvature $1/R_1 >> 1/R_2$ at the trough. Since liquid pressure is primarily balanced by capillary pressure due to curvature $1/R_1$, a greater liquid pressure is induced by a smaller radius of the cylinder. Thus, the positive difference in the pressures induces a perturbed flow from trough to the neighboring peak. Therefore, the system is unstable and breaks up the cylinder into droplets. However, for deformation with small wavelength, the curvature $1/R_2 >> 1/R_1$ at the trough. Therefore, the perturbed pressures at trough decrease and it can be smaller than perturbed pressure at the neighboring peak, driving the flow from the peak to the trough, and stabilizing the system.

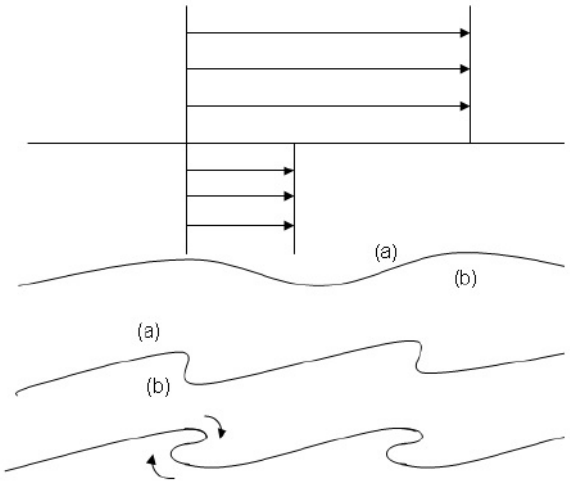

Figure 1.3: The speed of the fluid above is greater. The pressure is greater at crests (a) than at troughs (b). The upper part of the interface is carried by upper fluid causing the interface to overturn [39].

1.2.2 Kelvin-Helmholtz instability

The instability of uniform flow of incompressible fluids in two horizontal parallel infinite streams of different velocities and densities is known as the Kelvin-Helmholtz (KH) instability [39]. The name is also commonly used to describe the instability of the more general case where the variations of velocity and density are continuous and occur over a finite thickness, as in the gas-liquid interface during injection of a liquid jet.

The KH instability is produced by the action of pressures on the perturbed interface; the instability is often discussed as being due to shear, but shear stresses are not the major actor here and in any event could not be inserted into an analysis based on potential flow even when viscosity is not neglected [39]. The formation of the instability may be described in terms of the action of pressure in Bernoulli equation. Pressure is smaller where the velocity is larger (at the top fluid in Figure 1.3) and is large where velocity is small (in the bottom fluid). A small perturbation on the interface is magnified by the action of pressure, as the upper part of the interface is driven by upper fluid causing the interface to overturn and create KH waves, as shown in Figure 1.3.

1.2.3 Rayleigh-Taylor instability

The Rayleigh-Taylor (RT) instability is very important in liquid jet breakup. It is driven by acceleration when a liquid accelerates away from a gas or a lighter fluid. The signature of this instability is the waves which corrugate the free surface at the instant of acceleration. Ultimately, these wave crests will become fingers causing it to breakup [39].

Rayleigh [69] showed that a heavy fluid over a light fluid is unstable, as common experience dictates. He treated the stability of heavy fluid over light fluid without viscosity, and found

that a disturbance on the flat free surface grows exponentially like $\exp(\omega t)$ where

$$\omega = \left\{ \frac{kg(\rho_2 - \rho_1)}{\rho_1 + \rho_2} \right\}^{1/2}; \tag{1.1}$$

where ρ_2 is the density of the heavy fluid, ρ_1 is the density of the light fluid, g is the acceleration due to gravity and $k = \frac{2\pi}{\lambda}$ is the wavenumber and λ is the wavelength. The instability described by Equation (1.1) is catastrophic since the growth rate (ω) tends to infinity, at any fixed time (no matter how small) as the wavelength tends to zero.

Nature does not allow such a singular instability; for example, neglected effects like viscosity and surface tension enter the physics strongly at the shortest wavelength. These effects have been taken into account in the study of RT instability by later researchers. Surface tension eliminates the instability of the short waves; there is a finite wavelength depending strongly on viscosity as well as surface tension for which the growth rate is maximum. This is the wavelength that should occur in a real physical problem and would determine the wavelength on the corrugated fronts of breaking drops in a high-speed air flow.

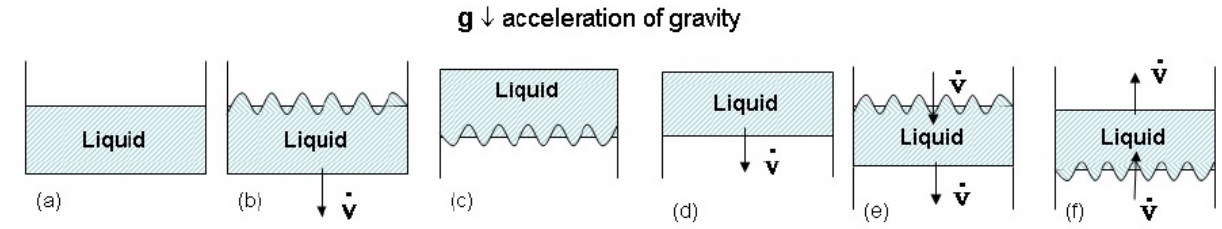

Figure 1.4: RT instability: (a) the liquid in the containers at rest is stable under gravity (Rayleigh 1890) but if the container is turned upside down as in (c) the liquid falls out. The liquid at rest in container can be destabilized by downward acceleration of the liquid $\dot{V} > g$ away from gas as in (b) and in the upside down case the liquid can be prevented from falling out by accelerating downward with $\dot{V} > g$ as in (d). If we open up the container and accelerates the liquid downward with $\dot{V} > g$, the top surface which accelerates away from the gas is unstable but the bottom surface which accelerates into the gas is stabilized as in (e), with the opposite effect when the acceleration is reversed as in (f) [39].

Taylor [85] extended Rayleigh's inviscid analysis to the case where a constant acceleration of the superposed fluids other than gravity is taken into account. Assuming a constant value for the acceleration, Taylor showed that when two superposed fluids of different densities are accelerated in a direction perpendicular to their unperturbed interface, the slightly perturbed surface is unstable if the acceleration is directed from the lighter to the heavier fluid. The Taylor instability depends strongly on the value of the acceleration. A more precise evaluation of the RT instability (Rangel & Sirignano [68], Tryggvason & Unverdi [87]) indicates a meta-stability. There actually must be a distortion of the surface so that the acceleration has a component tangent to the interface. This results in a non-zero cross product of the gradient of pressure and density, resulting in a baroclinic torque.

The idea behind Rayleigh and Taylor's instabilities are embodied in the cartoons and caption of Figure 1.4. These experiments show the difference between the theory of Rayleigh [69] who considered gravity g and Taylor [85] who considered the effect of the acceleration $\dot{V}$. The effect of acceleration destabilizes the liquid-gas surface which accelerates away from the gas and stabilizes the liquid-gas surface which accelerates toward the gas (Figure 1.4 (e)). The RT instability is very important in surface deformation of liquid jets since the liquid is constantly accelerating/decelerating away/towards the gas at different locations on the interface.

1.2.4 Liquid jet instability development

The wide range of liquid-jet applications have led to extensive investigations and have received much attention in the literature since the classical studies of Rayleigh. A considerable number of works on the instability of liquid sheets and jets are available in the literature. In this section, mainly the analyses related to planar liquid-sheet (and cylindrical jets in a few cases) instability are presented.

In the earlier analytical studies, the disintegration of liquid jets was framed in terms of instabilities, which are well known to be critical in the distortion of the liquid-gas interface and in the formation of ligaments torn from the jet core. In the classical studies, it was usual to study the instability by linearizing the nonlinear equations around the basic uniform flow followed by analysis of normal modes proportional to $\exp(\omega t + ikx)$; where k is the wavenumber, and $\omega = \omega_r + i\omega_i$ is the complex frequency. The real part of the frequency (ω_r) is the growth/decay rate of the perturbations, and the imaginary part (ω_i) represents the wave speed. It is clear that for positive ω_r the perturbations will grow unstably. It is also usual to assume that the fluids are inviscid and the amplitude of perturbations (ε) on the liquid-gas interface are much smaller than their wavelength (λ) as well as the sheet thickness ($2h$); i.e. $\varepsilon << \lambda$, $\varepsilon << h$.

The linear instability of a thin liquid sheet was first investigated by Squire [82] and Hagerty & Shea [25], where both liquid and gas phases were taken as inviscid and incompressible. They proved that there can only exist two modes of unstable waves on the two gas-liquid interfaces for liquid sheets in a stationary gas medium, corresponding to the two surface waves oscillating exactly in and out of phase. These two instability modes are commonly referred to as the sinuous (antisymmetric) and varicose (symmetric, dilational) modes, respectively, as schematically depicted in Figure 1.5. They also showed that the sinuous mode is always predominant under the typical conditions for practical applications. However, later studies revealed that this is not generally the case. They also performed the first experimental measurements of the wavelength and its growth rate for liquid sheets under various flow conditions, and the theoretical predictions were compared favorably with their experimental results.

The growth rate found by Squire [82] and Hagerty & Shea [25] were of the form

$$\frac{\omega_r}{kU_0} = \left\{ \frac{\hat{\rho}K}{(\hat{\rho}+K)^2} - \frac{kh}{We}\frac{1}{\hat{\rho}+K} \right\}^{1/2}; \tag{1.2}$$

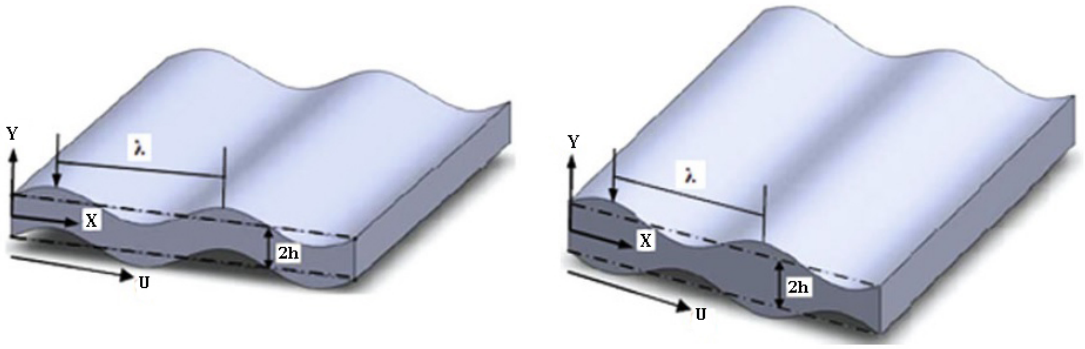

Figure 1.5: A schematic of the instability modes; Sinuous (left), Varicose (right).

where U_0 is the liquid sheet velocity, $\hat{\rho} = \rho_g/\rho_l$ is the gas-to-liquid density ratio, h is the sheet half thickness and $We = \rho_l {U_0}^2 h/\sigma$ is the Weber number. In this equation, $K = \tanh(kh)$ for the sinuous mode and $K = \coth(kh)$ for the varicose mode.

Figure 1.6, adopted from Sirignano & Mehring [81], provides the growth rate of various wavenumbers for both sinuous (antisymmetric) and dilational (symmetric) waves and for different We and $\hat{\rho}$ values. The results show that the varicose mode is more unstable for density ratios near unity, while for low We, the growth of sinuous waves dominate the growth of varicose waves due to the higher growth rates throughout the range of instability. The range of We considered in these studies are, however, much lower than the values encountered in many atomization applications of interest.

Dombrowski and Johns [19] combined a linear model for temporal instability analysis and a breakup model for an inviscid liquid sheet in a quiescent inviscid gas to predict the ligament and droplet sizes after breakup. The schematic of their wavy sheet is reproduced in Figure 1.7. The equation of motion of the neutral axis mid-way between the two gas-liquid interfaces was obtained for a sheet moving with velocity U_l through stationary gas. In this equation, the forces due to gas pressure, surface tension, liquid inertia, and viscosity were considered on an element of the sheet. As shown in the figure, waves grow on the sheet until they reach a critical amplitude. Tears occur in the crests and troughs and fragments

of sheet, corresponding to one-half wavelength, are broken off. The fragments contract by surface tension into unstable ligaments which subsequently break into drops. The diameter of the resulting cylindrical ligaments (d_L) were obtained via a mass balance for a sheet of thickness $2h$ and wavenumber of n; a relation between the size of droplets (d_D) and ligament diameter was also derived;

$$d_L = \sqrt{\frac{8h}{n}}, \qquad d_D^3 = \frac{2\pi d_L^2}{n}. \tag{1.3}$$

Li & Tankin [48] took into account the effects of liquid viscosity in their liquid sheet instability

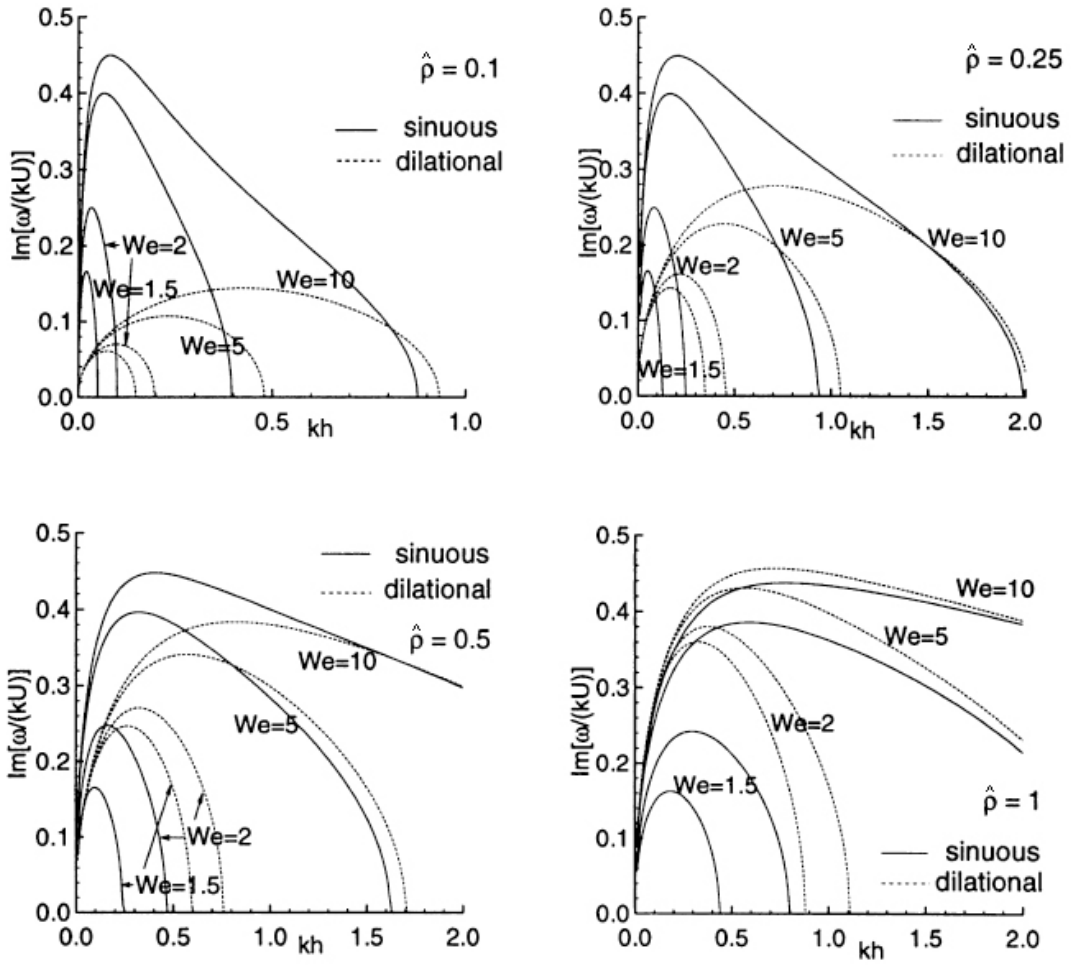

Figure 1.6: Dimensionless growth rate $\mathrm{Im}[\omega/(kU_0)]$ as function of kh for different values of We and $\hat{\rho}$, for inviscid liquid sheet [81].

analysis. They realized that, for sheets, the surface tension always opposes the onset and development of instability, while in cylindrical jets, it is destabilizing at low velocities and stabilizing at higher relative velocities. Li & Tankin called the instabilities that are caused by velocity difference between the gas and liquid for an inviscid liquid sheet (Squire's Equation 1.2) the aerodynamic instabilities. They then claimed that there is a range of instability wavelengths that is induced and enhanced by liquid viscosity, which they called the viscosity-enhanced instability. For low gas Weber numbers, the aerodynamic instability disappears, but the viscosity-enhanced instability still exists. Some simplified relations for the cut-off (neutral) and the dominant wavenumber (the wave number with maximum growth rate) for very thin liquid sheets were also provided. The dominant wavenumber of the viscous liquid sheet was found to be related to its counterpart for inviscid liquid for $kh << 1$ through the Ohnesorg number; $Oh = \sqrt{We}/Re = \mu_l/\sqrt{\rho_l h \sigma}$. Later, Li [47] developed a linear stability analysis of planar liquid sheets in gas streams of unequal velocities, and found that the instability is due to the velocity jump across the two liquid-gas interfaces and from one gas

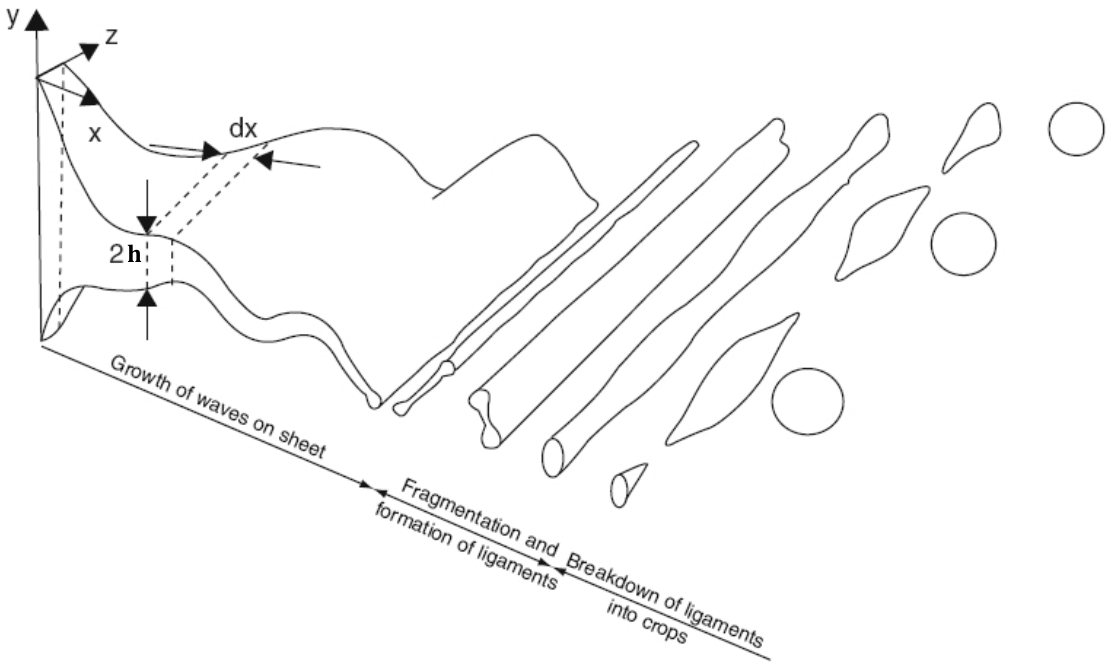

Figure 1.7: Instability of a thinning liquid sheet and its breakup steps [19].

stream to the other. Thus, the instability is related to the classical KH instability, and from the disturbance energy equation it was shown that the mechanism of instability is due to the interfacial pressure fluctuations.

The linear theory – employed in the above-cited works – does not offer a means for the liquid sheet breakup because during the growth of the sinuous mode of disturbances (predominant under practical conditions), the two gas-liquid interfaces remain a constant distant apart. Therefore, the liquid sheet breakup length, which is an important parameter in the spray modeling and spray system design, cannot be predicted based on the linear theory. In reality, the liquid sheet breakup processes – especially near the breakup region – are nonlinear. The most important nonlinear analyses employed in the literature are summarized in this section.

So far, only limited studies have been carried out on the nonlinearity of the liquid sheet breakup process. Clark & Dombrowski [9] were the first to analyze nonlinear liquid sheet disintegration through the perturbation expansion technique with initial disturbance amplitude as the perturbation parameter. It was found that sheet thinning is caused by the growth of the harmonic wave, with maximum thinning and subsequent rupture occurring at positions corresponding to 3/8 and 7/8 of the length of the fundamental wave. The theoretical results were also used to calculate the breakup length of attenuating liquid sheets produced by fan and swirl spray nozzles, and compared well with experimental measurements.

Rangel & Sirignano [68] used the vortex-sheet discretization method to investigate the nonlinear evolution of initially small disturbances at an interface separating two fluids of different density and velocity with effects of surface tension included. Their nonlinear calculations indicate the dominance of varicose oscillating modes when the density ratio is of the order of one, while sinuous waves prevail at lower gas densities. It was shown that sinuous disturbances may result in the formation of ligaments interspaced at half the wavelength of the fundamental mode [68].

Jazayeri and Li [35] developed up to the third-order nonlinear analysis to determine the breakup length of a liquid sheet. Their results indicate that, for an initially sinusoidal surface disturbance, the thinning and subsequent breakup of the liquid sheet is due to the nonlinear effects with the generation of higher harmonics as well as feedback into the fundamental harmonic. The effect of various flow parameters on the liquid sheet breakup time (or length) was investigated. It was found that the breakup time (or length) is reduced by an increase in the initial amplitude of disturbances, an increase in We and an increase in the density ratio, while it becomes asymptotically insensitive to the variations of We and $\hat{\rho}$ when their values become very large. It was also found that the breakup time (or length) is a very weak function of the wavenumber unless it is close to the cut-off wavenumbers [35]. The distance between the two interfaces vanishes near the half and full wavelength, which is different from the conclusions reached by Clark and Dombrowski [9] (described above), who found that the sheet breakup occurred at positions corresponding to 3/8 and 7/8 of the length of the fundamental wave. However, the liquid sheet breaks up at half-wavelength intervals, a result consistent with that of Clark and Dombrowski.

The breakup of thin planar liquid sheets due to the nonlinear growth of disturbances was determined by Tharakan et al. [86]. They studied the effects of We on the size of ligaments and found that the size and geometry of the ligaments formed during breakup vary with We. Antisymmetric waves, which spontaneously intensify at higher values of We, give rise to thin ligaments. At lower We, the initially formed antisymmetric waves get transformed into symmetric interfaces, giving rise to larger ligaments.

The optical measurement techniques such as shadowgraph and Schlieren imaging and laser-based techniques, e.g. Mie scattering imaging and laser-induced fluorescence produce obscure images from the regions of high droplet density near the nozzle since the light scatters from the surface of the droplets. The above mentioned reasons have made it a difficult, yet interesting, task for many researchers to develop various experimental techniques to study the

near nozzle jet instabilities. The transient behavior of liquid injection has been the subject of numerous experimental studies for planar liquid sheets (Crapper et al. [13], Mansour & Chigier [54], Lozano & Barreras [51], Carvalho et al. [7]), and cylindrical liquid jets (Varga et al. [88], Marmottant & Villermaux [55]).

Crapper et al. [13] made a photographic study of KH waves on thin liquid sheets, and found that, contrary to the two-dimensional theory, wave growth is critically dependent upon sheet velocity and distance from the origin. For a given operating condition, a vortex is formed upstream of each wave crest at a constant distance from the nozzle, and it is rapidly increased in size. The boundary layer breaks away from the surface of the wave when appreciable growth has occurred, attributed to the subsequent growth and movement of the vortex.

In a later study on the process of liquid sheet disintegration and breakup, Carvalho et al. [7] used three different experimental techniques to quantify the breakup lengths, disintegration frequencies and spray angles, and showed that the disintegration of the liquid sheet is associated with a periodic process, which is mainly dependent on the absolute air velocity and the air-liquid momentum ratio.

Within the context of numerical studies of gas-liquid turbulent two-phase flow phenomena, the traditional Reynolds-averaged Navier-Stokes (RANS) modeling approach could lead to poor predictions of highly unsteady and complex flow phenomena involving vortical structures due to the intrinsic time- or ensemble-averaging of governing equations. Large-eddy simulation can be used to overcome the problems associated with the averaging involved in RANS approach, but it may not be sufficient to understand the detailed mechanisms in a high-speed multiphase flow since small scales still need to be modeled. In this context, direct numerical simulation (DNS) can be a very powerful tool that not only leads to a better understanding of the fluid mechanics involved, but also provides useful databases for the potential development of physical models for liquid breakup and atomization in gas environments.

In one of the earliest numerical studies on the liquid-jet instability, Lozano et al. [53] implemented a 3D Lagrangian code based on vortex dynamics methods to track the air-liquid interfaces, treated as inviscid vortex sheets. Using the vortex dynamics and altering the initial perturbations orientation with respect to the flow direction, they were able to propose mechanisms to explain the generation of spanwise ligaments parallel to the nozzle and streamwise filaments. Their computations did not take into account the surface tension, though. Later on, Klein [40] performed a Direct Numerical Simulation (DNS) coupled with a Volume-of-Fluid (VoF) scheme for advection of the interface, and addressed the effect of Re on the global jet characteristics, as well as on some spectral properties and turbulence statistics. He was able to show that the turbulence level at the centerline is much lower compared to a single-phase jet.

In all the theoretical (linear and nonlinear) studies above, the instability growth rates have been the main focus. The parameters affecting the most dominant wavenumbers have been investigated and the overall breakup mechanism, breakup length and droplet size have been derived from simplified analyses. With the growth of experimental studies in this area, and with possibility of conducting research at higher Re and We, it was found that the liquid-jet breakup mechanism is more complicated than what the simplified theories are capable of presenting. More recently, the main objective of many experimental and computational studies has been to identify the liquid-jet breakup regimes, their domains of dominance, and the key parameters affecting them. The most important liquid-jet (planar and cylindrical) breakup categorizations developed throughout past decades are summarized in the next section.

1.2.5 Regimes of liquid-jet breakup

Reitz and Bracco [71], following the original work of Ohnesorge [59], identified the operational regimes of a round liquid-jet breakup into four distinct regimes. The regimes were separated by straight lines with negative slope on the log-log plot of We (or Oh) versus Re, as shown in Figure 1.8 reproduced by Sirignano and Mehring [81]. The first domain at lower values of We and Re is the Rayleigh capillary mechanism region. Aerodynamic interaction with the gas is not significant. Symmetric distortion occurs with the formation of droplets that have a diameter of the same order as the jet thickness. Next is the first wind-induced region, where sinuous oscillations occur resulting still in droplet sizes comparable to the jet thickness. The second wind-induced region results in smaller droplets, while the atomization region at the highest values of We and Re results in the smallest droplets. As We or Oh increases, the breakup length tends to decrease. The atomization regime is the domain where the breakup process essentially begins at the orifice exit and is of much broader practical interest but yet far less studied than the other three domains. The atomization domain is the focus of our study here.

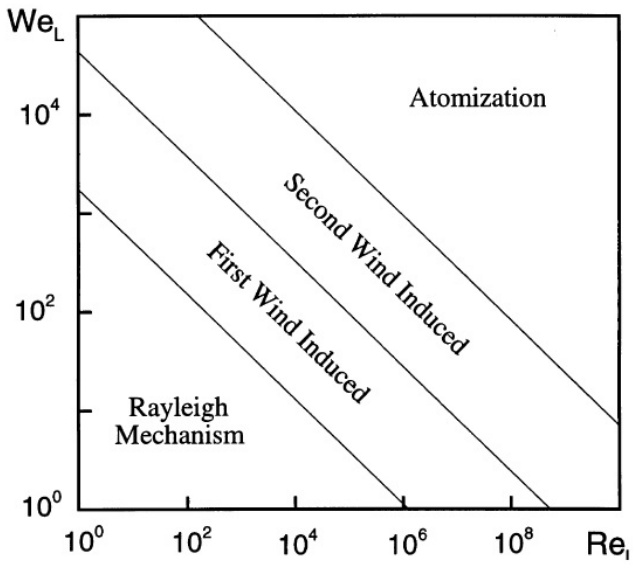

Figure 1.8: Modes of disintegration of round liquid jet on a log-log plot of Re vs. We [81].

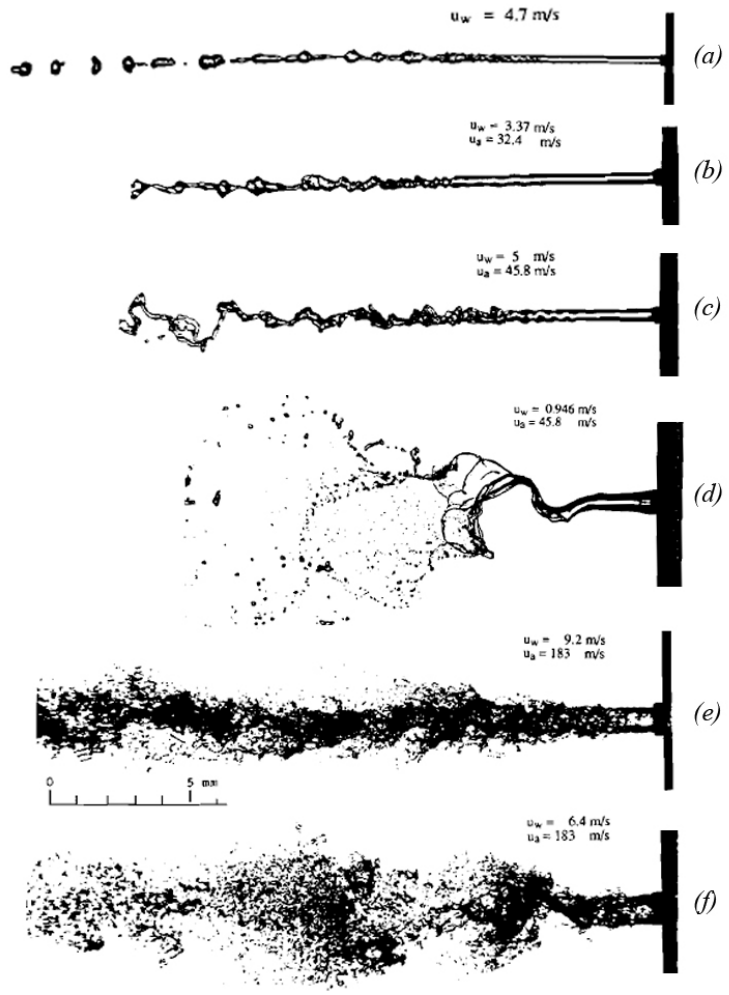

Figure 1.9: Coaxial round liquid jet disintegration modes [20]; axisymmetric Rayleigh breakup (a); non-axisymmetric Rayleigh breakup (first wind-induced) (b); non-axisymmetric Rayleigh breakup (second wind-induced) (c); membrane type breakup (d); fiber-type breakup (e); superpulsating disintegration submode (f).

Fargo and Chigier [20] studied the disintegration of air-assisted (coaxial) round liquid jets and observed several breakup regimes other than the ones that had been introduced already. A summary of their experiments are shown in Figure 1.9. All these experiments are performed at a fixed pressure; i.e. fixed gas density. At low Re and We (low liquid and gas velocities) breakup regimes similar to the ones introduced by Reitz and Bracco [71] were seen. The axisymmetric Rayleigh breakup leading to large droplet of order of magnitude of the jet diameter are seen at the lowest Re range (Figure 1.9a). At higher Re, the instabilities become non-axisymmetric and the aerodynamic effects become significant, corresponding

to the first and second wind-induced breakup regimes (Figures 1.9*b*,*c*). At higher Re, the atomization regime occurs, as shown in Figure 1.9(d)–(f). However, new breakup submodes are introduced in the atomization regime by Fargo and Chigier [20] based on the momentum flux ratio and the liquid Weber number. At higher We ($25 < We < 70$), the round jet develops into a thin liquid sheet (membrane), which forms KH waves and breaks up into drops. Owing to the small radius of curvature, the tip of the ligaments recede and a bulge is formed. If the momentum flux ratio is large enough, the aerodynamic pressure exerted by the gas can then blow up the sheet behind the bulge into a bag or membrane. This breakup regime is often referred to as membrane breakup (Figure 1.9*d*). At still higher Re_l and We ($100 < We < 500$), considerably finer ligaments are produced. Fibers are formed and then peel off the jet. The fibers break into drops via the Rayleigh mechanism. The length of these ligaments is about two to five times the initial jet diameter. From the ligaments, new fibers are peeled off. The diameter of the newly formed fibers increases with increasing axial distance from the nozzle exit. At these large We values, the breakup is said to occur in the form of fibers leading to the formation of smaller droplets (Figure 1.9*e*).

All the above categories can be divided into two submodes: pulsating jet disruption as the normal submode of atomization; and superpulsating jet disruption, which is connected to an extremely high periodical change between low- and high-density regions in the spray. An example of the superpulsating atomization submode is shown in Figure 1.9(f). By reducing Re_l and/or by increasing the aerodynamic We, the intact liquid length of round jets in a co-flowing gas stream decreases. Similarly, the axial distance at which the wave formation and spray pulsation begins also decreases. Nevertheless, the amplitude of the spray pulsations increases with increasing We and/or decreasing Re_l. Based on the experimental observations of Fargo and Chigier [20], if Oh based on aerodynamic Weber and Re_l is higher than about 0.01, the superpulsating submode dominates for the jet disintegration.

Establishing a regime diagram for the coaxial jets similar to that used for pressure atomizers

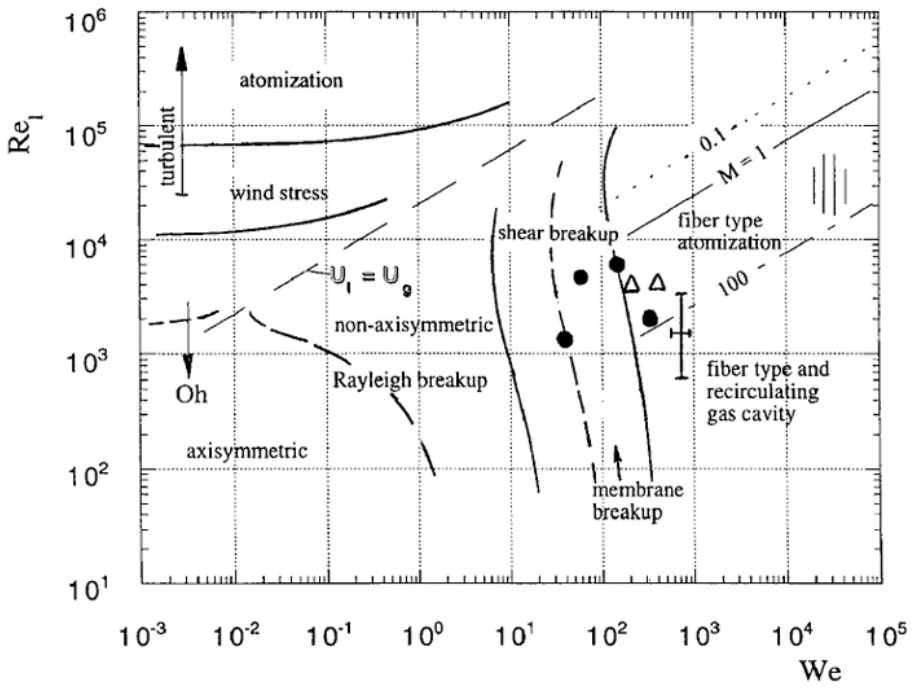

Figure 1.10: Breakup regimes of a coaxial round jet in the parameter space Re_l–We. Lines of constant M are calculated for water-air and $D = 7\ mm$. Here, $We = \rho_g U_g^2 D/\sigma$, $Re_l = \rho_l U_l D/\mu_l$, and $M = \rho_g U_g^2/\rho_l U_l^2$ [30].

(Figure 1.8) is considerably more complicated. The composition of such a diagram can be very cumbersome since one has to deal with a much larger number of nondimensional numbers. An attempt to establish such a diagram was made by Fargo & Chigier [20], which excludes the effect of momentum flux ratio $M = \rho_g U_g^2/\rho_l U_l^2$. A more complete diagram was proposed later by Hopfinger [30]. Hopfinger's diagram is reproduced in Figure 1.10 in a slightly modified form. The various breakup regimes are presented in the parameter space of Re_l and the aerodynamic Weber number. Lines of constant M appear as straight lines in this diagram. Unfortunately, there is not enough experimental data available to give the precise location of the different boundaries to any degree of accuracy, except when $We \to 0$. The farther to the right or top of the diagram, the finer is the spray.

Even though the general knowledge is that the breakup becomes more violent and the liquid core length becomes shorter as Re and We increase, a more careful study of the vortex

dynamics of the jet flow is needed to fully understand the surface deformation since counter-intuitive behaviors are sometimes seen in the jet breakup. Figure 1.11 (left) shows the photograph images taken by Rupe [73] who found that a fully-developed laminar jet of Figure 1.11(b) is more prone to breakup than a turbulent jet of Figures 1.11(c) and 1.11(d). In fact, the jet at $Re = 2200$ shows a burst at about $46D_0$ (estimated from the photograph image) whereas the turbulent jet at $Re = 53,000$ never shows such a violent motion. Pan and Suga [62] simulated the laminar case in Figure 1.11(b) and studied its vortex dynamics to explore the reason behind this behavior. The contours of vorticity and the liquid-jet surface are illustrated in Figure 1.11(e)–(h). They summarized their understanding of the vortical motion as follows: the radial motion due to the axial velocity rearrangement and the surface shear generate initial large-scale longitudinal vortex structures inside the liquid core. Then, those vortex motions are amplified due to the momentum supplied by surface instability and vice versa, growing up to further amplified longitudinal vortices which eventually stretch, distort and burst the liquid core from the inside. Vortex dynamics has been proven to be an important asset in studying the liquid surface deformation and is able to explain the various breakup regimes introduced in this section. This is one of the main objectives of the current study.

The transient behavior of liquid injection has been the subject of numerous experimental studies for planar liquid sheets as well [21, 51, 63, 83]. However, the breakup regimes are not well-categorized based on Re, We, and other parameters as was done for round jets. Typically, these experiments are conducted at atmospheric pressure with very low gas-to-liquid density ratios. Fraser et al. [21] defined three modes of sheet disintegration, described as rim, wave, and perforated-sheet disintegration. Later, Mansour and Chigier [54] suggested that two forces act on the rim of the liquid sheet. Surface tension forces pull the two rims toward the spanwise center of the sheet and this force is proportional to the square root of the surface tension. The inertial force acts in the axial direction and is proportional to $\sqrt{2gp/\rho}$. Without the air flow, the liquid sheet converges toward the axis as a result of

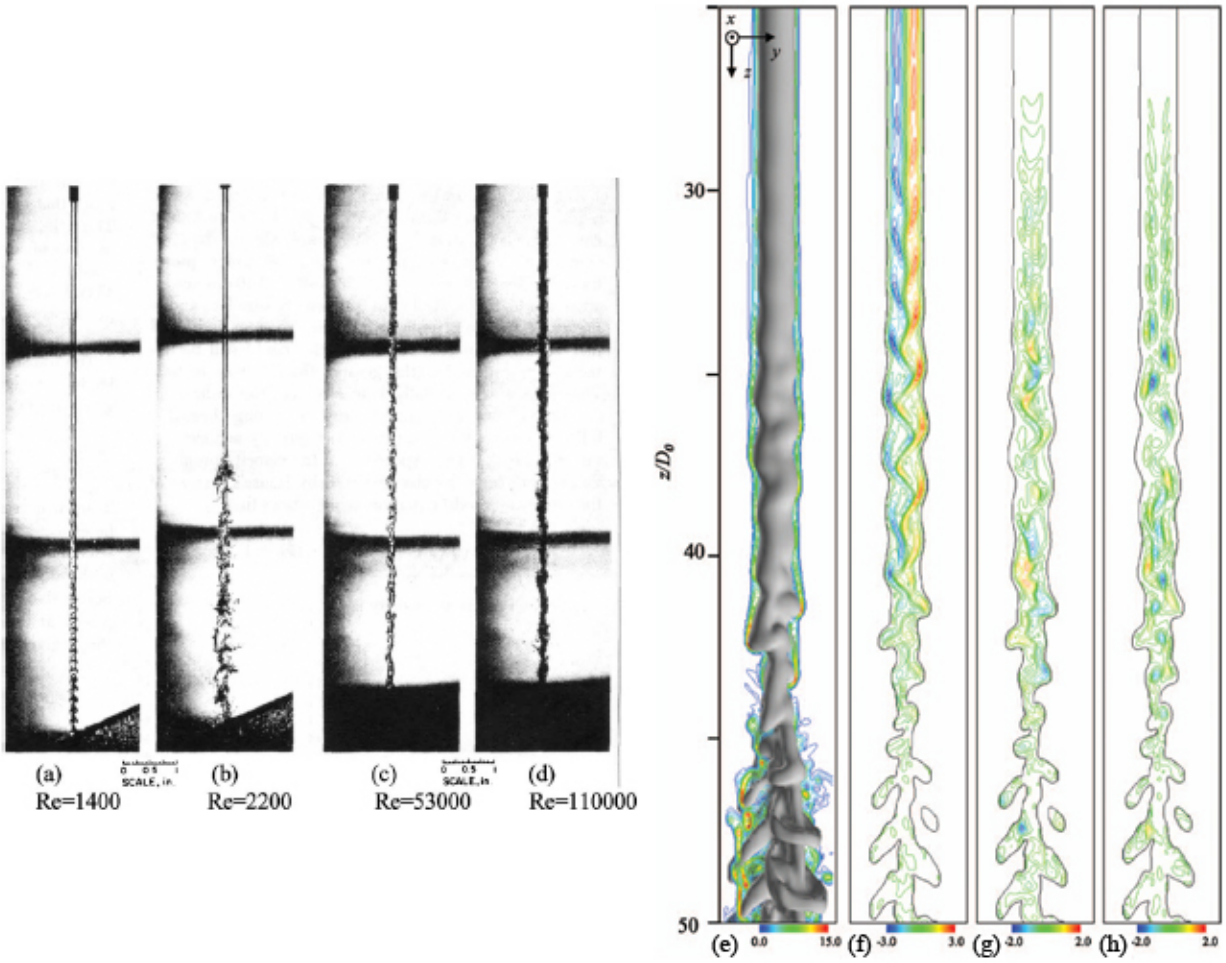

Figure 1.11: Experimentally taken photograph images of free-liquid jets by Rupe [73] (left); (a) and (b) jets from fully developed laminar pipe flows, fluid: glycerine-water mixture; (c) and (d) jets from fully developed turbulent pipe flows, fluid: water. Distribution of instantaneous vorticity fields in an axis plane of case (b) [62] (right); (e) $\sqrt{\omega_x^2 + \omega_y^2 + \omega_z^2}$ in the gas phase; (f) ω_x in the liquid phase; (g) ω_y in the liquid phase; and (h) ω_z in the liquid phase.

surface tension forces. There is a linear increase in convergence length with increases in liquid flow rate. Increasing the liquid flow rate results in small distortions developing on the sheet surfaces that are indicative of the transition to turbulence. The transition occurs at around $Re = 1471$ [54]. These turbulent disturbances are dampened in the downstream region. Turbulent energy production ceases at the nozzle exit and the liquid sheet tends to laminarize as a result of viscous dissipation of turbulent energy.

With an air flow, Mansour and Chigier [54] distinguished two modes of jet breakup: a "mechanical" effect that is due to the action of liquid pressure inside the nozzle and an aerodynamic effect that is due to the action of air friction. The mechanical effect can be best displayed by the large drops that can be seen around the rims of the sheet where the air-liquid relative velocity is low. Droplets detached from the rim become smaller as the liquid flow rate is increased while maintaining the same air pressure. As the liquid mass flow-rate increases, the liquid sheet issuing from the nozzle is drawn up into small but ordered "cell" structures. These structures are bounded by large diameter bridges (ligaments) containing thin membranes inside. The bridges are the origin of the large drops in the spray and the membranes contribute to the formation of the smaller droplets. Membrane shattering

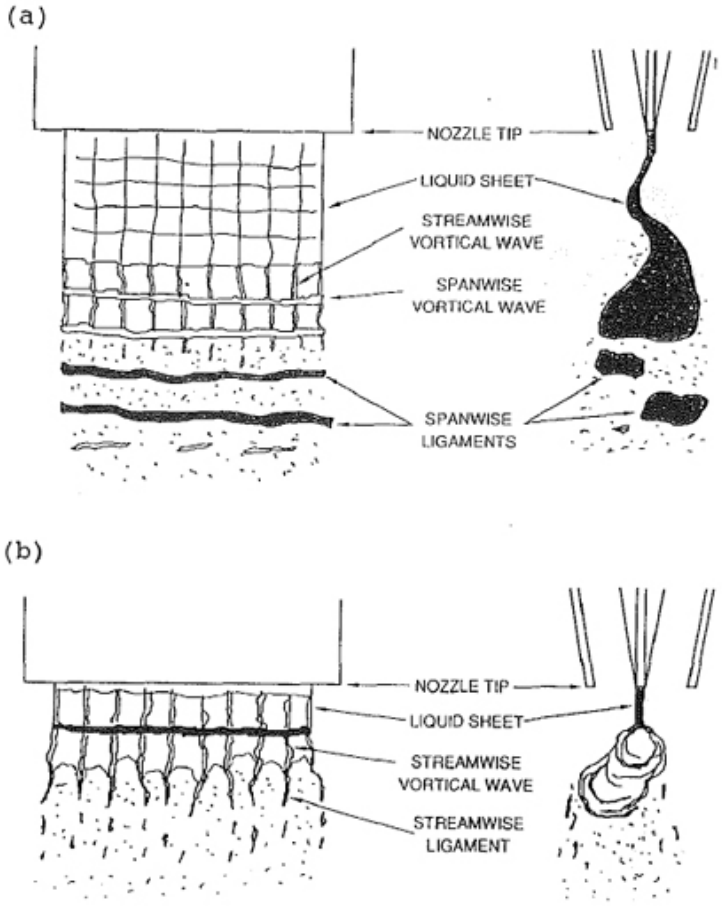

Figure 1.12: Schematic of face and side views detailing the structures in the breakup of a liquid sheet for (a) cellular breakup, and (b) stretched streamwise ligament breakup [83].

precedes the bridge breakup and a point is reached where the leading edge of the sheet is anchored to the remaining liquid only through the cell frame.

Around the same time, Stapper et al. [83] observed the same two liquid sheet breakup mechanisms in their experiments and described the characteristics of these breakup regimes. A schematic of the face and side views of the structures that form during the breakup of a sheet provided by Stapper et al. [83] is illustrated in Figure 1.12. The air-stream velocity is an order of magnitude greater than the liquid sheet velocity in their experiments. The "cellular breakup" occurs at higher relative air-to-liquid velocities, but where the breakup is well displaced from the nozzle tip. This breakup mechanism was also observed by Mansour and Chigier [54], as illustrated in Figure 1.13(a), and is characterized by the presence of spanwise vortical waves (vortical waves are associated with ligaments in this section) that are approximately equal in strength to the streamwise vortical waves. As the sheet is extruded by the shearing action of the air, the membranes stretch between the spanwise and streamwise vortical waves, forming cell-like structures (see Figure 1.13a). Eventually, the sheet is stretched to the point where (1) the streamwise vortical waves and connecting membranes burst, and (2) the spanwise vortical waves separate into spanwise ligaments. The small droplets in the resultant spray distribution originate from the bursting membranes. Larger droplets are associated with the breakup of the streamwise waves. The largest droplets are associated with the fragmentation of the spanwise ligaments.

The second breakup mechanism, referred to as "stretched streamwise ligament breakup" occurs at low liquid velocities. As shown in Figure 1.13(b) from Mansour and Chigier [54], this mechanism is dominated by the streamwise vortical waves in the breakup process. As the sheet is stretched by the co-flowing air, the streamwise vortices amplify with thin liquid membranes stretched in between. The sheet is a corrugated structure with the membranes stretched sinusoidally about the plane of the sheet. As a result, the membranes are stretched by the counter-rotation of the bounding vortices. When the membranes burst, the liquid film

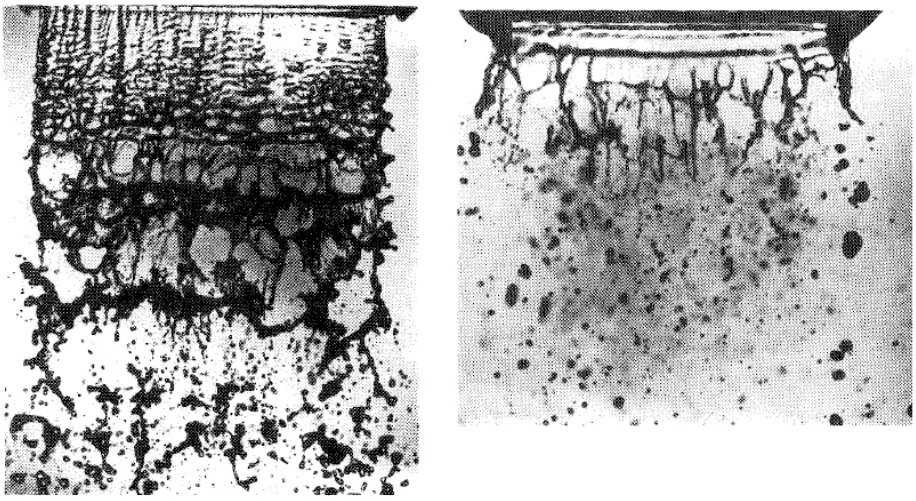

Figure 1.13: Cellular breakup of a water sheet with air co-flow, $\dot{m}_{liq} = 45.42\ g/s$ (a); stretched streamwise ligament breakup of a water sheet with air co-flow, $\dot{m}_{liq} = 11.34\ g/s$ (b) [54].

forms small drops, while the vortical waves form streamwise ligaments. These ligaments are then stretched by the shearing action of the air and transition to higher rotating velocities, and finally fragment into relatively large drops when the surface tension forces can no longer keep the ligaments intact. Stapper et al. [83] also showed that the variation in the liquid properties did not alter the general character of the two breakup mechanisms. However, the change in liquid properties had a pronounced effect on the time and length scales. Most of their study was focused on relatively low Re (e.g. 100–3000) and low We of $O(10^1$–$10^3)$.

The two breakup mechanisms introduced by Stapper et al. [83] were also seen by later experimentalists [51, 63]. Lozano and Barreras [51] used planar laser-induced fluorescence (PLIF) for the first time to visualize the air-flow field in the near field of an air-blasted breaking water sheet. They used the air-water momentum ratio to characterize different breakup regimes. Their two-phase flow visualization revealed detachment of the air boundary layer over the air-water interface behind the zones of strong curvature, and identified the pressure field induced by these vortices as a cause of the enhanced sheet flapping and instability growth. Their experiments were conducted at fairly high Re of $O(10^4)$ and low We of $O(10^3)$.

The cellular breakup mechanism was investigated for a planar liquid sheet with assisting air streams from an air-blast nozzle, by Park et al. [63]. They showed that the cell size decreases by increasing the relative velocity between the gas and liquid. The measured average size of cellular structures, and thus, the dominant wavelength was found to be proportional to the inverse square of the relative velocity between air and liquid, consistent with the linear temporal instability theory. They also found that turbulent transition does not affect the breakup length and time scales, as the length scale of turbulence is much less than a typical cell size by about one order of magnitude.

1.2.6 Droplet-size distribution

The common purpose of breaking a liquid stream into spray is to increase the liquid surface area so that subsequent heat and mass transfer can be increased or a coating can be obtained. The spatial distribution, or dispersion, of the droplets is important in combustion systems because it affects the mixing of the fuel with the oxidant, hence the flame length and thickness. The size, velocity, volume flux, and number density of droplets in sprays critically affect the heat, mass, and momentum transport processes, which in turn, affect the flame stability and ignition characteristics. Smaller drop size leads to higher volumetric heat release rates, wider burning ranges, higher combustion efficiency, lower fuel consumption and lower pollutant emissions. In some other applications however, small droplets must be avoided because their settling velocity is low and under certain meteorological conditions, they can draft too far downwind.

Most previous researches have attempted to assess the manner by which the final droplet-size distribution – after the atomization is fully developed – is affected by the gas and liquid properties and by the nozzle geometry [7, 18, 52, 54, 55, 58, 79, 83, 88]. General conclusions are that the Sauter Mean Diameter (SMD $= \Sigma N_i d_i^3 / N_i d_i^2$, where N_i is the number of droplets

per unit volume in size class i, and d_i is the droplet diameter) decreases with increasing relative gas-liquid velocity, increasing liquid density, and decreasing surface tension, while viscosity is found to have little effect [83].

Dombrowski and Hooper [18] developed theoretical expressions for the size of drops produced from fan spray sheets, and showed that under certain operating conditions in super atmospheric pressures, the drop size increases with ambient density. Verified experimentally, the drop size initially decreases, passing through a minimum with further increase of ambient density. They also showed that, for relatively thin sheets ($h/\lambda < 1.25$; h is sheet thickness and λ is the unstable wavelength), the drop size increases with the surface tension and the liquid density, but depends inversely on the liquid injection pressure and the gas density. For relatively thick sheets ($h/\lambda > 1.5$), however, the drop size is independent of surface tension or injection pressure and increases with increasing gas density. In another linear stability analysis, Senecal et al. [79] derived expressions for the ligament diameter for short and long waves. They showed that the ligament diameter is directly proportional to the sheet thickness, but inversely to the square root of gas Weber number (We_g). They also analytically related the final droplet size to the ligament diameter and the Ohnesorge number, and showed that the SMD decreases with time. The gas viscosity and the nonlinear physics of the problem, however, were neglected.

Mansour and Chigier [54] measured the SMD along and across the spray axis using a phase Doppler particle analyzer (PDPA). The PDPA method is based upon the principles of light scattering interferometry. Measurements are made at a small, non-intrusive optical probe volume defined by the intersection of two laser beams. As a particle passes through the probe volume, it scatters light from the beams into a multi-detector receiving probe. The phase shift between the Doppler burst signals from different detectors is proportional to the size of the spherical particles. SMD initially decreased followed by a gradual increase along the spray axis. The initial decrease was shown to be due to secondary atomization

and the subsequent increase was due to droplet coalescence. At all axial locations, SMD increased substantially and its velocity decreased notably from the central part toward the edge of the spray. The larger droplets seen around the rims of the sheet were due to the mechanical effects of the lower air-liquid relative velocity on the sheet edges. They also showed a significant reduction in droplet size by increasing the air-to-liquid mass-flux ratio.

Lasheras et al. [44] measured the SMD along the axis of air-assisted ($U_l << U_g$) round liquid jets using high-speed flow visualization and PDPA techniques, and showed that there is a non-monotonic variation of the droplet size measured along the central axis of the spray in the far-field; i.e. $x/D > 10$. The SMD decreases with axial distance (x) until it reaches a minimum at around $x/D \approx 20$–30; the SMD increases again as we move further downstream from that location. They described this behavior as the competition between turbulent breakup and coalescence effects. Assuming local isotropy and fully developed turbulence at the central axis of the jet, the argument made is that both turbulent breakup and coalescence depend only on the value of the dissipation rate of turbulent kinetic energy (ϵ).

The maximum droplet size that can withstand turbulent breakup is

$$d_c \propto \left[\frac{U_g^3}{D_g(1+m)}\right]^{-2/5} \left(\frac{\sigma}{\rho_g}\right)^{3/5}, \tag{1.4}$$

where m is the mass flux ratio and D_g is the gas nozzle diameter, while the maximum droplet size above which coalescence is negligible is $d_{max} \approx \mu_g/\rho_l\, \epsilon^{-1/4}$ [43]. Thus, in regions of high ϵ (after the length of the liquid core) turbulent breakup dominates, while further downstream, as ϵ quickly decays, turbulent breakup ends, and coalescence effects determine the drop size [44]. They did not visualize any droplet coalescence in the downstream region though.

Lozano et al. [51] correlated fluid properties, nozzle geometry and flow conditions with the mean droplet diameter obtained by laser diffractometry. They found that the mean diameter decreases with increasing gas velocity. For a fixed gas velocity and different liquid velocities,

the mean diameter has a minimum near the frequency maximum. At large downstream distances for a fixed gas velocity, the diameter always decreases with increasing momentum flux ratio due to secondary breakup.

At present, it is not possible to predict the droplet diameter distribution as a function of injection conditions. For combustion applications, many empirical correlations predict the droplet size as a function of injection parameters [45]; however, more detailed studies of fundamental breakup mechanisms are needed to construct predictive models. A summary of several of these expressions for airblast atomization was compiled by Lefebvre [45]. The dependence of the primary droplet size (d) on the atomizing gas velocity (U_g) is most often expressed as a power law, $d \propto U_g^{-n}$, where $0.7 \leq n \leq 1.5$. Physical explanations for particular values of the exponent n are generally lacking. Varga et al. [88] found that the mean droplet size is not very sensitive to the liquid jet diameter – actually opposite to intuition; the droplet size is observed to increase slightly with decreasing nozzle diameter. This effect was attributed to the slightly longer gas boundary-layer attachment length. They also observed a clear reduction in droplet size with lowering surface tension. The ratio of the water SMD to the ethanol SMD appeared to be very close to $\sqrt{\sigma_{water}/\sigma_{ethanol}} \approx \sqrt{3}$, which suggests the scaling $d \propto We_g^{-1/2}$, where We_g is the Weber number based on gas properties and jet diameter. Their study was limited to very low Oh ($\sim 10^{-3}$).

Marmottant and Villermaux [55] presented probability density functions (PDFs) of the ligament size and the droplet size in their experimental study of the round liquid spray formation. The ligament size d_l was found to be distributed around the mean in a nearly Gaussian distribution, but the droplet diameter d was more broadly distributed and skewed. Rescaled by d_l, which depends on the gas velocity U_g, the size distribution keeps roughly the same shape for various gas flows. The average droplet size after ligament breakup was found to be $d \simeq 0.4 d_l$, with its distribution $P(d)$ having an exponential fall-off at large diameters parameterized by the average ligament size $\langle d_l \rangle$; $P(d) \sim \exp(-nd/\langle d_l \rangle)$. The parameter

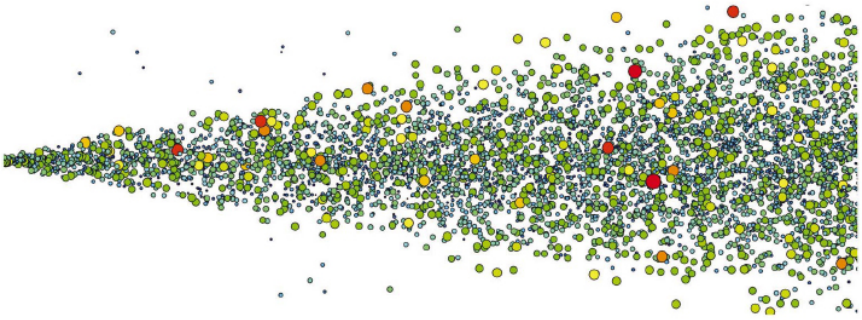

Figure 1.14: Cross-sectional view of the spray using Nukiyama-Tanasawa distribution as initial conditions. Contour color is scaled with the droplet size; red for large and blue for small droplets. Droplet gradation is shown. As a result, the droplet size increases outwardly (proportional to increasing radial direction) [94].

$n \approx 3.5$ slowly increased with U_g. The mean droplet size in the spray decreases like U_g^{-1}. Most of their experiments were at low Re and low We range.

Yoon [94] examined the initial droplet distributions at the liquid core for various Weber number and pulsing conditions. He found that the average droplet diameter tends to be larger and the droplet velocity is smaller at larger radii for each downstream location. The SMD decreases with increasing the axial location because of the gradual disappearance of the smaller droplets further downstream. Their simulations captured the expected reduction in the mean diameter with increasing We or jet velocity. Yoon [94] also showed that droplet gradation occurs due to the dynamic segregation of small and larger droplets in both the axial and radial directions. As shown in Figure 1.14, larger droplets are dispersed by the spray initial cone angle and subsequent interactions with turbulent eddies in the entrained air, while smaller droplets are generally swept toward the spray center line by aerodynamic drag interactions with the entrained air. He explained that these entrained smaller droplets maintain their launching velocity in the axial direction because (1) these small droplets are surrounded by the larger droplets and, thus, preserve their initial velocity; and (2) the entrained air affects the radial velocity of the small droplets only, not the axial component of the velocity.

In a later study, Yoon and Heister [95] studied the effects of We, jet speed and orifice length on the number of droplets and the SMD. They showed that for low speed jets, viscosity does not play a significant role in droplet sizes. As We increases many more atomization events occur and the jet loses more mass; hence SMD decreases while the number of droplets and the standard deviation of the droplet size increase. Their results matched perfectly with the correlations given by Wu et al. [93]. Wu et al. [93] provided both an empirical model and experimental observations for the SMD, emphasizing the role of turbulence in the process. They correlated SMD to We using the following model;

$$\frac{\text{SMD}}{D} = \frac{46.4}{We^{0.74}}. \tag{1.5}$$

where D is the nozzle diameter. Yoon and Heister [95] also showed a parabolic behavior with the number of droplets growing as the square of circulation around the rotating ring. The total number of droplets, number of drops per vortex ring, and its standard deviation all tend to increase with increasing the jet speed. Their results also indicate that more atomization events tend to occur with an increased orifice length. Even though the orifice length does not notably change SMD, the number of produced droplets and its standard deviation increase significantly by increasing the orifice length.

Herrmann [27] discussed the impact of grid resolution and refinement on the drop size PDF for the round jets, finding a significant decrease in SMD with increasing mesh resolution, as shown in Figure 1.15. Grid-independent drop sizes can be achieved for liquid structures resolved by at least six grid points. Breakup at the tip of the jet is dependent on the grid resolution, since increasing the grid resolution effectively decreases the automatic breakup length scale. Analyzing qualitatively the locations where drops are produced, Herrmann [27] found that a significant fraction is produced at or near the leading tip (Figure 1.15) since there the liquid jet should experience large aerodynamic forces due to large velocity differences between liquid and the essentially stagnant gas. Nonetheless, significant amounts of liquid

Figure 1.15: Impact of G-grid resolution at $t = 4\mu s$ for constant flow solver resolution $\Delta x = 1$ μm and $\Delta x_G = 1.56$ μm (left), $\Delta x_G = 0.78$ μm (center), and $\Delta x_G = 0.39$ μm (right). Only the region close to the liquid core is shown [27].

drops are also generated at the jet surface, so much that near the end of the computational domain the jet appears to disintegrate into large-scale, highly irregularly shaped liquid blobs.

Rather than measuring the droplet diameter and its distribution, Chesnel et al. [8] proposed a surface density equation to describe the subgrid spray characteristics. The surface density is defined as the ratio of the interface area with the considered control volume. Contrary to the droplet diameter, this variable is general enough to be applied to non-spherical liquid parcels such as ligaments, liquid sheets, etc. Besides the convection and diffusion of the surface density, they proposed a source term related to the physical phenomena that influence the production and/or the destruction of the interface area, including destruction of surface density due to the evaporation process, production of surface density due to liquid/gas mixing, and the production/destruction of surface density by the mean shear, turbulence, and liquid structure interactions. They plotted the variation of surface density and liquid fraction both along and across the injection axis, and observed a peak in the liquid volume fraction located at $r = 0.5D$ at an axial distance of $x = 5D$. This peak corresponds to an axial location where a strong velocity shear exists between the liquid and the gas phases.

In this zone, the interface is strongly deformed by the liquid-gas instabilities. Farther in the jet, at $x = 10D$ and $x = 20D$, the mean shear level drops lower. As a consequence, the profiles of standard deviation of volume fraction are much smoother and do not present specific peaks. Chesnel et al. [8] showed that the global surface density level increases with the injection velocity. The atomization process becomes more "efficient with increasing turbulent conditions imposed by the injection velocity.

More recently, Negeed et al. [58] analytically and experimentally studied the effects of nozzle shape and spray pressure on the liquid sheet characteristics. They showed that the SMD decreases by increasing Re_l or by increasing the water sheet We since the inertia force increases by increasing both parameters. The spray pressure difference was also shown to have a similar effect to Re_l on the mean droplet size. Their study was limited to very high Re_l values (10,000–36,000) and very low We_g values of $O(10^1)$.

1.2.7 Spray angle

The spray angle is a global quantity of considerable practical interest in atomization processes. In combustion chambers the spray angle needs to be controlled as it affects the mixing of the fuel with the oxidant, hence the flame length and thickness, which, in turn, affect the flame stability and ignition characteristics. Measuring the spray angle is also a proper way to measure the liquid sheet instability growth, which controls the rate and intensity of the atomization. In this section the most important relations that have been proposed in the literature to correlate different flow parameters to the spray angle are presented. For a round jet, the spray angle is also sometimes called the "cone angle", while it is usually called "wedge angle" for planar sheets.

Mansour and Chigier [54] examined the effects of air pressure and liquid flow rate on the spray angle in a liquid sheet disintegration with air co-flow. Substantial decrease in the

spray angle occurs as a result of increasing the liquid flow rate while maintaining the same air pressure. This behavior was related to the reduction in the specific energy of air per unit volume of liquid leaving the nozzle. Moreover, increasing the liquid flow rate reduces the air-liquid relative velocities at the interface, which is accompanied by a reduction in the amplitude of oscillations of the liquid sheet, corresponding to a decrease in the spray angle. Increasing the air pressure for a fixed liquid flow rate results in an increase in the spray angle. Here again, it is seen that the effect of increasing the specific energy of air per unit volume of liquid results in a substantial increase in the amplitude of oscillations of the liquid sheet. The initial perturbations are amplified at a much faster rate and the liquid sheet becomes highly unstable. The amplitudes of oscillation are the main parameters controlling the spray angle. Mansour and Chigier [54] measured a reduction in the spray angle from 125^o to 10^o as the liquid mass flow rate is increased from 10 to 65 g/sec.

The growth rate of the liquid-gas shear layer is related to the liquid jet core length, which for large gas velocities gives an angle $\tan\gamma \approx \sqrt{M}/6$; where M is the momentum flux ratio [43]. This relation remains valid as long as the liquid core remains cone-like, that is, as long as M is less than about 30, giving a maximum angle γ_{max} of about 40^o. The spray angle is generally larger than the liquid-gas shear layer angle γ (assuming a steady shear layer) because the inertia of the droplets allows them to escape the shear layer boundary. Raynal [70] measured spray angles α of about 50^o with respect to the liquid cone surface and this angle was found to depend only weakly on M. The stability analysis of Lasheras & Hopfinger [43] suggests a spray angle α of 45^o when $M^{1/2} >> 1$. Because the liquid cone angle increases with M, the total angle θ of the spray cone decreases with M from $\theta = 2(\alpha - \gamma/2) \approx 90^o$ to 60^o.

Carvalho et al. [7] performed detailed measurements of the spray angle versus gas and liquid velocities in a planar liquid film surrounded by two air streams in a range of Re from 500 to 5000. The results of their spray visualizations are recast in Figure 1.16. For low gas-to-

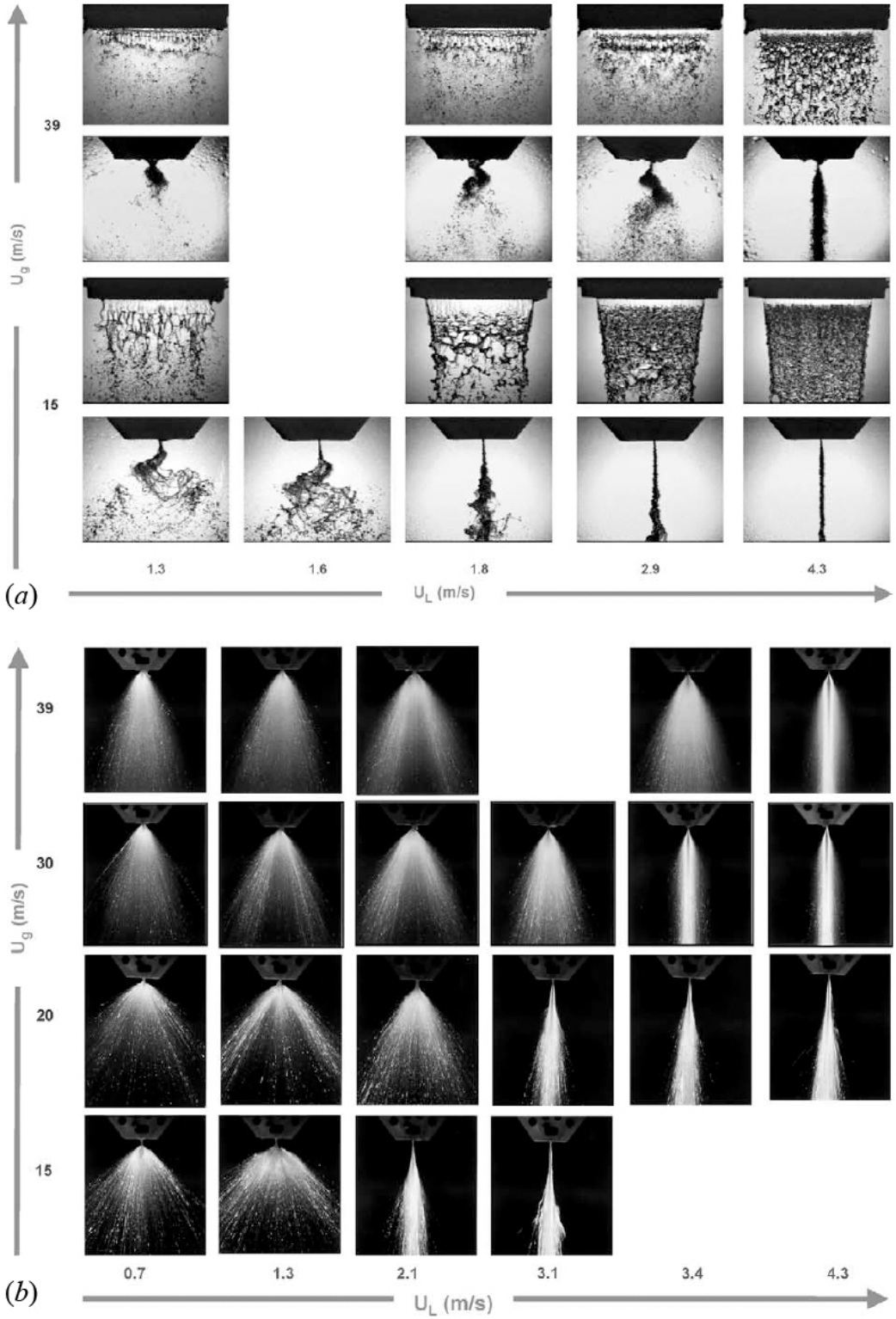

Figure 1.16: Visualization of the flat liquid film for different liquid and air velocities: (a) front view and side view of the liquid film for $U_g = 15$ m/s and $U_g = 39$ m/s, using strobe light illumination; (b) side view of the liquid film for $15 \leq U_g$ (m/s) < 39, using laser light sheet illumination [7].

liquid momentum ratio, the dilatational wave dominates the liquid film disintegration mode. The atomization quality is rather poor, with a narrow spray angle (e.g. $U_g = 15$ m/s and $U_l \geq 1.8$ m/s). For higher gas-to-liquid momentum ratios, sinusoidal waves dominate and the atomization quality is considerably improved, as the spray angle increases significantly (e.g. $U_G = 39$ m/s and $U_L \leq 3.9$ m/s). For considerably higher gas-to-liquid momentum ratios, namely with low liquid velocities or high gas velocities (e.g. $U_g = 15$ m/s and $U_l \leq 0.7$ m/s; or $U_g = 39$ m/s and $U_l \leq 2.9$ m/s), the liquid film emerging from the nozzle is rapidly torn into small fragments by the immediate interaction between the liquid and the impinging air streams. For considerably low gas-to-liquid momentum ratios, namely for high liquid velocities or low air velocities (e.g. $U_g = 15$ m/s and $U_l \geq 4.3$ m/s) no wave is seen on the liquid surface.

Figure 1.17 shows measured spray angles making use of the laser light sheet technique by Carvalho et al. [7]. For all operating conditions, regardless of the gas velocity, a region of maximum spray angle occurs, followed by a sharp decrease for higher values of liquid

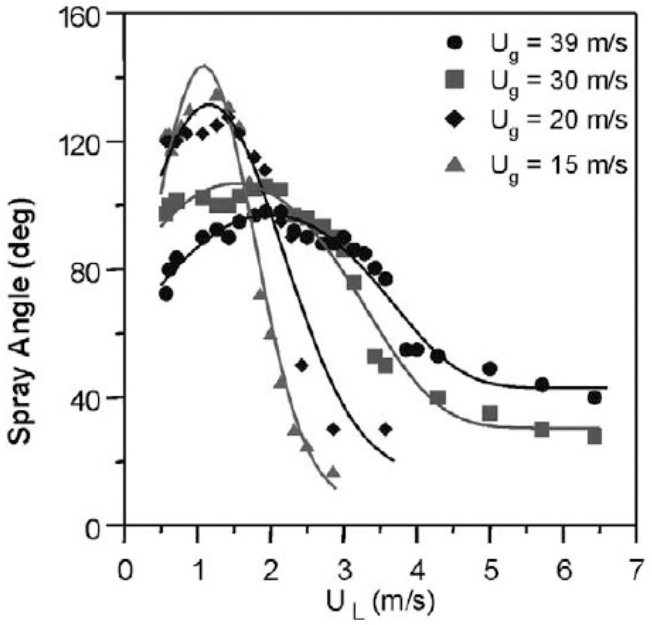

Figure 1.17: spray angles as function of liquid film velocity for $15 \leq U_G$ (m/s) < 39, using laser light sheet visualization [7].

velocity. The maximum values of the spray angle (e.g. for $U_g = 15$ m/s the maximum angle is observed at $U_l = 1.3$ m/s) are displaced for higher values of liquid velocity as the gas flow rate increases (e.g. for $U_g = 30$ m/s the maximum angle is observed at $U_l = 1.8$ m/s), the maximum value decreasing with gas flow rate.

Experimental measurements of Park et al. [63] show consistency with the results of Carvalho et al. [7]. At a fixed gas velocity, the spatial growth rate of the waves decreases with increasing liquid velocity. A higher gas velocity results in a larger wave amplitude and a higher growth rate with a shorter breakup length. This implies that the spatial growth rate cannot be predicted properly by the linear analysis in case of a high Weber numbers. Park et al. [63] also indicated an exponential increase in the wave amplitude with distance from nozzle exit.

Instability enhancing parameters in liquid sheets were analyzed by Sander and Weigand [74, 75]. They showed the significant influence of the mean axial velocity profile (resulting from the variation of the nozzle design) on the development of surface instabilities. The kinetic energy per unit mass of the inflow was found to be one of the major influencing parameters. It was also concluded that bubbly inflows do not enhance film instabilities; in fact, the bubble size and especially small sized bubbles can reduce instabilities and the spread rate.

1.2.8 3D single-phase vortex dynamics and jet instabilities

There have been several studies of the 3D jet instabilities from the vortex dynamics perspective. Most of them, however, do not address density and viscosity discontinuities. These studies have mainly focused on understanding and relating the vortex stretching [65], vortex tilting [42], and baroclinic effects [78] to the 3D single-phase instabilities. Earlier experimental studies in this field (Widnall & Sullivan [92], Widnall et al. [91], Breidenthal [6], Jimenez [38], Bernal & Roshko [4], Liepmann & Gharib [49]) have been followed and reproduced in

more detail by numerical simulations (Ashurst & Meiburg [3], Martin & Meiburg [56], Comte et al. [11], Collis et al. [10], Schoppa et al. [77], Brancher et al. [5], Danaila et al. [15]).

Pope [65] was the first to suggest that the stretching of turbulent vortex tubes by the mean flow has a significant influence on the process of scale reduction. Although not pointed out in his paper, this influence directly relates to the size of ligaments and pinched-off droplets in liquid jet disintegration process.

The existence of streamwise vortices in the planar mixing layers was reported by several experimentalists [4, 6, 38, 42]. Briedenthal's [6] flow visualizations of 2D mixing layers clearly showed the presence of a secondary vortex structure in the flow direction. In the planar view, these streamwise structures appeared as thin periodic streaks spaced with a certain spanwise wavelength. Jimenez [38] explored the fluctuations in the spanwise distribution of the mean velocity of a plane shear layer. He proposed that the deformation of the shear layer implies the presence of vorticity aligned in the transversal direction, which, when added to the classical spanwise component of vorticity (KH vortex) in the two-dimensional cores, suggests the longitudinal (streamwise) vortices. Bernal and Roshko [4] noticed that the streamwise vortex

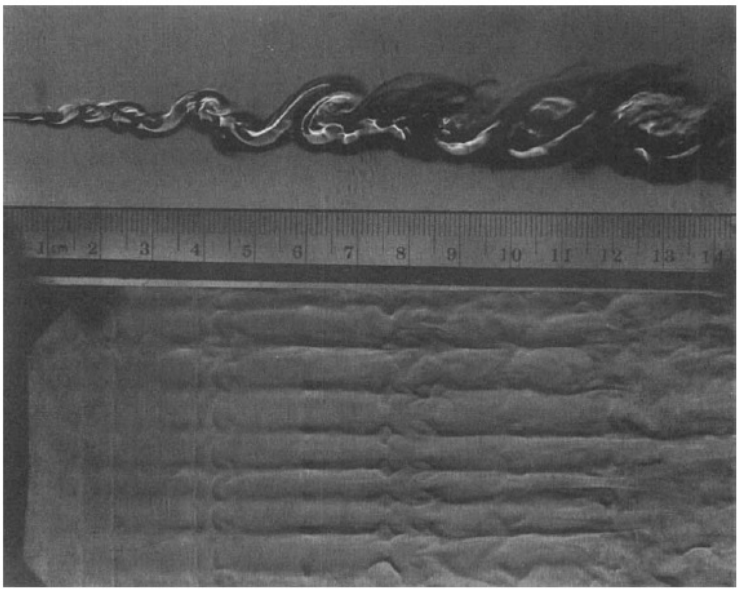

Figure 1.18: Instantaneous Schlieren picture of the helium-nitrogen mixing layer [4].

is actually a hairpin vortex that wraps around the primary spanwise vortices. Figure 1.18 is a photo from their experiments that shows the existence of streamwise vortex-lines (streaks). The hairpin vortex changes direction and thereby produces counter-rotating vortex pairs in the streamwise direction, as is illustrated in the schematic of Figure 1.19 from Bernal & Roshko. These warped vortex structures, linking adjacent pairs of primary KH vortices, align themselves with each other so that, in plan view they appear to be straight streamwise streaks, as seen in the top view of Figure 1.18.

Liepmann and Gharib [49] studied the role of streamwise vortex structures in the near-field evolution of a round water jet flowing into a water tank, using laser-induced fluorescence imagining. They examined that the initial vortex rings remain axisymmetric for a short distance until an azimuthal instability occurs. The secondary instability first develops in the braid region between vortex rings producing streamwise vorticity. Azimuthal instabilities develop from the rings too, although more slowly than in the braid region. This behavior is similar to the vortical structures observed in 3D mixing layers [4, 6, 38]. They did not discuss hairpin vortices for the round jet in connection with streamwise counter-rotating vortex pairing, though. Liepmann & Gharib [49] also showed that the number of azimuthal modes increases with Re, until a sudden drop occurs when the boundary layer undergoes

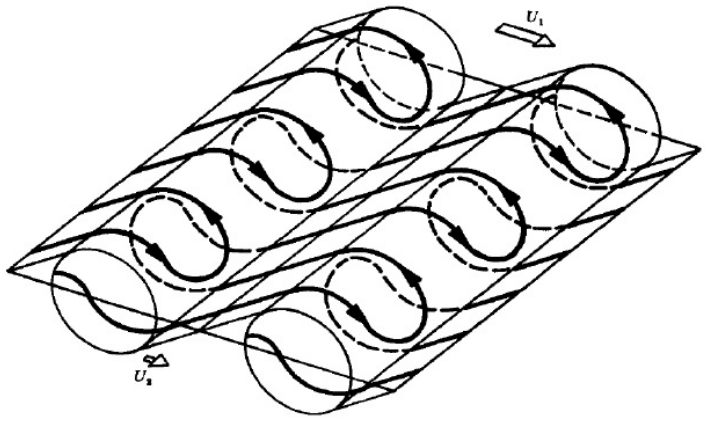

Figure 1.19: Topology of streamwise vortex lines showing hairpin vortices in 3D mixing layers [4].

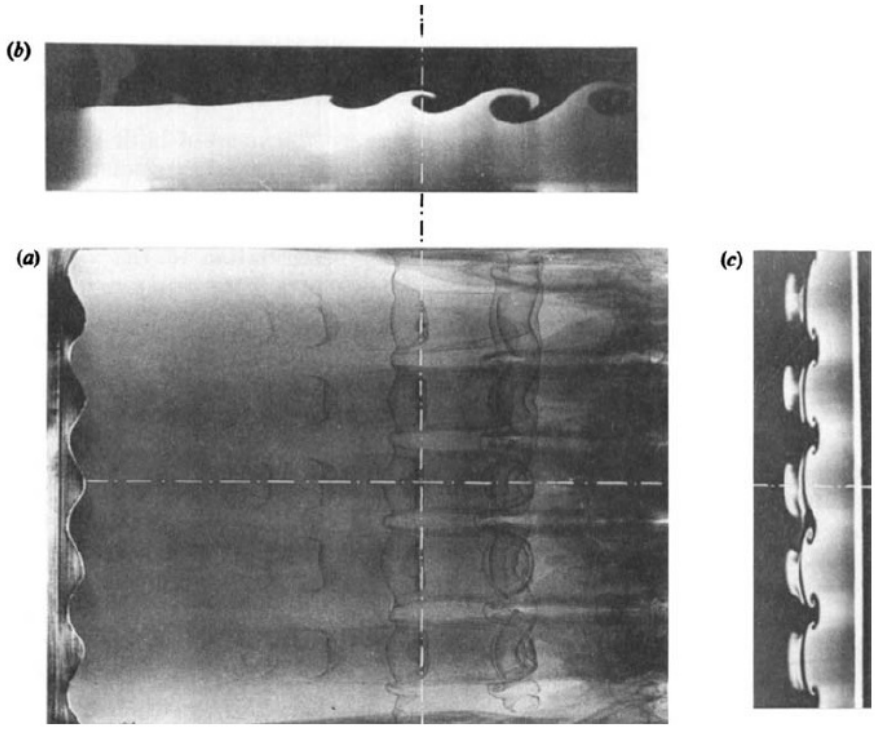

Figure 1.20: Composite flow visualization of the plane shear layer subjected to a single horizontal perturbation. Plan view obtained using the DIV technique (a); LTF simultaneous cross-cuts (b, c). Cross-cut side view of a vertical plane through the central axis of the channel (b); cross-cut end-view of a plane normal to the flow direction (c) [42].

transition to turbulence.

The 3D development of a plane free shear layer subjected to small sinusoidal horizontal (indentations) and vertical (corrugations) perturbations periodically placed along the span was experimentally studied by Lasheras & Choi [42]. Figure 1.20 obtained from their experiments, shows the appearance of hairpin vortices similar to what was observed by Bernal & Roshko [4]. Lasheras & Choi [42] attributed the appearance of three-dimensionality to the stretching along the principal direction of the positive strain. The maximum amplification occurs for the vortex lines near the braid region, where the positive strain is maximum. Therefore, they called these vortices "strain-oriented vortex tubes" and described a mechanism for evolution of the 3D instabilities, where vortices enhanced by stretching are pulled more strongly into the streamwise direction until there are a series of hairpins extending from

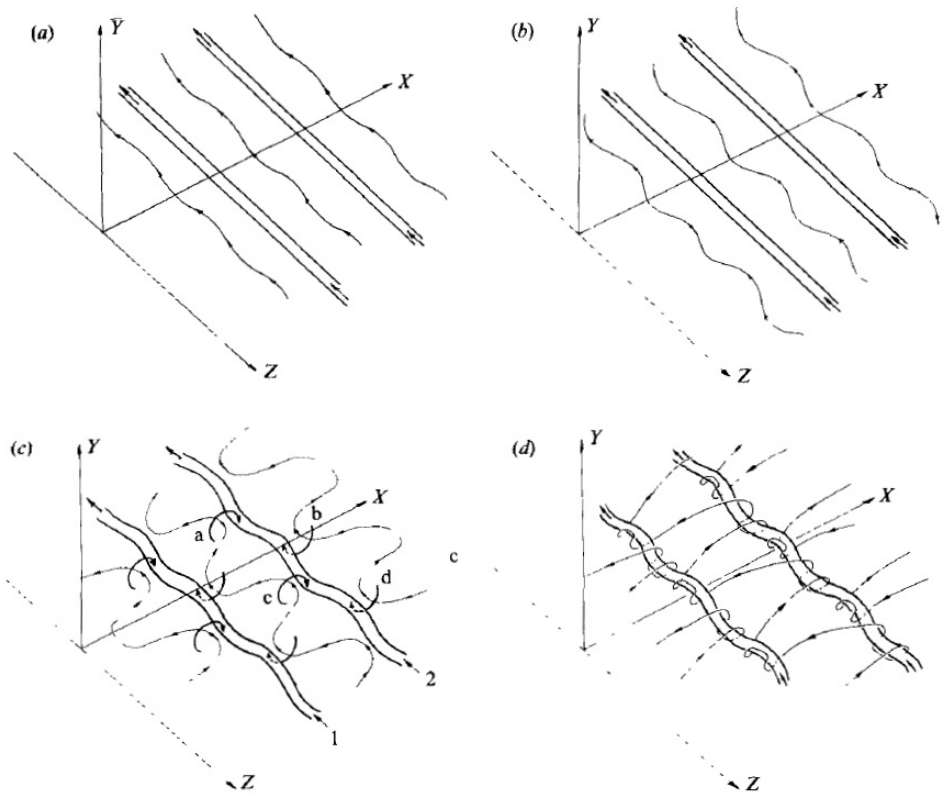

Figure 1.21: Schematic representation of the development of the 3D instability. The perturbation component of the vorticity existing in the braids is amplified through stretching. The maximum amplification occurs along the principal direction of the positive strain at the free stagnation point. Flow direction is along X [43].

the underside of one roller to the top of its neighbor. They also realized the non-uniformity in the wavelength of the consecutive vortex pairs and thereby, modified the schematic given by Bernal & Roshko [4] (Figure 1.19) to account for this variation. The schematic representation of the development of the hairpin vortices is given in Figure 1.21, taken from Lasheras & Choi [42].

The effect of stratification on streamwise vortex structure in the shear layer has been investigated experimentally by Schowalter et al. [78]. Figure 1.22 shows a cartoon for the behavior of the layers in the cross-section of a KH roller [78]. The baroclinic torque will form two vortex sheets of opposite sign along the unstable interface. Each vortex sheet will cause a tilting of the other, which will lead to a greater cross product of the pressure gradient and

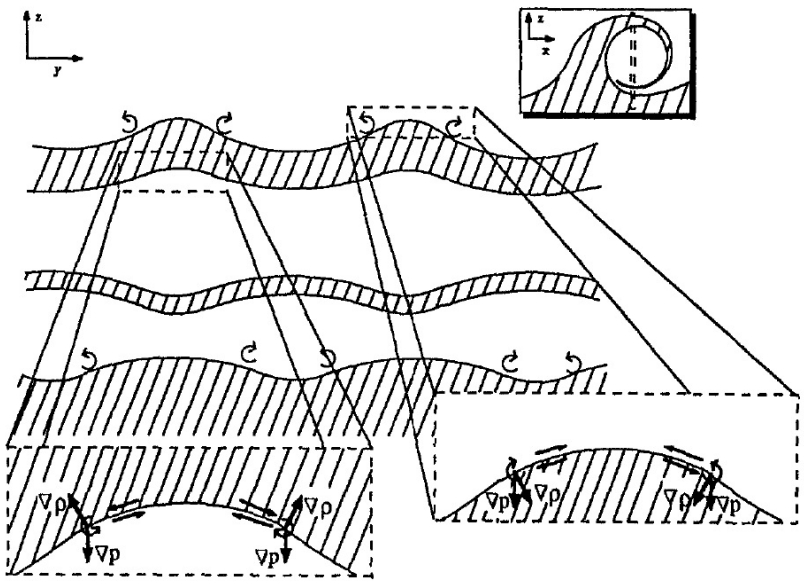

Figure 1.22: Effect of baroclinic torque on streamwise vortex tubes and the mechanism for the formation of the baroclinically generated vortices [78].

the density gradient, leading to a stronger torque, further tilting, and so on. In conclusion, Schowalter et al. [78] assert that one may refer to the RT instabilities as being baroclinically generated. In their studies, the hydrostatic pressure is assumed to be dominant, and thus the pressure gradient is always directed downward. In most atomization processes however, this is not usually the case since the flow experiences huge acceleration.

The onset of the azimuthal instability of the 3D round jet is known as the deformation of the primary axisymmetric vortex rings, first observed experimentally by Widnall et al. [92]. The vortex ring was found to be unstable to bending waves. A simple theoretical model was proposed to predict the unstable modes observed in the experiments. The wavenumber of the most amplified mode was dependent on the radius of the vortex ring. The azimuthal mode number is equivalent to the number of lobes of the deformed vortex ring. The mode number predicted by Widnall et al. [92] varied between 7 and 9.

Numerical investigations of the 3D homogeneous round jets (a fluid flowing into a like-density fluid) exposed to azimuthal and streamwise perturbation (by Brancher et al. [5])

was an attempt to show that the development of the Widnall instability on the primary vortex rings and the evolution of the Bernal & Roshko streamwise vortices, generated by the instability of the braid, could be deeply intertwined. Brancher et al. [5] also showed that the most unstable mode was three. Unforced simulations of Danaila et al. [15] predicted a mode number equal to four for homogeneous jets. Although Widnall instability plays an important role in producing the azimuthal instability on the vortex ring, formation of streamwise counter-rotating vortex pairs is responsible for generation of the side jets (lobes). Both experimental observations [42, 49] and numerical computations [5, 15] show that the number of the lobes increases by increasing the jet Reynolds number.

1.2.9 Vortex dynamics of two-phase jets

In the first studies of the role of streamwise vorticity in round liquid jets flowing into a gas, Jarrahbashi & Sirignano [33] and Jarrahbashi et al. [34] showed how lobe and ligament formation mechanisms relate to augmentation of streamwise vorticity. They also showed that a natural mode number of lobes exists for a given configuration and cannot be changed by weak forcing; however, strong forcing can produce lobes of different mode numbers associated with the mode number of the velocity perturbations. They also studied the contributions of the azimuthal and radial vortex tilting and axial vortex stretching, and the baroclinic effect on the production of streamwise vorticity for several density ratios. The baroclinic effect was found to be the dominant mechanism in production of streamwise vorticity for lower density ratios at early times. However, azimuthal and radial vortex tilting overcome the baroclinic effect later. They came to the conclusion that, generally, the importance of baroclinic vorticity generation (RT instability) has been overemphasized in the literature, especially at very high pressures, and other important aspects of vorticity dynamics and similarities with liquid injection into like-fluid have been neglected [33].

Shinjo & Umemura [80] showed that ligament creation is strongly correlated with its local velocity field, as the strong shear near the liquid surface deforms the liquid surface. Nearby vortices determine the ligament formation direction. Axisymmetric vortices make ligaments normal to the injection axis and streamwise vortices make ligaments parallel to the injection axis. Even though the vortex dynamics have not been detailed in their study, their analysis shows that vortex dynamics would be an insightful tool for understanding and controlling the surface deformation and ligament formation in two-phase flows.

1.3 Research goals

As mentioned earlier in this chapter, the main focus of this research is on 3D, transient computations of planar liquid streams through a high pressure ambient gas. The main goal is to identify different breakup mechanisms in the atomization regime (Chapter 3) and to detail and explain those mechanisms from vortex dynamics perspective (Chapter 4). The temporal cascade of length scales and the sheet spread rate are also to be analyzed and quantified during the the early stages of the jet development (Chapter 5). A brief list of the scientific goals are in the introduction of each chapter.

The present thesis is organized as follows; computational methods and mesh study are discussed in Chapter 2. The results of the temporal 3D liquid-segment simulations are presented in Chapter 3. In this chapter, three distinct breakup mechanisms are identified and categorized on a Re_l vs. We_g diagram. The effects of different flow parameters on the atomization domains are discussed, and the characteristic time scales of each breakup mechanism is presented.

In Chapter 4, a connection between the surface dynamics (growth of instabilities) and vortex dynamics is investigated. A vortex dynamics approach is used to explain the different

breakup mechanisms introduced in Chapter 3. The similarities and differences between the hairpin vortex structures seen in the two-phase planar jet flow and the 3D mixing layers [4] and homogeneous single-phase flows [42, 49] are also described in this chapter. The effects of density ratio on the production of streamwise vorticity (3D instability) is investigated. For this matter, the vortex stretching and vortex tilting effects (strain-vorticity interaction), and baroclinicity are quantified and compared to find the dominant cause of 3D instability at different domains.

Chapter 5 presents the temporal analysis of the length scale cascade and jet spread rate during the different atomization domains. Both PDFs and mean length scales are quantified and compared against the most important flow parameters; i.e. Re_l, We_g, density ratio, viscosity ratios, and wavelength-to-sheet-thickness ratio. The key parameters affecting each stage of the cascade process are identified. The spray expansion rate and mass-averaged length scales are also evaluated and compared in this chapter.

The usefulness and relevance of the temporal studies to a real atomization process are established in Chapter 6, where our temporal results are compared to spatially developing full-jet simulations. It is shown that the temporal studies are valid and useful in portraying the deformations in the upstream region of the jet cap, where the instabilities follow a periodic behavior. The effects of addition of coaxial gas flow (and the corresponding velocity ratio) on the breakup mechanisms is also analyzed in this chapter. Chapter 7 presents the concluding remarks and a summary of the most important outcomes of this study.

Chapter 2

Computational modeling

In this chapter, the numerical methods that have been used to solve the incompressible and unsteady Navier-Stokes equations will be discussed. This includes the discretization of the convection-diffusion problem (QUICK algorithm), the coupling of velocity and pressure through SIMPLE algorithm, and the application of the level-set (LS) and volume-of-fluid (VoF) methods to track the liquid-gas interface. In later sections, the flow configuration, and the boundary and initial conditions are introduced. A dimensional analysis is presented to derive the most important non-dimensional groups in the atomization process. This chapter ends with some grid refinement tests and verification of the code with some model tests.

Use has been made of the previously developed unsteady multidimensional code with the finite-volume solver of the Navier-Stokes equations for the liquid stream and the adjacent gas, uniform staggered griding scheme, and level-set method for liquid-gas interface tracking applied by Dabiri [14]. The VoF method is added to the code for its better performance in mass conservation at lower density ratios compared to the LS method.

2.1 Governing equations

The governing equations are the continuity, momentum and LS/VoF equations. Since both the gas and the liquid are incompressible in this study, the continuity equation is

$$\boldsymbol{\nabla} \cdot \mathbf{u} = 0; \tag{2.1}$$

however, it is not possible to have an abrupt change in the density and viscosity at the interface of the two phases because of the numerical difficulties that are involved, and there are a few cells that are not completely filled with either one of the fluids, and thus, have a different density than either gas or the liquid. For this matter, density and viscosity are allowed to vary smoothly across a few mesh points at the liquid-gas interface, as will be discussed later. The equations of fluid motion are Navier-Stokes equations which in an incompressible flow and considering the viscous and surface tension forces and neglecting the gravitational forces have a conservative form as follows;

$$\frac{\partial(\rho \mathbf{u})}{\partial t} + \boldsymbol{\nabla} \cdot (\rho \mathbf{u}\mathbf{u}) = -\boldsymbol{\nabla} p + \boldsymbol{\nabla} \cdot (2\mu \mathbf{D}) + \mathbf{F}; \tag{2.2}$$

where $\mathbf{D}$ is the strain rate tensor,

$$\mathbf{D} = \frac{1}{2}\left[(\boldsymbol{\nabla}\mathbf{u}) + (\boldsymbol{\nabla}\mathbf{u})^T\right]; \tag{2.3}$$

and $\mathbf{F}$ is the surface tension force per unit volume

$$\mathbf{F} = -\sigma\kappa\delta(d)\mathbf{n}. \tag{2.4}$$

In the equations above, $\mathbf{u} = u\mathbf{i} + v\mathbf{j} + w\mathbf{k}$ is the velocity vector, ρ and μ are the density and viscosity of the fluid, respectively, p is the static pressure, σ is the surface tension coefficient,

κ is the surface curvature, $\delta(d)$ is the Dirac delta function, d is the distance from the interface, and $\mathbf{n}$ is the unit vector normal to the liquid-gas interface. The entire strain rate tensor has been used in the viscous diffusion term because the viscosity varies near the interface zone, and this will introduce extra terms in the momentum equations in each direction, which include the viscous variation effects. This will be discussed in the next section.

2.1.1 Finite-Volume formulation for variable properties

The viscous stress term in the Navier-Stokes equations for an incompressible flow with variable properties in the cartesian coordinates can be written as follows (for the first component)

$$
\begin{aligned}
&\left[\boldsymbol{\nabla}\cdot(\mu(\boldsymbol{\nabla}\mathbf{u}+\boldsymbol{\nabla}\mathbf{u}^T))\right]_1 = \\
&= \frac{\partial}{\partial x}\left[2\mu\frac{\partial u}{\partial x}\right] + \frac{\partial}{\partial y}\left[\mu\Big(\frac{\partial u}{\partial y}+\frac{\partial v}{\partial x}\Big)\right] + \frac{\partial}{\partial z}\left[\mu\Big(\frac{\partial u}{\partial z}+\frac{\partial w}{\partial x}\Big)\right] \\
&= \boldsymbol{\nabla}\cdot(\mu\boldsymbol{\nabla}u) + \frac{\partial}{\partial x}\left(\mu\frac{\partial u}{\partial x}\right) + \frac{\partial}{\partial y}\left(\mu\frac{\partial v}{\partial x}\right) + \frac{\partial}{\partial z}\left(\mu\frac{\partial w}{\partial x}\right) \\
&= \boldsymbol{\nabla}\cdot(\mu\boldsymbol{\nabla}u) + \mu\frac{\partial}{\partial x}(\boldsymbol{\nabla}\cdot\mathbf{u}) + \frac{\partial\mu}{\partial x}\frac{\partial u}{\partial x} + \frac{\partial\mu}{\partial y}\frac{\partial v}{\partial x} + \frac{\partial\mu}{\partial z}\frac{\partial w}{\partial x};
\end{aligned}
\tag{2.5}
$$

where the second term is zero due to the incompressibility of the fluids (Equation 2.1). As we write the momentum equation in the following form, the last three terms in Equation (2.5) will be included in the source term S, in addition to the pressure gradient and surface tension forces.

$$
\frac{\partial(\rho u)}{\partial t} + \boldsymbol{\nabla}\cdot(\rho\mathbf{u}u) = \boldsymbol{\nabla}\cdot(\mu\boldsymbol{\nabla}u) + S. \tag{2.6}
$$

The complete form of the momentum equation in each direction could be written as:

- *x-momentum:*

$$\frac{\partial(\rho u)}{\partial t} + \boldsymbol{\nabla} \cdot (\rho \mathbf{u} u) = -\frac{\partial p}{\partial x} + \boldsymbol{\nabla} \cdot (\mu \boldsymbol{\nabla} u) + \frac{\partial \mu}{\partial x}\frac{\partial u}{\partial x} + \frac{\partial \mu}{\partial y}\frac{\partial v}{\partial x} + \frac{\partial \mu}{\partial z}\frac{\partial w}{\partial x} + F_x; \quad (2.7)$$

- *y-momentum:*

$$\frac{\partial(\rho v)}{\partial t} + \boldsymbol{\nabla} \cdot (\rho \mathbf{u} v) = -\frac{\partial p}{\partial y} + \boldsymbol{\nabla} \cdot (\mu \boldsymbol{\nabla} v) + \frac{\partial \mu}{\partial x}\frac{\partial u}{\partial y} + \frac{\partial \mu}{\partial y}\frac{\partial v}{\partial y} + \frac{\partial \mu}{\partial z}\frac{\partial w}{\partial y} + F_y; \quad (2.8)$$

- *z-momentum:*

$$\frac{\partial(\rho w)}{\partial t} + \boldsymbol{\nabla} \cdot (\rho \mathbf{u} w) = -\frac{\partial p}{\partial z} + \boldsymbol{\nabla} \cdot (\mu \boldsymbol{\nabla} w) + \frac{\partial \mu}{\partial x}\frac{\partial u}{\partial z} + \frac{\partial \mu}{\partial y}\frac{\partial v}{\partial z} + \frac{\partial \mu}{\partial z}\frac{\partial w}{\partial z} + F_z. \quad (2.9)$$

2.2 Numerical methods

A finite-volume discretization on a staggered grid has been considered in this study. The conservation equations come from the balance in the flux going in and coming out of the control volume. Therefore, accurate calculation of these fluxes is of great importance. Third-order accurate QUICK scheme has been used for spatial discretization and the Crank-Nicolson scheme has been used for time-marching treatment in this research. SIMPLE algorithm has been used for velocity-pressure coupling. In this section these algorithms will be reviewed briefly.

2.2.1 QUICK discretization

The Quadratic Upwind Interpolation for Convective Kinetics (QUICK) was first introduced by Leonard [46]. The method is based on a three-point upstream-weighted quadratic interpolation technique for cell face values on a staggered grid. This scheme has been shown to

have a better accuracy than central difference scheme while retaining the transportiveness property of the upwind scheme. The face value of the scalar quantity ϕ is obtained from a quadratic function passing through two bracketing nodes (on each side of the face) and a node on the upstream side (Figure 2.1).

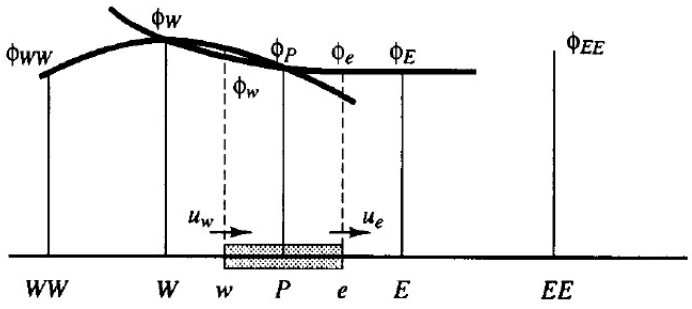

Figure 2.1: Quadratic profiles used in QUICK scheme

A uniform grid spacing is used here for simplicity but the concept can be easily extended to nonuniform grids. The value of ϕ at the interface of the cell is calculated by fitting a quadratic polynomial to three consecutive nodes – the two nodes located at either side of the surface and another node on the upstream side. For example, when $u_w > 0$ and $u_e > 0$ a quadratic fit through WW, W and P is used to evaluate ϕ_w, and a further quadratic fit through W, P and E to calculate ϕ_e. For a uniform grid the value of ϕ at the cell face between two bracketing nodes i and $i-1$ and upstream node $i-2$ is given by the following formula [46];

$$\phi_{face} = \frac{6}{8}\phi_{i-1} + \frac{3}{8}\phi_i - \frac{1}{8}\phi_{i-2}. \tag{2.10}$$

Using this formula, the value of the scalar ϕ at the west cell face can be written as:

$$\phi_w = \begin{cases} \frac{6}{8}\phi_W + \frac{3}{8}\phi_P - \frac{1}{8}\phi_{WW} & \text{for } u_w > 0 \\ \frac{6}{8}\phi_P + \frac{3}{8}\phi_W - \frac{1}{8}\phi_E & \text{for } u_w < 0 \end{cases} \tag{2.11}$$

and a similar relation for the east cell face value ϕ_e.

There have been several papers addressing the practical implementation of the QUICK scheme, but among them Hayase et al. [26] presented a consistent formulation of QUICK scheme, which is more stable and also fast converging. This scheme is used here. In this formulation, the interpolated values of the scalar function are rearranged as

$$\phi_w = \begin{cases} \phi_W + \frac{1}{8}[3\phi_P - 2\phi_W - \phi_{WW}] & \text{for } u_w > 0 \\ \phi_P + \frac{1}{8}[3\phi_W - 2\phi_P - \phi_E] & \text{for } u_w < 0 \end{cases} \tag{2.12}$$

and

$$\phi_e = \begin{cases} \phi_P + \frac{1}{8}[3\phi_E - 2\phi_P - \phi_W] & \text{for } u_e > 0 \\ \phi_E + \frac{1}{8}[3\phi_P - 2\phi_E - \phi_{EE}] & \text{for } u_e < 0 \end{cases} \tag{2.13}$$

The terms in the brackets are treated as source terms using the values from previous iteration. Hence, the values of ϕ at interface are given as an upwind estimation plus a corrective source term. The advantage of this approach is that the main coefficients in the discretized equation are positive and satisfy the requirements for conservativeness, boundedness and transportiveness. The QUICK scheme is third order accurate.

2.2.2 Crank-Nicolson discretization scheme

The Crank-Nicolson method is a second-order and implicit finite difference scheme for discretizing the unsteady term of the momentum equations. The method was developed by Cranck & Nicolson [12]. This method is unconditionally stable for discretizing the time

derivative. Applying the Crank-Nicolson method to time derivative of $\mathbf{u}$ is as follows:

$$\frac{\partial \mathbf{u}}{\partial t} = F(\mathbf{u}, \mathbf{x}, t, \frac{\partial \mathbf{u}}{\partial \mathbf{x}}, \frac{\partial^2 \mathbf{u}}{\partial \mathbf{x}^2}); \tag{2.14}$$

$$\frac{\mathbf{u}_i^{n+1} - \mathbf{u}_i^n}{\Delta t} = \frac{1}{2}\left[F_i^{n+1}(\mathbf{u}, \mathbf{x}, t, \frac{\partial \mathbf{u}}{\partial \mathbf{x}}, \frac{\partial^2 \mathbf{u}}{\partial \mathbf{x}^2}) + F_i^n(\mathbf{u}, \mathbf{x}, t, \frac{\partial \mathbf{u}}{\partial \mathbf{x}}, \frac{\partial^2 \mathbf{u}}{\partial \mathbf{x}^2})\right]; \tag{2.15}$$

The function F must be discretized spatially with a central difference or QUICK scheme.

2.2.3 SIMPLE algorithm

The acronym SIMPLE stands for Semi-Implicit Method for Pressure-Linked Equations. The algorithm was originally put forward by Patankar and Spalding [64], and is essentially a guess-and-correct procedure for the calculation of pressure on the staggered grid arrangement.

To initiate the SIMPLE calculation process a pressure field p^* is guessed. Discretized momentum equations are solved using the guessed pressure field to yield velocity components u^* and v^*. Then a pressure correction equation which represents the continuity equation is solved to give the pressure correction variable p'. Once the pressure correction field is known, the correct pressure field and velocity components are obtained.

The SIMPLE algorithm gives a method of calculating pressure and velocities. The method is iterative, and when other scalars are coupled to the momentum equations the calculation needs to be done sequentially. The sequence of operations in a CFD procedure which employs the SIMPLE algorithm is given in Figure 2.2. The equations that need to be solved in each step are also shown there.

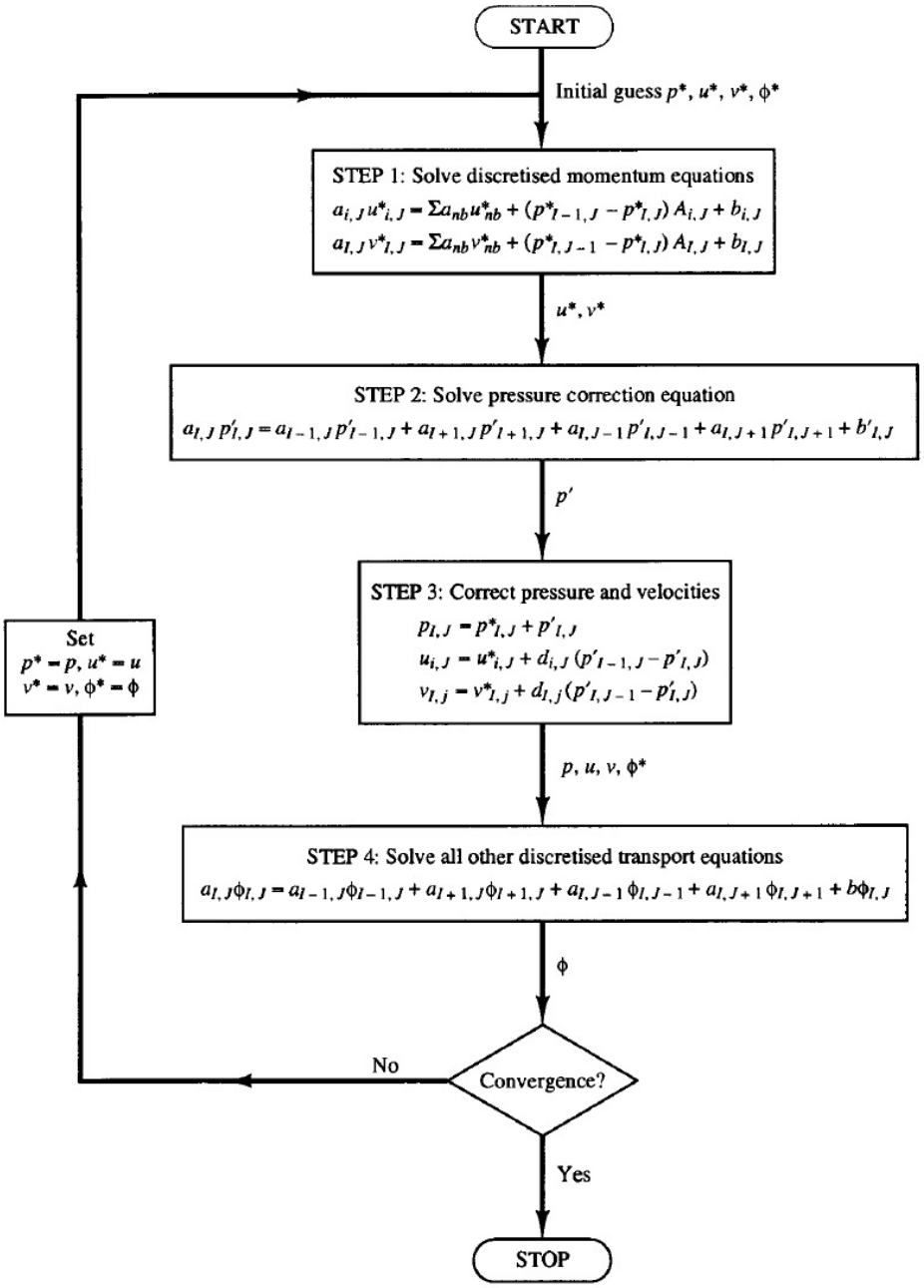

Figure 2.2: The SIMPLE algorithm flow chart [89].

2.3 Interface tracking approach

Tracking the interface between two phases and modeling its physics such as surface tension is of great importance in studying multiphase flows. Several methods have been developed to handle the difficulties in interfacial modeling. The surface marker method or the front-

tracking method explicitly tracks the position of the interface by updating the position of marker points on it. For example, Tryggvason & Unverdi [87] and Glimm et al. [24] used this method to study Rayleigh-Taylor instabilities. Popinet & Zaleski [66] did an accurate balance of surface tension forces on a finite volume method by explicit tracking of the interface. The method was applied only for 2D calculations because of the geometrical complexity appearing in the 3D calculation. The drawback of the front-tracking method is the difficulty in capturing the topological changes in the phases, such as breakup or coalescence of liquid drops, specially in 3D calculations.

In the limit of inviscid flow, the interface could be modeled as a vortex sheet with zero thickness. Rangel & Sirignano [68] performed a nonlinear analysis of temporal instability of a liquid sheet using this idea. From the momentum equation on sides of the interface and a balance of interfacial forces, they derived an equation for the evolution of circulation on the interface for a case with density discontinuity and surface tension. The velocity field was also found by the Biot-Savart law from the vorticity field.

Volume-of-Fluid (VoF) is another method developed to treat the multiphase flows. In this method, a scalar parameter in each discretized cell is defined as the volume fraction of cell filled with one of the phases. This scalar is updated in time by considering the convection from and to neighboring cells. Even though it is harder to track back the volume of fluid to find the interface, this method is very popular because of its high accuracy in mass conservation. This method is used in our study for lower density ratio cases. A review of different methods of interface tracking and surface tension modeling is developed by Scardovelli & Zaleski [76].

In this work, the level-set (LS) method is employed to track the interface and model its physics (except for lower density ratios where the VoF method is used). The LS method has been developed by Osher and his coworkers (see Zhao et al. [99], Sussman et al. [84], and Osher & Fedkiw [60]). In this method, the interface between two phases is defined as the zero

level set of a scalar function called LS function and denoted by ϕ. The LS function is defined over the whole computational domain as a signed distance function from the interface, i.e. it has positive values on one side of the interface (gas phase), and negative values on the other side (liquid phase) and the magnitude of the LS at each point in the computational domain is equal to the distance from that point to the interface.

2.3.1 Level-set method

The LS function ϕ is defined as a smooth distance function allowing us to give the interface a thickness fixed in time. Density, viscosity and surface tension all depend on the LS function being a distance function. In this algorithm, the interface Γ is the zero level set of ϕ,

$$\Gamma = \{\mathbf{x} \,|\, \phi(\mathbf{x}, t) = 0\}\,.$$

We take $\phi < 0$ in the liquid region and $\phi > 0$ in the gas region. Therefore, we have

$$\phi(\mathbf{x}, t) \begin{cases} > 0 & \text{if } \mathbf{x} \in \text{the gas} \\ = 0 & \text{if } \mathbf{x} \in \Gamma \\ < 0 & \text{if } \mathbf{x} \in \text{the liquid} \end{cases} \tag{2.16}$$

By virtue of the boundary conditions, $\mathbf{u}$ is continuous across the interface. Since the interface moves with the fluid particles, the evolution of ϕ is then given by

$$\frac{\partial \phi}{\partial t} + \mathbf{u} \cdot \boldsymbol{\nabla} \phi = 0. \tag{2.17}$$

Equation (2.17) is called the LS equation. If the initial distribution of the LS is a signed distance function, after a finite time of being convected by a nonuniform velocity field, it

will not remain a distance function. Therefore, we need to re-initialize the LS function in such a way that it will be a distance function (with property of $|\boldsymbol{\nabla}\phi| = 1$) without changing the zero LS (position of the interface). Suppose $\phi_0(x)$ is the LS distribution after some time step and is not exactly a distance function. This can be re-initialized to a distance function by solving the following partial differential equation (Sussman et al. [84]):

$$\frac{\partial d}{\partial \tau} = \text{sign}(\phi)(1 - |\boldsymbol{\nabla} d|); \tag{2.18}$$

with initial condition

$$d(\mathbf{x}, 0) = \phi_0(\mathbf{x});$$

where τ is a psuedo time. The steady solutions of Equation (2.18) are distance functions with property $|\boldsymbol{\nabla} d| = 1$. Furthermore, since $\text{sign}(0) = 0$, then $d(\mathbf{x}, t)$ has the same zero LS as $\phi(\mathbf{x})$. Therefore, we simply solve Equation (2.18) to steady state and then replace $\phi(\mathbf{x})$ by $d(\mathbf{x}, \tau_{\text{steady}})$.

The 5th order accurate Weighted Essential Non-Oscillatory (WENO) scheme of Jiang & Peng [37] has been used to solve the re-initialization Equation (2.18) in every time step.

For the multiphase flow, if Ω_l and Ω_g are defined as the domain occupied by the liquid and the gas, respectively, the Navier-Stokes equations in each of the domains can be written as

$$\rho_l \frac{\mathrm{D}\mathbf{u}_l}{\mathrm{D}t} = -\boldsymbol{\nabla} p_l + 2\mu_l \boldsymbol{\nabla} \cdot \mathbf{D}_l \ , \quad \boldsymbol{\nabla} \cdot \mathbf{u}_l = 0 \ , \quad \mathbf{x} \in \Omega_l \tag{2.19}$$

$$\rho_g \frac{\mathrm{D}\mathbf{u}_g}{\mathrm{D}t} = -\boldsymbol{\nabla} p_g + 2\mu_g \boldsymbol{\nabla} \cdot \mathbf{D}_g \ , \quad \boldsymbol{\nabla} \cdot \mathbf{u}_g = 0 \ , \quad \mathbf{x} \in \Omega_g \tag{2.20}$$

where subscripts g and l denote the gas and liquid phases, respectively. The boundary

conditions on the liquid-gas interface are

$$(2\mu_l \mathbf{D}_l - 2\mu_g \mathbf{D}_g) \cdot \mathbf{n} = (p_l - p_g - \sigma\kappa)\mathbf{n} \quad \text{and} \quad \mathbf{u}_l = \mathbf{u}_g \; ; \quad \mathbf{x} \in \Gamma \tag{2.21}$$

where Γ is the liquid-gas interface, $\mathbf{n}$ is the unit vector normal to the interface towards the gas phase, $\kappa = \nabla \cdot \mathbf{n}$ is the curvature of the interface and σ is the surface tension coefficient.

The normal unit vector $\mathbf{n}$, drawn from the liquid into the gas, and the curvature of the interface κ can easily be expressed in terms of $\phi(\mathbf{x}, t)$;

$$\mathbf{n} = \left.\frac{\boldsymbol{\nabla}\phi}{|\boldsymbol{\nabla}\phi|}\right|_{\phi=0} \quad \text{and} \quad \kappa = \boldsymbol{\nabla} \cdot \mathbf{n} = \boldsymbol{\nabla} \cdot \left.\left(\frac{\boldsymbol{\nabla}\phi}{|\boldsymbol{\nabla}\phi|}\right)\right|_{\phi=0}. \tag{2.22}$$

Expanding Equation (2.22) in Cartesian coordinates leads to the following equation for the curvature of the interface in a 3D problem (x, y, z);

$$\kappa = \frac{\phi_{xx}(\phi_y^2 + \phi_z^2) + \phi_{yy}(\phi_x^2 + \phi_z^2) + \phi_{zz}(\phi_x^2 + \phi_y^2) - 2\phi_x\phi_y\phi_{xy} - 2\phi_y\phi_z\phi_{yz} - 2\phi_z\phi_x\phi_{xz}}{(\phi_x^2 + \phi_y^2 + \phi_z^2)^{3/2}}. \tag{2.23}$$

The governing equations for the fluid velocity (Equations 2.19 & 2.20) along with their boundary condition (Equation 2.21) can be written as a single equation containing both liquid and gas properties in the whole domain, $\Omega = \Omega_l \cup \Omega_g$;

$$\rho(\phi)\frac{\mathrm{D}\mathbf{u}}{\mathrm{D}t} = -\boldsymbol{\nabla}p + \boldsymbol{\nabla} \cdot (2\mu(\phi)\mathbf{D}) - \sigma\kappa(\phi)\delta(\phi)\mathbf{n}. \tag{2.24}$$

Since the density and viscosity are constant in each fluid, they then take on two different values depending on the sign of ϕ;

$$\rho(\phi) = \rho_l + (\rho_g - \rho_l)H(\phi); \tag{2.25}$$

and

$$\mu(\phi) = \mu_l + (\mu_g - \mu_l)H(\phi); \tag{2.26}$$

where $H(\phi)$ is the Heaviside function given by

$$H(\phi) = \begin{cases} 0, & \text{if } \phi < 0, \\ \frac{1}{2}, & \text{if } \phi = 0, \\ 1, & \text{if } \phi > 0. \end{cases} \tag{2.27}$$

Therefore, the incompressible flow of a liquid-gas mixture could be treated as an incompressible flow of a variable density fluid with surface tension modeled as a body force per unit volume.

2.3.2 Interface thickness

In order to solve Equation (2.24) numerically, it should be modified slightly due to the sharp changes in ρ and μ across the interface front and also due to the numerical difficulties presented by the Dirac delta function $\delta(\phi)$ contained in the surface tension force $\mathbf{F}$. To alleviate these issues, the interface is given a fixed thickness that is proportional to the spatial mesh size. This allows replacing $\rho(\phi)$ and $\mu(\phi)$ by a smoothed density and viscosity which is denoted as $\rho_\varepsilon(\phi)$ and $\mu_\varepsilon(\phi)$ and is given by

$$\rho_\varepsilon(\phi) = \rho_l + (\rho_g - \rho_l)H_\varepsilon(\phi), \tag{2.28}$$

and

$$\mu_\varepsilon(\phi) = \mu_l + (\mu_g - \mu_l)H_\varepsilon(\phi), \tag{2.29}$$

with smoothed Heaviside function

$$H_\varepsilon(\phi) = \begin{cases} 0, & \text{if } \phi < -\varepsilon, \\ \frac{1}{2}(\frac{\phi+\varepsilon}{\varepsilon}) + \frac{1}{2\pi}\sin(\frac{\pi\phi}{\varepsilon}), & \text{if } |\phi| \leq \varepsilon, \\ 1, & \text{if } \phi > \varepsilon; \end{cases} \tag{2.30}$$

where ε represents the half thickness of the interface and has the value of 1.5Δ, where Δ is the cell size. The variation of $H_\varepsilon(\phi)$ across the three interface cells is plotted in Figure 2.3. This Heaviside function corresponds to a Delta function that can be used to evaluate the surface tension force;

$$\delta_\varepsilon(\phi) = \frac{dH_\varepsilon}{d\phi} = \begin{cases} \frac{1}{2\varepsilon}\left[1 + \cos(\frac{\pi\phi}{\varepsilon})\right] & \text{if } |\phi| \leq \varepsilon \\ 0 & \text{otherwise} \end{cases} \tag{2.31}$$

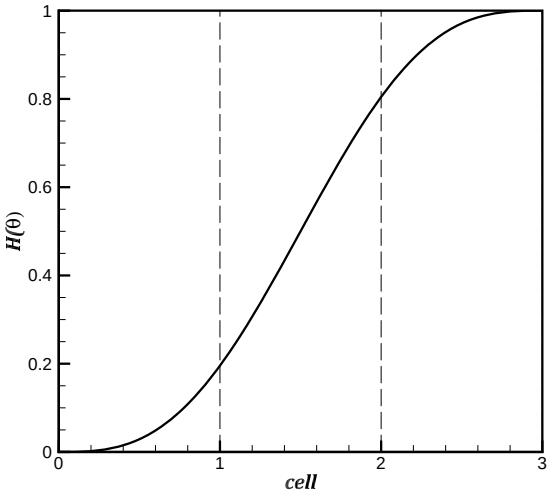

Figure 2.3: The smoothed Heaviside function variation across the interface.

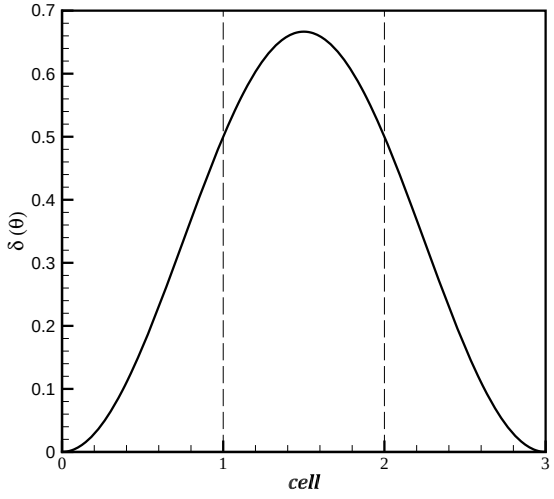

Figure 2.4: The modified Delta function variation across the interface.

The variation of the modified Delta function across the interface cells is plotted in Figure 2.4. Introduction of the modified Heaviside and Delta functions allows the density and viscosity to vary smoothly across the interface cells, and is not in consistent with our earlier assumption that the density is constant within each liquid or gas zone. This might result in minor errors which are negligible in this context. At lower density ratios (higher density gradient), this error cannot be neglected, and it poorly affects the mass conservation of the LS method. Therefore, the VoF method is employed at lower density ratios to remedy this issue.

2.3.3 Volume-of-Fluid method

In the Volume-of-Fluid (VoF) method at low density ratios, a transport equation similar to the LS Equation (2.17) is used for the volume fraction f, also called the VoF variable, in order to describe the temporal and spatial evolution of the two phase flow [28];

$$\frac{\partial f}{\partial t} + \mathbf{u} \cdot \boldsymbol{\nabla} f = 0, \tag{2.32}$$

where the VoF variable f represents the volume of (liquid phase) fluid fraction as follows:

$$f(t) = \begin{cases} 0, & \text{outside of liquid pahse} \\ 0 < f < 1, & \text{at the interface} \\ 1, & \text{inside the liquid phase.} \end{cases} \tag{2.33}$$

The normal direction of the fluid interface is found where the value of f changes most rapidly. With this method, the free surface is not defined sharply; instead, it is distributed over the height of the cell. Since fluid properties are required every time step in order to solve the Navier-Stokes equations, the density and viscosity change continuously based on Equations (2.25) and (2.26). However, in these equations, the argument of the Heaviside function is

replaced by f, in the VoF method.

The formulation for the fully conservative momentum convection and volume fraction transport, the momentum diffusion, and the surface tension are treated explicitly. To ensure a sharp interface of all flow discontinuities and to suppress numerical dissipation of the liquid phase, the interface is reconstructed at each time step by the PLIC (piecewise linear interface calculation) method proposed by Rider & Kothe [72]. The liquid phase is transported on the basis of its reconstructed distribution. The capillary effects in the momentum equations are represented by a capillary tensor as introduced by Scardovelli & Zaleski [76].

2.4 Flow configuration

The computational domain, shown in Figure 2.5(a), consists of a cube, which is discretized into uniform-sized cells. The liquid segment, which is a sheet of thickness h_0 ($h_0 = 50$ μm for the thin sheet and 200 μm for the thick sheet), is located at the center of the box and is stationary in the beginning. The domain size in terms of the sheet thickness is $16h_0 \times 10h_0 \times 10h_0$, in the x, y and z directions, respectively, for the thin sheet, and $4h_0 \times 4h_0 \times 8h_0$ for the thick sheet. The liquid segment is surrounded by the gas zones on top and bottom. The gas moves in the positive x- (streamwise) direction with a constant velocity ($U = 100$ m/s) at top and bottom boundaries, and its velocity diminishes to the interface velocity with a boundary layer thickness obtained from 2D full-jet simulations, as shown in Figure 2.6. In the liquid, the velocity decays to zero at the center of the sheet with a hyperbolic tangent profile. This computational box resembles a segment of the liquid sheet far upstream of the jet cap, as shown in Figure 2.5(b). This sub-figure shows the starting behavior of a spatially developing full liquid jet injected with constant velocity U_l into quiescent gas. A Galilean transformation of the velocity field shows that the gas stream flows upstream with respect to the liquid jet with a relative velocity $U_{rel} = U_l$ (denoted

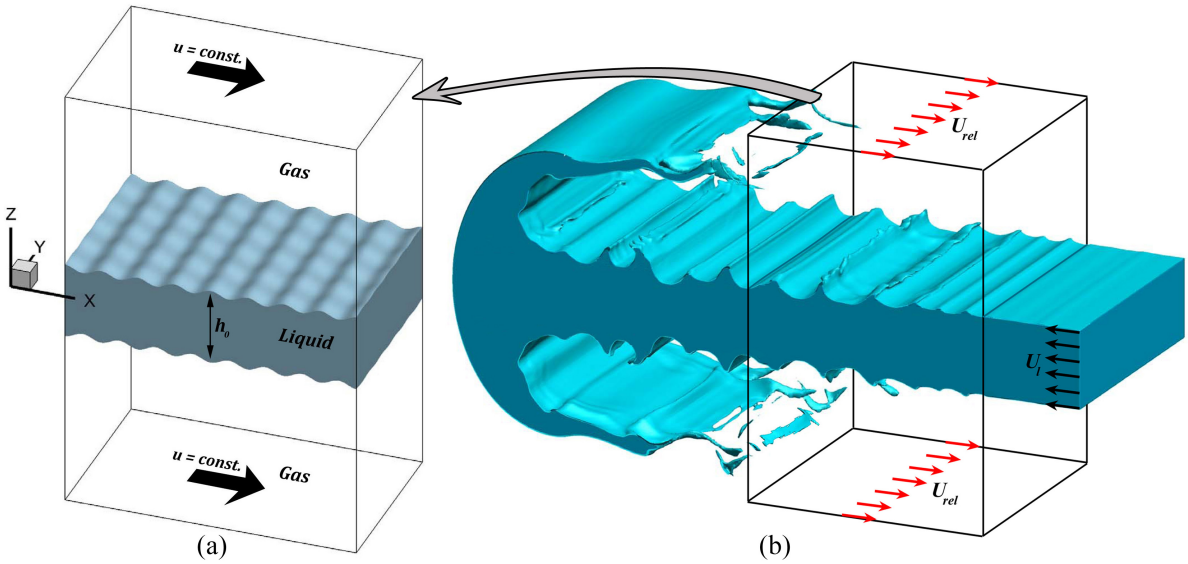

Figure 2.5: The computational domain with the initial liquid and gas zones (a), and a spatially developing full liquid jet (b).

by the red arrows) in the box shown in Figure 2.5(b). Our temporal study focuses on this region of the jet stream away from the jet cap, where previous studies indicate that surface deformations are periodic [80]. The relevance of the temporal computational box will be detailed in Chapter 6.

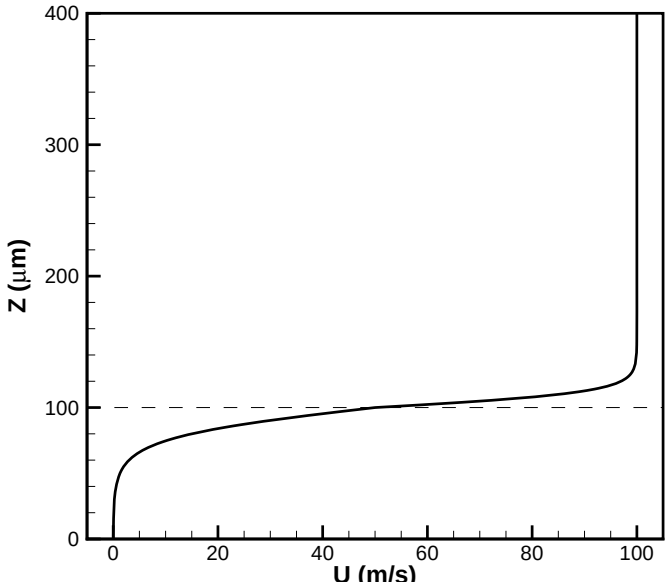

Figure 2.6: Initial streamwise velocity profile, obtained from the 2D full jet computations. The dashed-line indicates the initial location of the interface.

This study involves a temporal computational analysis with a relative velocity between the two phases. Due to friction, the relative velocity decreases with time. Furthermore, the domain is several wavelengths long in the streamwise direction so that some spatial development occurs. In order to reduce the dependence of the results on details of the boundary conditions, specific configurations (e.g., air-assist or air-blast atomization) are avoided. However, calculations are made with the critical non-dimensional parameters in the ranges of practical applications, as will be described in Section 2.5.

As shown in Figure 2.5, the liquid-gas interface is initially perturbed symmetrically on both sides with a sinusoidal profile and predefined wavelength and amplitude obtained from the 2D full-jet simulations (see Ref. [96]). Two analyses without forced or initial surface perturbations – the full-jet 2D simulations (Figure 17 of Ref. [96]) and the initially non-perturbed 3D simulations (Figure 4.45 in Chapter 4) – show KH wavelengths in the moderate range of 80–125 μm over a wide range of Re_l, We_g and density ratio studied here. In order to expedite the appearance and growth of the KH waves, initial perturbations with wavelength of 100 μm are imposed on the interface with a small amplitude of 4 μm. This amplitude is small enough that subharmonics would have a chance to form and grow. Similar to [33], our results show that at higher Re_l and lower density ratio, smaller waves appear superimposed on the initial perturbations. The waves also merge to create larger waves at lower We_g. Both streamwise (x-direction) and spanwise (y-direction) perturbations are considered in this study. Periodic boundary conditions for all components of velocity as well as the LS/VoF variables are imposed on the four sides of the computational domain; i.e. the x- and y-planes. A summary of the boundary conditions is presented mathematically in Table 2.1.

The fluid properties are summarized in Table 2.2. A wide range of Re and We at high and low density and viscosity ratios are covered in this study. Kerosene (paraffin) with density of 804 kg/m^3 is used as the liquid, and air at high pressure (35 atm) is considered as the surrounding gas. The velocity difference between the liquid film and the gas is considered to

Boundary	Condition	formulation
yz-planes	periodic	$\mathbf{u}_N = \mathbf{u}_2$, $\mathbf{u}_1 = \mathbf{u}_{N-1}$
xz-planes	periodic	$\mathbf{u}_N = \mathbf{u}_2$, $\mathbf{u}_1 = \mathbf{u}_{N-1}$
Top & bottom planes	constant streamwise velocity, zero normal gradients	$u = 100$ m/s, $\frac{\partial v}{\partial z} = 0$, $\frac{\partial w}{\partial z} = 0$

Table 2.1: The boundary conditions of Figure 2.5.

Fluid Properties	Liquid (Kerosene)	Gas (air)
Dynamic viscosity, μ (kg/m.s)	2.7×10^{-3}	1.8×10^{-5}
Density, ρ (kg/m^3)	804	40.0 (at 35 atm)
Surface tension coefficient, σ (N/m)	0.028	–
Jet velocity, U (m/s)	0	100

Table 2.2: Fluid properties.

be 100 m/s. The tabulated values are only for the base case; for other cases with different Re and We, the liquid viscosity and surface tension coefficient are obtained from the given Re and We values, respectively; the gas properties are calculated from the desired density and viscosity ratios. The range of dimensionless parameters will be provided in next section.

2.5 Dimensional analysis

The main purpose of this study is to investigate the growth rate of the 3D instabilities and their corresponding features, e.g. lobe, ligament and droplet formation, and vortex interactions, as well as to find the dominant wavelength of those 3D instabilities. The most important parameters that affect the instability growth rate ω (or the time at which the instabilities occur first) could be written as,

$$\omega \text{ (or } t) = f(\rho_l, \rho_g, \mu_l, \mu_g, h_0, \lambda \text{ (or } k), U, \sigma); \tag{2.34}$$

where λ is the wavelength of the initial KH instabilities on the liquid-gas interface. $k = 2\pi/\lambda$ is the instabilities wavenumber, and U is the far-field gas velocity. Using dimensional analysis, Equation (2.34) can be reduced to the following dimensionless form

$$\frac{\omega}{kU} \text{ (or } \frac{Ut}{\lambda}) = \Phi\big(\frac{\rho_g}{\rho_l}, \frac{\mu_g}{\mu_l}, \frac{\lambda}{h} \text{ (or } kh), \frac{\rho_l U h_0}{\mu_l}, \frac{\rho_l U^2 h_0}{\sigma}\big); \tag{2.35}$$

The first two parameters in Equation (2.35) are the gas-to-liquid density ratio and viscosity ratio; the third group is the wavelength-to-sheet-thickness ratio, and the last two dimensionless parameters are the Reynolds number and the Weber number (based on the liquid properties and sheet thickness), respectively.

It is also useful to write the momentum Equation (2.24) in dimensionless form. The following dimensionless variables are used for non-dimensionalization:

$$\begin{aligned} x^* = \frac{x}{h_0}, \quad \mathbf{u}^* = \frac{\mathbf{u}}{U}, \quad t^* = \frac{tU}{h_0} \\ p^* = \frac{p}{\rho_l U^2}, \quad \rho^* = \frac{\rho}{\rho_l}, \quad \mu^* = \frac{\mu}{\mu_l}; \end{aligned} \tag{2.36}$$

where the asterisks denote dimensionless variables. Substitution of these variables into Equation (2.24) and dropping the asterisks we obtain;

$$\frac{\partial \mathbf{u}}{\partial t} + \mathbf{u} \cdot \boldsymbol{\nabla} \mathbf{u} = -\frac{\boldsymbol{\nabla} p}{\rho(\phi)} + \frac{1}{\rho(\phi)} \left(\frac{1}{\mathrm{Re}} \boldsymbol{\nabla} \cdot (2\mu(\phi)\mathbf{D}) - \frac{1}{\mathrm{We}} \kappa(\phi)\delta(\phi)\mathbf{n} \right). \tag{2.37}$$

The density and viscosity now become

$$\rho(\phi) = \eta + (1-\eta)H(\phi) \quad \text{and} \quad \mu(\phi) = \zeta + (1-\zeta)H(\phi) \tag{2.38}$$

where $H(\phi)$ in here is the Heaviside function as introduced earlier. η is the liquid-to-gas density ratio, and *zeta* is the liquid-to-gas viscosity ratio;

$$\eta = \frac{\rho_l}{\rho_g}, \quad \text{and} \quad \zeta = \frac{\mu_l}{\mu_g}. \tag{2.39}$$

In order to keep the convention, the gas-to-liquid density and viscosity ratios are used, which are the reciprocal of η and ζ as defined above. So, the most important dimensionless groups in this study are the Reynolds number (Re), the Weber number (We), as well as the gas-to-liquid density ratio ($\hat{\rho}$) and viscosity ratio ($\hat{\mu}$), as defined below. The initial wavelength-to-sheet-thickness ratio (Λ) is also an important parameter.

$$Re = \frac{\rho_l U h}{\mu_l}, \quad We = \frac{\rho_l U^2 h}{\sigma}, \quad \hat{\rho} = \frac{\rho_g}{\rho_l}, \quad \hat{\mu} = \frac{\mu_g}{\mu_l}, \quad \Lambda = \frac{\lambda}{h_0}. \tag{2.40}$$

The initial sheet thickness h_0 is considered as the characteristic length, and the relative gas-liquid velocity U as the characteristic velocity. The subscripts l and g refer to the liquid and gas, respectively. Theoretically, if the flow field is infinite in the streamwise direction (as in our study), a Galilean transformation shows that only the relative velocity between the two streams is consequential. Spatially developing flow fields, however, are at most semi-infinite so that both velocities at the flow-domain entry and their ratio (or their momentum-flux ratio) are important. A wide range of Re and We at high and low density and viscosity ratios is covered in this study. The range of dimensionless parameters analyzed in this study are given in Table 2.3. The range of parameters considered here covers the more practical ranges usually seen in most atomization applications; however, higher $\hat{\rho}$ (high pressures) and higher We values are also studied to fully explore and portray their effects.

Re ranges from 320, which is in laminar regime, up to $5,000$, which is completely turbulent.

Parameter	Re	We	$\hat{\rho}$	$\hat{\mu}$	Λ
Range	320–5000	3000–100,000	0.05–0.9	0.0005–0.05	0.5–2.0

Table 2.3: Range of dimensionless parameters.

We varies from 3000, indicating a very large surface tension, up to $100,000$ which corresponds to a very low surface tension case. $\hat{\rho}$ comprises three different orders of magnitudes, from a very high density difference ($\hat{\rho} = 0.05$) to a value of $\hat{\rho} = 0.9$ indicating an almost like-density liquid and gas. The same story goes on for $\hat{\mu}$; the chosen values include a highly viscous gas ($\hat{\mu} = 0.1$) and an almost inviscid gas with very low $\hat{\mu}$. The wavelength-to-thickness ratio contains a very long KH wavelength in orders of the sheet thickness (thin sheet, $\Lambda = 2$), and a short initial wavelength, half of the sheet thickness (thick sheet, $\Lambda = 0.5$).

2.6 Mesh study

A uniform staggered grid is used with the mesh size of 2.5 μm and a time step of 5 ns – finer grid resolution of 1.25 μm is used for the case with higher We ($We > 72,000$) or higher Re ($Re = 5000$). The grid independency tests were performed previously by Jarrahbashi & Sirignano [33], Jarrahbashi et al. [34], and Zandian et al. [96]. They showed that the errors in the size of the ligaments, penetration length of the liquid jet and the magnitude of the velocity computed using different mesh resolutions were within an acceptable range. The effects of the mesh size, the thickness of the fuzzy zone between the two phases, where properties have large gradients to approximate the discontinuities, and mass conservation of the LS method have been previously addressed by Jarrahbashi & Sirignano [33]. The effects of mesh resolution on the most important flow parameters, e.g. surface structures, velocity and vorticity profiles, are studied in detail in this section. The domain-size independency was also checked in both streamwise and spanwise directions to make sure that the resolved

wavelengths were not affected by the domain length or width. The normal dimension of the domain was chosen such that the top and bottom boundaries remain far from the interface at all times, so that the surface deformation is not directly affected by the boundary conditions. In addition, accuracy tests and validation with experiments and other numerical approaches were performed previously [14, 33], and will not be repeated here.

The computational grid should be able to resolve well the boundary layer of the gas and liquid near the interface in order to capture the frequency and growth of the interfacial instabilities accurately [22]. More importantly, the requirement for sufficient numerical resolution to compute the formation of holes and corrugations on the lobes indeed is a stricter restriction on the mesh size in the current study. To assess the effects of grid resolution on the numerical results of the DNS simulation of the atomization, three grid resolutions are considered in this section: M1, M2, and M3, with $\Delta = 5$ μm, 2.5 μm, and 1.25 μm, respectively.

Figure 2.7 shows the mass conservation error in different mesh resolutions. The vertical axis measures the instantaneous volume of the liquid phase V normalized by the initial volume of the liquid in the domain V_0. The coarse grid M1 clearly has the largest mass loss with

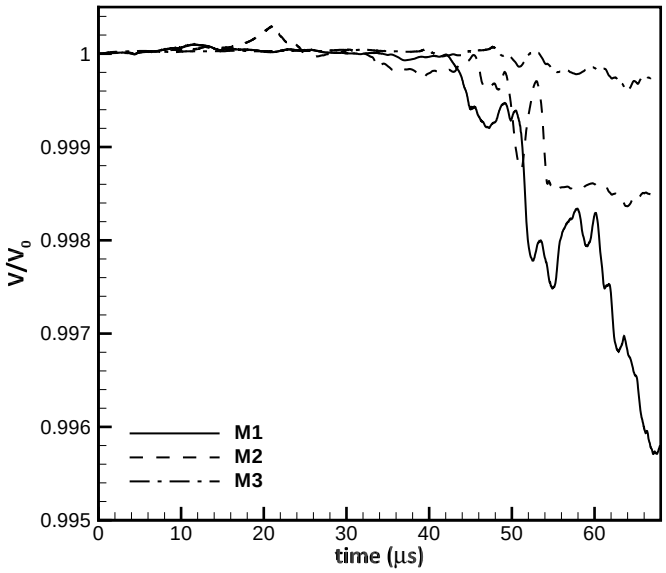

Figure 2.7: Mass conservation check for different mesh resolutions.

an error of around 0.5% near the end of the computation. The M2 and M3 grids, however, both have fair mass conservation with low errors of 0.15% and $< 0.1\%$, respectively. The results shown in Figure 2.7 are for a case with $\hat{\rho} = 0.05$. At higher density ratios, the mass conservation is significantly better.

A close-up view of the different liquid surface structures found in different atomization domains are shown in Figure 2.8 for different mesh resolutions of the same cases and at the same time steps. Figures 2.8(a–c) show the effects of mesh resolution on depicting the hole formation. Physically, holes are formed on the liquid lobes only when the lobe thickness is very small ($O(10)$ nm) and the disjoining pressure becomes active [50]. Here in the simulations, holes appear when the thickness of the liquid lobe (sheet) decreases to about the cell size Δ. Since mechanisms of sheet rupture, such as disjoining pressure, are absent in the

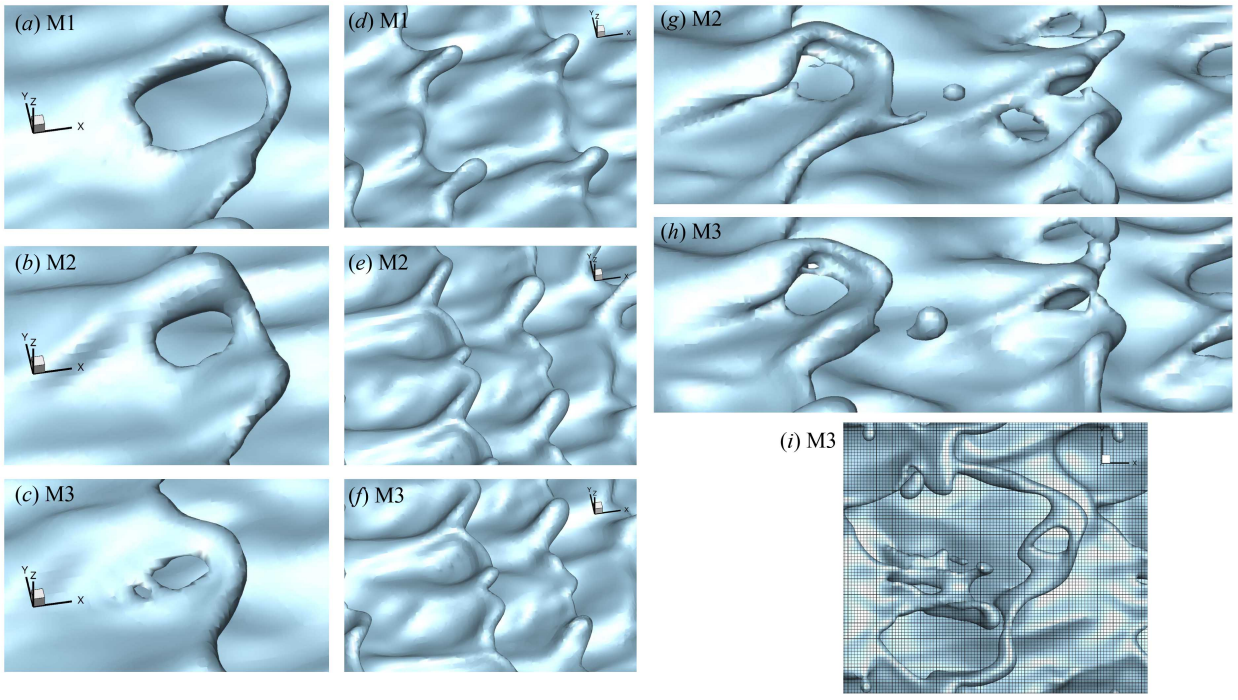

Figure 2.8: Close-up view of the liquid surface structures formed at the wave crest for different mesh resolutions. Hole formation for $Re_l = 2500$ and $We_g = 7250$ at 90 μs (a–c); corrugation formation for $Re_l = 5000$ and $We_g = 7250$ at 90 μs (d–f); droplet formation for $Re_l = 2500$ and $We_g = 7250$ at 95 μs (g–h). Comparison of the relative sizes of holes, ligaments and droplets with the grid size for $Re_l = 5000$ and $We_g = 36,000$ at 13 μs (i). $\hat{\rho} = 0.1$, $\hat{\mu} = 0.0066$ and $\Lambda = 0.5$ for all images.

present study, and because of this numerical cutoff criterion, the initial perforation of the liquid sheets is highly dependent on the mesh resolution. As can be seen in Figures 2.8(a–c), the M1 grid does not have enough resolution to capture the hole formation accurately. The holes form much sooner and expand much faster in the M1 grid compared to the other two finer grids. As seen in Figure 2.8(c), the large perforation seen on the lobe is a result of merging of several smaller holes on the liquid sheet, which can be captured only by a high resolution grid such as M3. The entire size of the hole is fairly similar for the M2 and M3 grids. The lobe rim is much thicker for finer resolutions. Consequently, a further increase of mesh resolution will only delay the pinch-off point but will not affect the ligaments formed from the expansion of the holes. Hole formation and rim dynamics are well captured by the M2 and M3 grids.

At high Re_l, corrugations form on the lobe rim (as will be described in Chapter 3). There are typically three or four such small scale corrugations (per wavelength) on the lobe rims, each having a size (thickness) of around 15–25 μm. Clearly, the M1 grid does not have enough resolution to capture these corrugations, and only the larger ligaments are resolved (Figure 2.8d). The M2 and M3 grids both resolve the corrugations correctly with very similar sizes and structures (Figures 2.8e,f). Figures 2.8(g,h) compare the droplet formation and the cascade of structures for the M2 and M3 grids. The general aspects of the process, e.g. size and location of the lobes, ligaments, and holes and thickness of the rims, are fairly similar for both grids. However, as described before, because of the numerical cut-off criterion, the holes form and expand slightly sooner (< 1 μs) for the M2 grid. The size of the resolved droplets and ligaments are also slightly smaller in the M2 grid. This is similar to what was seen by Ling et al. [50] and Jarrahbashi & Sirignano [33] in their studies of the grid resolution. It is well known that the size of corrugations and the resulting ligaments and droplets decrease as Re_l and We_g increase. In the current study, the M3 grid is used only for those higher Re_l and We_g values, and for the rest of the cases the M2 grid is adequate to capture the physics of the cascade process. As shown in Figure 2.8(i) for a high $Re_l = 5000$ and high $We_g = 36,000$,

the M3 grid resolution is fine enough to capture the smallest holes, ligaments, and droplets. The radii of curvature of the corrugations and holes and ligaments can go down to around 6 μm, which can be resolved well only by the M3 grid with $\Delta = 1.25$ μm.

Since a major part of this study is concerned with the vortex dynamics of the cascade process (Chapter 4), it is important that we resolve the velocity and vorticity in the gas-liquid mixing layer correctly. A comparison of the streamwise velocity and spanwise vorticity profiles near the wave crest at an early time ($t = 10$ μs) and a later time ($t = 70$ μs) are shown in Figure 2.9. These profiles are obtained at the front-most tip of one of the lobe crests at two distinct times. All three grids resolve the gas and liquid boundary layers correctly at early times, with the M1 profile slightly shifted towards the sheet center near the interface (Figure 2.9*a*). The gas vorticity layer δ_g imposed in this simulation is initially $\approx$ 200 μm, and the velocity gradient, hence the vorticity magnitude near the interface, increases with time (see Figure 2.9*c*). At later times (Figure 2.9*c*,*d*), the M1 grid fails to capture the velocity profile correctly and is also unable to resolve the small scale velocity fluctuations and the small vortices near the interface. The M2 and M3 grids, however, resolve the velocity fluctuations similarly with very little difference, and vividly portray the location and amplitude of those fluctuations. The liquid sheet bulk velocity increases in the meantime.

In terms of calculating the vorticity, Figure 2.9(b) shows that the magnitude of the spanwise vorticity obtained from M1 grid is significantly lower than that of M2 and M3 even at early times. The location of the vorticity peak is also closer to the sheet center and inside the liquid phase because the velocity gradient and the vorticity magnitude cannot be predicted correctly with the M1 grid. At later times (Figure 2.9*d*), this difference between the vorticity magnitudes of M1 and M2/M3 becomes even more noticeable, where the M1 grid cannot resolve the small vortices. The M2 and M3 grids have much better consistency in resolving the number of peaks, their locations and their magnitudes; however, the M3 grid is required

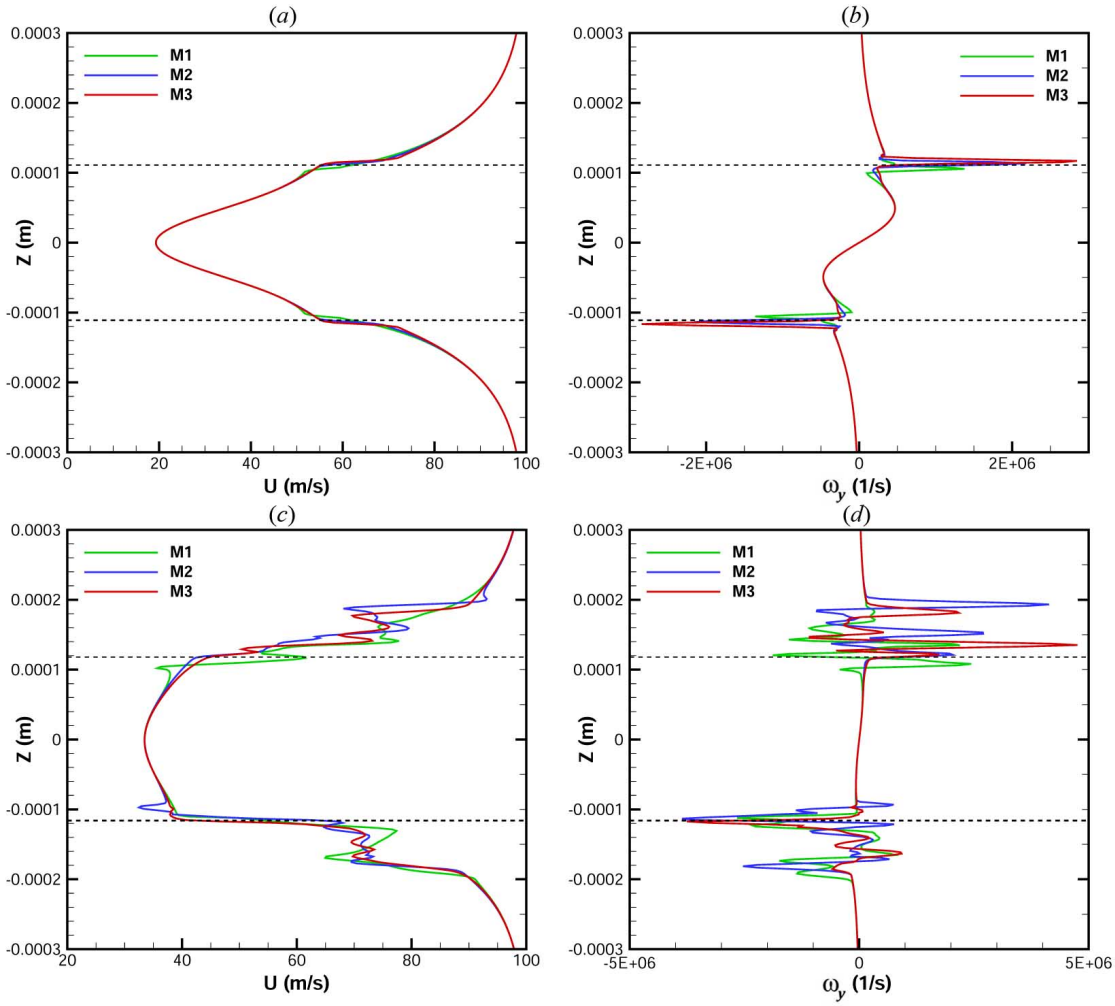

Figure 2.9: The streamwise velocity profile and the spanwise vorticity profile near the wave crest for different mesh resolutions at an early time $t = 10$ μs (a),(b), and at a later time $t = 70$ μs (c),(d). The gas-liquid interface locations are denoted by the dashed lines.

for capturing all the vortices correctly at such high Re_l values. The spanwise vorticity is not equally distributed between the two phases, and it mainly sits on the gas side since the vorticity thickness (and the boundary layer thickness) is larger in the gas phase compared to the liquid phase. The inclination of the vortices towards the gas phase is more pronounced at lower density ratios [29].

Experiments and simulations show that as KH waves amplify, the convective velocity of the waves becomes very close to the Dimotakis speed [17] defined as $U_D = (U_l + \sqrt{\hat{\rho}} U_g)/(1 + \sqrt{\hat{\rho}})$. Considering the case shown in Figure 2.9(a) with $\hat{\rho} = 0.5$ and $U_l = 20$ m/s, Dimotakis speed

gives $U_D \approx 53$ m/s. The interface velocity (at the base of the KH wave) in our simulation (Figure 2.9*a*) indicates a value of $U_{int} \approx 52$ m/s, which agrees well with the expected Dimotakis wave speed.

Chapter 3

Breakup mechanisms and atomization domains

The liquid sheet breakup mechanisms and the cascade of surface structures in the atomization regime are presented in this chapter. While increasing relative gas-liquid velocity has been shown to produce smaller droplets, the mechanism for breakup has not been clearly established yet. The common notion is that the shear causes spanwise waves to form on the surface of the sheet, and the waves grow and separate from the sheet in the form of ligaments, which then fragment into droplets [83]. There have been several numerical and experimental studies on liquid-sheet breakup; however, until recently, none of them have been able to explain the breakup mechanisms and delineate the flow parameters affecting those mechanisms.

None of the studies presented in Section 1.2.4 of Chapter 1 addressed the 3D nonlinear behavior and, thus, none addressed the key behavior for high Re and high We flows – a form of transitional turbulence in the range of interest in practical atomizers. Addressing these behaviors will be the main focus of this chapter.

3.1 Problem description

Even though several types of breakup mechanisms and the corresponding ligament and droplet sizes have been introduced by several experimentalists, they have not clearly identified the domain in which these breakups occur. Moreover, many of the studies focused on very low Re and We, which is far from the domain of interest in most applications. Generally, experiments have not been able to reveal the details of the smaller structures that develop during cascade of atomization (the work of Marmottant & Villermaux [55] is an exception) and only the quality of the developed ligaments and droplets at the end of the breakup has been discussed. In this regard, the numerical simulations have proven to be a much better tool to investigate the mechanisms of the primary atomization.

A list of computational studies on planar and round liquid jets is given in Table 3.1. The range of each non-dimensional parameter and the type of the study are also denoted in this table. In one of the earliest numerical studies on the liquid-jet instability, Lozano et al. [53] implemented a three-dimensional Lagrangian code based on vortex dynamics to track the air-liquid interface, treated as inviscid vortex sheets. Using the vortex dynamics and altering the initial perturbation orientation with respect to the flow direction, they were able to propose mechanisms for generation of spanwise and streamwise ligaments.

Scardovelli and Zaleski [76] analyzed the response to spanwise perturbations of the two-dimensional base flow in their 3D simulations at very low Re and We. They were able

Study	Configuration	Type of study	Re	We	$\hat{\rho}$	$\hat{\mu}$
Lozano et al. [53]	planar	temporal	∞	$O(10^5)$	not reported	NA
Scardovelli & Zaleski [76]	planar	temporal	1000	300–2000	0.1	not reported
Desjardins & Pitsch [16]	planar	temporal	2000–3000	500–2000	0.025	0.025
Shinjo & Umemura [80]	round	spatial	1000–3000	3000–30,000	0.04	0.007
Herrmann [27]	round	spatial	5000	17,000	0.03	0.01
Jarrahbashi et al. [33, 34]	round	temporal	320–16,000	2000–230,000	0.05–0.9	0.002–0.035
Zandian et al. [96]	planar	temporal	500–10,000	3000–72,000	0.5–0.9	0.0001–0.01

Table 3.1: List of computational studies on liquid jets, their parameters range, jet configuration, and type of study.

to distinguish two scenarios by which 3D flows set in. For small 3D perturbations, the simulation remains 2D until the sheet breaks up and a cylinder with spanwise axis pinches off. Subsequently, the capillary instability gives a 3D structure to the flow. In contrast, for higher 3D perturbations, the rim-like edge concentrates in protruding ligaments that will be subject to the capillary instability. However, the unstable cylinder is now streamwise oriented. The formation of streamwise ligaments is also observed in real experiments on shear layers [55].

A detailed numerical investigation of turbulent liquid jets in quiescent air at low density ratio was conducted by Desjardins & Pitsch [16] to identify the key atomization mechanisms, and to analyze the effects of the jet Re and We. Their work was limited to very low We compared to the range of interest for common liquid fuels and high-pressure operations. They found that liquid turbulence plays an important role in the generation of the first droplets, while the KH instabilities are not visible at early times. Several detailed atomization mechanisms have also been identified by them, such as bubble formation through sweep-ejection events and ligament generation due to bubble bursting or droplet collision. The instantaneous liquid-gas interface in their computations showed some hole formation near the tips of a few of the liquid sheets expelled from the planar jet core, tearing of those sheets and formation of the ligaments due to tearing for Re and We equal to 2000 and 1000, respectively. They did not explain the mechanisms of hole formation, though.

Computational studies of Shinjo & Umemura [80] on the primary atomization of a round liquid jet injected into high-pressure still air, at higher We than that of Desjardins & Pitsch [16], indicated ligament formation from the development of holes in the liquid crests. They showed that disturbances propagate upstream from the liquid jet tip through vortices and droplet re-collision. They claimed that collision of the droplets – broken from the ligaments formed at the back of the mushroom-shaped cap – with the liquid-jet core formed holes on the lobes. When the lobe surface area increased and its rims became thicker, the lobe surface

punctured to form two or three ligaments as the hole extended to the tip of the lobe.

Lobe perforation leading to ligament formation similar to the mechanism observed by Shinjo & Umemura [80] was also observed by Jarrahbashi & Sirignano [33] for larger gas-to-liquid density ratios. However, unlike the claims of Shinjo & Umemura [80], holes formed on the lobes even before the ligaments form and break up into droplets. Therefore, most probably, droplet collision with the liquid-jet core is not the only factor, nor even the major factor, promoting hole formation [34]. Computational simulations of round liquid jets by Herrmann [27] showed the disintegration of the liquid core to ligaments and droplets, and also predicted the droplet sizes. However, ligament formation mechanisms were not addressed.

The liquid jet from a round orifice during the transient start-up and steady mass flux periods of a high pressure injector was studied via Navier-Stokes and LS computations by Jarrahbashi & Sirignano [33] and Jarrahbashi et al. [34]. A wide range of $\hat{\rho}$, Re, and We were covered. The role of vorticity dynamics was examined via post-processing. They showed that the 3D instability starts as a result of the appearance of counter-rotating pairs of streamwise vortices in between two consecutive vortex rings, which are actually hairpin vortices wrapped around the vortex rings, and produce the first lobes. They also found that, for low $\hat{\rho}$, ligaments mostly form due to elongation of the lobes themselves; however, most of the ligaments form as a result of hole tearing at higher $\hat{\rho}$.

In the latest numerical analysis by Zandian et al. [96], various breakup patterns are identified at different flow regimes for a wide range of $\hat{\mu}$, Re and We similar to the range covered by Jarrahbashi & Sirignano [33], and high density ratios of a thin liquid sheet. Two distinct mechanisms were proposed regarding breakup of the liquid lobes into droplets: i.e. hole formation and expansion, and ligaments formation due to stretching of the lobes, which happen at low/medium and high Re values, respectively. The cascade of structures and their cause was explained from a vorticity dynamics perspective.

The goals of this chapter are to detail and explain (i) cascade of structures on the liquid surface with time, including lobe, ligament, and droplet formations; (ii) character of the breakup mechanisms at different flow conditions; (iii) the effects of density ratio, viscosity ratio, and sheet thickness on the liquid sheet breakup; and (iv) proper definition of the time scale of each of the breakup mechanisms, which would help predict the dominant mechanism at different flow conditions.

3.2 Results and discussion

3.2.1 Atomization classification

Three different processes for liquid surface deformation and breakup are identified – each applying in a different domain of the liquid Reynolds (Re_l) and Weber (We_l) numbers. The liquid structures seen in each cascade process are sketched in Figure 3.1, where the evolution of a liquid lobe is shown from a top view of Figure 2.5(a); i.e. in the negative z-direction. At high Re_l these breakup characteristics change based on the Ohnesorge number ($Oh = \sqrt{We_l}/Re_l$). At relatively high Re_l (> 2500), two of these mechanisms were observed in our computations, as follows: (i) at high Oh and high Re_l, the lobes become thin and puncture, creating holes and bridges. The bridges break as the perforation expands, and create ligaments. The ligaments then stretch and break up into droplets by capillary action. This domain is indicated as Atomization Domain II, and its process is hereafter called $LoHBrLiD$, based on the cascade or sequence of the structures seen in this domain; e.g. $Lo \equiv$ Lobe, $H \equiv$ Hole, $Br \equiv$ Bridge, $Li \equiv$ Ligament, and $D \equiv$ Droplet. (ii) At low Oh and high Re_l, lobe perforations are not seen at early times; instead, many corrugations form on the lobe front edge and stretch into ligaments. This process occurs in Atomization Domain III and is called $LoCLiD$ ($C \equiv$ Corrugation). This cascade process results in ligaments

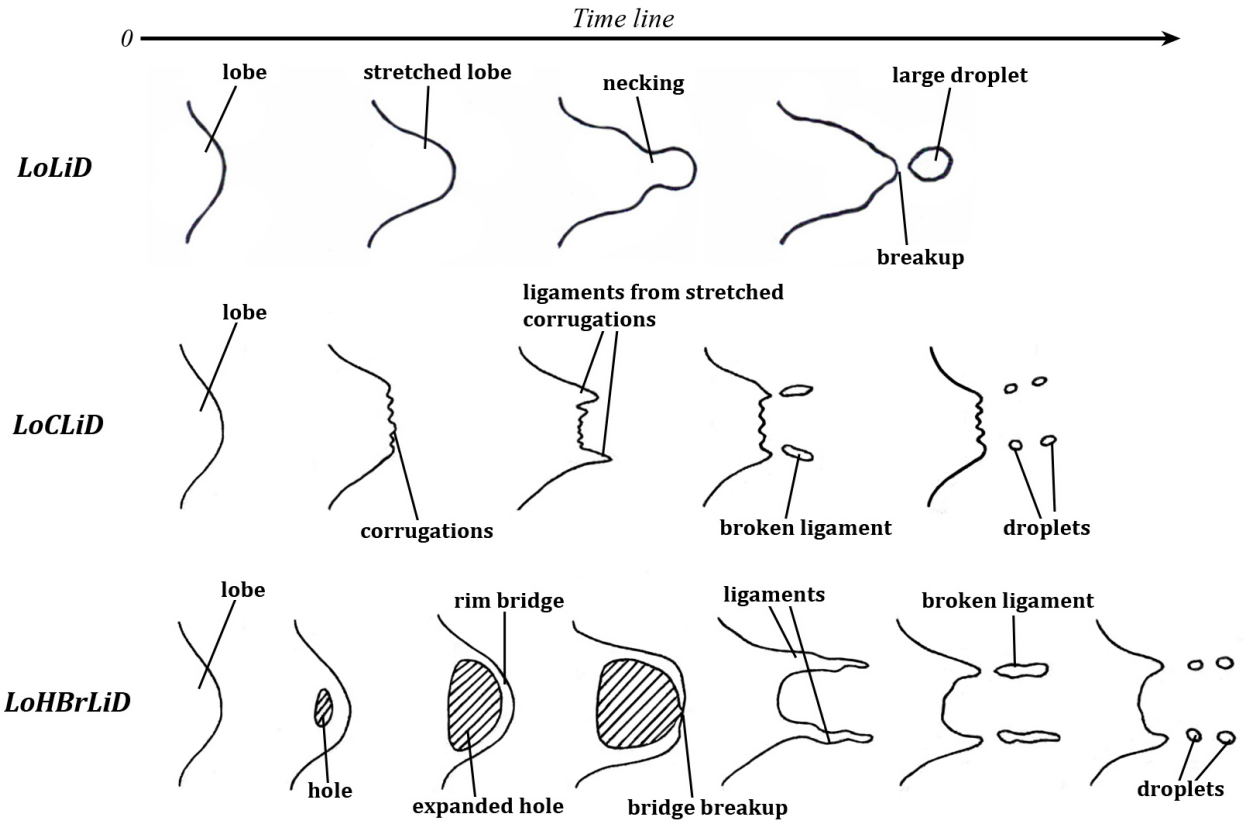

Figure 3.1: Cascade of structures for the $LoLiD$ (top), $LoCLiD$ (center), and $LoHBrLiD$ (bottom) processes; sketch showing the top view of a liquid lobe undergoing these processes. The gas flows on top of these structures from left to right, and time increases to the right.

and droplets without the hole and bridge formation steps in between. The ligaments formed in this process are typically shorter and thinner, compared to the long and thick ligaments in the former mechanism. The third mechanism follows a $LoLiD$ process and occurs in Atomization Domain I, at low Re_l and low We_l, but with some difference in the details from the $LoCLiD$ process. The main difference between the two ligament formation mechanisms at high and low Re_l is that, at higher Re_l the lobes become corrugated before stretching, and then the corrugations are stretched into ligaments. Thereby, each lobe may produce multiple ligaments, which are typically thinner and shorter than those at lower Re_l. At low Re_l, on the other hand, because of the higher viscosity, the entire lobe stretches into one thick and usually long ligament. The droplets produced in Domain I, at low Re_l, are fairly large compared to those of Domain III.

More cases were computed near the border of Domains I/III and II, showing that there is a transitional region in which both lobe/ligament stretching and hole formation mechanisms are seen simultaneously. Based on the cases that have been run, and also from the physics of the problem, it seems that the liquid viscosity, and thus the liquid Re, has the most significant effect on the stretching characteristic, while the surface tension and the gas inertia, thus the gas We, has an important role in the hole formation. Pursuant to this notion, different breakup characteristic domains are defined in the parameter space of the liquid Reynolds (Re_l) and gas Weber (We_g) numbers. Using We_g allows embedding the effects of density ratio in the classification. Thus, a generic diagram is produced that represents all density

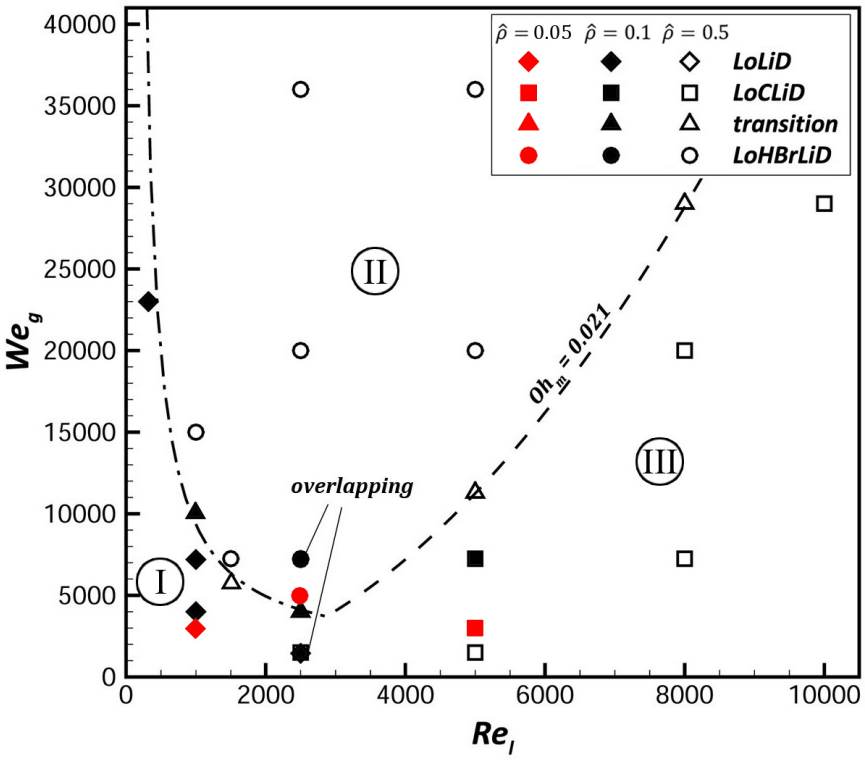

Figure 3.2: The breakup characteristics based on We_g and Re_l, showing the $LoLiD$ mechanism (Atomization Domain I) denoted by diamonds, the $LoHBrLiD$ mechanism (Atomization Domain II) denoted by circles, the $LoCLiD$ mechanism (Atomization Domain III) denoted by squares, and the transitional region denoted by triangles. The cases with $\hat{\rho} = 0.1$ are shaded, while the hollow symbols denote cases with higher $\hat{\rho} = 0.5$. The red symbols denote the cases with lower $\hat{\rho} = 0.05$. The $\hat{\rho} = 0.1$ and $\hat{\rho} = 0.5$ cases that overlap at the same point are noted. $-\cdot-\cdot-$, transitional boundary at low Re_l; and $- - -$, transitional boundary at high Re_l.

ratios on a single plot, which identifies the three atomization sub-domains defined above, shown in Figure 3.2.

The high and low density-ratio cases that overlap in this diagram are indicated in Figure 3.2. The transitional region at low Re_l follows a hyperbolic relation, i.e. $We_g = A/Re_l$, denoted by dash-dotted line, while at high Re_l limit, it follows a parabolic curve, i.e. $We_g = B^2 Re_l^2$, denoted by dashed line. The constant B is a critical value of the product of Oh and the square root of density ratio, and hereafter is defined as a modified Oh, i.e. Oh_m. Oh_m is defined using the gas We and liquid Re, i.e. $Oh_m \equiv \sqrt{We_g}/Re_l = \sqrt{\hat{\rho}} \times Oh$. The critical Oh_m at the boundary for high Re_l then becomes $Oh_{m_c} = B \approx 0.021$.

Thus, two parameters, A and B, are used to define the domain boundary. At high Re_l, we have parameter B. The parameter B involves four forces, and is the ratio of the product of liquid viscous force and square root of gas inertia to the product of liquid inertia and square root of surface tension force. Asymptotically, the domain boundary goes to constant B (constant Oh_m) at high Re_l. The second parameter is $A \sim We_g \times Re_l$. It is the ratio of the product of gas inertia and liquid inertia to the product of surface tension force and liquid viscous force. Again, four forces are involved. At low Re_l, the domain boundary approaches $A = const.$ as an asymptote.

Clearly, four forces are involved in different ways at the two (left and right) boundaries. The connection between vortex dynamics and surface dynamics near the right (high Re_l) and left (low Re_l) boundaries will be examined in Chapter 4, where the liquid structure cascade processes in each domain will be explained. The two borderlines can be combined into a single function with some extra constants for a better fit as follows;

$$We_g = \frac{A}{Re_l + \epsilon} + B^2 Re_l^2 + C, \tag{3.1}$$

where A, B and C are empirical constants, and ϵ is a small parameter for better curve

fitting. As Re_l gets very large, we would retain the parabolic function (second term) with the constant B being the product of critical Oh and $\sqrt{\hat{\rho}}$. In the limit where Re_l gets very small, the hyperbolic function (first term) dominates and gives the asymptote.

The We_g and Re_l variables in Equation (3.1) can be normalized by their values at the minimum point on the parabola-like boundary of Figure 3.2 ($Re_r = 2500$ and $We_r = 4900$). The new minimum point then becomes $We_n = 1$ and $Re_n = 1$, and the coefficients a, b and c would become of order unity (the subscript n means that the variables have been normalized). The normalized boundary equation then becomes

$$\frac{We_g}{We_r} = \frac{a}{\frac{Re_l}{Re_r} + \epsilon} + b^2 \left(\frac{Re_l}{Re_r} \right)^2 + c, \tag{3.2}$$

with the normalized coefficients that best fit our transitional boundary

$$a = 0.816, \quad b = 0.75, \quad c = -0.4, \quad \epsilon = -0.04 \ . \tag{3.3}$$

Based on these results, there are different characteristic times for formation of holes and stretching of lobes/ligaments. At the same Re_l, as surface tension increases (decreasing We_g), the characteristic time for hole formation becomes larger, hence delaying the hole formation. Thereby, most of the earlier ligaments are formed due to direct stretching of the lobes and corrugations, while hole formation is hindered (Domain III). On the other hand, as liquid viscosity increases (decreasing Re_l and increasing Oh_m), while keeping We_g the same, the characteristic time for ligament stretching gets larger if Re_l is high. In this case, the hole formation prevails compared to the ligament stretching, resulting in more holes on the lobes surface (Domain II). At very low Re_l, the characteristic time of the hole formation is also influenced by the liquid viscosity and gets larger with decreasing Re_l; thus, the breakup mechanism switches back to direct stretching as Re_l is sufficiently lowered (Domain I).

In conclusion, the transitional region is not monotonic on a We_g vs. Re_l diagram, and has a minimum value around $Re_l \approx 2500$. Thus, if We_g is less than a certain value (around $We_g = 5,000$), the ligament stretching mechanism will always prevail regardless of Re_l. At higher We_g ($> 5,000$), the $LoLiD$ and $LoCLiD$ processes are dominant in Domains I and III at very low and very high Re_l values, respectively, but there exists a Domain II between them where hole formation prevails.

The atomization processes are functions of Re_l and We_g only. The following sub-sections will show that the qualitative behavior is not much affected by the viscosity ratio (thus the gas Re); the influence of density ratio appears only through We_g, and the effect of sheet thickness appears only through Re_l and We_g.

3.2.2 Reynolds and Weber numbers effects

As discussed above, Re_l and We_g are the main parameters affecting the breakup mechanism. The atomization regime is divided into three sub-domains, each having a distinct atomization cascade during their early breakup: (i) $LoLiD$ process at low Re_l and low We_g in Atomization Domain I; (ii) $LoHBrLiD$ process at high We_g and moderate Re_l in Domain II; and (iii) $LoCLiD$ process at high Re_l and low We_g in Domain III, which involves corrugation formation. There is also a transitional region between Domains I/III and II, where each cascade process occurs locally. In this section, these processes and the cascade of structures are discussed in detail.

Four cases are presented in this section for a thick liquid sheet ($\Lambda = 0.5$). Each of these cases was chosen from a separate domain identified in Figure 3.2 – one from Domain II at $Re_l = 2500$ and $We_g = 7,250$, one from Domain III at high $Re_l = 10,000$ and low $We_g = 29,000$, one from Domain I at very low $Re_l = 320$ and low $We_g = 23,000$, and the last one from the transitional region with $Re_l = 5000$ and $We_g = 11,300$. Except for

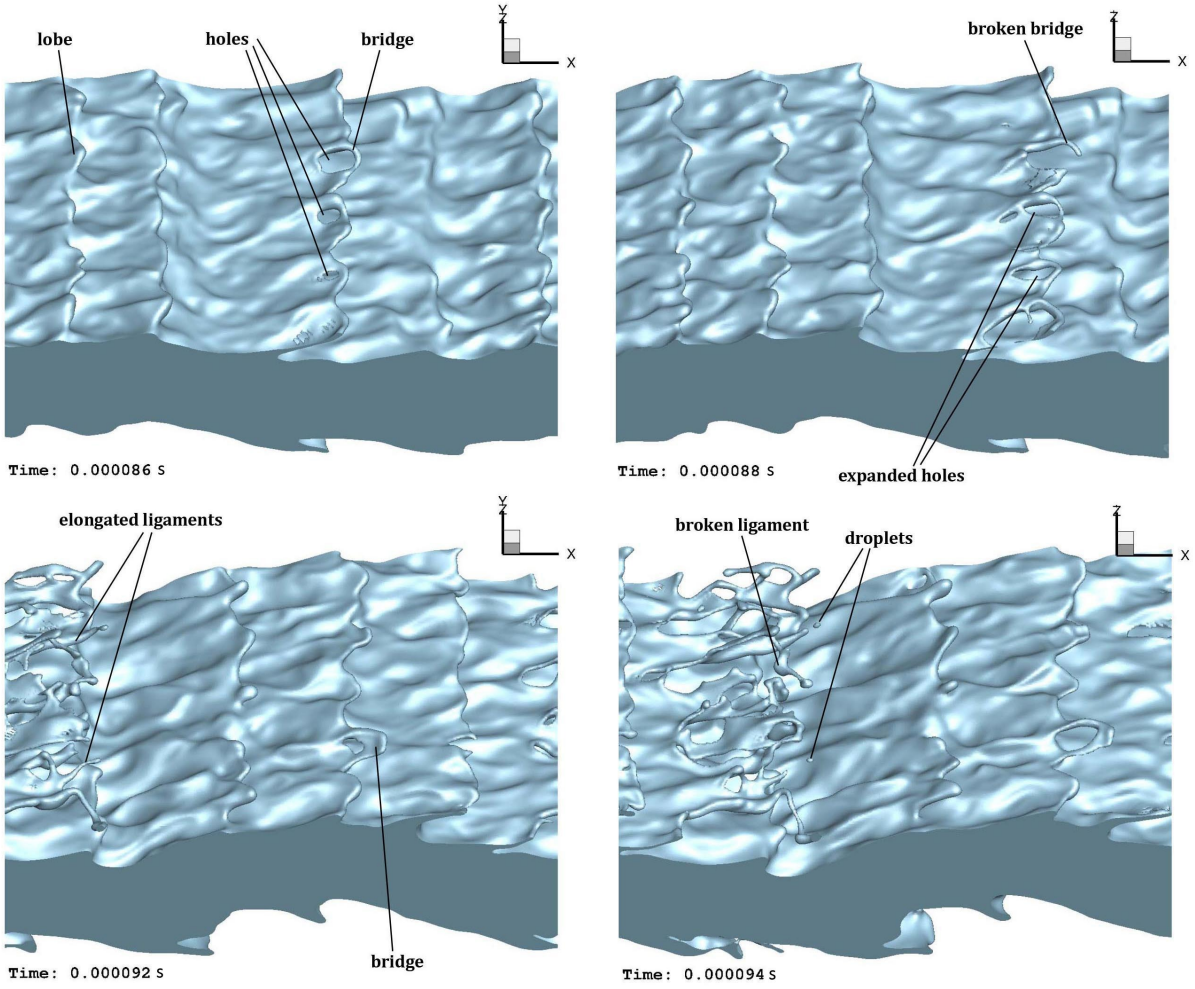

Figure 3.3: Liquid surface deformation for the $LoHBrLiD$ process (Atomization Domain II) at different times, for a thick liquid sheet $h = 200$ μm; $Re_l = 2,500$, $We_g = 7,250$, $\hat{\rho} = 0.5$ and $\hat{\mu} = 0.0066$ ($Oh_m = 0.034$). Time is indicated on the left bottom corner of each frame.

the third case which is at a low density ratio of 0.1, the rest of the cases are at $\hat{\rho} = 0.5$. The following figures show the atomization cascades occurring in each domain. In all of the figures, the gas flows over the liquid sheet in the positive x-direction, from left to right.

Figure 3.3 shows the liquid surface deformation in a period between 86 μs to 94 μs, for a thick sheet with $Re_l = 2500$ and $We_g = 7,250$ ($Oh_m \approx 0.034$). Based on the criterion that was introduced in Figure 3.2, this case falls into Atomization Domain II with the $LoHBrLiD$ cascade process. The lobes puncture to make holes at 86 μs. The holes expand and create bridges, which later break up and create one or two ligaments at 88 μs, depending on the

breakup location. The ligaments stretch (at 92 μs) and break into droplets at later times (94 μs). The final ligaments of this domain are comparatively long and thick.

Figure 3.4 shows the surface deformation for a thick liquid sheet with high $Re_l = 10,000$ and $We_g = 29,000$ ($Oh_m \approx 0.017$) during 80–86 μs. The liquid sheet atomization does not involve hole and bridge formation in this domain (III) and follows the $LoCLiD$ process. The lobe edges are not as smooth as in the previous case and several corrugations are formed on the edge of the lobes at 82 μs. The corrugations stretch into ligaments later. In this domain,

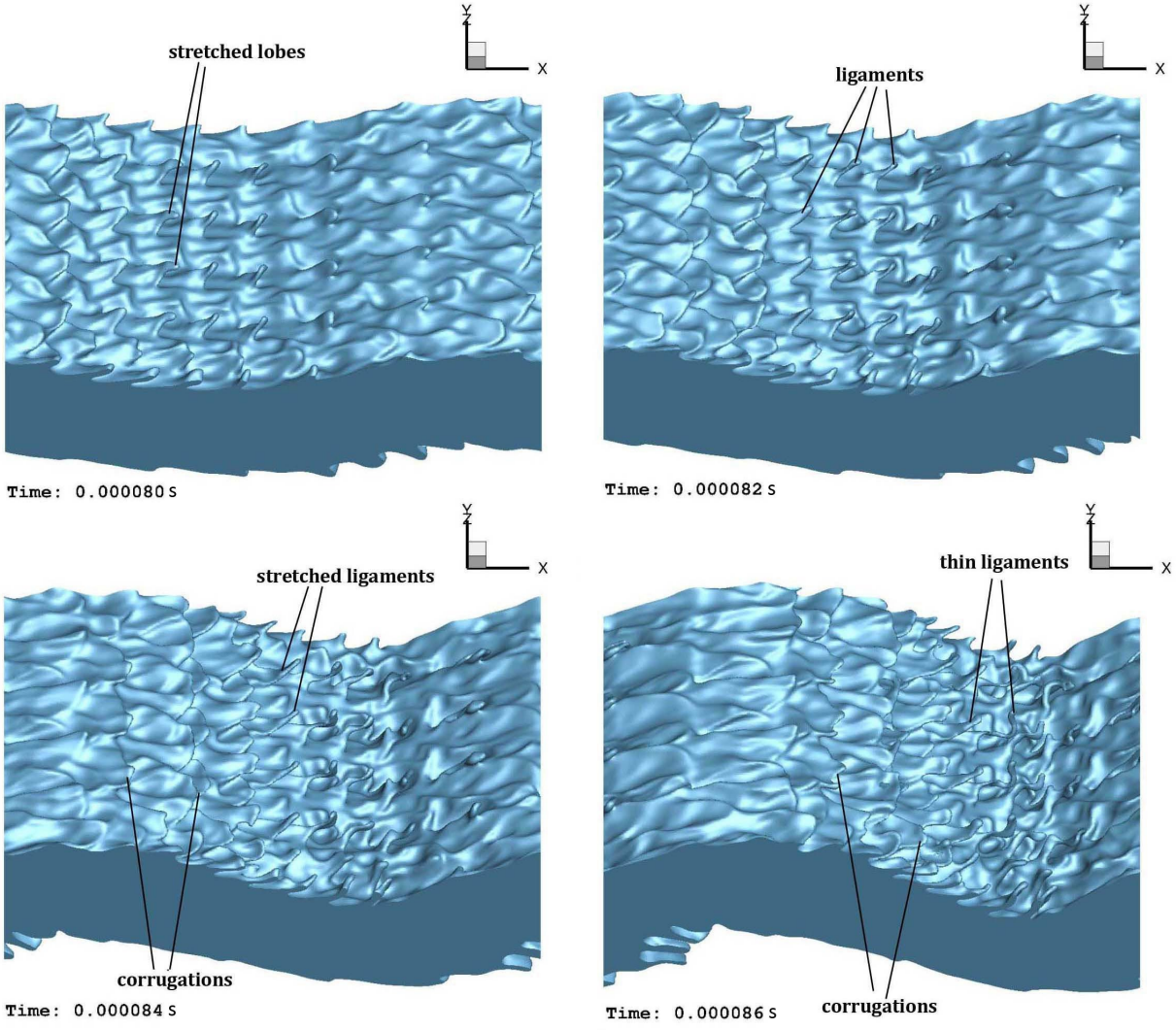

Figure 3.4: Liquid surface deformation for the $LoCLiD$ process at high Re_l (Atomization Domain III) at different times, for a thick liquid sheet $h = 200$ μm; $Re_l = 10,000$, $We_g = 29,000$, $\hat{\rho} = 0.5$ and $\hat{\mu} = 0.0066$ ($Oh_m = 0.017$).

each lobe may produce multiple ligaments. The ligaments look thinner and shorter, compared to the earlier case. This breakup characteristics agree with the classification introduced in Figure 3.2.

Figure 3.5 shows the atomization of a thick liquid sheet in the transitional region. In this case, $Re_l = 5000$ and $We_g = 11,300$, resulting in $Oh_m = 0.021$, placing this case in the transitional category. Both hole formation and lobe stretching mechanisms are seen simultaneously at different locations on the liquid surface. Thus, the characteristic times of these mechanisms are comparable. Which mechanism prevails depends on the balance between the surface

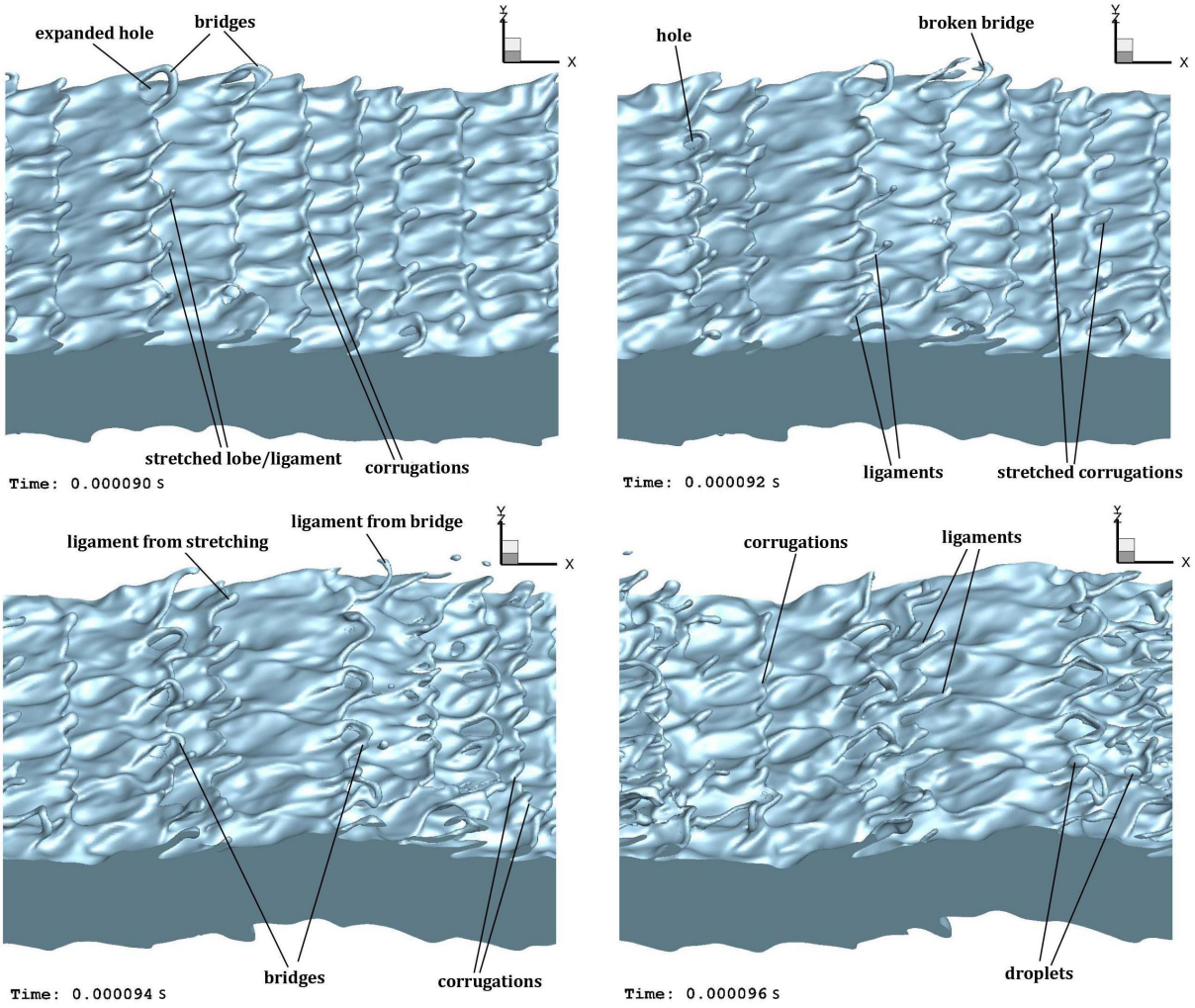

Figure 3.5: Liquid surface in the transitional region at different times, for a thick liquid sheet $h = 200$ μm; $Re_l = 5,000$, $We_g = 11,300$, $\hat{\rho} = 0.5$ and $\hat{\mu} = 0.0066$ ($Oh_m = 0.021$).

tension and viscous forces. If the surface tension force dominates, the hole formation is hindered and lobes are stretched instead. On the other hand, if the viscous effects are dominant, it is more difficult to stretch the lobes into ligaments, and more holes and bridges are formed instead. Since the characteristic times of these two effects are of the same order in the transitional zone, the prevailing mechanism varies locally. Thus, both processes occur at different parts of the sheet surface. The ligaments that are formed due to the bridge breakup are longer and thicker than those formed from direct stretching of the corrugations.

At low Re_l and low We_g, the $LoLiD$ process prevails. This is shown in Figure 3.6 for a case at a very low $Re_l = 320$ and $We_g = 23,000$ ($Oh_m = 0.475$). This case falls into Atomization Domain I as predicted in Figure 3.2; i.e. lobes stretch directly into ligaments, without any perforations on the lobes. The ligaments that are formed at low Re_l are much thicker and longer than those of the higher Re_l, and the broken droplets are also larger; The results at high Oh and low $\hat{\rho}$ (Figure 3.6) are consistent with the numerical results of Jarrahbashi et al. [34] (see their Figures 25 and 26), and the experimental results of Marmottant & Villermaux [55] for round liquid jets, and the numerical results of Scardovelli & Zaleski [76]

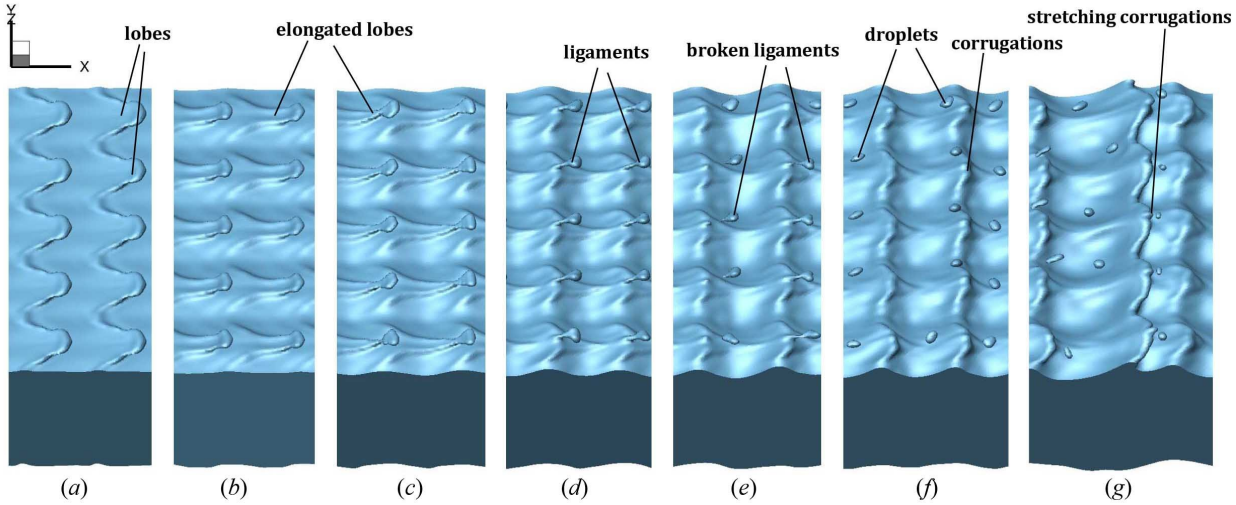

Figure 3.6: Liquid surface showing the $LoLiD$ process at low Re_l (Atomization Domain I), for a thick liquid sheet ($\Lambda = 0.5$) at low $\hat{\rho}$; $Re_l = 320$, $We_g = 23,000$ ($Oh_m = 0.475$), $\hat{\rho} = 0.1$ and $\hat{\mu} = 0.0022$, at (a) 26 μs, (b) 36 μs, (c) 40 μs, (d) 44 μs, (e) 46 μs, (f) 48 μs, and (g) 52 μs.

(see their Figure 18) for planar liquid sheets.

To clarify the breakup regimes at low Re_l and to understand the Re_l effects on the surface deformation better, lower Oh_m cases are studied by increasing Re_l and decreasing We_g.

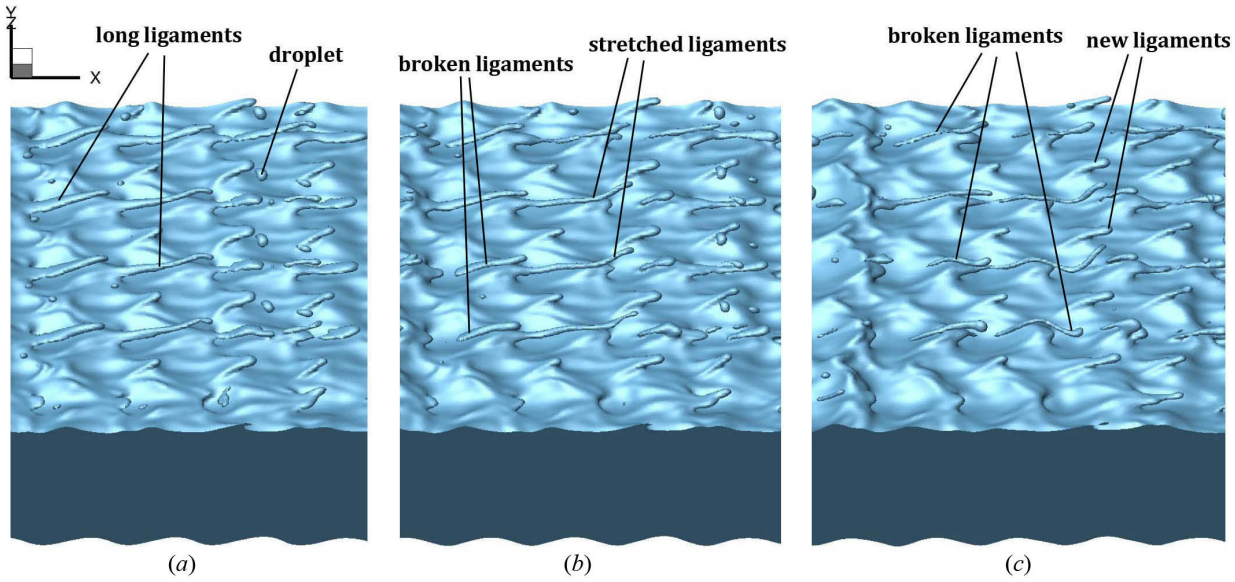

Figure 3.7: Liquid surface deformation in Domain I through time, for a thick liquid sheet ($\Lambda = 0.5$) at low $\hat{\rho}$; $Re_l = 1000$, $We_g = 7,200$ ($Oh_m = 0.085$), $\hat{\rho} = 0.1$ and $\hat{\mu} = 0.0022$, at (a) 40 μs, (b) 42 μs, and (c) 44 μs.

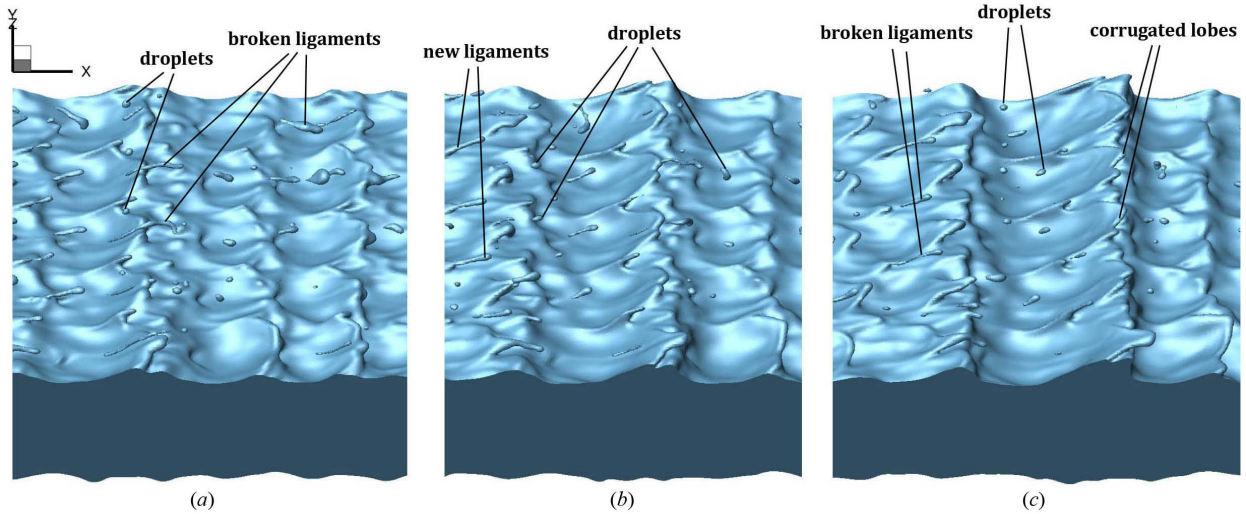

Figure 3.8: Liquid surface deformation in Domain I at later times, for a thick liquid sheet ($\Lambda = 0.5$) at low $\hat{\rho}$; $Re_l = 1000$, $We_g = 7,200$ ($Oh_m = 0.085$), $\hat{\rho} = 0.1$ and $\hat{\mu} = 0.0022$, at (a) 46 μs, (b) 48 μs, and (c) 50 μs.

Figure 3.7 depicts the liquid surface deformation at $\hat{\rho} = 0.1$, $Re_l = 1000$ and $We_g = 7,200$ ($Oh_m = 0.085$). This case still falls in Domain I. Since surface tension has increased and liquid viscosity is lower compared to that of Figure 3.6, the ligaments are stretched longer; compare Figures 3.6 and 3.7. The ligaments break at 42 μs and new ligaments are formed at the breakup location, as shown in Figure 3.7(c) at $t = 44$ μs. The broken ligaments later break into droplets due to capillary instability; see Figure 3.8. Corrugations are formed at the location of primary ligament breakup, which will stretch into new ligaments at a later time. The droplets and ligaments formed here are smaller and thinner than those of the lower Re_l shown in Figure 3.6.

In the next sections, the effects of density ratio, sheet thickness and viscosity ratio are studied to give a more complete picture of the atomization categories. In Chapter 4, the contribution of different factors in formation of the streamwise vorticity are examined at high and low density ratios to establish the physical explanation required to better understand the role of $\hat{\rho}$ in the cascade process. The characteristic time for each of these mechanisms is determined in Section 3.2.7. The characteristic time scales guide us in normalizing (generalizing) the temporal behaviors; i.e. the cascade of the length scales and the sheet expansion.

3.2.3 Density-ratio effects

Since liquid Weber number (We_l) is usually used in the liquid jet atomization literature rather than We_g, it would be interesting to see the effects of $\hat{\rho}$ on the atomization cascades using We_l parameter. $\hat{\rho}$ has a clear effect on We_g; decreasing $\hat{\rho}$ at the same We_l decreases We_g. Figure 3.9 shows that increasing $\hat{\rho}$ brings the transitional boundary closer to the Re_l axis on a We_l–Re_l diagram. The lowest borderline in this figure is actually the same for the We_g–Re_l diagram also, since it represents a density ratio of unity ($We_l = We_g$ for $\hat{\rho} = 1.0$). As $\hat{\rho}$ is lowered, the transitional curve between Domains I/III and II moves to higher values

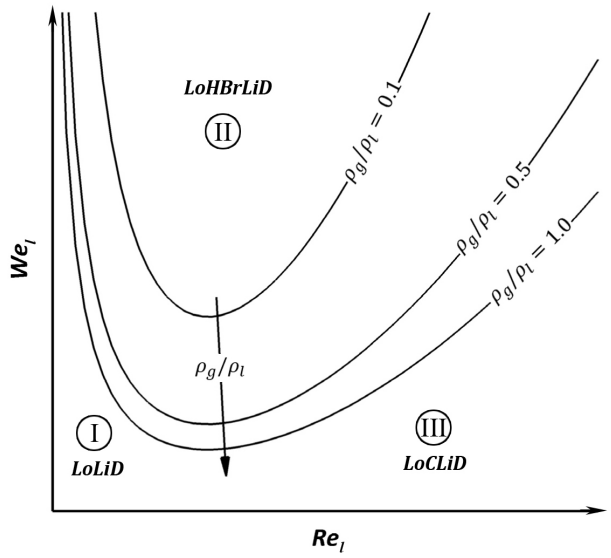

Figure 3.9: Effect of density ratio on the atomization domains on a We_l–Re_l diagram.

in the We_l–Re_l diagram. This means that, in reality, the points with medium We_l, that were formerly in Domain II at higher $\hat{\rho}$, might fall in Domains I or III at the lower density ratio; i.e. a case that is closely above the borderline curve (in Domain II) for $\hat{\rho} = 1.0$ will fall below the borderline curve (in Domains I or III) if $\hat{\rho}$ is reduced to 0.1 at the same We_l. This is true for all data points in the area between the $\hat{\rho} = 0.1$ and $\hat{\rho} = 1.0$ curves. In conclusion, Domains I and III expand on the We_l–Re_l diagram as $\hat{\rho}$ is lowered, and the lobe/ligament stretching becomes more dominant over a larger area of the We_l–Re_l diagram.

A case at low $\hat{\rho} = 0.1$ and low $Re_l = 320$ and high $We_l = 230,000$ (in Domain I) was shown earlier in Figure 3.6, which followed a $LoLiD$ process in its early breakup. The same case but with a higher $\hat{\rho} = 0.5$ is shown in Figure 4.2. Both cases are at a very low Re_l but very high We_l, resulting in $Oh = 1.5$. However, We_g and Oh_m are different in these two cases due to the difference in $\hat{\rho}$. We_g of the case with $\hat{\rho} = 0.1$ was $23,000$, which places this case under the transitional boundary curve in Figures 3.2 and 3.9; i.e. in Domain I. However, as $\hat{\rho}$ is increased to 0.5, We_g becomes much higher ($= 115,000$). Thus, the case with $\hat{\rho} = 0.5$ falls in Domain II on top of the transitional curve in both Figures 3.2 and 3.9. Figure 4.2 shows the surface deformation for this case, and manifests that its atomization cascade follows well

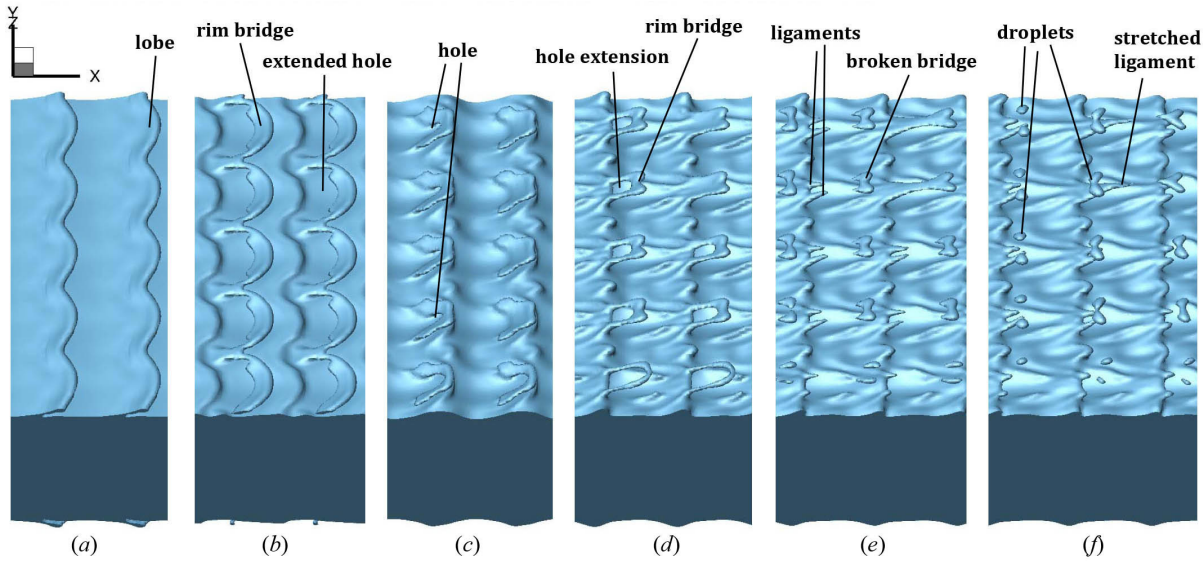

Figure 3.10: Liquid surface deformation in Domain II through time, for a thick liquid sheet ($\Lambda = 0.5$) at high $\hat{\rho}$; $Re_l = 320$, $We_g = 115,000$ ($Oh_m = 1.05$), $\hat{\rho} = 0.5$, and $\hat{\mu} = 0.0022$, at (a) 18 μs, (b) 22 μs, (c) 26 μs, (d) 28 μs, (e) 30 μs, and (f) 32 μs.

our scenario; i.e. holes and bridges form and break into ligaments and droplets. This proves that density ratio has a substantial effect on the breakup process through We_g.

A closer look at Figures 3.6 and 4.2 reveals that, $\hat{\rho}$ also affects the time scale of the droplet formation and the shape of the lobes. Droplets form much sooner and the lobes are more stretched at higher $\hat{\rho}$, which involves hole formation. The lobes are thinned in the spanwise (y) direction at lower $\hat{\rho}$ but in the normal (z) direction at higher $\hat{\rho}$.

3.2.4 Sheet thickness effects

Two different sheet thicknesses have been analyzed in this study; the thin sheet with $h = 50$ μm resulting in $\Lambda = 2.0$, and the thick sheet with $h = 200$ μm resulting in $\Lambda = 0.5$. The sheet thickness affects Oh_m ($= \sqrt{\hat{\rho}}\mu_l/\sqrt{\rho_l h \sigma}$); therefore, it can change the atomization characteristics especially at high Re_l, even at constant fluid properties and flow velocity. Recall that the transitional boundary between Domains II and III is a parabolic curve with

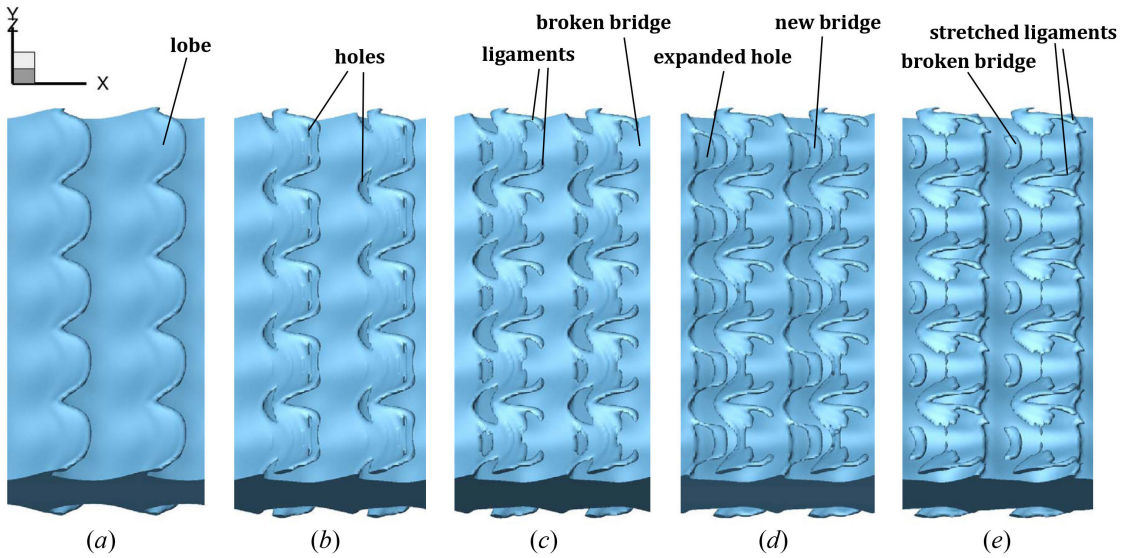

Figure 3.11: Liquid surface deformation in Domain II through time, for a thin liquid sheet ($\Lambda = 2.0$); $Re_l = 320$, $We_g = 115,000$ ($Oh_m = 1.05$), $\hat{\rho} = 0.5$, and $\hat{\mu} = 0.0022$, at (a) 10 μs, (b) 11 μs, (c) 12 μs, (d) 13 μs, and (e) 14 μs.

constant Oh_m (see Figure 3.2). A thicker jet would have smaller Oh_m at the same flow conditions and the same fluid properties; thus, with increasing sheet thickness, the atomization cascade would move away from Domain II, towards Domain III, as Oh_m is lowered below the critical $Oh_m \approx 0.021$ (see Figure 3.2).

The sheet thickness effects are embedded in We_g and Re_l parameters, and it does not change the atomization characteristics on its own if We_g and Re_l are kept constants. The case shown in Figure 3.11 has the same Re_l, We_g, and $\hat{\rho}$ as those of Figure 4.2, but with a thinner sheet ($h = 50$ μm compared to 200 μm in Figure 4.2). The results show that the sheet thickness alone does not alter the atomization mechanism, as both thin and thick sheets (Figures 3.11 and 4.2, respectively) manifest the same $LoHBrLiD$ cascade process. An increase in the sheet thickness delays the breakup process though, thus, affecting the time scales of the structure cascade and droplet formation. This will be discussed in Section 3.2.7.

3.2.5 Viscosity ratio effects

In order to check the effects of viscosity ratio ($\hat{\mu}$) on the atomization cascades and their time scales, different viscosity ratios in the range $O(10^{-3}) < \hat{\mu} < O(10^{-1})$ have been studied at several different Re_l and We_g values in each domain. Figure 3.12(a) compares the surface of two liquid sheets with different viscosity ratios at 22 μs – both in Atomization Domain II. Even though the viscosity ratios are two orders of magnitude apart, the surfaces are very similar. Both cases follow the $LoHBrLiD$ cascade process, and the size and shape of the holes and bridges (ligaments) are very similar at each time; the lower $\hat{\mu}$ case manifests slightly larger size perforations. Figure 3.12(b) also compares two very different $\hat{\mu}$ cases from Atomization Domain III. Both cases follow the $LoCLiD$ process, and the size and shape of lobe corrugations and ligaments are fairly equal at 50 μs.

From above discussion and the results illustrated in Figure 3.12, it is concluded that $\hat{\mu}$ does not alter the atomization process; thus, the threshold between Domains I/III and II (the transitional region) is independent of $\hat{\mu}$, which also has negligible effect on hole formation

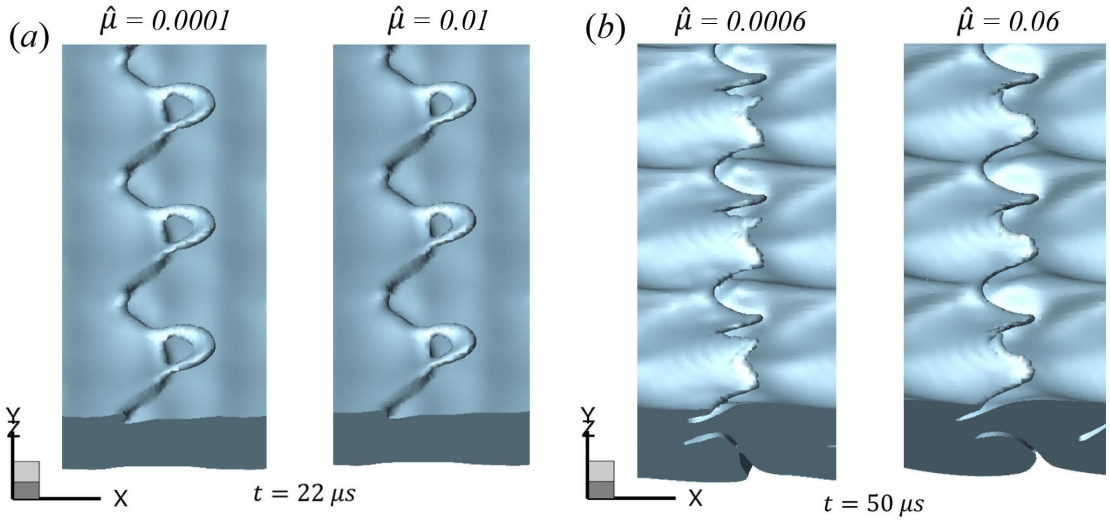

Figure 3.12: Liquid surface deformation for two different viscosity ratios in Domain II; $Re_l = 2500$, $We_g = 7250$, $\hat{\rho} = 0.5$ (a); liquid surface deformation for two different viscosity ratios in Domain III; $Re_l = 5000$, $We_g = 7250$, $\hat{\rho} = 0.5$ (b).

and lobe/ligament stretching time scales. In other words, the ligament stretching mechanism is liquid dominated, as far as the viscosity is concerned; i.e. the gas viscosity does not have a substantial role in ligament stretching. However, the gas density is significant in the hole formation mechanism, as discussed before.

3.2.6 Comparison with other planar and round jet computations

In order to verify our findings of the atomization categories in the We_g–Re_l map and to check their dependence on the jet geometry (planar vs. circular), a similar diagram for round liquid jets has been built using the numerical results of Jarrahbashi et al. [34]. In their work, both Re and We are based on the initial liquid jet diameter. Their values are transformed to We_g and Re_l based on jet radius for the purpose of comparison. The results of other numerical studies (Refs. [16, 27, 80]) are also compared qualitatively, where possible.

All of the cases studied by Jarrahbashi et al. [34] are shown in the We_g–Re_l plot in Figure 3.13 (right plot). The cases are grouped into the three atomization categories we introduced; i.e. $LoHBrLiD$, $LoLiD/LoCLiD$ (stretching either with or without corrugations), and the transitional domain. Since frame by frame surface deformation at the early breakup stages was not given in Ref. [34], clear distinction between the two stretching mechanisms was not possible, hence, both $LoLiD$ and $LoCLiD$ cases were put in the same group (denoted by squares in Figure 3.13). Even though most of their results were for low Re_l and high We_g, they show some similarity in behavior with the planar liquid jets in different domains. With the newly defined Re_l and We_g based on the jet radius, instead of the diameter, all of the data points fall in the proper zones in this diagram without notably altering the domains boundary. The transitional boundary follows the same Equation 3.2, with the coefficients

$$a = 0.816, \quad b = 1.07, \quad c = -0.4, \quad \epsilon = 0.04, \tag{3.4}$$

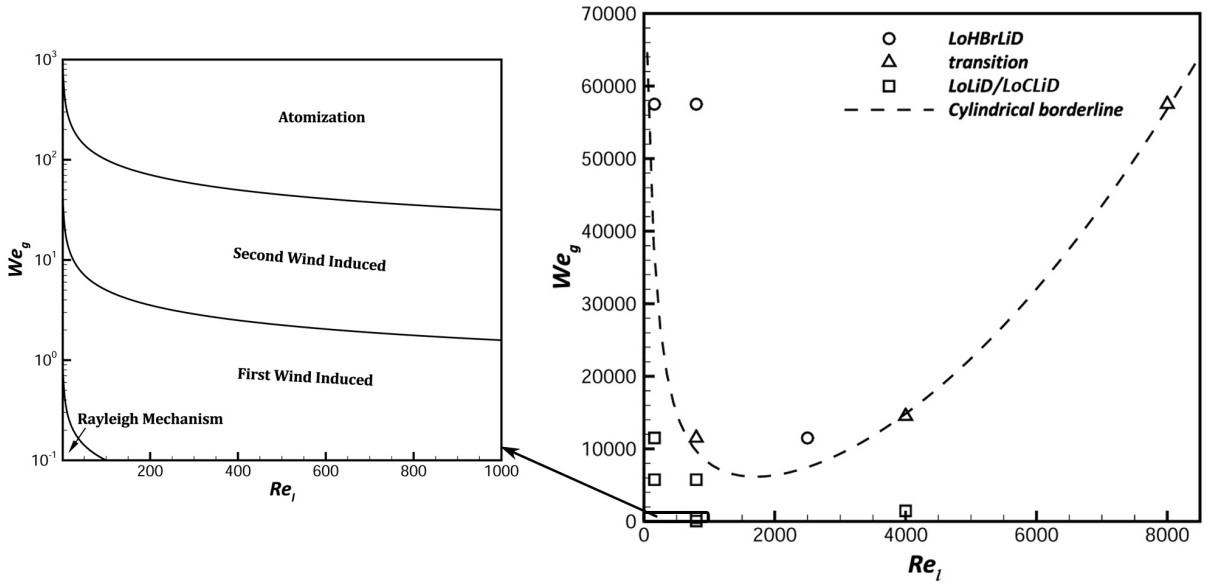

Figure 3.13: The operation regimes of a round liquid-jet breakup by Reitz and Bracco [71] recast on a We_g (log-based) vs. Re_l plot (left); The breakup characteristics based on Re_l and We_g (using jet radius) for round liquid jets, from the results of Jarrahbashi et al. [34] (right). The three breakup categories are shown by symbols, along with the transitional boundary obtained from planar liquid sheet diagram with minor modification (dashed line).

and the same reference values for Re_l and We_g; i.e. $Re_r = 2500$ and $We_r = 4900$. Only b has changed from the planar jet result. Above this transitional boundary the hole formation mechanism prevails and below this curve the lobe/ligament stretching is the primary atomization cascade.

The left plot in Figure 3.13 shows the hyperbolas that bound the atomization regime from the three other regimes of a round liquid-jet breakup presented by Reitz and Bracco [71] (shown earlier in Figure 1.8), on a blown-up view of the lower left corner of our diagram on the right. The purpose of putting these two plots side-by-side is to emphasize that the Atomization Domain dwarfs the other domains in both parameter range and importance in practical spray formation. Yet, surprisingly this domain is the least studied of all.

Re_l for the planar liquid sheets studied by Desjardins & Pitsch [16] was in the range 2000–3000, and the highest We_g in their study was $O(10^2)$, which as they assert, puts all their cases in the Second Wind-Induced breakup regime (see the left image in Figure 3.13), even

though this regime was originally described for round jets [71]. Thus, all their results could be considered to be in the *LoLiD* group in our classification. Even though only a few figures at different steps of sheet breakup were presented there, they summarized the atomization processes in three essential steps: (i) initial corrugation of the interface (i.e. formation of lobes); (ii) formation and stretching of liquid ligaments; and (iii) rupture of the ligaments, leading to droplet formation. They also mention that the ligaments are typically oriented in the streamwise direction, and there is no sign of hole formation in their results. This is consistent with our descriptions of Domain I.

Shinjo & Umemura [80] studied a smaller range of Re_l (< 1500) and slightly higher We_g (< 500) than Desjardins & Pitsch [16] for a round liquid jet. They studied startup of a full liquid-jet injected into a gas, including the shredding of the cap. The range of Re_l and We_g puts their cases in the *LoLiD* group. The strong shear near the liquid surface deforms the liquid surface, inducing ligament formation, as described by Shinjo & Umemura [80]. They suggest that the main mechanism for ligament formation is the stretching of the sheared liquid surfaces (lobes); however, most of the ligaments and droplets are formed near the mushroom-shaped tip of the jet not the main body of the liquid jet, and ligament formation occurs first from the tip edge. They also observed hole formation on the lobes; however, it was not due to the vortex motion, but due to the inertial motion from the re-collision of the broken droplets from the tip edge. Thus, the hole-formation mechanism seen in their study is different from ours, since the jet tip physics are not included in our study of the liquid-sheet segment. Herrmann [27] studied a round liquid jet with similar range of We_g as Shinjo & Umemura and slightly higher Re_l ($= 2500$) (based on nozzle radius). He did not witness any hole formation in the liquid jet breakup, and only ligament stretching was observed. Since his Re_l was higher than Shinjo & Umemura's, more corrugations and smaller and thinner ligaments were observed in his study, which is in agreement with our findings.

The experimental results of Hoyt & Taylor [31] for round liquid jets at a very high Re_l

of $O(10^5)$ show similar atomization characteristics with very small corrugations and very thin ligaments as our results for Domain III. Even though their study focuses on spatial development of a liquid jet and ours is temporal, a qualitative comparison with their results shows that as Re_l increases, the length scale of the ligaments and corrugations becomes smaller – consistent with what has been found here.

From the analysis in this section, we conclude that the atomization domains are generic, fairly independent of the liquid jet geometry. The same domains can be classified on the We_g–Re_l diagram with very minor modifications for both planar or round liquid jets.

3.2.7 Structure cascade time scales

As mentioned earlier, there are two different characteristic times for the formation of holes and the stretching of lobes and ligaments. At the same Re_l (high Re_l), as the surface tension increases (decreasing Oh and We_l), the characteristic time for hole formation becomes larger, delaying the hole formation. Thus, for lower Oh (or We_l), most of the earlier ligaments are formed due to direct stretching of the lobes and/or corrugations, while the hole formation is halted. On the other hand, at relatively large Re_l (> 3000), as liquid viscosity is increased (decreasing Re_l and increasing Oh), at the same We_l, the ligament-stretching time gets larger. In this case, hole formation prevails compared to the ligament stretching mechanism, resulting in more holes on the liquid lobes.

Figure 3.14 shows the first time at which a hole forms for three different We_l values at high $Re_l = 5000$ and high $\hat{\rho} = 0.5$. The other dimensionless parameters are the same for all three cases. As We_l increases, from left to right, the hole formation time decreases. The first hole is formed at 52 μs for $We_l = 14,400$ (the left-most image), and at around 13 μs for $We_l = 72,000$. This indicates that the hole formation characteristic time should be inversely proportional to We_l. The holes expand more rapidly at higher We_l. At high Re_l,

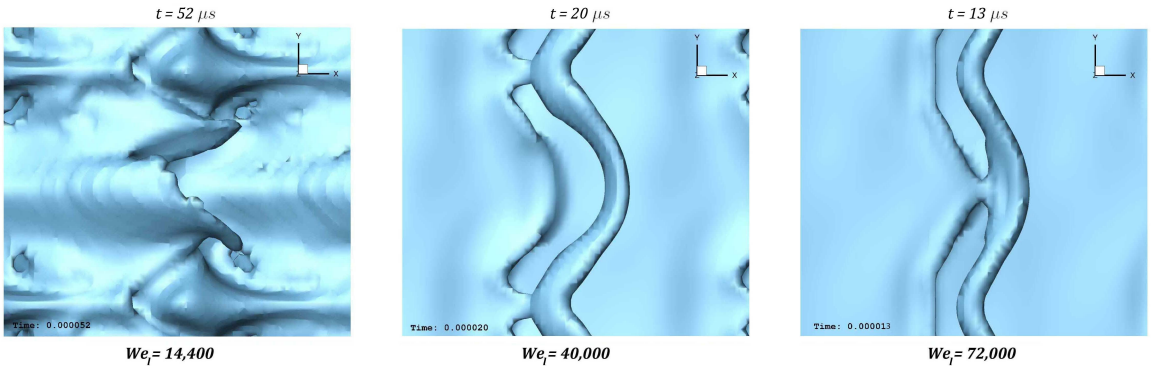

Figure 3.14: The time at which the first hole forms at different We_l values; $Re_l = 5000$, $\hat{\rho} = 0.5$, and $\hat{\mu} = 0.0066$. The time and We_l are indicated on top and bottom of each image, respectively.

the hole formation is delayed as $\hat{\rho}$ decreases. Thus, the hole-formation time scale should also be inversely proportional to $\hat{\rho}$. This effect may be combined with the effect of We_l by using the gas We_g rather than the liquid We_l.

The time scales are non-dimensionalized using the freestream gas velocity (U) and the sheet thickness (h), as characteristic velocity and length. Figure 3.15 shows the non-dimensional lobe/ligament stretching time scale ($U\tau_s/h$) as a function of Re_l at several We_g values. τ_s is the dimensional characteristic time for ligament stretching and corresponds to the first time when a ligament is formed. The stretching time scale is proportional to the reciprocal of Re_l and has negligible dependence on We_g (see Figure 3.15). All of the cases at We_g values from 1500 to 29,000 fit well on the same curve k_0/Re_l; where k_0 is a nondimensional constant.

Based on the results presented in Figures 3.14 and 3.15, two different characteristic times are formed at high Re_l – one for each mechanism – involving surface tension and viscosity. The hole-formation characteristic time (τ_h) is directly proportional to the surface tension and inversely proportional to the density ratio, while the stretching characteristic time (τ_s) is proportional to the liquid viscosity. Thus, the following two nondimensional characteristic

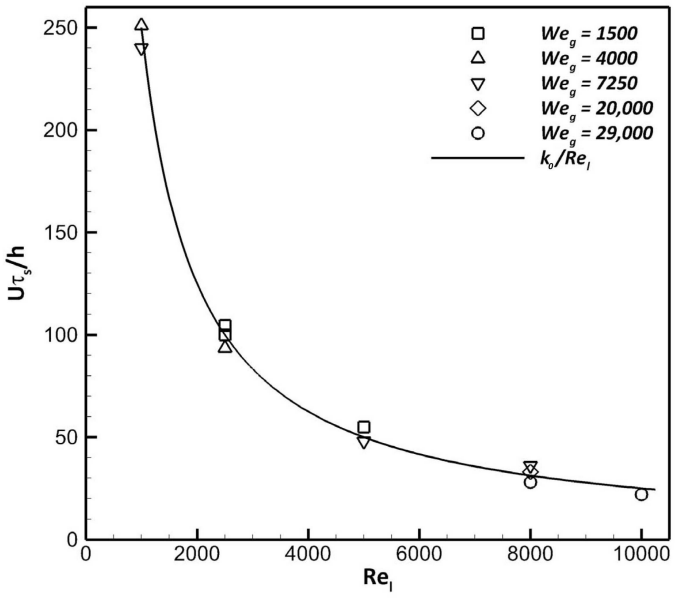

Figure 3.15: Nondimensional stretching time scale versus Re_l at different We_g values.

times are proposed for these mechanisms;

$$\frac{U\tau_s}{h} \propto \frac{\mu_l}{\rho_l U h} = \frac{1}{Re_l}, \tag{3.5}$$

$$\frac{U\tau_h}{h} \propto \frac{\sigma}{\rho_g U^2 h} = \frac{1}{We_g}. \tag{3.6}$$

As indicated in the equations above, the characteristic times can be written in terms of the sheet thickness and jet velocity. In this form, the hole-formation nondimensional time becomes inversely proportional to We_g, while the stretching nondimensional time is inversely related to Re_l. However, real times are independent of the thickness and only depend on the fluid properties. Clearly, h/U is a convenient normalizing time. Aside from its accord with our results, these time scales are consistent with intuition. The surface tension hinders hole formation, thus increasing its time scale, while liquid viscosity resists stretching, hence increasing the stretching characteristic time. Also, the time scales for both mechanisms become larger for the same dimensionless parameters as the jet becomes thicker. The case

with $Re_l = 2500$ and $We_g = 7,250$ and $h = 200$ μm perforates first at around 82 μs (Figure 3.3), while a jet with the same Re_l and We_g, and $h = 50$ μm perforates at around 20 μs, which is almost 4 times less than that of the thicker sheet.

Combination of the two Equations (3.5) and (3.6) yields a relation between the two time scales at high Re_l regions of interest, involving Oh_m;

$$\frac{U\tau_h}{h} \propto \left(\frac{U\tau_s/h}{Oh_m}\right)^2. \tag{3.7}$$

In the transitional region, near the boundary, where the two characteristic times are of the same order, both hole formation and corrugation stretching appear at different parts of the liquid surface, as shown in Figure 3.5.

At low Re_l (< 3000) range, the liquid viscosity has an opposite effect on the hole formation and ligament stretching. As shown in Figure 3.2, near the left boundary, the time scale of the stretching becomes relatively smaller than the hole-formation time scale as Re_l is reduced at a constant We_g. Hence, there is a move back to ligament stretching from hole formation with decreasing Re_l at a fixed We_g. It is concluded that a term should be added in the hole-formation time scale, which becomes larger at lower Re_l. At higher Re_l, however, this term would vanish, with a return to the time scale in Equation 3.6. In order to generalize the hole-formation time scale, a term is added with the reciprocal of Re_l as its coefficient to fix the opposite behavior seen at lower Re_l. The new, more general, nondimensional time scale then becomes

$$\frac{U\tau_h}{h} \propto \frac{\sigma}{\rho_g U^2 h}(1 + \frac{k}{Re_l}) = \frac{1}{We_g}\left(1 + \frac{k}{Re_l}\right), \tag{3.8}$$

where k is a nondimensional constant. The stretching time scale does not need any modification for low Re_l (see Figure 3.15).

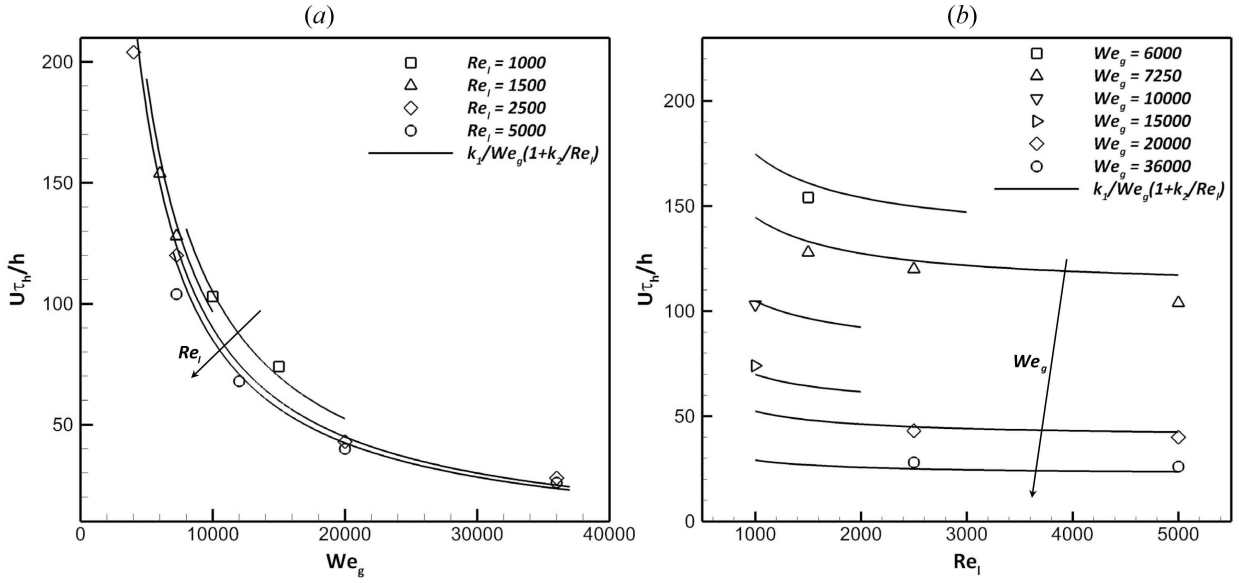

Figure 3.16: Nondimensional hole-formation time scale versus We_g at different Re_l values (a), and versus Re_l at different We_g values (b).

Figure 3.16(a) shows the nondimensional hole-formation time scale versus We_g at different Re_l values. The hyperbolic relation between the hole-formation time scale and We_g at any constant Re_l is evident. As Re_l decreases, the hyperbolas shift upward. The solid lines represent Equation 3.8, where k_1 and k_2 are nondimensional constants. As Re_l increases, the hyperbolic curves get closer to one another, meaning that the effect of Re_l becomes less important at higher Re_l. At very high Re_l, the term in parenthesis in Equation 3.8 approaches unity and Equation 3.6 is retained.

The results shown in Figure 3.16(a) indicate that Re_l is not as unimportant as We_g was for τ_s (shown in Figure 3.15). Figure 3.16(b) shows the dependence of the hole-formation time scale on Re_l at different We_g values. At a constant We_g, the nondimensional hole-formation time is a hyperbolic function of Re_l but with a much slighter slope in the range considered here. As We_g increases these hyperbolas (solid lines) move down in Figure 3.16(b). The dependence of τ_h on We_g compared to Re_l becomes clear as we compare Figure 3.16(b) with Figure 3.16(a). At very high We_g (the bottom curves in Figure 3.16b), the hole-formation characteristic time becomes almost independent of Re_l for the range of Re_l considered in

this plot. The solid lines become almost straight horizontal lines as We_g becomes very large.

Combining Equations 3.5 and 3.8, the relation between the two time scales becomes

$$\frac{U\tau_h}{h} \propto \left(\frac{U\tau_s/h}{Oh_m}\right)^2 \left(1 + \frac{k}{Re_l}\right). \tag{3.9}$$

At high Re_l (> 3000), the second parenthesis approaches unity and the earlier derived relation in Equation 3.7 is retained. At very low Re_l limit (< 200), the asymptotic relation between the two time scales becomes

$$\frac{U\tau_h}{h} \propto \frac{1}{Re_l}\left(\frac{U\tau_s/h}{Oh_m}\right)^2 = \frac{Re_l}{We_g}\left(\frac{U\tau_s}{h}\right)^2. \tag{3.10}$$

So, at low Re_l, the hole formation and the ligament stretching time scales are not related only by the modified Ohnesorge number; the flow Re_l also has a substantial role in the atomization cascade at low Re_l.

3.3 Conclusions

Temporal development of surface waves on planar jets and their breakup into droplets are studied numerically. Three main atomization cascades are identified. The atomization characteristics are well categorized on a parameter space of gas Weber number (We_g) versus liquid Reynolds number (Re_l). The gas-to-liquid density ratio affects the breakup process, thereby making We based on liquid density less important as a correlation factor. The Rayleigh Domain, First Wind-Induced Domain, and the Second Wind-Induced Domain collectively occupy a minor portion of the We_g vs. Re_l diagram. Furthermore, the atomization portion is now separated as three sub-domains. Atomization Domain I has a lobe-ligament-droplet ($LoLiD$) cascade; Domain II involves a lobe-hole-bridge-ligament-droplet ($LoHBrLiD$) cas-

cade; and Domain III shows a lobe-corrugation-ligament-droplet ($LoCLiD$) cascade.

At high Re_l, the breakup characteristics change based on a modified Ohnersorge number ($Oh_m = \sqrt{We_g}/Re_l$). At high Oh_m, the lobes thin and perforate to form bridges, which eventually break into one or two ligaments. At lower Oh_m, the hole formation is hindered and instead, the lobe rims corrugate and stretch into small ligaments. There is also a transitional region, where both mechanisms co-exist. The transition region at high Re_l follows a constant Oh_m line.

At low Re_l, the transitional region follows a hyperbolic function in the We_g–Re_l plot. At low We_g and low Re_l, the lobes stretch directly into ligaments. The ligaments created in this domain are fairly thick and long, and result in larger droplets. As We_g is increased while keeping Re_l low, the hole formation process prevails. Thus, the hole formation process dominates over a wide range of low and high Re_l, but only over moderate to high We_g. Below a critical We_g, hole formation is completely hindered at all Re_l. These atomization cascades are independent of the jet geometry (planar or round). Furthermore, a very similar correlation describes the boundaries between different atomization domains for the planar and round jets.

Viscosity ratio has no substantial effect either on the cascade processes or their time scales, while the effect of sheet thickness is described only through Re_l, We_g, and Oh_m. Increasing the sheet thickness delays the hole formation and the lobe/ligament stretching process.

Different characteristic time scales were introduced for the hole formation and lobe stretching – mainly related to the surface tension and liquid viscosity, respectively. At any flow condition, the mechanism having a smaller characteristic time is the dominant process. In the transitional region, both characteristic times are of the same order; thus, both mechanisms occur simultaneously and the cascade of liquid structures varies locally. The two characteristic times are related to each other by Oh_m, which involves the We_g and Re_l.

Chapter 4

Vortex dynamics of the primary atomization

Vortex dynamics concepts can shed further light on surface deformation of a liquid jet in the primary atomization process – a cascade involving the formation of smaller and smaller liquid structures. The Kelvin-Helmholtz (KH) instability at the liquid-gas interface promotes the growth of spanwise vorticity waves forming coherent vortices. These vortices evolve into hairpins with counter-rotating streamwise legs [4]. The streamwise and spanwise vortical waves combine to produce different surface structures, e.g. lobes, bridges, and ligaments, which eventually break up into droplets. The link between the vortex dynamics and surface dynamics in primary atomization is important, but rarely explored and poorly understood. This study is an attempt to fill that gap. Vortex dynamics concepts are employed in this chapter to explain the surface dynamics observed at each atomization domain introduced in Chapter 3.

4.1 Problem description

Earlier computational works on the breakup of liquid streams at higher We and Re (i.e. in the atomization range) focused on the surface dynamics using either VoF or LS methods [16, 27, 80]. More recently, Jarrahbashi & Sirignano [33] and Jarrahbashi et al. [34] numerically simulated the temporal behavior of round jets and we computed the temporal behavior of planar jets (in Chapter 3) with additional data analysis that related the vorticity dynamics to the surface dynamics. Several significant accomplishments were presented in Chapter 3 [97]: (i) three breakup mechanisms were identified and their zones of occurrence were specified on the We_g versus Re_l map; (ii) the most important actions in each of the three breakup domains were explained; (iii) the effects of density ratio, viscosity ratio, and sheet thickness on the breakup domains were described; (iv) characteristic times for each of these breakup domains were correlated with key parameters; and (v) the same breakup domains were shown to apply for round jets and planar jets with a very similar We_g versus Re_l map.

In recent years, a number of analyses for spatially developing instability and breakup of liquid streams have appeared. They do add interesting and useful information; however, all of those analyses are at relatively low values of Weber number ($We_g < 100$). That is, although some of those works are described as "atomization" studies, they all fit better under the classical characterization of "wind-induced capillary instabilities" defined by Ohnesorge [59] and Reitz & Bracco [71]. Ling et al. [50] use 3D direct numerical simulation (DNS) and resolve the smaller scales; they treat air-assisted injection of a planar sheet and give detailed discussion about the challenge of numerical accuracy. While they mention briefly vortex dynamics and the use of the λ_2 method, little detail is given. Zuzio et al. [100] include "preliminary" results for sheet breakup in their 3D DNS analysis. The other papers give analyses that are linear [61], two-dimensional inviscid [57], two-dimensional [1, 22], or 3D large-eddy simulations [1]. Of course, these methods cannot resolve the smaller structures that form during the cascade process of the breakup. An analysis with spatial development offers some advantage

with practical realism over temporal analysis. At the same time, the additional constraints imposed by the boundary conditions remove generality in the delineation of the important relevant physics. For these reasons, we follow the path with temporal-instability analysis in the classical atomization (high We_g range) provided by Jarrahbashi & Sirignano [33], Jarrahbashi et al. [34]. The goal is to reveal and interpret the physics in the cascade process known as atomization. Note that some spatial development is provided when the temporal analysis covers a domain that is several wavelengths in size. Using linear theory, relations between spatially developing results and temporal results have been demonstrated for single-phase flows [23] and two-phase flows [22].

Jarrahbashi et al. [34] showed that important spray characteristics, e.g. droplet size and spray angle, differed in different ranges of We, Re, and density ratio. Therefore, further studies of the breakup mechanisms are needed to better understand the causes of these differences. Consequently, there are unresolved questions to be addressed in this chapter: What are the details of the liquid dynamics in each breakup domain? What causes the difference in the breakup cascade? What roles do surface tension, liquid viscosity, and gas density (i.e. pressure) play? How do the roles of streamwise vorticity (i.e. hairpin vortices) differ in the three breakup domains? How does the behavior of a jet flow into a like-fluid (e.g. water into water or air into air) compare with liquid-jet flow into gas? The answers to these questions would be crucial in understanding and controlling the ligament and droplet size distribution in the primary atomization of liquid jets.

Empirical evidence [45] has long been available that spray character differs significantly for differing values of Re and We. Jarrahbashi et al. [34] showed that different breakup mechanisms result in differing spray angles and droplet-size distributions. Thus, we see that, for control of spray character, it is very valuable to understand the details of the cascade processes for each of the identified atomization domains. Control and optimization, although not addressed in this study, motivate the detailed exploration and the behavioral

Case	Re_l	We_g	$\hat{\rho}$	$\hat{\mu}$
D1a	320	23000	0.1	0.002
D1b	1000	3000	0.05	0.01
D2a	5000	20000	0.5	0.006
D2b	2500	5000	0.05	0.01
D3a	5000	7250	0.5	0.006
D3b	5000	3000	0.05	0.01

Table 4.1: The main cases studied with their dimensionless parameter values

characterizations reported here.

Our objectives for the planar jet are to (i) explain the mechanisms of surface deformation and breakup in the three domains introduced in Chapter 3 using more sophisticated data analysis for the vortex dynamics (i.e. the λ_2 method); (ii) determine the importance of streamwise vorticity (i.e. hairpin vortices) in the breakup mechanisms; (iii) identify the generation mechanisms for the streamwise vorticity; and (iv) learn the differences in generation and role of the spanwise and streamwise vorticity at low and high density ratios.

A wide range of Re_l and We_g at high and low density ratios is covered in this study. The main six cases studied in this chapter are presented in Table 4.1. The cases are called in a "Dnx" format, where "n" presents the Domain number (1, 2 or 3), and "x" presents the range of the case ("a" for high density ratio, and "b" for low density ratios). Two cases – one at high $\hat{\rho}$ and fairly high We_g, and one at low $\hat{\rho}$ and low We_g – are studied in each domain to clearly show the effects of density ratio on the vortex dynamics of each atomization process. The "b" cases are more practical and in the ranges usually seen in most atomization applications. The range of parameters for other cases presented in this article is indicated in their corresponding figure captions.

4.1.1 Data analysis

Our goal is to study the vorticity dynamics as well as the liquid surface dynamics in order to understand breakup mechanisms at different flow conditions. To this end, λ_2 contours at different cross-sections of the domain are analyzed in time. Here, we briefly review the definition of the λ_2 method.

An objective definition of a vortex should permit the use of vortex dynamics concepts to identify coherent structures (CS), to explain formation and evolutionary dynamics of CS, and to explore the role of CS in turbulence phenomena. Jeong and Hussain [36] define a vortex core as a connected region with two negative eigenvalues of $\boldsymbol{S}^2 + \boldsymbol{\Omega}^2$; where, $\boldsymbol{S}$ and $\boldsymbol{\Omega}$ are the symmetric and anti-symmetric components of $\boldsymbol{\nabla}\mathbf{u}$; i.e. $S_{ij} = (u_{i,j} + u_{j,i})/2$ and $\Omega_{ij} = (u_{i,j} - u_{j,i})/2$. If λ_1, λ_2, and λ_3, are the eigenvalues such that $\lambda_1 \geq \lambda_2 \geq \lambda_3$, this definition is equivalent to the requirement that $\lambda_2 < 0$ within the vortex core, since λ_3 is always negative because the sum of the normal viscous stresses is zero. This definition is proven to meet the requirements for existence of a vortex core in different flow conditions [36], while the vortex identification by the Q-criterion [41] may be incorrect when vortices are subjected to a strong external strain [36], as in our study.

4.2 Results and discussion

In this section, the vortex dynamics associated with each of the breakup mechanisms are analyzed to explain the hole formation, the corrugation formation and the lobe/ligament stretching at different Reynolds and Weber numbers. For this purpose, one case is picked from each domain (see Figure 3.2), and its vortex dynamics are studied using the λ_2 criterion. The gas flows in the positive x-direction, from left to right, in all of the figures in this section.

4.2.1 Vortex dynamics and surface dynamics

To interpret the surface deformation via vorticity concepts and to more clearly delineate the complex 3D flow physics, the dual approaches of vortex dynamics and surface wave dynamics are employed. The language of wave dynamics focuses on crests, troughs, and lobes, while the vortex-dynamics terminology refers to vortex rollers (eddies), braids, and hairpins. The instability starts from the initially symmetric KH waves. The crest of the KH waves, when amplified and slightly stretched in the flow direction, is referred to as "KH crest". As the 3D character of instability develops, "KH crests" divide into distinct "lobes". The forward-most tip of the lobe is referred to as "spanwise crest", and the region between two adjacent crests is called "spanwise trough". In terms of the vorticity dynamics, the "KH crests" and "KH troughs" are equivalent to "vortex rollers" and "braids", respectively; see Figure 4.1.

The spanwise vorticity rolls up as KH rollers. The braid connects two adjacent rollers separated in x, which stretch the fluid in between. There are two modes of unstable waves, corresponding to the two surface waves oscillating exactly in or out of phase, commonly referred to as the sinuous (anti-symmetric) and varicose (symmetric) modes, respectively

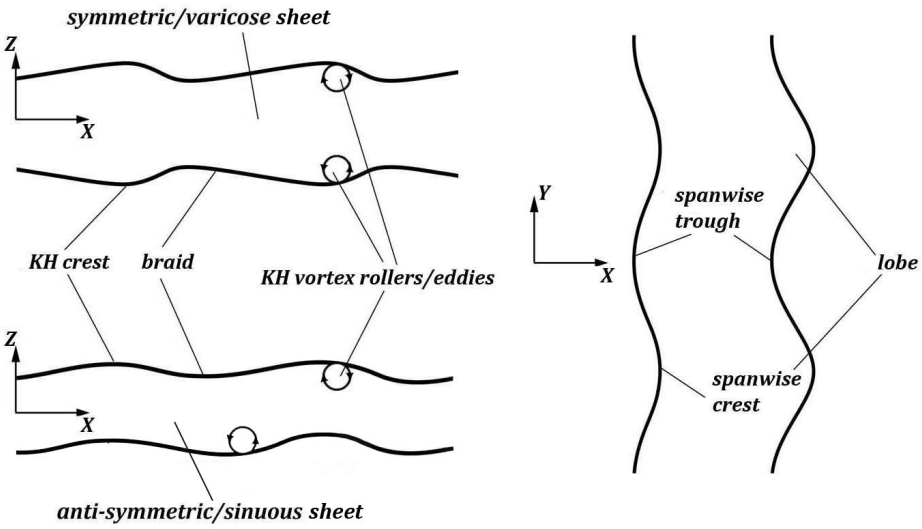

Figure 4.1: Terminology used for vorticity and liquid-gas interface deformations from side-view (left), and top view (right).

(discussed in Chapter 1); see Figure 4.1.

4.2.2 Hole and bridge formations (*LoHBrLiD* mechanism)

The $LoHBrLiD$ mechanism occurs at medium Re_l and high We_g; see Figure 3.2. This process is shown in Figure 4.2. The lobes form and thin on the primary KH wave crests. The middle section of the lobes (the braid), where the highest strain occurs, thins faster and thus perforates, creating a hole and a bridge on the lobe rim. Bridges become thinner as the holes expand. Finally, the bridges break and create one or two ligaments depending on the breakup location. The ligaments stretch and eventually break into droplets under capillary action.

At lower We_g, the surface tension force resists the formation of holes. In this range, usually one hole forms on the liquid lobe and stretches into a large one. At higher We_g, lobes thin much easier since the resistance due to the surface tension forces is not large enough to

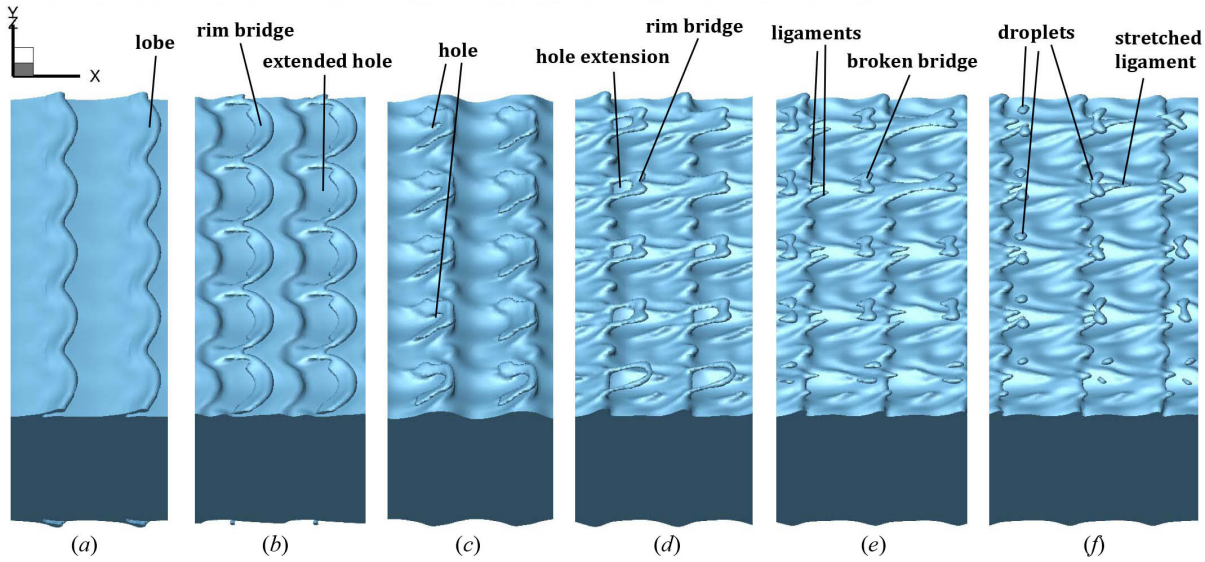

Figure 4.2: Liquid surface deformation in the $LoHBrLiD$ mechanism; $Re_l = 320$, $We_g = 115,000$ ($Oh_m = 1.06$), $\hat{\rho} = 0.5$, and $\hat{\mu} = 0.0022$, at $t = 18$ μs (a), 22 μs (b), 26 μs (c), 28 μs (d), 30 μs (e), and 32 μs (f).

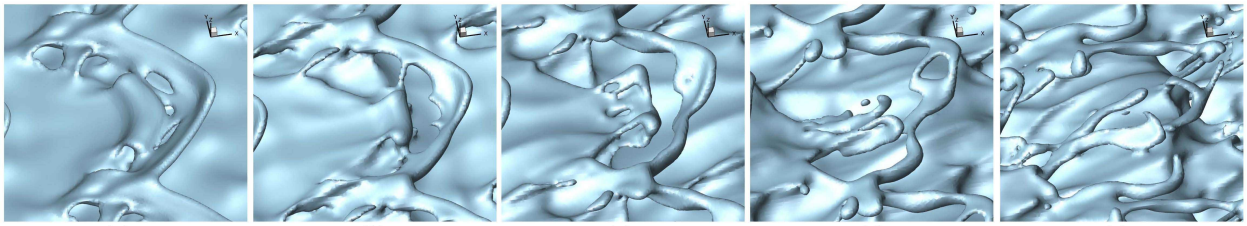

Figure 4.3: Close-up view of the hole formation and expansion on a single liquid lobe; $Re_l = 5000$, $We_g = 36,000$, $\hat{\rho} = 0.1$, and $\hat{\mu} = 0.0066$. $t = 10$ μs (a), 11 μs (b), 12 μs (c), 13 μs (d), 14 μs (e).

stabilize the growth of the instabilities. In this range usually several small scale holes appear at different locations on the lobe, as seen in the close-up view of Figure 4.3(a). As these perforations grow, several of these holes merge to create larger holes (Figure 4.3b), and a thick liquid bridge is created on the lobe rim (Figure 4.3c). As the lobes continue to stretch and the holes continue to expand, the bridges become thinner (Figure 4.3d) and finally break to create several ligaments (Figure 4.3e). The mechanism of hole formation, to be discussed in this section, is believed to be the same at high and low We_g and density ratios; the only difference is in the time, location and size of the holes.

Case D2a (Table 4.1), which falls in the $LoHBrLiD$ class, is chosen in this section to study and explain the vortex dynamics in the hole-formation mechanism. At the end of this section, Case D2b is studied to clarify the effects of lowering density ratio. Zandian et al. [96] and Jarrahbashi et al. [34] related the hole formation to the overlapping of the hairpin vortices that form on the braids. Their finding is confirmed here and more details in the vortex overlapping process are revealed. In this section, λ_2 contours are elucidated in two cross-sections in x–z planes – one passing through the spanwise crest and the other through the trough – along with the instantaneous liquid-gas interface (red lines) position at different times.

Figure 4.4(a) shows the formation of lobes and hairpin vortices that occur on the braid on both top and bottom sheet surfaces, at very early time $t = 6$ μs. The vortex structure is

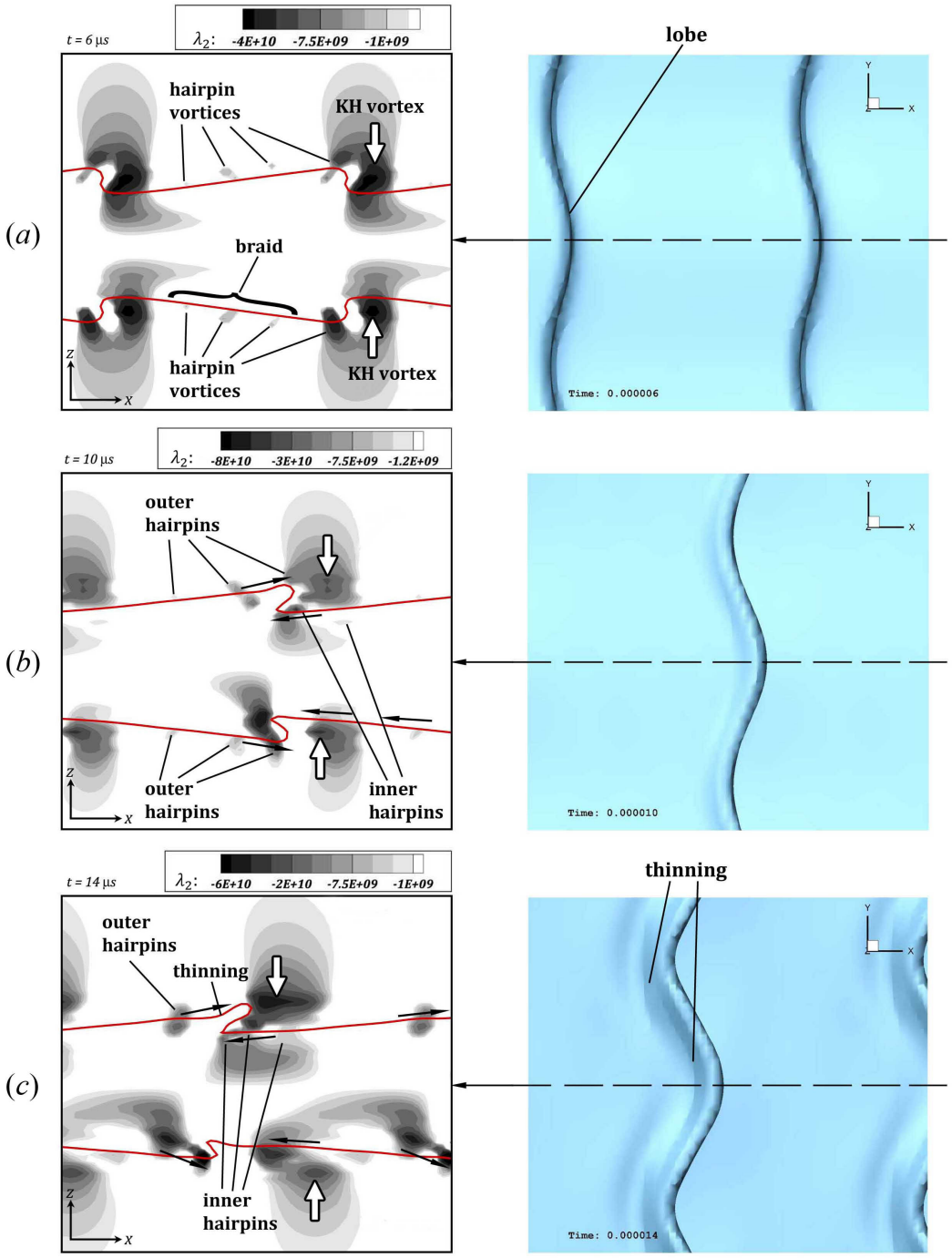

Figure 4.4: λ_2 contours on the spanwise crest (left), and the top view of the liquid surface (right), at $t = 6$ μs (a), 10 μs (b), and 14 μs (c) of Case D2a.

symmetric at this time and consists of a large vortex just downstream of the wave, which is hereafter called the *"KH vortex"* (indicated by the white arrows), and hairpin vortices on the braid, between two adjacent KH rollers. The location of the vortices relative to the

interface are the same on the spanwise crest and trough cross-sections at this time; i.e. the vortices on the spanwise trough cross-section (not shown here) are slightly upstream of those on the spanwise crest; see the top views of Figure 4.4. The vortices have some undulations in x and manifest a hairpin structure similar to what was observed by Bernal ad Roshko [4]. Lasheras and Choi [42] attributed the appearance of three-dimensionality to the stretching along the principal direction of the positive strain. The maximum amplification of the vortex lines occurs near the braid region, where positive strain is the maximum. Therefore, they called these hairpin vortices "strain-oriented vortex tubes" and described a mechanism for evolution of the 3D instabilities, where vortices enhanced by stretching are pulled more strongly into the streamwise direction until a series of hairpins extend from the underside of one roller to the top of its neighbor. A similar mechanism is seen here for the two-phase flow.

As shown in Figure 4.4(b), the upstream hairpins are pulled downstream by the KH vortex on the outer side of the roller, while the downstream hairpins are pulled upstream on the inner side of the KH roller (easily understood from a frame fixed with the KH vortex). The direction of the streamwise hairpin stretch is determined by the global induction of the KH roller, as indicated by the black arrows in Figure 4.4(b). Martin & Meiburg [56] explained that the sign of the streamwise vorticity component is determined by the competition between global and local inductions; i.e. between the overall effect of the vorticity field and the locally self-induced velocity of a vortex tube. While the global induction effect continues to determine the sign of the streamwise braid vorticity, the direction of the streamwise vorticity component in the crest region is determined by the local induction of the vortex tube [56].

The motion of the upstream and downstream hairpins on the outer and inner sides of the KH roller – due to the roller's induced motion – causes these two hairpins to align spanwise and overlap – one layer locating on the outer surface of the lobe, i.e. on the streamwise wave crest, and the other layer on the inner side of the lobe. This hairpin overlapping has

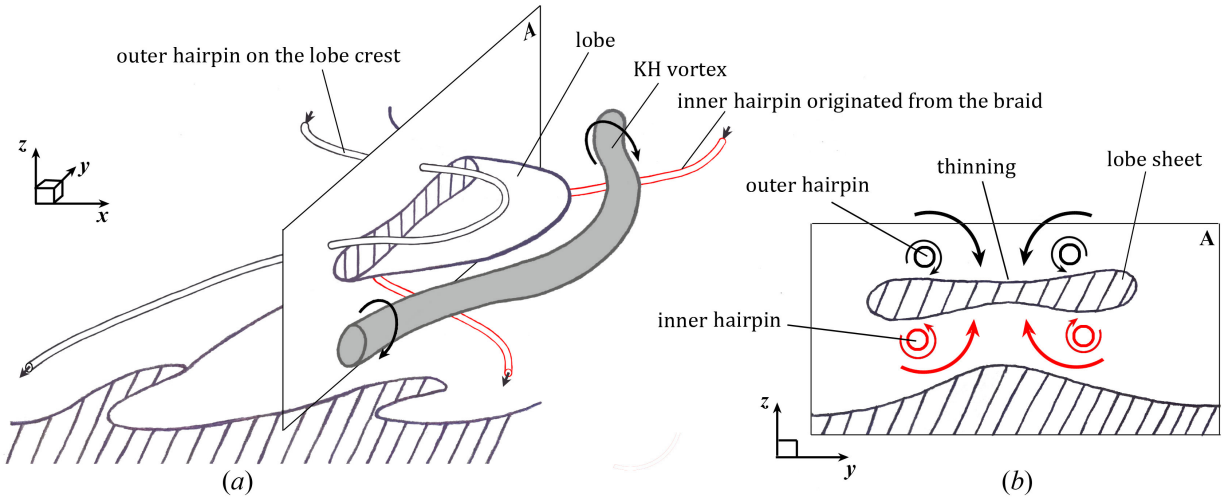

Figure 4.5: 3D Schematics showing the overlapping of the two hairpin vortices – one from the lobe crest (outer black tube, pointing downstream), and the other from the braid (inner red tube, pointing upstream) (a); A is the plane in which (b) is drawn; cross-sectional view of the A-plane, showing the thinning of the lobe sheet due to the combined induction of the two oppositely orientated overlapping hairpins (b). The vortex schematics are periodic in x- and y-directions.

been observed and explained in both mixing layers (see figures 3 through 6 of Comte et al. [11]) and in two-phase round jets (see figure 9 of Jarrahbashi et al. [34]). Comte et al. [11] discuss helical pairing of the oppositely-oriented hairpins and the formation of diamond-shaped vortex-lattice structures. As shown in the illustrative sketches of Figure 4.5 and also described by Jarrahbashi et a. [34], the liquid sheet between a pair of these overlapping, oppositely-pointed hairpins becomes thinner.

Figure 4.5(a) schematically depicts two overlapping hairpin vortices in the liquid-gas interface region – one outer vortex originating from the lobe crest and stretching downstream (the slender black tube), and the other inner vortex originating from the braid and stretching upstream (the red tube). The KH vortex is shown by the thicker gray tube in this figure. Figure 4.5(b) shows a cross-sectional view of the vortex structure along with the lobe located between the two hairpin vortices on the A-plane of Figure 4.5(a). The induced velocity of the two oppositely oriented overlapping hairpin vortices (see the qualitative streamlines shown by the black and red arrows in Figure 4.5b) pushes the top surface of the lobe downward and the

bottom surface upward, causing the lobe to become thinner in the middle and thus becoming vulnerable to puncture at that region. This occurs at $t = 16$ μs, on the top surface of the liquid sheet, as shown in Figure 4.6. Three λ_2 isosurfaces are shown in this figure: the gray isosurface denotes the KH vortex (the gray tube in Figure 4.5); the green isosurface denotes the outer hairpin (the black hairpin in Figure 4.5); and the red isosurface denotes the inner hairpin (the red hairpin in Figure 4.5). The λ_2 isosurface tracks the strength of the vorticity but circulation on its surface is not constant (as it is not a vortex surface); thus, it slightly differs from the surface of a vortex tube. The λ_2 magnitude of each isosurface is denoted in the figure caption. The KH vortex in Figure 4.6 is the strongest (i.e., greatest circulation) and, at its core, has larger λ_2 values than the hairpins; however, the outer isosurface, with a lower λ_2 value, is depicted to give a better indication of its size. The hairpin overlapping region is denoted by a hatched area in Figure 4.6(b). The overlapping of the outer and inner hairpins can be clearly observed in Figure 4.6(c), where the gray KH vortex isosurface and the blue liquid surface have been removed from the box drawn in Figure 4.6(a). The

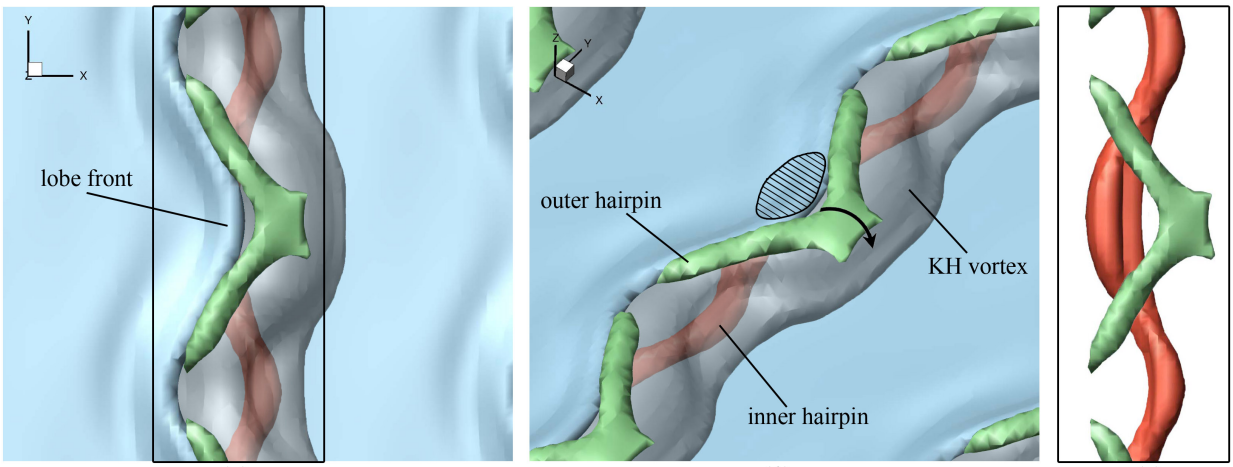

(a) (b) (c)

Figure 4.6: λ_2 isosurfaces in a top close-up view of a liquid lobe in Case D2a (a), and a 3D view of the same snapshot (b), at $t = 16$ μs. Top view of the box drawn in image (a), showing the overlapping of the red and green isosurfaces without the blockage of the gray KH isosurface and blue liquid surface (c). The isosurface values are: $\lambda_2 = -2 \times 10^{10}$ s^{-2} (gray), -3×10^{10} s^{-2} (green), and -3×10^{9} s^{-2} (red). The gray isosurface is made transparent in subfigures (a) and (b) to display the inner hairpin underneath it. The hatched area denotes the approximate hairpin overlapping region, where the hole would appear on the lobe later.

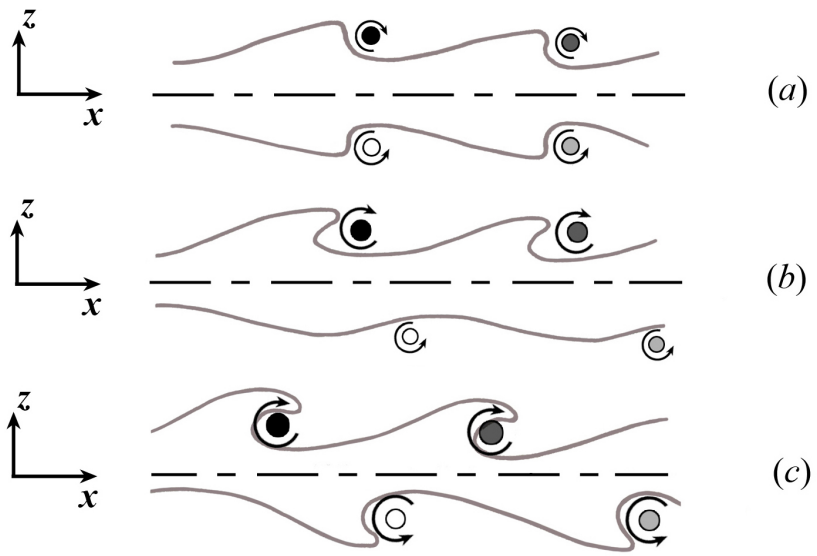

Figure 4.7: Schematic showing the transition of a symmetric thin sheet (a) to antisymmetric mode (c). The dashed lines denote the sheet center plane. The black and dark gray circles denote the two adjacent KH vortices on the top surface, and the light gray and white circles are two adjacent KH vortices on the bottom surface.

hatched area shows the zone where the lobe thinning occurs and the first hole forms a few microseconds later; see Figures 4.8 and 4.9(a).

The sketches in Figure 4.7 show the transition of a thin sheet from a symmetric mode to an antisymmetric mode with the qualitative location of the KH vortices at the two liquid surfaces. In the beginning, the top and bottom sheet surfaces as well as their KH vortices are symmetric with respect to the center-plane, as shown in Figure 4.7(a). All plane jets in reality exit with symmetric perturbations because of the long-wavelength perturbations due to the upstream chamber's Helmholtz resonance modes or driving compressor blade wakes, but the antisymmetric mode has a much higher growth rate and thus eventually dominates. The true physical explanation of this transition is intriguing, but remains somewhat elusive, and deserves careful examination and explanation. Ashurst & Meiburg [3] showed that the loss of symmetry in the two vortex layer calculation is related to the enhancement and reduction of relative streamwise displacements for filaments in the stronger layer by the addition of the second layer of vorticity.

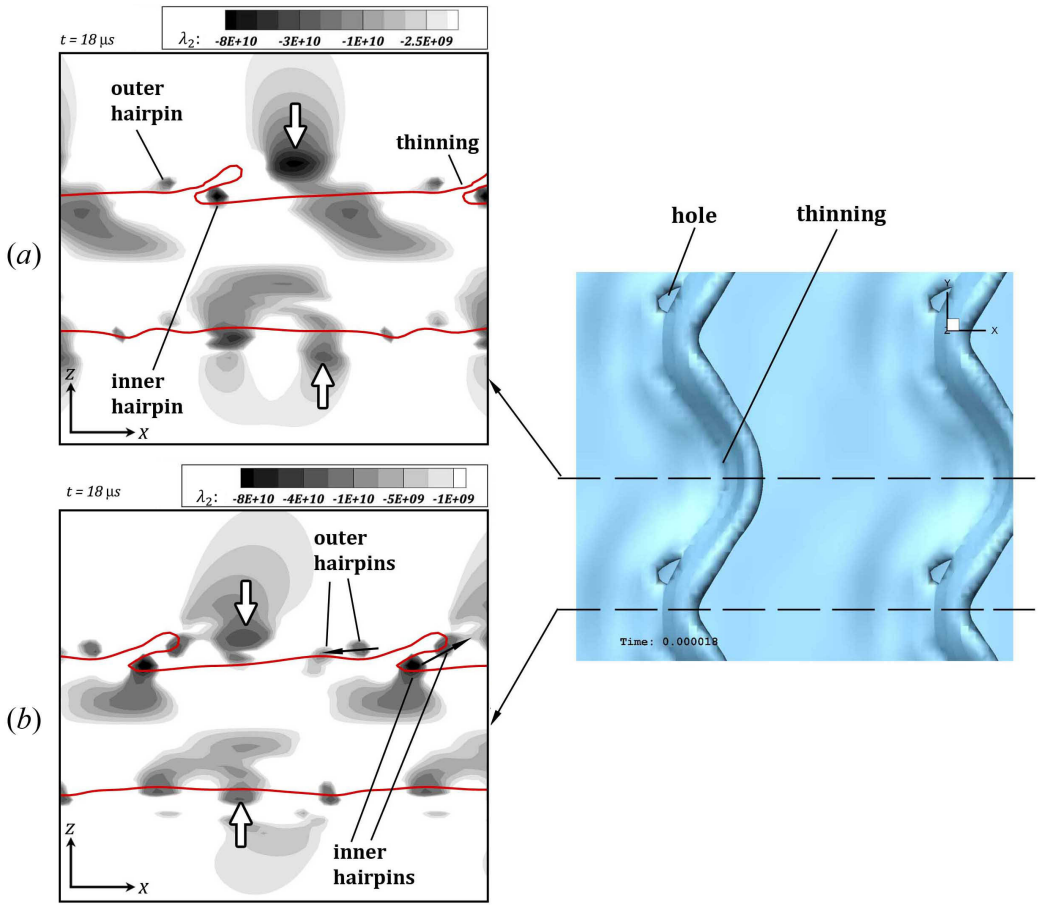

Figure 4.8: λ_2 contours on the spanwise crest (a), and the spanwise trough (b), and the top view of the liquid surface (right), at $t = 18$ μs of Case D2a.

Due to this transition towards antisymmetry, the KH rollers on one of the layers (the bottom layer in our case) are not able to stretch the bottom lobes and cause the hairpins overlapping at early times; thus, lobe formation and thinning are delayed on the bottom surface. This corresponds to the instant in Figure 4.7(b) and the period 18–34 μs in our simulation, shown in Figures 4.8 through 4.13. As the sheet gets thicker, i.e. the two vorticity layers get more independent, the transition towards antisymmetry is delayed, and both sides have time to roll up the surface waves and stretch them into lobes. For the rest of this section, our focus will be only on the top interface where lobe stretching and hole formation are evident at early times.

As Figure 4.8 shows, the KH vortex starts to move away from the KH wave at 18 μs.

However, it has had enough time to roll the lobe and make the overlapping occur on the top sheet surface. Notice that the KH vortex on the trough cross-section (Figure 4.8*b*) is still closer to its original location compared to the same vortex on the crest cross-section (Figure 4.8*a*). As described earlier, this results in further stretching of the hairpins near the sides of the lobe compared to its crest; hence, holes occur sooner near the lobe sides than at the lobe crest. This motivates the idea that the KH vortex location and strength are important in formation or inhibition of holes at early times. The KH vortex transition and structure is directly related to the liquid viscosity, thus Re_l. At high Re_l, even though vorticity diffusion is slower, the fluids motion is less constrained by the viscous forces; thus, the KH vortices advect away from the interface much easier, and do not acquire enough time

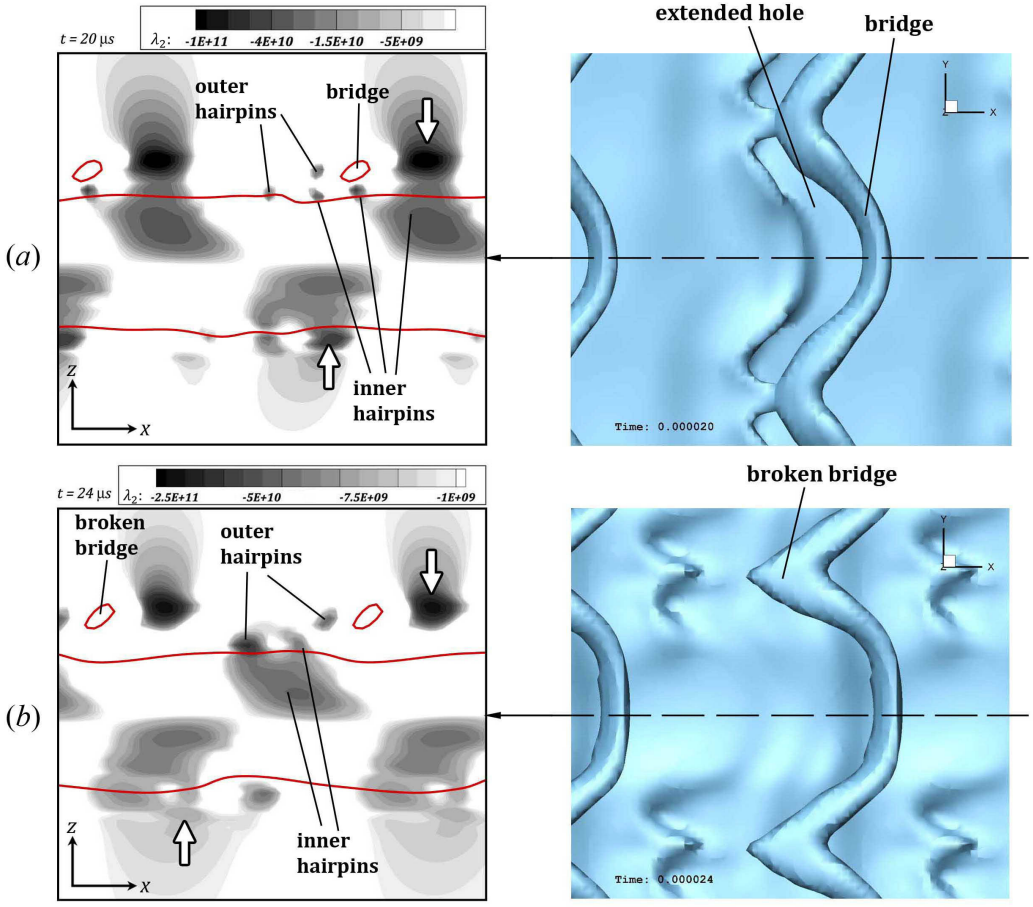

Figure 4.9: λ_2 contours on the spanwise crest (left), and the top view of the liquid surface (right), at $t = 20$ μs (*a*), and 24 μs (*b*) of Case D2a.

to roll up the lobes and stretch the hairpins. Hole formation also depends on the surface tension. The inertia should have enough strength to overcome the surface tension forces in order to perforate the lobe. In conclusion, the $LoHBrLiD$ mechanism becomes less probable as We_g decreases or Re_l becomes very high or very low; see Figure 3.2.

λ_2 contours of Figure 4.9 clearly show the overlapping of the outer and inner hairpins at the location of the holes. The holes expand and create bridges at $t = 20$ μs (Figure 4.9a). Meanwhile, the KH vortices advect both downstream and away from the interface. Later at 24 μs (Figure 4.9b), the bridges break and create spanwise ligaments. If the bridge breakup would have happened at the spanwise crest instead of its trough, the resulting two ligaments would have been streamwise oriented, as in the sketch of Figure 3.1.

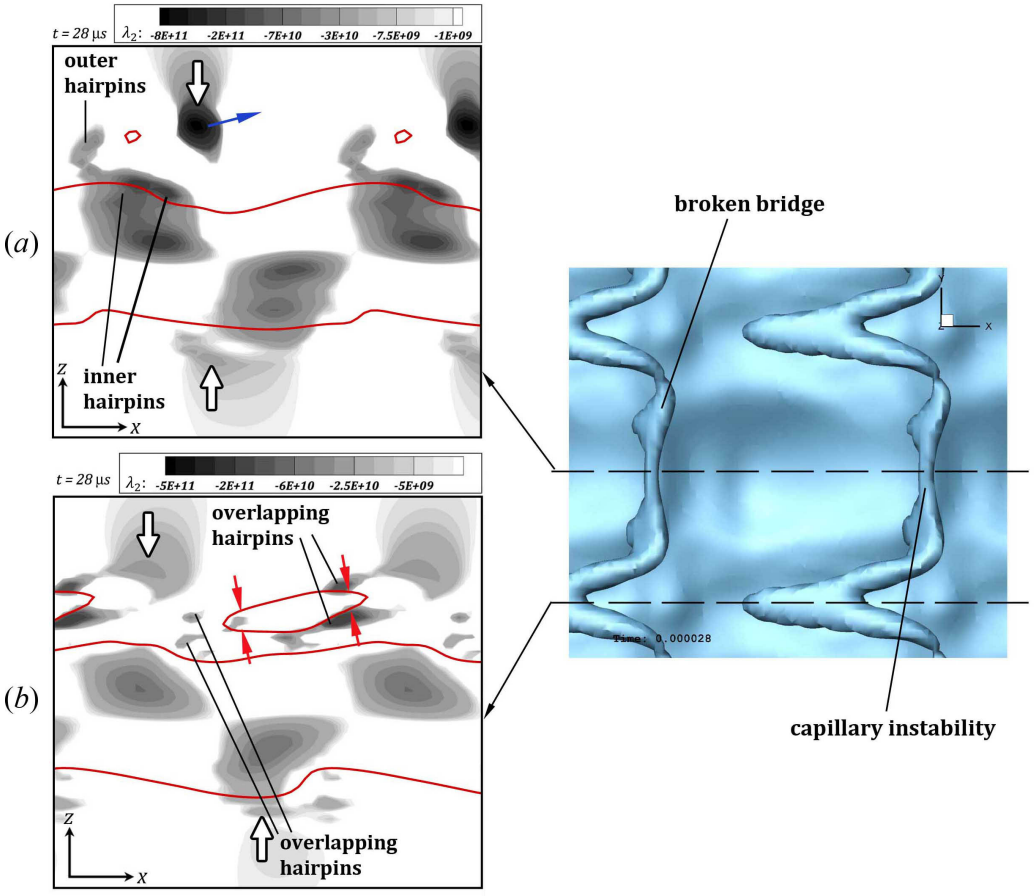

Figure 4.10: λ_2 contours on the spanwise crest (a), and the spanwise trough (b), and the top view of the liquid surface (right), at $t = 28$ μs of Case D2a.

The broken bridges undergo capillary instability and break further into droplets and smaller ligaments, as shown in Figures 4.10 and 4.13. Meanwhile, the hairpin vortices that are overlapping near the spanwise trough, thin the bridges, as has been indicated by the red arrows in Figure 4.10(b). This thinning along with the stretching of the bridges by the induced velocity of the KH roller deforms the bridge and makes it thinner and on the verge of further breakup. This completes the $LoHBrLiD$ breakup mechanism at primary atomization. The liquid interface at this time has become completely antisymmetric (Figure 4.10) following the KH vortices that became antisymmetric earlier.

The role of vortices in the $LoHBrLiD$ breakup mechanism is summarized schematically in Figure 4.11. This figure shows the liquid surface and also the qualitative location of the nearby vortices at four consecutive times. At an early time t_1, hairpin vortices form on the braids due to the strain caused by the neighboring KH vortices. The hairpins closer to the KH wave crest – shown by black lines – are stretched downstream, and the hairpins near the KH wave trough – shown by red lines – are stretched upstream by the induced motion of the KH rollers. The hairpin parts that are stretched downstream are rolled over the KH vortex tube, and are denoted by solid lines, while the hairpin parts that are stretched upstream are pulled under the KH vortex tube, and are denoted by dashed lines.

Later at t_2, the KH vortices deflect more under the induction of the hairpin vortices. The KH vortex stretches the lobes over itself and covers underneath the lobe surface at later times (see bottom images of Figure 4.11). The black and red hairpins that roll over and under the KH vortex, respectively, overlap later at the center of the lobe as well as the two sides of the lobe; i.e. at the spanwise troughs. These overlapping regions have been denoted in Figure 4.11 at t_3. The lobe sheet fills the vertical gap between these overlapping hairpins, causing the lobe to become thinner and thus vulnerable to puncture at the overlapping regions, as was described in Figure 4.5.

Whether the liquid sheet subject to these conditions punctures or not depends on other flow

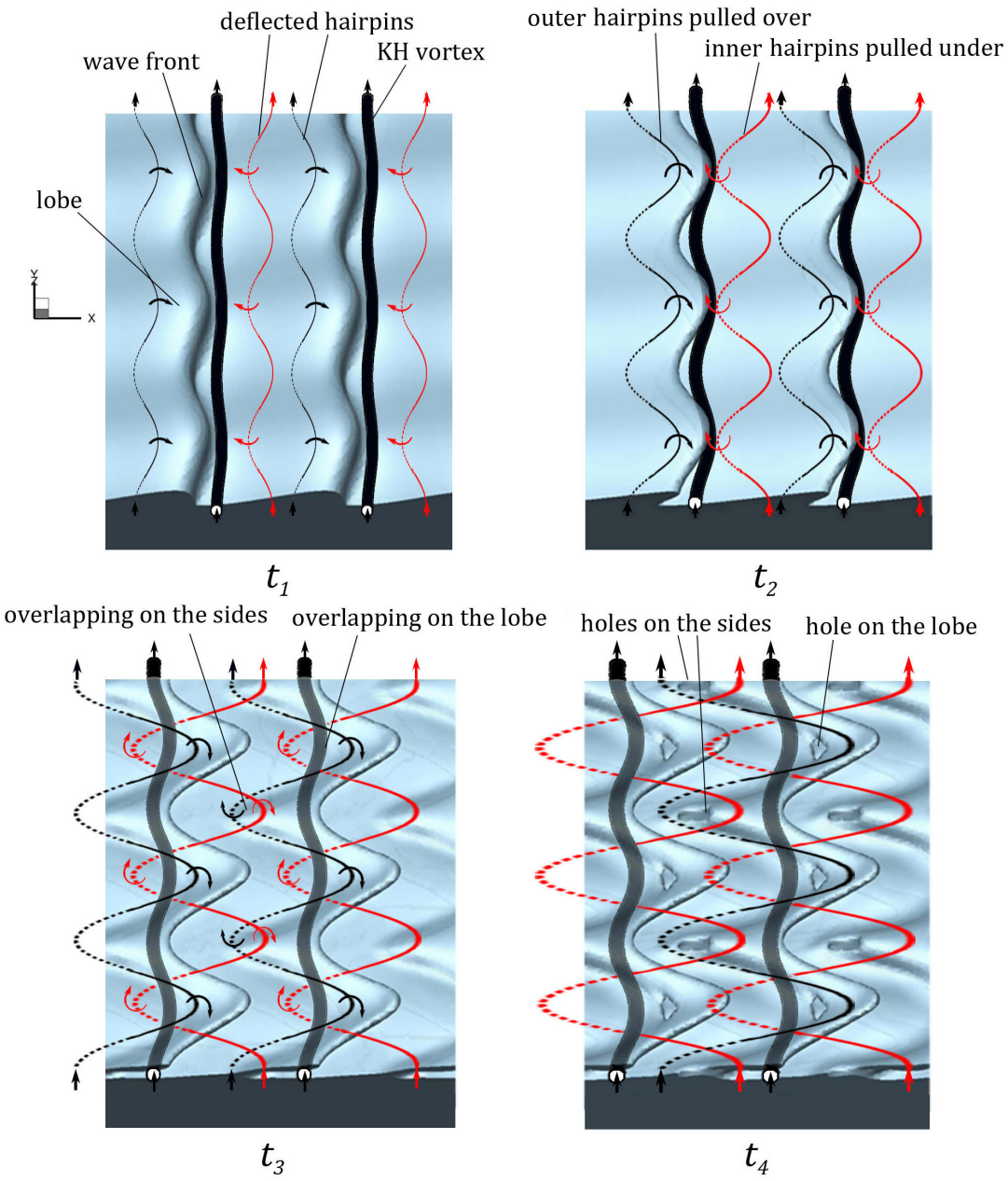

Figure 4.11: Schematics of the $LoHBrLiD$ process at four consecutive times. The liquid/gas interface is shown in blue, and the KH vortex by black tubes. The red and black lines denote the inner and outer hairpin vortices near the KH wave trough and crest, respectively. The solid or dashed lines denote where the hairpins are stretched upstream and inward, or downstream and outward, respectively.

conditions, particularly the surface tension. At high We_g (high Oh_m), the hole formation prevails and the lobes perforate at the predicted locations, as shown at t_4 in Figure 4.11. As the overlapping hairpin filaments continue to stretch, the holes also stretch and expand,

creating even larger holes and thinner bridges. If We_g is not large enough, the liquid lobe in the overlapping region can recover instead. In this case, hole formation is inhibited and the lobes stretch directly into ligaments via *LoLiD* or *LoCLiD* mechanisms, as discussed later.

The mechanism of hole formation at low density ratios is similar to the high $\hat{\rho}$ described in Figure 4.11, with minor differences. Figure 4.12 shows the vortex structures and the lobe deformation at 90–94 μs for $\hat{\rho} = 0.05$ (Case D2b). Three λ_2 isosurfaces corresponding to the KH vortex (gray), the outer hairpin (green), and the inner hairpin (red) are shown in Figure 4.12(a) at 90 μs. The liquid surface has been removed from this image to reveal all the vortex structures, but the black solid line indicates the location of liquid lobe front edge for comparison. The liquid surface at the same time is shown in Figure 4.12(b). The outer and

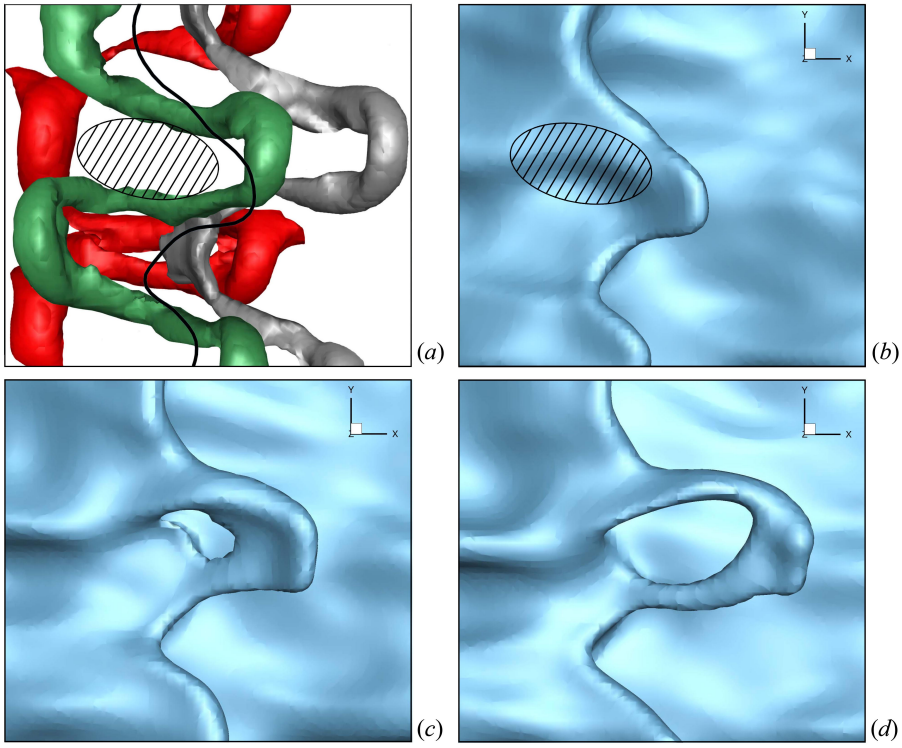

Figure 4.12: λ_2 isosurface in a top close-up view of a liquid lobe in Domain II at low density ratio (Case D2b) at 90 μs (a); the solid black line shows the lobe front edge location and the hatched area shows the location of hairpin overlapping. The isosurfaces represent: the KH vortex with $\lambda_2 = -4 \times 10^9$ s^{-2} (gray), the outer crest hairpin with $\lambda_2 = -6 \times 10^9$ s^{-2} (green), and the inner trough hairpin with $\lambda_2 = -3 \times 10^9$ s^{-2} (red). Lobe surface showing the hole formation from a top view at 90 μs (b), 92 μs (c), and 94 μs (d) of Case D2b.

inner hairpins at this low $\hat{\rho}$ stretch and wrap around the KH vortex in opposite directions, and overlap on top and bottom of the lobe. The difference here is that the hairpins are more stretched and the overlapping region is more elongated in the streamwise direction, as shown by the hatched area in Figures 4.12(a,b). The holes that are formed near the hatched area at later times (Figures 4.12c,d) are also more elongated in the streamwise direction compared to the high $\hat{\rho}$ case shown in Figure 4.9, where the holes were more spanwise oriented. This finding agrees with the predictions of hole location by Jarrahbashi et al. [34] (see their figure 20). There when the gas density increased, the edge curvature decreased and the locations of the holes in neighboring lobes became closer to each other. This caused the neighboring holes to merge and expand the hole in the azimuthal (spanwise) direction.

The breakup mechanism involving hole and bridge formation and the role of vortical structures in this regard were discussed in this section via consecutive tracking of λ_2 contours near the interface. Vortex dynamics is able to explain the breakup process at high We_g and medium Re_l. In the remainder of this section, λ_2 contours along with the interface location are shown at a few later time steps to track the deformation of the ligaments and also to see the evolution of the surface waves after the KH vortices have left the interface.

Figure 4.13 shows λ_2 contours of the liquid jet in the period 30–34 μs. Even though the original KH vortex (denoted by the white arrow) is now advected downstream and away from the waves, the vorticity contours on the braid stretch and collect at the crest of the new KH waves and create new KH vortices (Figure 4.13a). These vortices roll a new KH wave and stretch new sets of lobes similar to the original ones; see Figure 4.13(b). The direction of the induced motion by these new vortices are indicated by the black arrows in Figure 4.13(b). The direction in which the fluids are swirling around the KH vortices are also denoted by the blue curly arrows. At 34 μs, the sheet and the vortices are antisymmetric with half a wavelength phase difference between the top and bottom surfaces in the streamwise direction. The vortices on the bottom side are now nearly stationary with respect to the interface;

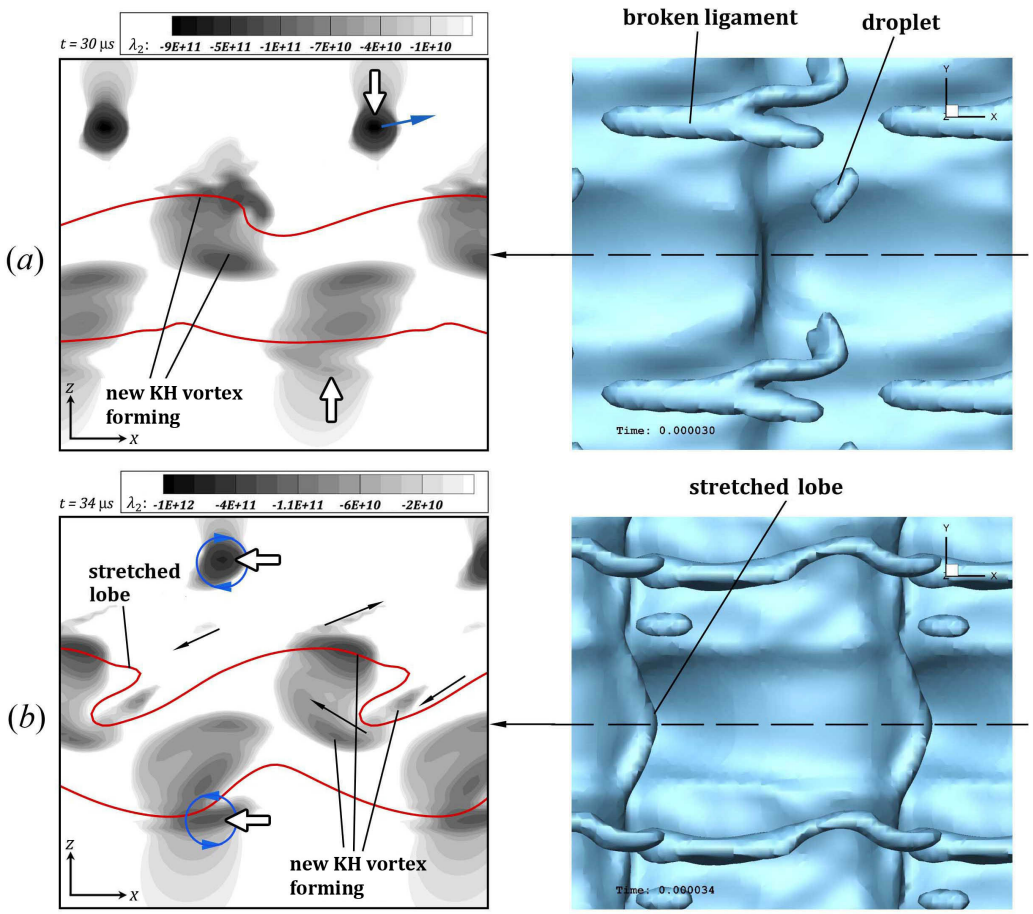

Figure 4.13: λ_2 contours on the spanwise crest (left), and the top view of the liquid surface (right), at $t = 30$ μs (a), 32 μs (b), and 34 μs (c) of Case D2a.

hence, they have enough time to roll the waves and form stretched lobes on the bottom surface (Figure 4.13b). As the new lobes get stretched, new pairs of hairpins form on their braids, and the whole $LoHBrLiD$ process repeats, creating new holes, bridges, ligaments, and droplets. Meanwhile, the formerly broken bridges undergo capillary instability and thin at the necks and break into droplets, as shown in the right image of Figure 4.13(b).

Overlapping of the oppositely oriented hairpins is the cause of lobe perforation, as described in this section; however, the locations of the perforations and the direction and rate of their growth depend on the overlapping location with respect to the lobe sheet. What was presented in this section was an ideally simple case to explain the process. In reality, the hairpin structures can be more irregular than what was presented here, which would

shift the overlapping zones and hence change the location of the first perforations. More hole formation examples are presented by Jarrahbashi et al. [34] and Zandian et al. [96]. Jarrahbashi et al. [34] also showed the direction in which the holes merge and expand at high and low density ratios.

4.2.3 Corrugation formation at high Re_l ($LoCLiD$ mechanism)

The $LoCLiD$ mechanism occurs at high Re_l and low We_g (low Oh_m), as indicated in Figure 3.2. This process is shown in Figure 4.14. The lobes form similar to the previous case, but do not stretch as much. Corrugations form on the lobes' front edge and stretch to create ligaments. Multiple ligaments are formed per lobe, typically shorter and thinner compared to the ligaments seen in the $LoHBrLiD$ Domain. Eventually, the ligaments detach from the liquid jet and break up into droplets by capillary action. These droplets are consequently smaller than the ones formed in the $LoHBrLiD$ mechanism. Sequential evolution of λ_2 contours on y-plane cross-sections are used in this section to delineate the physics of this process and more particularly describe why lobes do not perforate but get corrugated at higher Re_l and lower We_g. Case D3a (see Table 4.1) is analyzed in this section; at the end

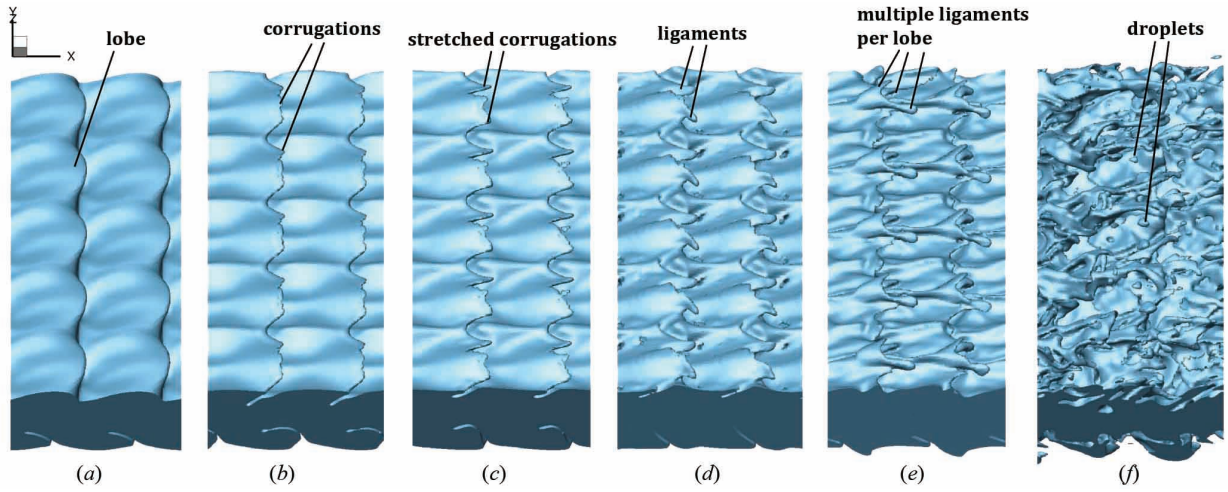

Figure 4.14: Liquid surface deformation following the $LoCLiD$ mechanism in Case D3a, at $t = 44$ μ (a), 48 μs (b), 50 μs (c), 52 μs (d), 56 μs (e), and 60 μs (f).

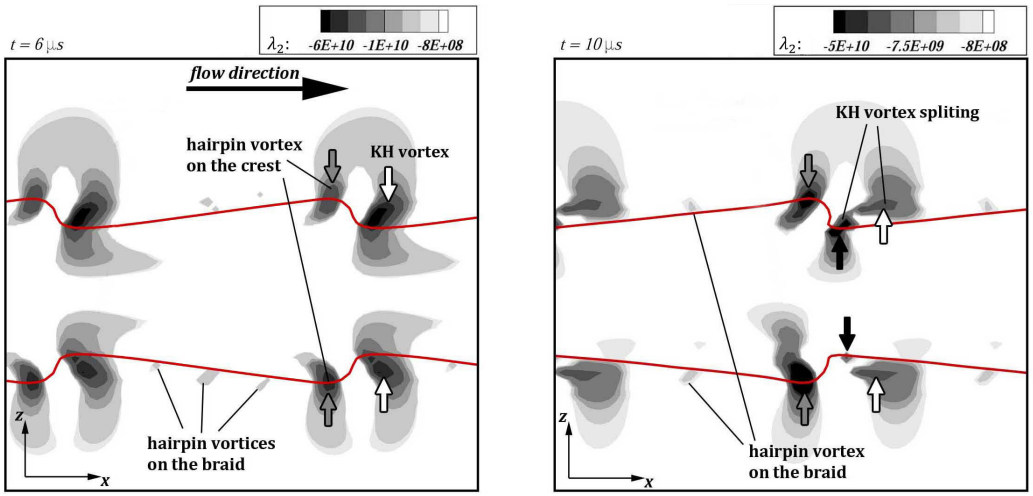

Figure 4.15: λ_2 contours on the spanwise crest cross-section, at $t = 6$ μs (a), and 10 μs (b) of Case D3a.

of this section, the effects of lower density ratio are described by analyzing Case D3b.

Figure 4.15 shows λ_2 contours on a y-plane passing through the spanwise crest at 6 μs and 10 μs. Since the vortex structure passing through the spanwise trough has similar features, albeit with some phase difference with respect to the vortices at the spanwise crest, it will not be shown here. In the beginning, the vorticity field contains a series of hairpin filaments on the braid and a stronger KH vortex just downstream of the KH wave crest (indicated by the white arrows). The hairpins are stretched by the neighboring rollers as discussed before. As also described by Martin & Meiburg [56], since stretching is the most intense in the downstream half of the braid region, hairpin vortices acquire a larger streamwise component in the upstream neighborhood of a vortex roller, i.e. on the lobe crest, than its downstream side; i.e. on the trough. Hence, the hairpin filaments that are closer to the streamwise wave crest (denoted by the gray arrows) are stronger than the upstream braid hairpins. Ashurst & Meiburg [3] also found that, while in one vortex layer the filaments at the center between two spanwise rollers experience the most stretching, if a second vortex layer is added, the filaments with the strongest spanwise modulation will be located closer to the downstream roller; i.e. three-dimensionality occurs first in the downstream half of the braid region. The

vorticity field as well as the sheet itself are initially symmetric with respect to the center plane. The hairpin filaments reside near the interface, slightly inclined towards the gas zone.

At high Re_l, inertia dominates the viscous forces and the fluid particles are more free to move around as the viscous forces do not produce enough resistance against their motion – especially in the gas zone. The higher velocity of the gas layer compared to the liquid layer causes the KH roller to split into two vortices at 10 μs (see Figure 4.15*b*); this process is shown schematically in Figure 4.16 and using the λ_2 isosurfaces in Figure 4.17. The outer part of the KH vortex (indicated by the white arrow in Figure 4.15*b*), which resides in the

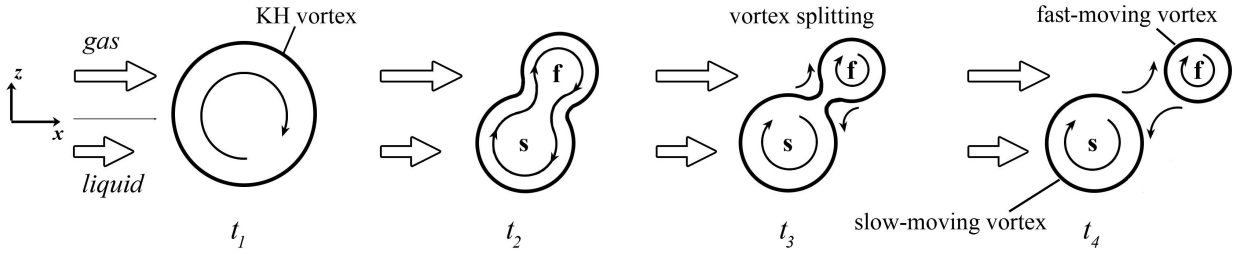

Figure 4.16: Schematic of how KH vortex splits into a slow-moving vortex (denoted by s) in the liquid and a fast-moving vortex (denoted by f) in the gas zone, at four consecutive times. The qualitative velocity magnitudes are denoted by the straight arrows in the gas and the liquid. The vortices are nearly uniform in the y direction, normal to the paper.

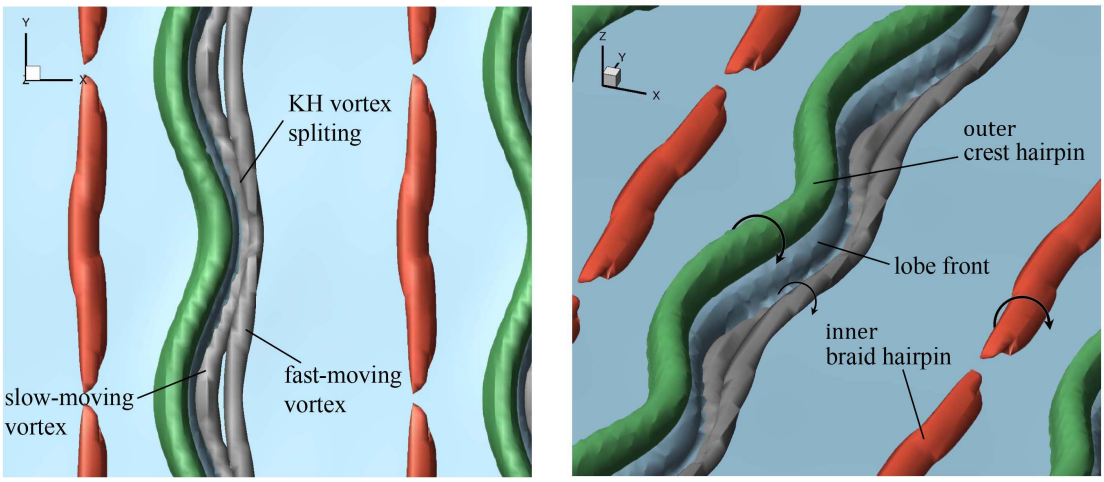

Figure 4.17: λ_2 isosurfaces in a close-up view of a liquid lobe in Case D3a, from a top view (*a*), and a 3D view (*b*), at $t = 12$ μs. The isosurface values are: $\lambda_2 = -8 \times 10^{10}$ s^{-2} (gray), -4×10^{10} s^{-2} (green), and -10^{10} s^{-2} (red). The liquid surface is shown in blue.

fast-moving gas layer, separates from the part that is inside the surface of the lower speed liquid (indicated by the black arrow in Figure 4.15*b*). The splitting of the KH vortices starts at 10 μs (Figure 4.15*b*) and continues until 12 μs (Figure 4.17). The gray, green, and red λ_2 isosurfaces in Figure 4.17 denote the KH vortex, the outer (crest) hairpin, and the inner (braid) hairpin, respectively (the magnitude of each λ_2 isosurface is indicated in the caption). The split slow- and fast-moving vortices are denoted by 's' and 'f' in Figure 4.16, respectively.

As demonstrated in Figures 4.16 and 4.18(a), part of the KH vortex that resides in the faster moving gas, near the liquid interface, advects downstream with the gas, while the slow-moving vortex (indicated by the black arrow in Figure 4.18a) advects more slowly with the interface velocity, remaining stationary relative to the liquid surface. The two vortices are completely separated at t_4 in Figure 4.16, corresponding to $t = 16$ μs in our simulation (see Figure 4.18*b*). This vortex separation has two significant consequences. (i) The slow-moving vortex (black vortex) downstream of the KH wave is not strong enough to curl the KH wave and stretch the lobe downstream over itself. Consequently, the outer hairpins do not overlap in x with the inner trough hairpins, as in the $LoHBrLiD$ Domain; hence, the hole formation is inhibited at early times. (ii) The fast-moving vortex (the white vortex) gets closer to the

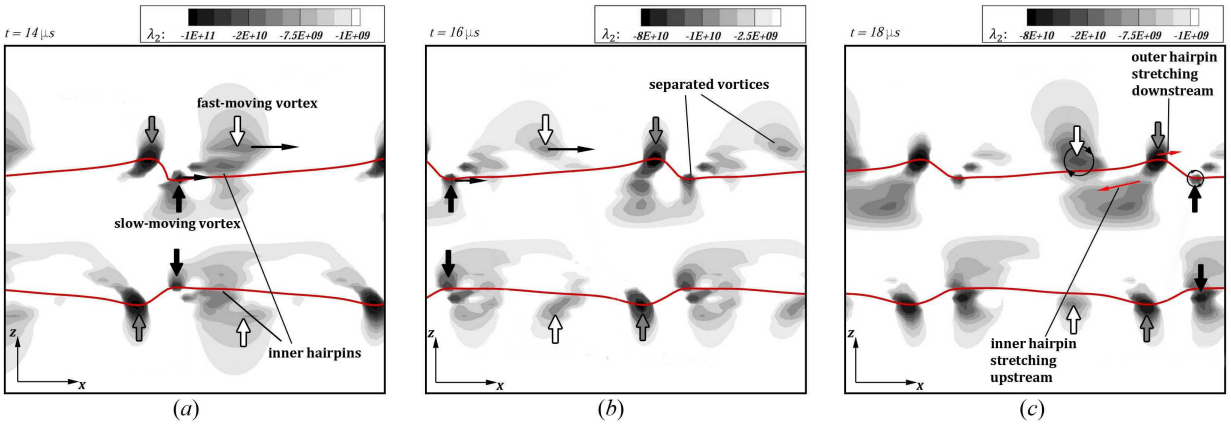

Figure 4.18: λ_2 contours on the spanwise crest cross-section, at $t = 14$ μs (a), 16 μs (b), and 18 μs (c) of Case D3a.

downstream outer hairpin as it advects away from the upstream hairpins, residing in the vicinity of the trough; see Figure 4.18(b). This successive variation in the distance between the hairpins and the fast-moving vortex induces a fluid motion that stretches the hairpins in the opposite directions, resulting in a less-orderly hairpin structure with more undulations, as shown schematically in Figure 4.19.

After splitting of the KH vortex into fast- and slow-moving vortices (t_2 in Figure 4.19), the fast-moving vortex ($1f$) advects downstream over the outer hairpin (t_3 in Figure 4.19). As the faster-moving vortex ($1f$) passes over the hairpin, its induced motion pulls the crest of the hairpin in the upstream direction under vortex $1f$, causing the hairpin to undergo an undulation with smaller local wavelength (≈ 45 μm). Meanwhile, the tip of the hairpin (now having two crests) is stretched downstream over the neighboring slow-moving vortex ($2s$), and the trough of the hairpin is stretched upstream under the upstream slow-moving

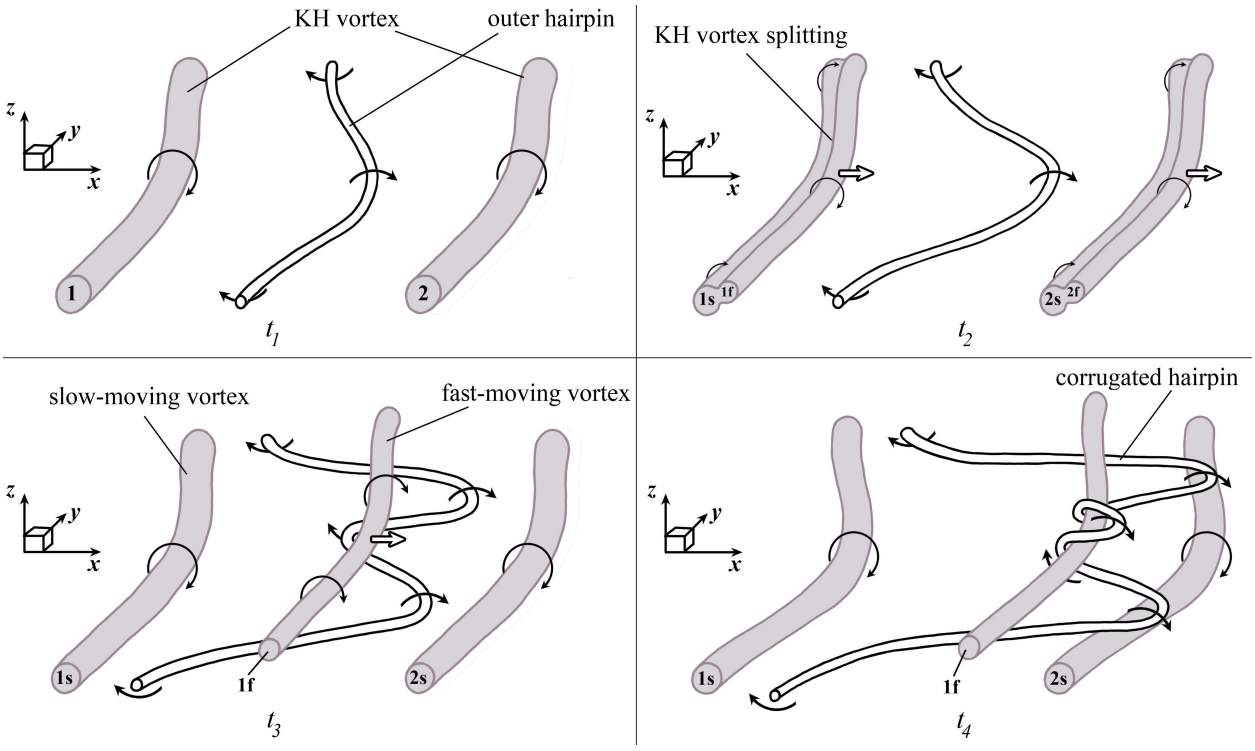

Figure 4.19: Schematic of the hairpin undulation formation under the influence of the fast-moving KH vortex (denoted by $1f$) at four consecutive times t_1–t_4, from a frame of reference moving with the slow-moving KH vortices (denoted by $1s$ and $2s$).

vortex ($1s$) (t_3 in Figure 4.19). The streamwise stretching on different parts of the hairpins are indicated by the black curly arrows. As the faster-moving vortex ($1f$) moves further downstream, the newly formed undulation wraps around it and stretches downstream, as shown at t_4 in Figure 4.19. Therefore, another turn is created on the hairpin vortex and the local wavelength of the undulations decreases (15–35 μm). As the fast-moving vortex keeps moving downstream, the hairpin corrugations stretch with it. It will be shown below that this hairpin structure results in less stretched (slower stretching) and more corrugated lobes. The direction of the streamwise stretch on the hairpin filaments – based on the velocity field induced by the two split rollers – is denoted by the red arrows in Figure 4.18(c). The sheet is still symmetric at this moment, while the vortices have lost their symmetry with respect to the center-plane. The fast-moving vortex ($1f$) finally reaches the downstream slower-moving vortex ($2s$) and combines with it to create a stronger KH vortex, which stretches the now corrugated hairpin in the downstream direction.

To better understand the consequence of hairpin vortex structure on the liquid surface deformation at high Re_l and low We_g, the evolution of the vortices and the interface in the $LoCLiD$ process (Domain III) are schematically depicted in Figure 4.20 at four consecutive instances. At an early time t_1, the braid regions connecting the emerging KH rollers become progressively more depleted of vorticity. The spanwise vortices on the braid deflect due to the induced motion of the neighboring KH rollers in both the upstream and downstream directions – creating the hairpin vortex structures with a spanwise size equal to the spanwise perturbation wavelength (100 μm). Two hairpins are formed on the braid – one located near the lobe crest, called the outer hairpin and denoted by the black line (corresponding to the green isosurface in Figure 4.17), and the other slightly upstream near the trough, called the inner hairpin and denoted by the red line (corresponding to the red isosurface in Figure 4.17). The deflected hairpin filaments form the lobes as they are stretched by the KH roller. So far, the process is similar to the $LoHBrLiD$ process.

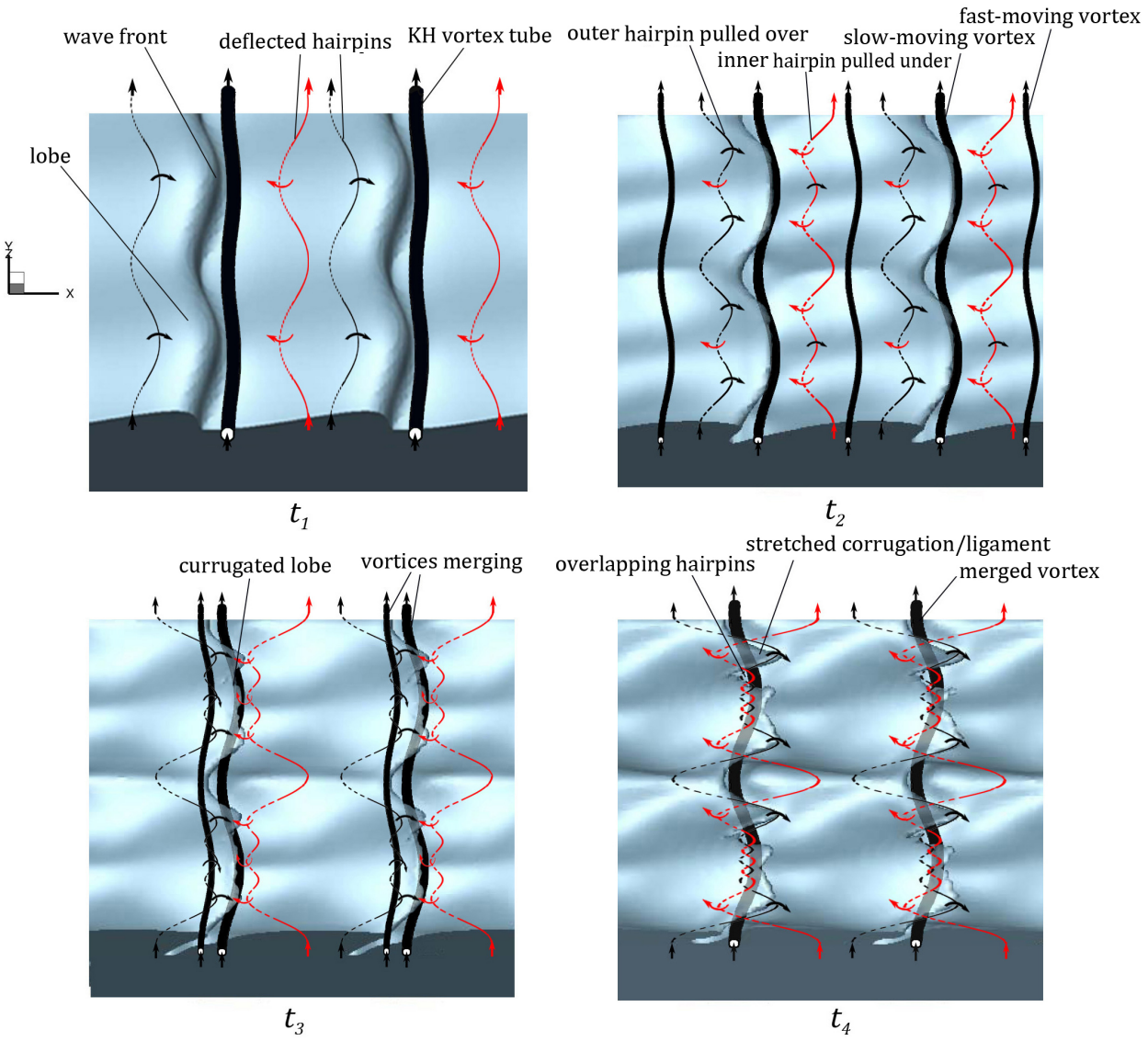

Figure 4.20: Schematic of the *LoCLiD* process at four consecutive times. The liquid surface is shown in blue, and the the KH vortex is denoted by the black tube. The red and black lines denote the inner and outer hairpin vortices near the trough and crest of the KH wave, respectively. The solid and dashed lines indicate the parts of the hairpins that are stretched upstream and inward, or downstream and outward, respectively.

As discussed earlier and demonstrated in Figure 4.19, the hairpin vortices get corrugated under the influence of the fast-moving vortex that hovers over the interface after splitting of the KH vortex. This corresponds to t_2 and t_3 in Figure 4.20. Only the deformation of the outer hairpin (black hairpin) was shown in Figure 4.19; the inner hairpin (red hairpin) undergoes the same process, but in the opposite direction – stretching downstream and over

the fast-moving vortex. The upstream turns and bends on the hairpins prevents further downstream stretching of the lobes. Consequently, the lobes are less stretched and more blunt compared to the lobes in Domain II (compare t_2 in Figure 4.20 with t_2 in Figure 4.11). The fast-moving vortex moves closer to the interface to merge with the downstream slow-moving vortex and later passes through the lobe and reaches the slower vortex below the lobe. In this process, the faster vortex carries along the corrugated outer hairpin that is wrapping around it. Consequently, the corrugated outer hairpins penetrate through the lobe and locate underneath the lobe in contrast to Domain II, where the outer hairpins were located on top of the lobe. Since this process occurs quickly, the corrugated hairpins do not have enough time to completely wrap around the faster vortex and create a combined vortex; therefore, after the merging of the two split KH vortex counterparts, only two pairs of undulated hairpins – which are separate from the KH vortex – remain on top and bottom of the reformed KH vortex, right below the lobe. The liquid surface approximately follows the hairpin structures with some delay at this high Re_l range – as the vortex lines are nearly material lines. Because of these shorter hairpin wavelengths, corrugations with length scales comparable to the local hairpin wavelengths (15–25 μm) form on the front-most edge of the lobes, as shown in Figure 4.20 at t_3. Both experimental observations [43, 49] and numerical simulations [5, 15] for homogeneous jets show that the size of vortex pairs (lobes in two-phase flows) decreases with increasing Re_l.

Upon creation of a stronger KH vortex downstream of the KH waves at t_4 – after merging of the fast- and slow-moving vortices – the new KH roller, which is now located under the lobe (now a thicker tube) is strong enough to stretch the hairpins and the corrugations. The two hairpin layers overlap as illustrated in Figure 4.20 at t_4. In this figure, the dashed lines represent the hairpins stretching upstream and on the streamwise trough, i.e. lower surface of the gas tongue, while the solid lines denote parts of the hairpins that are stretched downstream below the lobe; i.e. upper surface of the gas tongue.

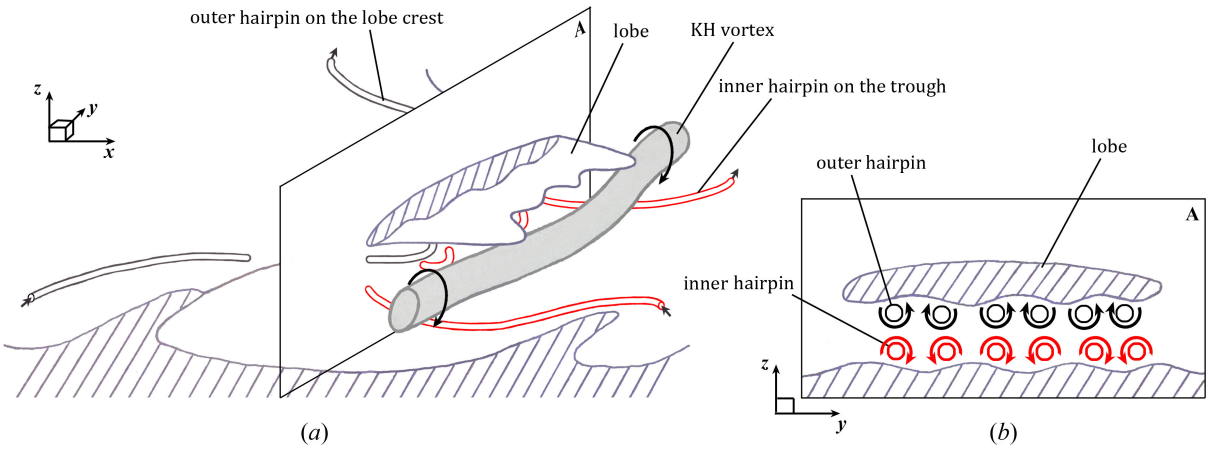

Figure 4.21: 3D Schematics showing the overlapping of the outer hairpin (black slender tube) and the inner hairpin (red tube) resulting in formation of lobe corrugations (a) – A is the plane in which (b) is drawn; cross-sectional view of the A-plane showing the corrugation formation and thinning of the gas tongue due to the combined induction of the overlapping hairpins (b). The vortex schematics are periodic in x- and y-directions.

The illustrative sketches of Figure 4.21 show the corrugated hairpin structures and their position with respect to the lobe in the $LoCLiD$ process (corresponding to t_4 in Figure 4.20). The black tube represents an outer hairpin on the lobe crest and the red tube represents an inner hairpin on the streamwise trough (originating from the braid). The two hairpin layers – after getting corrugated due to the induced motion of the two halves of the split KH vortex (see t_2 and t_3 in Figure 4.19) – overlap under the lobe, as shown in Figure 4.21(a). Following the fluid motion induced by the vortex pairs, the lobe front edge gets corrugated with comparable length scales to the hairpin undulation wavelength; see Figure 4.21(a). The layer of the outer hairpin (black tube) is located underneath the lobe (on top of the gas layer), and the layer of the inner hairpin (red tube) is located on top of the interface at the trough; see Figure 4.21(b). The induced flow creates undulations on both the bottom surface of the lobe and the trough surface. The combined induction of the two oppositely oriented overlapping hairpin layers thins the gas layer that fills the vertical gap underneath the lobe; i.e. the lobe collapses on the liquid sheet as the bottom surface of the lobe descends and the trough surface ascends; see the qualitative streamlines in Figure 4.21(b).

As the counter-rotating pairs of hairpins stretch under the induction of the KH vortex, the corrugations on the lobes stretch with them and form thin ligaments (see t_4 in Figure 4.20). The ligaments stretch downstream and break up into droplets as they undergo capillary instabilities (the ligament breakup mechanism is discussed in Section 4.2.4). In the meantime, the eddies cascade into smaller vortical structures as transition to turbulence occurs. The smaller vortices are moved towards the gas by the induction of the larger eddies. The outward movement of the vortices spreads the droplets in the normal direction, helps the expansion of the spray angle, and enhances the two-phase mixing.

The process of lobe-sheet collision after the merging of the two split KH vortices is shown in the side views of the liquid sheet along with λ_2 contours near the interface in Figure 4.22. The antisymmetric vortices, which now are strong enough to stretch the lobes, create antisymmetric KH waves, at 44 μs (Figure 4.22a). The hairpin vortices on the KH wave crest and trough stretch in the opposite directions following the induced fluid motion of the KH roller. Following the direction of the swirl, the hairpin projections on the trough are stretched upstream from the inner side of the roller, while the hairpin projections on the KH crest are stretched downstream from the outer side of the roller. The direction of streamwise stretch on the fluid elements is shown by the red arrows in Figure 4.22.

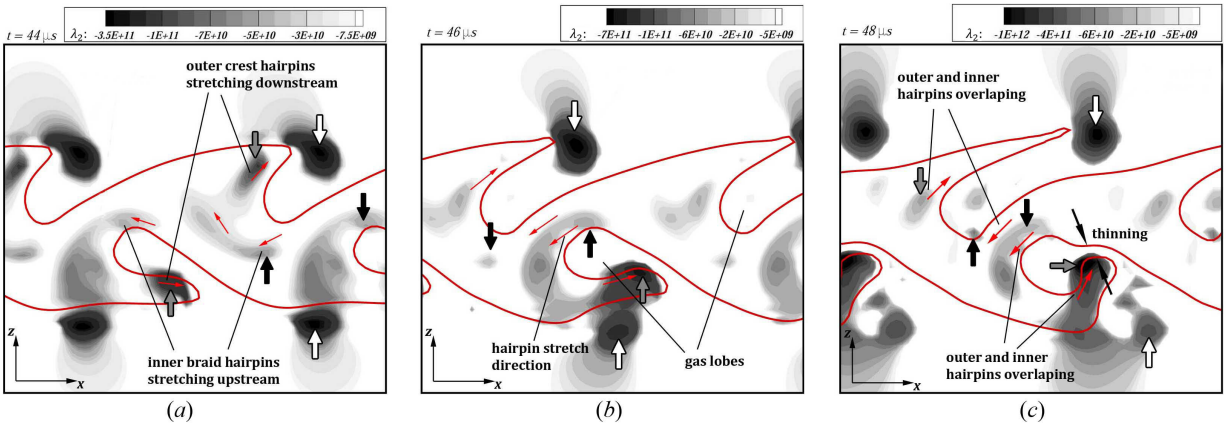

Figure 4.22: λ_2 contours on the spanwise crest cross-section, at $t = 44$ μs (a), 46 μs (b), and 48 μs (c) of Case D3a.

Recall that at lower Re_l the two overlapping hairpins lie above and below the lobe and cause its thinning. At higher Re_l, on the other hand, the outer and inner hairpins are inside the liquid (very close to the surface), and overlap on outer and inner sides of the gas layer that penetrates under the lobe. To understand this better, consider the opposite perspective; i.e. the layer of gas that fills the vertical gap underneath the KH waves can be considered as an upstream-pointed gas tongue, surrounded by the liquid; see Figure 4.22(b). The combined induction of the overlapping hairpins thins the tongue similarly to the process described in Figure 4.5. The thinning regions are indicated by the two thin black arrows in Figure 4.22(c). Since it would be confusing to describe a hole formation in the tongue, we could interpret this phenomenon as the collapse of the lobe on the jet, encapsulating the gas in between.

Figure 4.23 shows the top view of a corrugated lobe and the λ_2 contours at three spanwise (y–z) planes passing though the lobe body (plane A–A), through lobe corrugations (plane B–B), and through the braid (plane C–C), at 50 μs. The λ_2 contours clearly show the vortical structures suggested by the schematics of Figure 4.21. Upstream of the lobe front, at plane A–A, one downstream stretching vortex pair is seen just underneath the lobe – indicated by the black curly arrows – and three upstream stretching counter-rotating vortex pairs are seen just above the trough surface – indicated by the red curly arrows. At this cross section, the red hairpin shows the three vortex pairs shown in Figure 4.21(b), but the black hairpin still has the main two legs and does not manifest undulations in this plane. That is, the undulations have not stretched enough to reach the A–A plane yet. The effects of these vortex pairs on the liquid surface is evident in this figure. Moving slightly downstream, in plane B–B, both black and red hairpins manifest three vortex pairs, located under the lobe and above the trough, respectively. The λ_2 contours at this cross-section agree well with the scenario depicted in Figure 4.21(b) on plane A. However, the vortex pairs are not nicely aligned in y, as shown in Figure 4.21(b). The distance between the two legs of each vortex pair has been denoted on the figure. As indicated before, the vortex undulations with wavelengths in the range 15–35 μm are seen in this picture. The creation of bumps

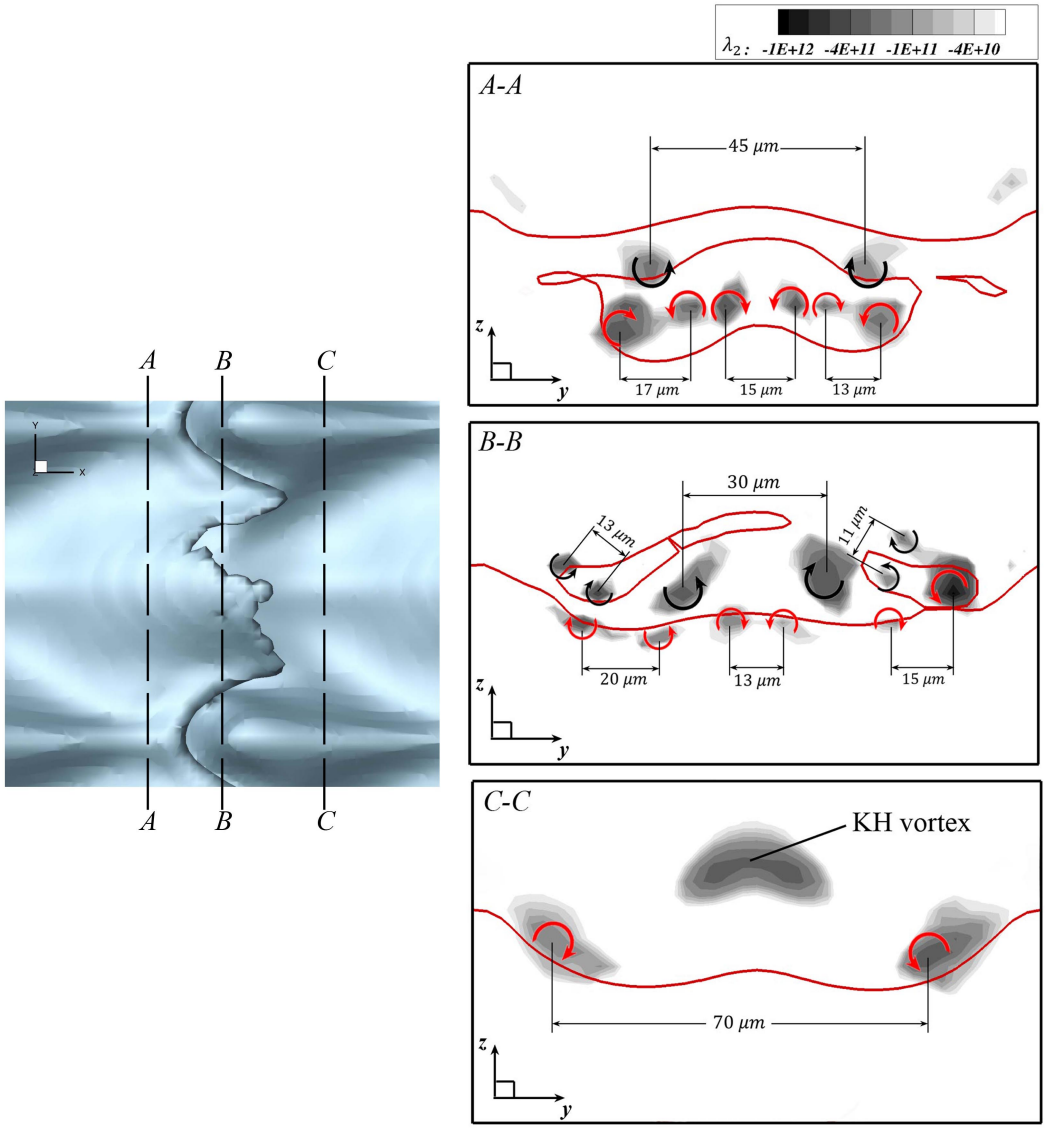

Figure 4.23: Top view of a liquid lobe in Case D3a at $t = 50$ μs (left), and the λ_2 contours on three yz-cross-sections (right); A–A passing upstream of the lobe front (top), B–B passing through the corrugations (center), and C–C passing downstream of the lobe (bottom).

and craters on the liquid surface induced by these vortex pairs is also seen here. Further downstream, on plane C–C, only the two main legs of the red hairpin and parts of the KH vortex are seen. This is what would be expected based on the 3D schematic of Figure 4.21(a). The distance between the two legs of this hairpin vortex is 70 μm at this cross section. The wavelength of the undulations and the scale of surface corrugations presumably depend on other parameters such as surface tension and liquid viscosity; however, analysis of the effects

of these parameters is beyond the scope of this article and would be an interesting subject for a prospective study.

The mechanism of corrugation formation at lower $\hat{\rho}$ is similar to what was shown above in this section. However, the hairpins are not as easily bent (corrugated more slowly) as in high density ratios and, consequently, the number of corrugations are less. Figure 4.24 shows the vortex structures along with the images of a lobe from a top view in the 64–68 μs period of Case D3b (see Table 4.1). The vortex structures in Figure 4.24(a) correspond to the liquid lobe in Figure 4.24(b). The liquid surface has been removed from Figure 4.24(a) to show all the vortices under the liquid surface; to facilitate the comparison between the

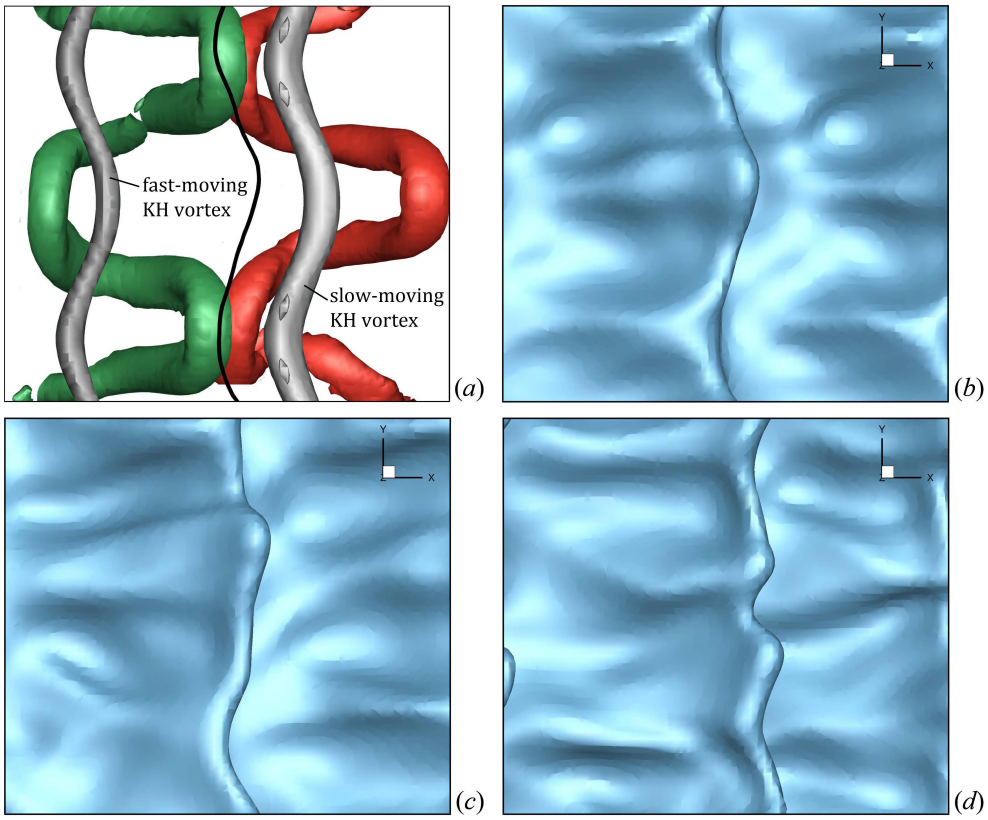

Figure 4.24: λ_2 isosurface in a top close-up view of a liquid lobe in Domain III at low density ratio (Case D3b) at 64 μs (a); the solid black line shows the lobe front edge. The isosurfaces represent: the fast- and slow-moving KH vortices with $\lambda_2 = -7 \times 10^{10}$ s^{-2} (gray), the outer crest hairpin with $\lambda_2 = -4 \times 10^{10}$ s^{-2} (green), and the inner trough hairpin with $\lambda_2 = -3 \times 10^{10}$ s^{-2} (red). Lobe surface showing the corrugation formation from a top view at 64 μs (b), 66 μs (c), and 68 μs (d) of Case D3b.

vortex structures and surface structures, the lobe front edge is denoted in this figure by the solid black line. The outer hairpin (green isosurface) and the fast-moving KH vortex still lie above the lobe surface at 64 μs, while the inner hairpin (red isosurface) and the slow-moving KH vortex lie underneath the lobe and closely downstream of the lobe front. Following the illustrations in Figure 4.19 (at t_3 and t_4), the tip of the outer hairpin stretches upstream while the inner hairpin stretches downstream under the influence of the fast-moving vortex. This process creates the hairpin undulations and increases the number of counter-rotating vortex pairs along the lobe span. However, comparison of Figures 4.24(a) and 4.23 reveals that the hairpin corrugation appears much more quickly at high gas density, as three pairs of counter-rotating hairpins are seen at an earlier time in Figure 4.23. At low gas density, the hairpins are not easily deflected and bent; the reason is conjectured to be the lower gas inertia. While the hairpins are in the gas, the lower inertia of the gas slows down the process of hairpin deflection. By the time the outer hairpin and the fast-moving vortex move into the liquid, the hairpin deformation hastens and another turn forms at its trough (at the center of Figure 4.24a), where the green hairpin stretches downstream, over the fast-moving vortex. Thereafter, the number of undulations increases and the corrugations stretch. The relatively higher inertia of the neighboring liquid retards the rate of growth of the instability. That is, the reaction of the hairpins to the KH vortex is slowed.

Figure 4.24 confirms that the lobe deformation is in fact an outcome of the KH and hairpin vortex distortions, not the other way around. The vortex and liquid structures at 64 μs, shown in Figures 4.24(a,b), prove that the vortex deformation precedes the surface deformation. At this time, the hairpins have been already distorted and manifest two pairs of counter-rotating streamwise vortices near the lobe front, while the lobe front itself does not show any corrugation. At later times (Figures 4.24c,d), two corrugations start to form following the structure of the undulated hairpins. This transforms the lobe from a singular protrusion to two smaller ones growing out of the corrugated rim. While the lobe rim stretches under the influence of the KH vortex (after the two split counterparts merge), it

also retracts towards the center by the capillary forces. This brings the hairpins and the corrugations closer to the center of the lobe, as seen in Figure 4.24(d). This retraction is faster at lower We_g; compare Figures 4.24 and 4.23.

4.2.4 Lobe and ligament stretching at low Re_l ($LoLiD$ mechanism)

At low Re_l and low We_g, the surface tension force resists perforation. The liquid viscosity is also fairly high and damps the small scale corrugations on the lobe front edge. Consequently, the entire lobe stretches slowly into a thick and long ligament, which eventually breaks into large droplets. This terminates the $LoLiD$ breakup mechanism, which prevails in Domain I, shown in Figure 3.2. The $LoLiD$ process is shown step by step in Figure 4.25. The case shown in this figure (Case D1a) is taken for vortex analysis in this section. λ_2 contours on y-planes and λ_2 iso-surfaces in the interface vicinity are used in this section to explain the vortex dynamics of the $LoLiD$ process.

As shown in Figure 4.26(a), the process starts with a large KH roller downstream of the KH wave (denoted by the white arrow), hairpin filaments on the braid, and a much stronger

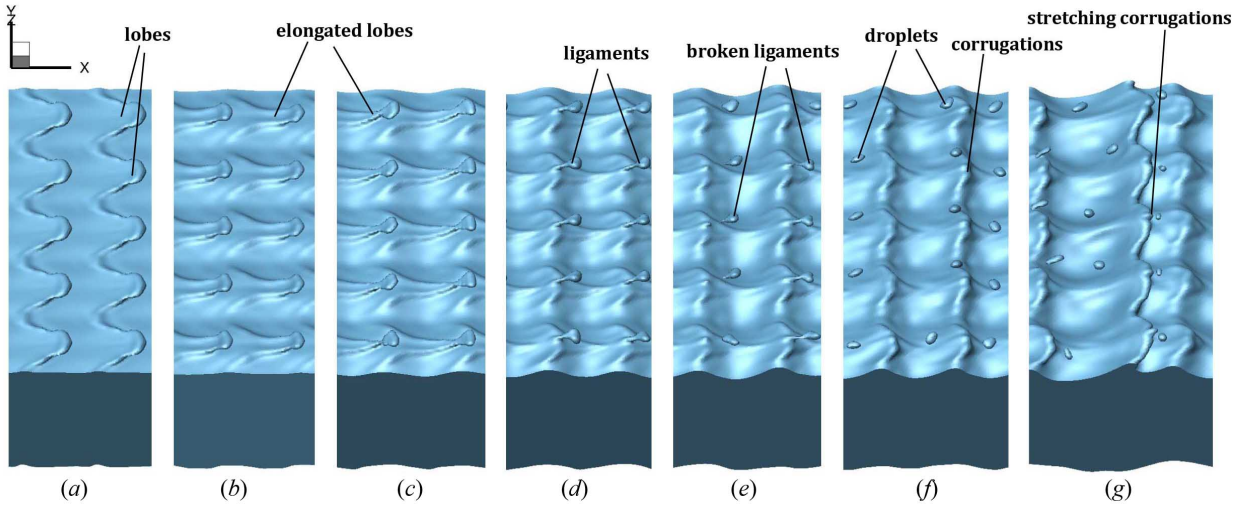

Figure 4.25: Liquid surface deformation following the $LoLiD$ mechanism in Case D1a, at $t = 26$ μs (a), 36 μs (b), 40 μs (c), 44 μs (d), 46 μs (e), 48 μs (f), and 52 μs (g).

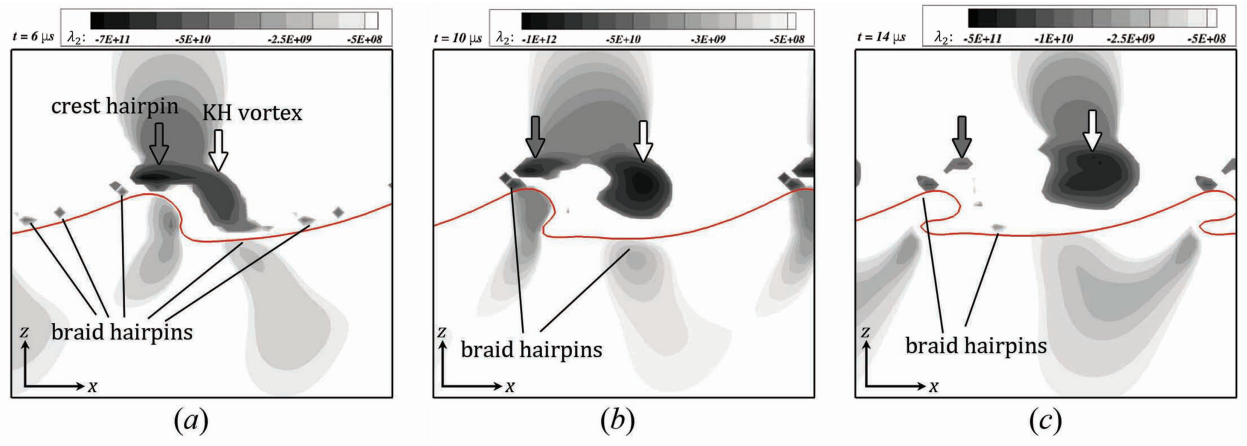

Figure 4.26: λ_2 contours on the spanwise crest cross-section, at $t = 6$ μs (a), 10 μs (b), and 14 μs (c) of Case D1a.

hairpin filament on the KH wave crest (denoted by the dark gray arrow). Because of the high gas viscosity, the KH vortex diffuses much faster into the gas and at 6 μs the vortex core is entirely in the gas zone. Since the gas phase has higher velocity compared to the liquid phase, the gas distant from the liquid surface advects faster with respect to the interface. Hence, a few microseconds later, say at 10 μs (Figure 4.26b), the entire KH roller advects downstream with respect to the interface as its core moves farther from the interface via diffusion. The KH roller gains speed as it moves away from the interface. In contrast, the hairpin filaments that are closer to the liquid surface remain almost stationary with respect to the interface; see Figure 4.26(c). The KH vortex gets larger with time as it diffuses; compare Figures 4.26(a-c).

The KH roller reaches the neighboring downstream crest hairpin at 16 μs (Figure 4.27a). Meanwhile, the braid hairpins overlap with the crest hairpins, constraining the lobe sheet in between. So far, the vortex dynamics manifest the conditions required for hole formation, i.e. overlapping of two oppositely-oriented hairpins on top and bottom of the lobe, as well as for corrugation formation; i.e. constant pull in opposite directions induced by a moving vortex hovering over the hairpins. However, none of these structures are seen on the lobe at this moment (see Figure 4.25a). The inhibition of hole formation is due to the high surface

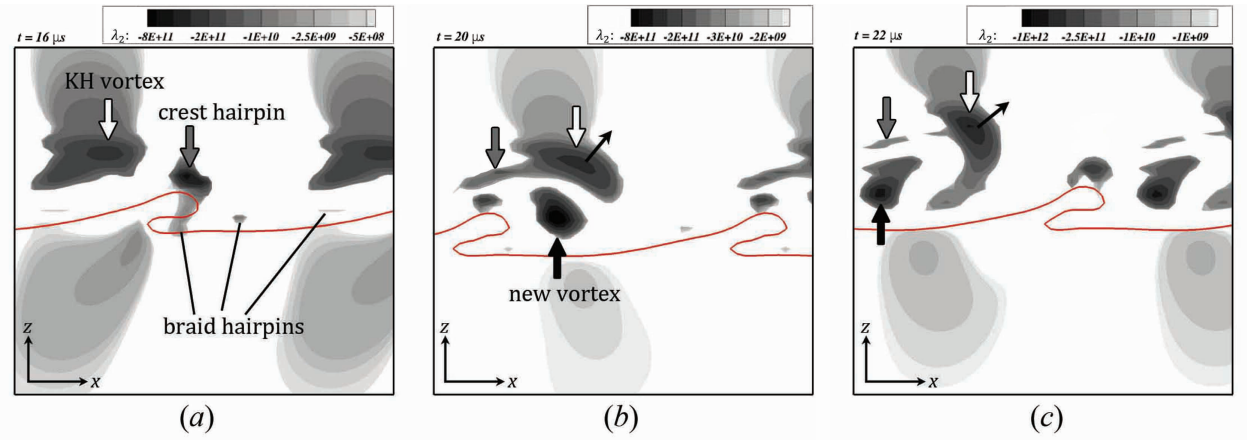

Figure 4.27: λ_2 contours on the spanwise crest cross-section, at $t = 16$ μs (a), 20 μs (b), and 22 μs (c) of Case D1a.

tension. In such a low We_g, the inertia and viscous forces are not strong enough to overcome the surface tension force to stretch and thin the lobe; hence, the lobe perforation is inhibited. Also, because of the high liquid viscosity at such a low Re_l, the liquid surface deformation is much slower. Hence, the corrugation formation on the lobe edge does not occur as quickly as for the higher Re_l. Small scale corrugations are damped by both the high viscous and high surface tension forces. Thus, the lobe slowly stretches into a thick ligament. Moreover, the KH roller is also farther away from the interface in this case compared to the $LoCLiD$ process (compare Figures 4.27a and 4.18c), which means that it has a much weaker influence on the hairpin filaments.

The tip of the KH wave acts like a backward-facing step for the gas flow and a temporary recirculation zone forms immediately downstream of the wave, as shown in Figure 4.28. This is very similar to the scenario seen at low density ratios by Hoepffner et al. [29]. They also showed that the head of the wave appears to the gas stream as a fixed obstacle, with the ensuing vortex shedding. The high strain rate at the braid depletes the vorticity upstream of the braid and collects the vorticity into a new vortex just downstream of the KH wave, in the recirculation zone at 20 μs. This new vortex is indicated by the thick black arrow in Figure 4.27(b) and the black circles in Figure 4.28. When the KH roller (vortex 1) passes

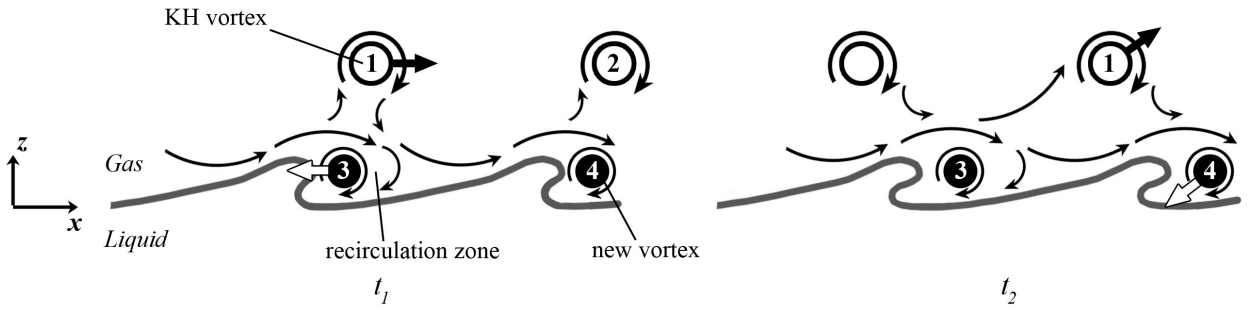

Figure 4.28: Schematic of the recirculation zone downstream of the KH wave. The hollow circles denote the KH vortex and the black circles denote the newly formed vortex in the recirculation zone. The induction of each vortex on the neighboring vortices is indicated by the straight arrows with the same shading as the source vortex. The curly arrows qualitatively indicate the streamlines near the interface.

over the KH wave front (see t_1 in Figure 4.28), the mutual induction of this roller and the new vortex (vortex 3) causes the KH roller to advect farther downstream, further stretching the KH vortex. The local induction of each vortex on the neighboring vortices is indicated by the straight arrows of the same shading as the source vortex in Figure 4.28. When the KH vortex (vortex 1) passes over the downstream wave at 22 μs (Figure 4.27*c*), the mutual induction of the vortices pushes away the KH vortex, advecting it in the z-direction; see t_2 in Figure 4.28. The stronger induction by vortex 4 pushes vortex 1 in the direction normal to the line connecting the centers of the two vortices (in the direction of the black arrow). Vortex 3 also induces a flow that would bring vortex 1 closer to the interface; however, this induction is much weaker as vortex 3 is more distant from vortex 1 compared to vortex 4. The new vortex wraps under and around the KH roller at its crest and later over the trough of the adjacent downstream KH roller, as shown in Figure 4.29. Thus, this new vortex (the red tube in Figure 4.29) transforms into a hairpin vortex that is stretched between two adjacent KH vortices and wraps around them at their crests and troughs.

Schematics of the vortex structures corresponding to $t = 26$ μs (shown in Figure 4.30*a*) are illustrated in Figure 4.29. The KH vortex has a larger undulation in this domain compared to the other two domains and is also farther away from the interface in the gas zone (compare

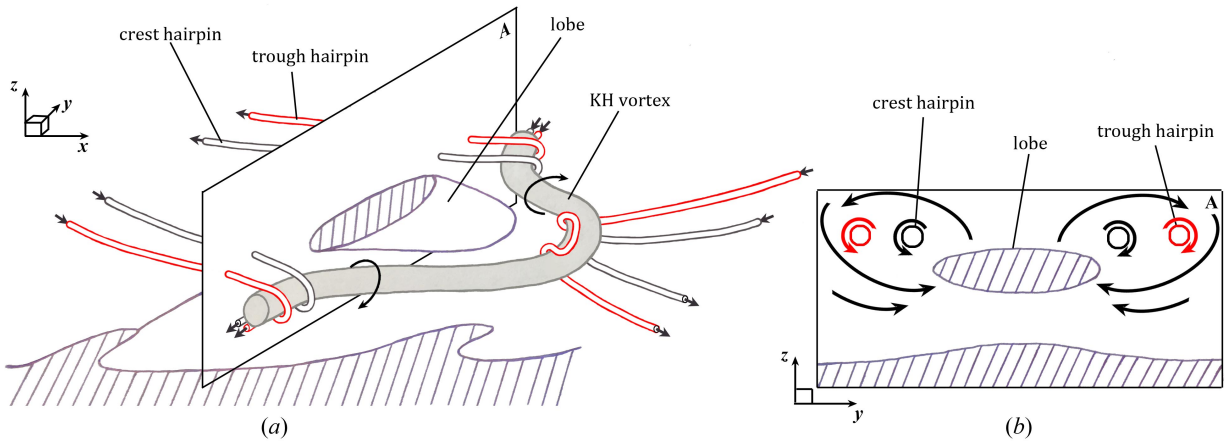

Figure 4.29: 3D Schematics showing the vortex structures in the *LoLiD* Domain (a) - A is the plane in which (b) is drawn; cross-sectional view of the A-plane, showing the spanwise squeezing of the lobe by induced flow of the hairpin vortices (b). The vortex schematics are periodic in x- and y-directions.

Figure 4.29 with Figures 4.5 and 4.21). Two pairs of counter-rotating hairpins – one on the lobe crest (the black tube), and the other on the trough (the red tube) – stretch and wrap around the KH vortex (Figure 4.29a). Notice that the red hairpin in Figure 4.29 is actually the new vortex that was formed at the wave front end and was indicated by the black arrows in Figures 4.27 and 4.30. These hairpins are periodic in both spanwise (y) and streamwise (x) directions; i.e. the tubes that emerge at the bottom corner or the left side of Figure 4.29(a), re-enter from the top corner or the right side of the sketch, respectively. As shown in the cross-sectional view of the A-plane passing through the lobe in Figure 4.29(b), both the black and the red hairpins are located slightly above and on both sides of the lobe at this moment. While the flow induced by the KH vortex creates a streamwise flow on top and bottom of the lobe, the gas flow induced by these two counter-rotating hairpins (shown by the curly arrows is Figure 4.29b) generates a spanwise flow towards the lobe midplane. Consequently, the lobe is both squeezed in the spanwise direction – via the induced flow of the hairpins – and stretched in the streamwise direction by the induced flow of the KH vortex. The gas flow induced by the hairpins also lifts the lobe in the z-direction; see Figure 4.29(b).

While the KH vortex keeps diffusing due to the high gas viscosity, the dark gray and black

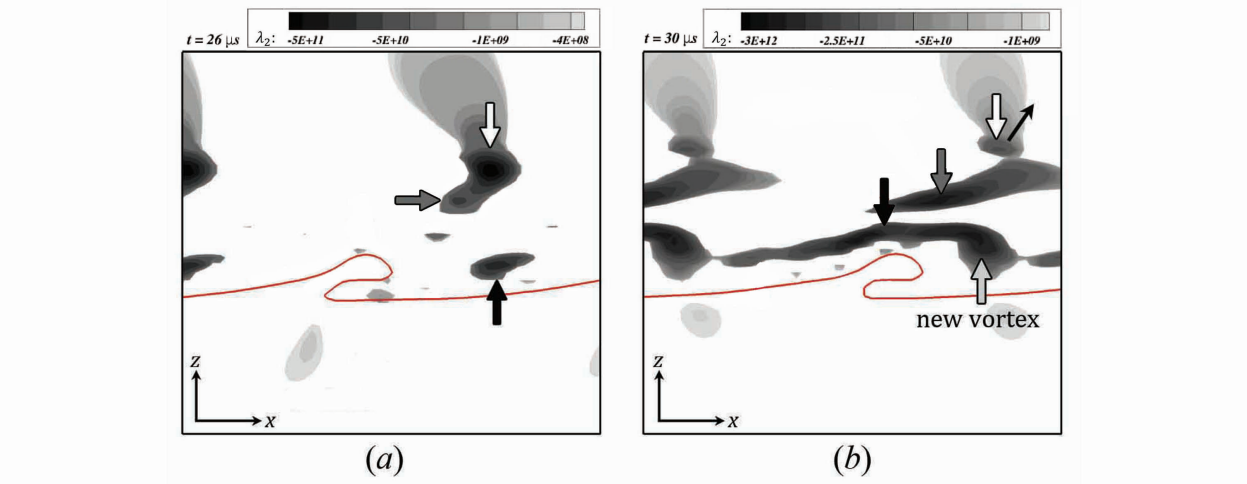

Figure 4.30: λ_2 contours on the spanwise crest cross-section at $t = 26$ μs (a), and 30 μs (b) of Case D1a.

vortices wrap around it and are stretched with it as it moves downstream (Figure 4.30b). Meanwhile, another vortex forms downstream of the wave crest at 30 μs, indicated by the light gray arrow in Figure 4.30(b). This vortex advects downstream closely hovering over the interface at 36 μs, while new vortices keep forming downstream of the KH wave crest at the

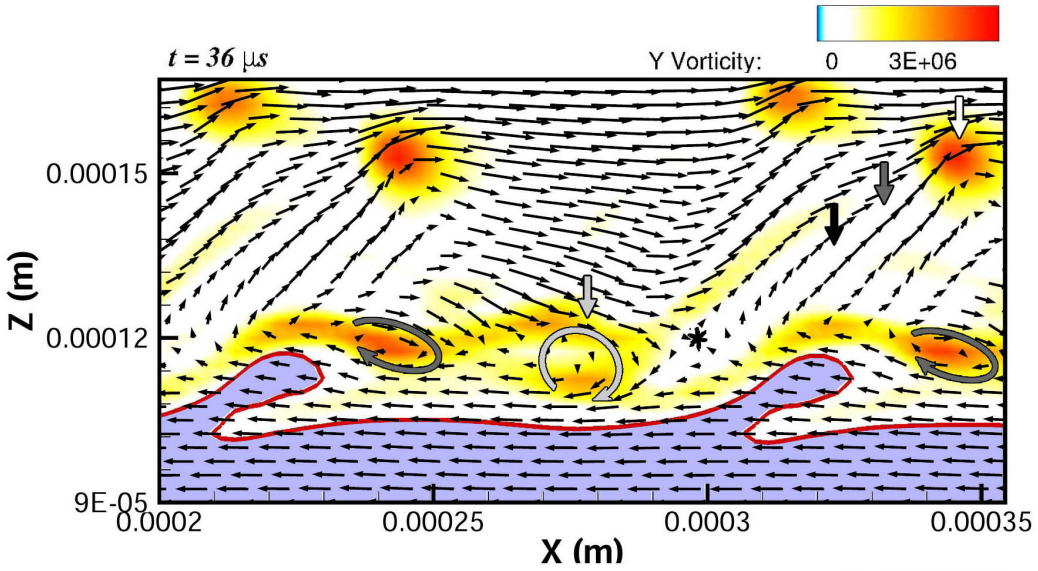

Figure 4.31: Velocity fluctuation vector field with respect to the average velocity of the vortex cores near the interface, and ω_y contours on the spanwise crest cross-section at $t = 36$ μs of Case D1a. The thick arrows refer to the vortices shown in figure 4.30(c). The star symbol marks the saddle point, and the liquid is shown in light blue.

recirculation zone to replace it; see Figure 4.31. Hoepffner et al. [29] were the first to identify this vortical mechanism at low density ratios. Similar to Figure 4.31, they showed that two vortices exist in the gas – one is at the instant of leaving the shelter of the wave (the dark gray curly arrow in Figure 4.31), and the second further downstream is the result of the previous shedding event (the light gray curly arrow in Figure 4.31). The induced motion of these vortices entrains the gas and draws it under the protruding lobe (follow the velocity vectors in the gas zone near the interface in Figure 4.31). As is well-known, the streamwise strain rate is highest at the saddle [32, 43]. The location of the saddle point is marked by a star symbol in Figure 4.31. The vortices that reach the saddle point stretch in the streamwise direction and transform into hairpin vortices with streamwise legs. The location of the black and dark gray hairpins that are wrapping around the KH vortex are denoted by straight arrows of the corresponding vortex color. Since these vortices are mostly streamwise at this cross-section, they do not have ω_y contours. The streamwise elongation of the vortices progressively aligns the two counter-rotating legs of the hairpins in the streamwise direction. The self-induction of the counter-rotating legs of the KH vortex and the hairpin vortices, moves the vortex tubes in the normal direction away from the interface, as shown schematically in Figure 4.32.

The temporal evolution of the vortex structures in the *LoLiD* process is illustrated in Figure 4.33 from a top view of the liquid surface. The liquid surface is illustrated in the right

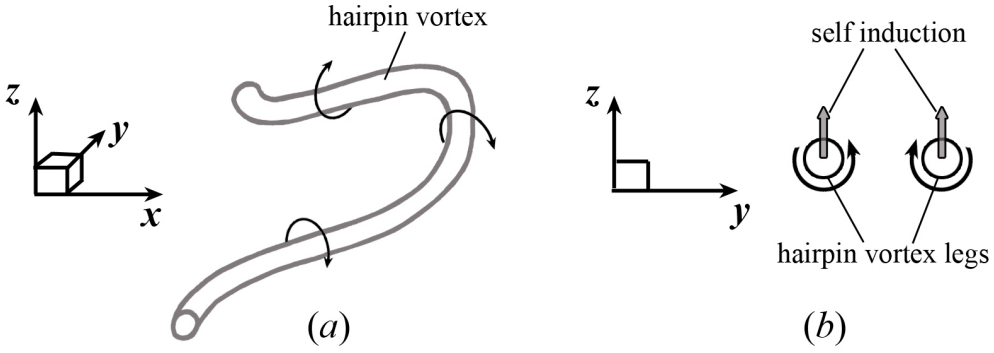

Figure 4.32: Schematic showing the self-induction of the streamwise counter-rotating hairpin legs (a), and in a yz-plane crossing the legs (b). The gray arrows in (b) show the direction of the self-induction.

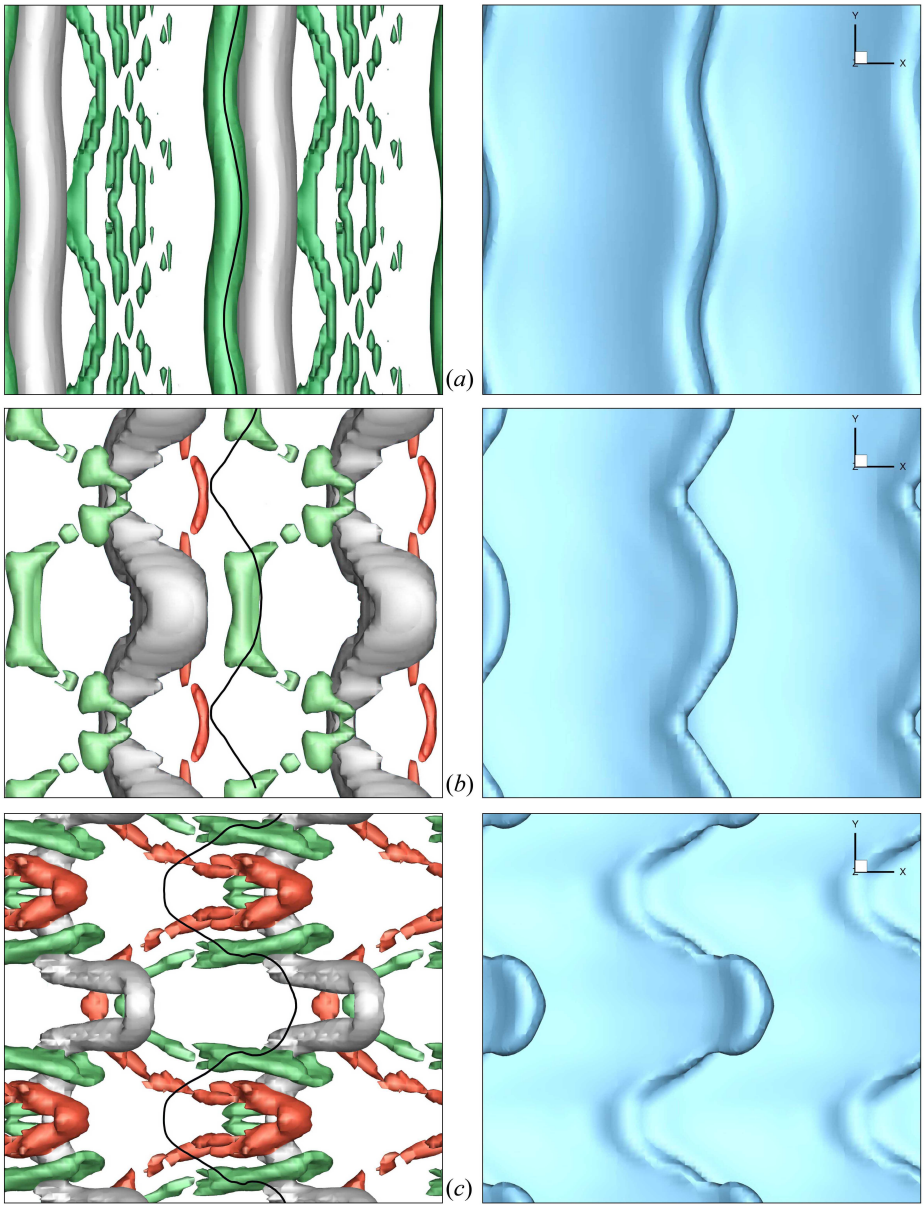

Figure 4.33: λ_2 isosurface in a top close-up view of a liquid lobe in Domain I (Case D1a) on the left and the liquid surface from a top view on the right, at $t = 6$ μs (a), 16 μs (b), and 26 μs (c). The solid black line on the left images shows the location of lobe front edge. The isosurfaces represent: the KH vortex with $\lambda_2 = O(-10^{10})$ (gray), the crest hairpin with $\lambda_2 = O(-10^{11})$ (green), and the trough hairpin with $\lambda_2 = O(-10^{11})$ (red).

panel of this figure, and the λ_2 isosurfaces (vortex filaments) are depicted in the left panel. In the beginning of the process (Figure 4.33a), the KH vortex (gray tube) and the crest hairpin filament (green tube) are completely spanwise oriented (in the y-direction). The braid hairpins (thinner green tubes) are also primarily spanwise with some undulations and are half

a wavelength (180°) out of phase with respect to the crest hairpins in y. This is consistent with the findings of Jarrahbashi et al. [34] for non-homogeneous round jets, and Danaila et al. [15] for like-density jets. At 16 μs, the KH vortices stretch more; the hairpins on the braid also collect into the crest hairpin and manifest higher undulations (green isosurface in Figure 4.33b). The trough vortex (red isosurface), which was first seen in Figure 4.27(b) (indicated by black arrow) also manifests at this time. Both the green and the red vortex filaments slide underneath the KH roller at the spanwise wave crest (lobe crest), and wrap over it at the spanwise wave trough (lobe sides). The wave front has been marked with solid black line in Figure 4.33 to help find the location of the lobe crest and trough with respect to the vortices. The KH roller in this process is more stretched than the other two mechanisms (compare Figure 4.33 with Figures 4.11 and 4.20).

The vortices become streamwise near the braid in both spanwise crest and trough at 26 μs (Figure 4.33c). Except for the tip of the KH roller, which is still spanwise, the rest of the vortex structures are nearly streamwise-oriented. Both the green and the red hairpins wrap around the KH vortex on top of each other (see Figures 4.29a and 4.33c). As the vortices get stretched in the streamwise direction, the lobes follow their shape and get thinner in the spanwise direction because of the induced gas flow by the hairpin legs; compare the shape of the lobes with that of the KH vortex just downstream of the lobe in Figure 4.33(c) to observe their similarity. A neck starts to form on the lobe edge right between the two hairpins on the two sides of the lobe. This completely follows the mechanism introduced in Figure 4.29.

Figure 4.34 shows the cascade and deformation of the vortex filaments in the period 6 μs – 52 μs. The λ_2 isosurfaces are colored by the streamwise velocity contours here. The vortices start from a spanwise orientation and gradually turn streamwise. The vortex structures cascade from thick and uniform vortices to thin and chaotic structures as they stretch. The gradual departure of the vortices away from the liquid surface is also shown in this figure, where the KH roller, indicated by the white arrow, starts on the liquid surface at

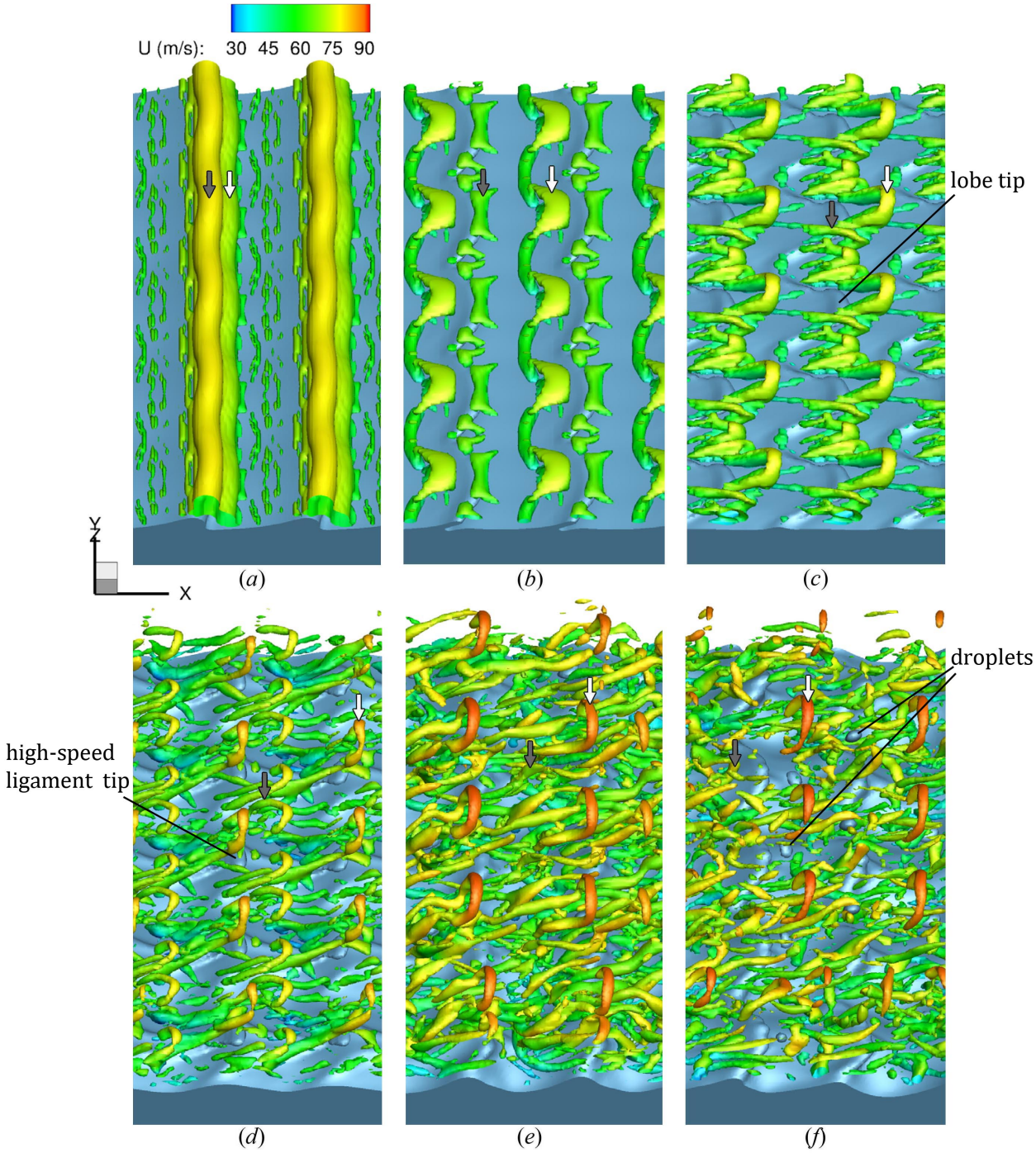

Figure 4.34: Temporal evolution of the vortices indicated by the λ_2 iso-surface colored by the streamwise velocity contours, at $t = 6$ μs (a), 16 μs (b), 26 μs (c), 40 μs (d), 48 μs (e), and 52 μs (f) of Case D1a. The liquid surface is shown in blue. The arrows refer to the vortices denoted in Figures 4.26–4.30.

6 μs (Figure 4.34a) and advects away from the interface as it gets streamwise due to the self-induction process described in Figure 4.32.

At 40 μs (Figure 4.34d), almost all of the vortex structures have become streamwise except for a short section at the tip of the KH roller. This confirms that the vortices become streamwise-oriented as they get close to the saddle point. Meanwhile, the vortices cascade into smaller structures due to turbulence; compare Figures 4.34(c) and 4.34(d). As the legs of the hairpins get closer to each other, the mutual-induction of the legs lifts the hairpins in the normal direction (Figure 4.32), and locates the hairpins above the lobes. The lobes get thinner as the streamwise counter-rotating legs induce a gas flow in the spanwise direction towards the lobe midplane, squeezing the lobe and transforming it into a ligament. Ligament creation is strongly correlated with its local velocity field, and is induced by the local shear, as indicated by Shinjo & Umemura [80]. Nearby vortices determine the ligament formation direction. Spanwise vortices form ligaments normal to the injection direction, i.e. spanwise, and streamwise vortices form ligaments parallel to the injection direction; i.e. streamwise. The influence of the vorticity field on the ligament orientation is consistent with the findings of Shinjo & Umemura [80]. Following the streamwise-oriented hairpin vortices in the *LoLiD* process, mostly streamwise ligaments form in Domain I.

Velocity contours in Figure 4.34(e) show that the streamwise velocity of the vortices increases at higher z-levels. This can be clearly seen from the gradient of colors from green (50 m/s) – near the liquid surface – to red (90 m/s) – at the tip of the KH vortex. The liquid surface also experiences a similar velocity gradient, where the velocity at the tip of the lobe is higher compared to its root; i.e. where the lobe connects to the liquid sheet. This velocity gradient manifests how the lobe elongates under the streamwise strain and forms the ligament. The ligaments finally pinch-off and create droplets, as shown in Figure 4.34(f). The ligament pinch-off follows the short-wave breakup mode introduced by Shinjo & Umemura [80]. The ligament acts as a very small round liquid jet emanating from the sheet surface. The ligament tip pressure is high in the beginning and contracts due to surface tension and pushes the inner part along the ligament axis (Figure 4.35a). This motion emanates compression waves in the upstream direction and a neck forms. The tip bulb grows as it absorbs the liquid

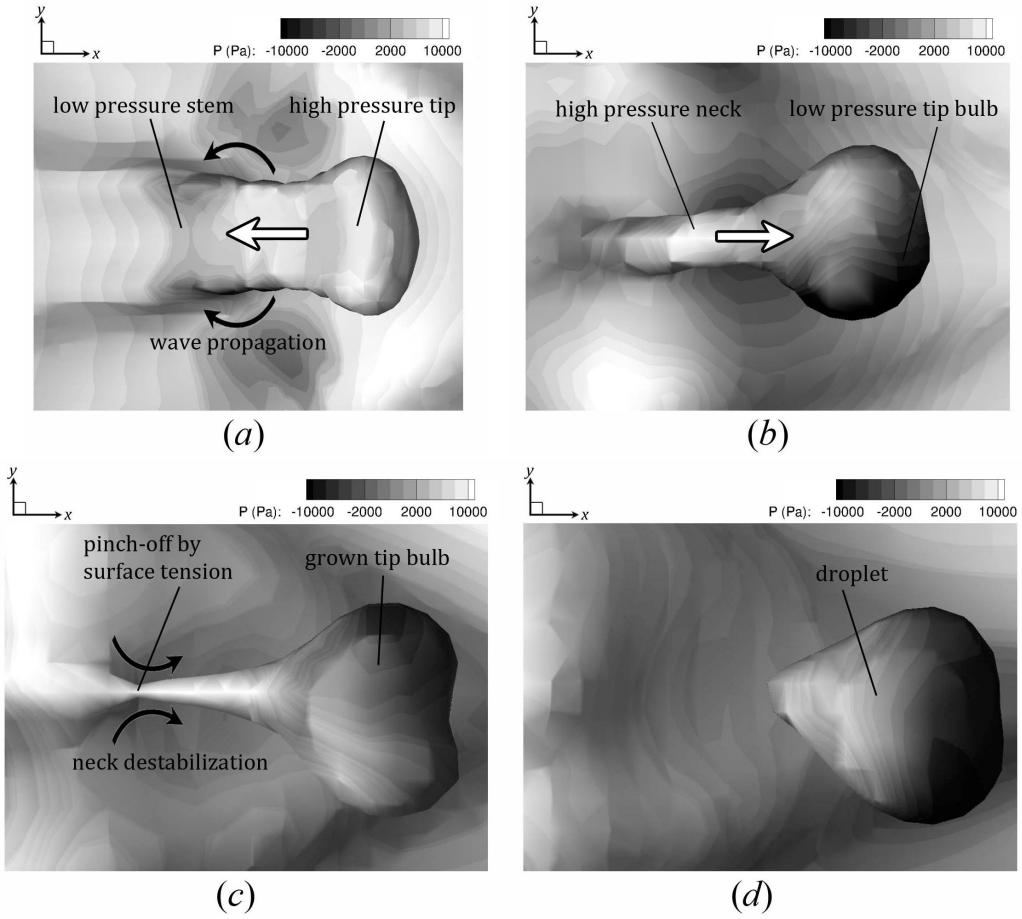

Figure 4.35: Pressure contours on the surface of a ligament at $t = 42$ μs (a), 44 μs (b), 45 μs (c), and 46 μs (d) of Case D1a, showing the ligament pinch-off following the short-wave breakup mode.

from the upstream liquid sheet by contraction (Figure 4.35b). As the tip bulb size grows, its inner pressure drops. Consequently, the tip bulb sucks the liquid further from the neck, as shown in Figure 4.35(b) – causing the neck to become narrower. When the neck becomes thin enough and its pressure high enough, the circumferential surface tension cuts the neck and a droplet pinches off (Figure 4.35c). This process reiterates from the beginning, and the next droplets pinch off identically. The droplets fly away from the interface under the vortex induction and gain a higher velocity than the liquid sheet; therefore, the droplets advect downstream with respect to the jet (Figure 4.34f).

The vortex structures and lobe deformation at low $\hat{\rho}$ (Case D1b) are shown in Figure 4.36.

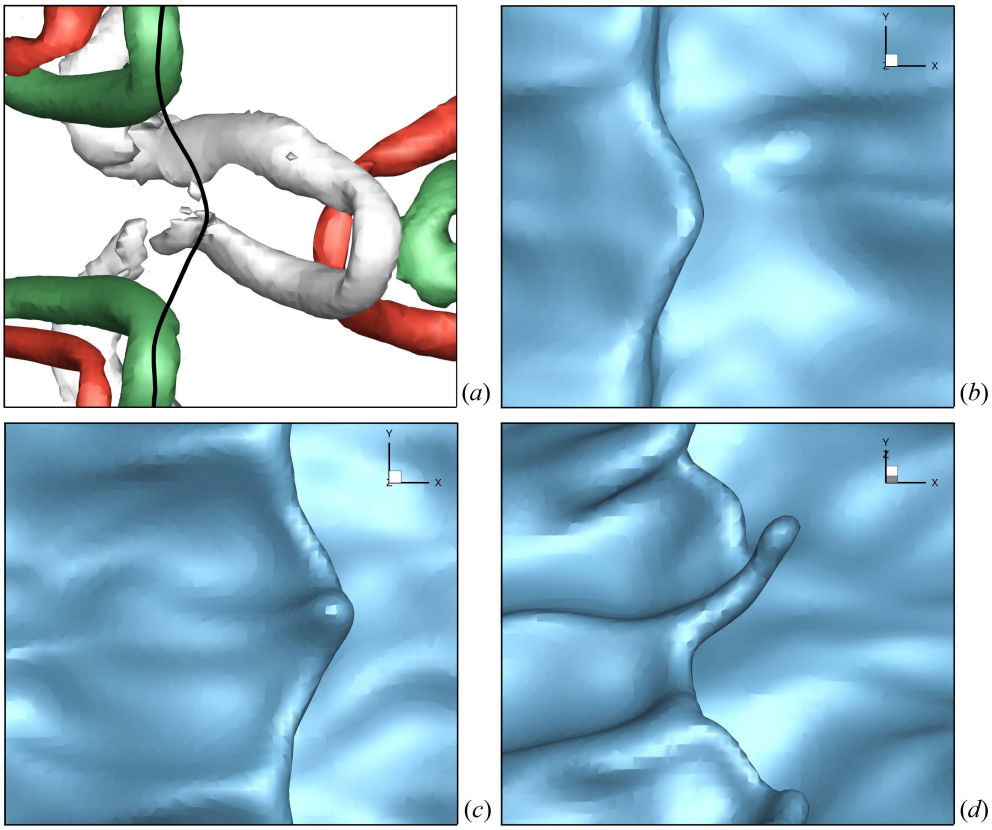

Figure 4.36: λ_2 isosurface in a top close-up view of a liquid lobe in Domain I at low density ratio (Case D1b) at 16 μs (a); the solid black line shows the lobe front edge. The isosurfaces represent: the KH vortex with $\lambda_2 = -10^{11}$ s^{-2} (gray), the outer crest hairpin with $\lambda_2 = -2 \times 10^{11}$ s^{-2} (green), and the inner trough hairpin with $\lambda_2 = -3 \times 10^{11}$ s^{-2} (red). Lobe surface showing the corrugation formation from a top view at 16 μs (b), 18 μs (c), and a 3D view at 22 μs (d) of Case D1b.

The lattice made by the KH vortex and the hairpin vortices is very similar to what was proposed in Figure 4.29 for high density ratios. The only difference being that as gas density decreases, the KH vortices are less bound to the liquid and depart from the interface much easier and meanwhile stretch in both streamwise and normal z-directions (Figure 4.36a). All the vortices in Figure 4.36(a) exist in the gas zone and above the liquid interface. Following this vortex deformation, the lobe is squeezed and thinned in the spanwise direction, while being stretched and lifted by the KH vortex normally outward. This causes the ligaments to protrude farther and faster in the normal direction (Figure 4.36d) compared to higher $\hat{\rho}$. This figure also proves that the vortex deformation leads the surface deformation, and not

the other way around.

As will be discussed in Section 4.2.5, when $\hat{\rho}$ gets higher, i.e. higher We_g, the vortices are closer to the interface and are less stretched, and more spanwise rather than streamwise oriented. Hence, the gas flow that is induced by the KH vortex shears the lobe from its top and bottom sides. In this scenario, the lobe thins in the normal direction instead of the spanwise direction, as shown schematically in Figure 4.37(a). The blue curly arrows illustrate the qualitative streamlines in this situation, and the red straight arrows denote the direction of lobe squeeze. The shear due to the gas flow induced by the spanwise vortices stretches the lobe in streamwise direction and thins the lobe and makes it more vulnerable to puncture. This is consistent with the map in Figure 3.2; as We_g increases, the breakup mechanism shifts from $LoLiD$ to $LoHBrLiD$.

At lower $\hat{\rho}$ and lower We_g (Domain I), the vortices are more stretched in the streawise direction. In this domain ($LoLiD$ mechanism), the streamwise legs of the hairpin vortex on the two sides of the lobe induce a gas flow in the spanwise direction towards the lobe midplane, which squeezes and thins the lobe in the spanwise direction and transforms it into a thick ligament, as shown schematically from the top view of a lobe in Figure 4.37(b). A neck forms at the location of the red arrows. The induced motion of the hairpin legs also lifts the lobe in the z-direction. Eventually, the ligament pinches off at the neck and a droplet

Figure 4.37: Schematic showing the lobe thinning in the normal direction in the $LoHBrLiD$ process from a xz plane (a), and lobe thinning in the spanwise direction in the $LoLiD$ process from a xy plane (b).

forms following the short-wave mode discussed above.

In summary, whether the lobe thins in the z-direction and perforates or thins in the y-direction and forms a ligament depends on the orientation of the vortices in the vicinity of the lobe. The spanwise vortices result in hole formation and spanwise bridges, while streamwise vortices result in spanwise lobe compression and streamwise ligament stretching.

4.2.5 Streamwise vorticity generation

The streamwise vorticity (ω_x) is crucial in initiation of the three-dimensional instability on liquid jets. ω_x generation via vortex stretching and vortex tilting – i.e. strain-vorticity interactions – and baroclinic effects are studied in this section for a low density ratio of 0.05 and a high density ratio of 0.5. The contributions of the different terms in the vorticity equation to ω_x generation are compared at two distinctly different density ratios, to understand the role of $\hat{\rho}$ in the liquid-jet breakup. Specifically, the generation of the three-dimensionality on the liquid sheet interface is addressed in this section. Jarrahbashi & Sirignano [33] performed a similar analysis for the round jet at several different density ratios. They showed for a $\hat{\rho}$ of 0.01 that the baroclinic effect, i.e., the Rayleigh-Taylor (RT) instability, is the dominant cause of the initiation of 3D structures. This is consistent with the suggestion of Marmottant & Villermaux [55] who performed their experiment at lower pressures and gas density. However, for a $\hat{\rho}$ of 0.1 or greater, Jarrahbashi & Sirignano [33] showed that the azimuthal tilting and radial tilting of the ring vortices are the dominant effects in streamwise vorticity generation.

The complete vorticity equation is

$$\frac{\mathrm{D}\boldsymbol{\omega}}{\mathrm{D}t} = (\boldsymbol{\omega}\cdot\boldsymbol{\nabla})\mathbf{u} - \boldsymbol{\omega}(\boldsymbol{\nabla}\cdot\mathbf{u}) + \boldsymbol{\nabla}\times\left(\frac{\boldsymbol{\nabla}\cdot\boldsymbol{\tau}}{\rho}\right) + \frac{1}{\rho^2}\boldsymbol{\nabla}\rho\times\boldsymbol{\nabla}p + \boldsymbol{\nabla}\times\boldsymbol{F_\sigma}, \tag{4.1}$$

where $\mathbf{u}$ and $\boldsymbol{\omega}$ are the velocity and vorticity vectors, respectively. $\boldsymbol{\tau}$ is the viscous stress tensor, and $\boldsymbol{F_\sigma}$ is the surface tension force. Since the fluids are incompressible in this study, the second term on the right hand side is zero. A simple dimensional analysis shows that the viscous diffusion term (the third term on the right hand side) scales as $\mu U/\rho\Delta^3$, which for a typical case considered in our study, e.g. $\mu = O(10^{-3})$ kg/(m.s), $U = O(10)$ m/s, $\rho = O(10^3)$ kg/m^3, and a mesh size of $\Delta = 2.5$ μm, gives a magnitude of $\approx O(10^{10})$ s^{-2}. The surface tension term (the last term) scales as $\sigma\kappa/\rho\Delta^2$; which for a typical case with $\sigma = O(10^{-2})$ N/m, and a radius of curvature of 100 μm ($\kappa = 10^4$ m^{-1}), also gives a result in the order of 10^{10} s^{-2}. As will be shown in this section, these two terms are 2 to 3 orders of magnitude smaller than the other terms in Equation 4.1, and therefore have negligible contributions to vorticity generation; thus, the rate of change of ω_x is approximately

$$\frac{\mathrm{D}\omega_x}{\mathrm{D}t} = \omega_x\frac{\partial u}{\partial x} + \omega_y\frac{\partial u}{\partial y} + \omega_z\frac{\partial u}{\partial z} + \frac{1}{\rho^2}\left[\frac{\partial\rho}{\partial y}\frac{\partial p}{\partial z} - \frac{\partial\rho}{\partial z}\frac{\partial p}{\partial y}\right], \tag{4.2}$$

where ω_x, ω_y, ω_z, and u denote the streamwise, spanwise, and cross-stream (normal) vorticities, and streamwise velocity, respectively. The terms on the right-hand-side denote streamwise stretching, spanwise tilting, normal tilting, baroclinic effect due to normal pressure gradient, and baroclinic effect due to spanwise pressure gradient, respectively. Density gradient is normal to the liquid interface: i.e. approximately in the z direction. The spanwise density gradient, i.e. $\partial\rho/\partial y$, is negligible compared to $\partial\rho/\partial z$, since the sheet cross-section remains fairly rectangular during early instability development. Yet, this term accounts for the baroclinic effect, which can deform the interface in the spanwise direction.

In the cases studied in this section, no initial perturbation is imposed on the liquid surface. Except for numerical errors which for our purpose correspond to small random physical disturbances, all terms in the ω_x generation equation (Equation 4.2) are initially zero. Namely, the first and the third terms are zero because there is no vorticity components in the x and z-directions initially, and the second term is zero since the streamwise velocity is uniform in

the spanwise direction. The baroclinic terms are identically zero since density and pressure gradients in the y-direction are initially zero.

Since the streamwise (ω_x) and normal vorticities (ω_z) cannot be generated, but can be enhanced, the main source of ω_x generation at early times is either the spanwise vorticity tilting or the baroclinic torque, which become non-zero as a result of small perturbations of u and p in the spanwise direction. This intuition is consistent with the results of Jarrahbashi & Sirignano [33] in round jets at early times, where for a wide range of $\hat{\rho}$, the baroclinic torque and the azimuthal vortex tilting terms are dominant for the first 5 μs of their computations; however, they might be overtaken later by other terms. Baroclinicity becomes more pronounced at lower density ratios, since the density gradient across the interface is higher.

In the data analysis, the gradients have been calculated and averaged over the computational interface thickness that equals three mesh points in the z and tangential directions. The terms in Equation (4.2) are:

- Streamwise vortex stretching: $\omega_x \dfrac{\partial u}{\partial x}$
- Spanwise vortex tilting: $\omega_y \dfrac{\partial u}{\partial y}$
- Normal vortex tilting: $\omega_z \dfrac{\partial u}{\partial z}$
- Baroclinic vorticity generation: $\dfrac{1}{\rho^2}\left[\dfrac{\partial \rho}{\partial y}\dfrac{\partial p}{\partial z} - \dfrac{\partial \rho}{\partial z}\dfrac{\partial p}{\partial y}\right]$

Since the peak of the streamwise vorticity occurs at the wave braids (as shown by Figure 4.43a), the absolute value of the four above-mentioned terms are averaged only at the braid region. Both top and bottom surfaces have been considered in this measurement.

Two different density ratios have been analyzed in this section. The non-dimensional characteristics of these two cases are: $Re_l = 2500$, $We_l = 14,400$, $\hat{\mu} = 0.0066$, and $\hat{\rho} = 0.05$

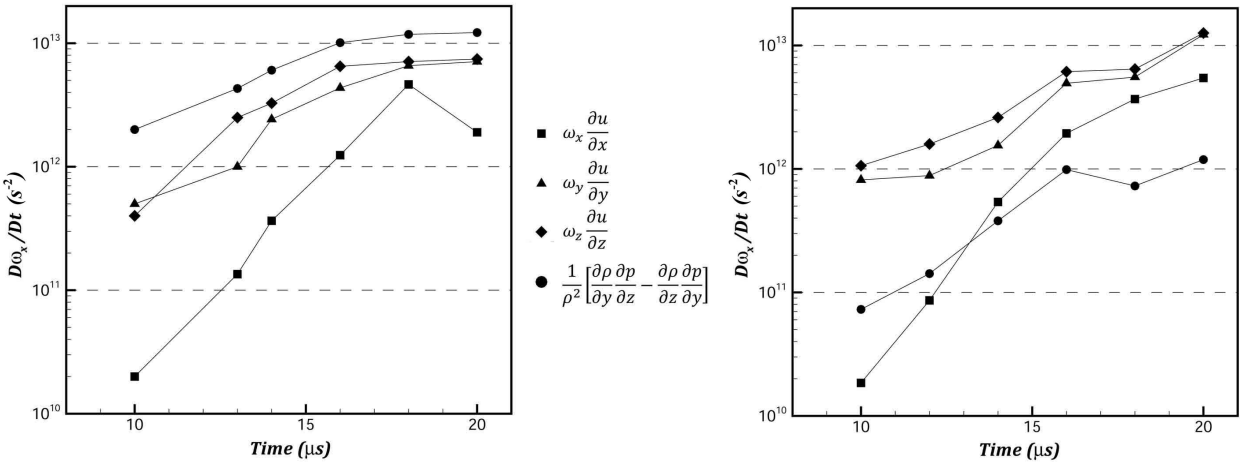

Figure 4.38: Contributions of streamwise vortex stretching (squares), spanwise vortex tilting (triangles), normal vortex tilting (diamonds), and baroclinicity (circles) to the generation of ω_x at the liquid surface for two density ratios; $Re_l = 2500$, $We_l = 14,400$, $\hat{\mu} = 0.0066$; $\hat{\rho} = 0.05$ (left), and $\hat{\rho} = 0.5$ (right).

and 0.5. The sheet thickness is $h = 50$ μm, and no initial perturbation is imposed on the liquid-gas interface.

Figure 4.38 shows the contribution of each term in the generation of ω_x for the high and low density ratios, in the first 20 μs. Baroclinicity (circles) is the most important factor at low density ratio, since the density gradient normal to the interface is higher, and also the local density in the gas zone near the interface is lower (see the baroclinic vorticity generation expression given above). However, at high $\hat{\rho}$, baroclinicity is the least significant. Baroclinicity is only slightly larger than the streamwise stretching (squares) in the beginning of the computations for high $\hat{\rho}$, but it is outrun by this term at about 13 μs and remains the lowest of all terms thence. The baroclicinc vorticity generation term is an order of magnitude smaller than the vortex stretching and tilting terms at the end of the computations.

In both low and high density ratios, the spanwise and normal tilting seem to be more important than the streamwise stretching for the first 20 microseconds. The spanwise tilting is high because the initially spanwise vortex lines are gradually tilted in the streamwise direction. The normal tilting is also high since the velocity gradient is much higher in the

normal direction ($\partial u/\partial z$), in the beginning of the computations. The streamwise stretching however has the highest growth rate and almost reaches the magnitude of vortex tilting at about 20 μs. Later on, as ω_x grows, the vortex stretching becomes more significant. These results are consistent with the findings of Jarrahbashi & Sirignano [33] for round liquid jets. Jarrahbashi & Sirignano [33] also concluded that, generally, the importance of baroclinic vorticity generation (RT instability) has been overemphasized in the literature, especially at very high pressures, and other important aspects of vorticity dynamics and similarities with injection into an alike fluid have been neglected. As described by them and also evident in our figures, the vortex tilting terms are the largest at early times; however, new findings show some cancellations, discussed below.

Figures 4.39 and 4.40 show the contours of the four ω_x generating terms at 13 μs, on a y-plane and x-plane, respectively. The spanwise and normal vortex tilting terms (Figures 4.39b,c and 4.40b,c) are stronger than the streamwise stretching, but with opposite signs. As demonstrated in Figure 4.38, the two vortex tilting terms are also nearly equal. A closer look at their equations explains the reason:

$$\omega_y \frac{\partial u}{\partial y} = \boldsymbol{\frac{\partial u}{\partial z}\frac{\partial u}{\partial y}} - \frac{\partial w}{\partial x}\frac{\partial u}{\partial y}, \tag{4.3}$$

$$\omega_z \frac{\partial u}{\partial z} = \frac{\partial v}{\partial z}\frac{\partial u}{\partial z} - \boldsymbol{\frac{\partial u}{\partial y}\frac{\partial u}{\partial z}}. \tag{4.4}$$

The two terms in bold font are exactly the same but have opposite signs. Thus, the only difference in the magnitudes of the spanwise and normal tilting comes from the other terms (the second term in Equation 4.3 and the first term in Equation 4.4). However, since these terms deal with gradients of v and w of $O(1)$, which are two orders of magnitude smaller than u of $O(10^2)$, they are much smaller than the boldface terms, at the beginning of the

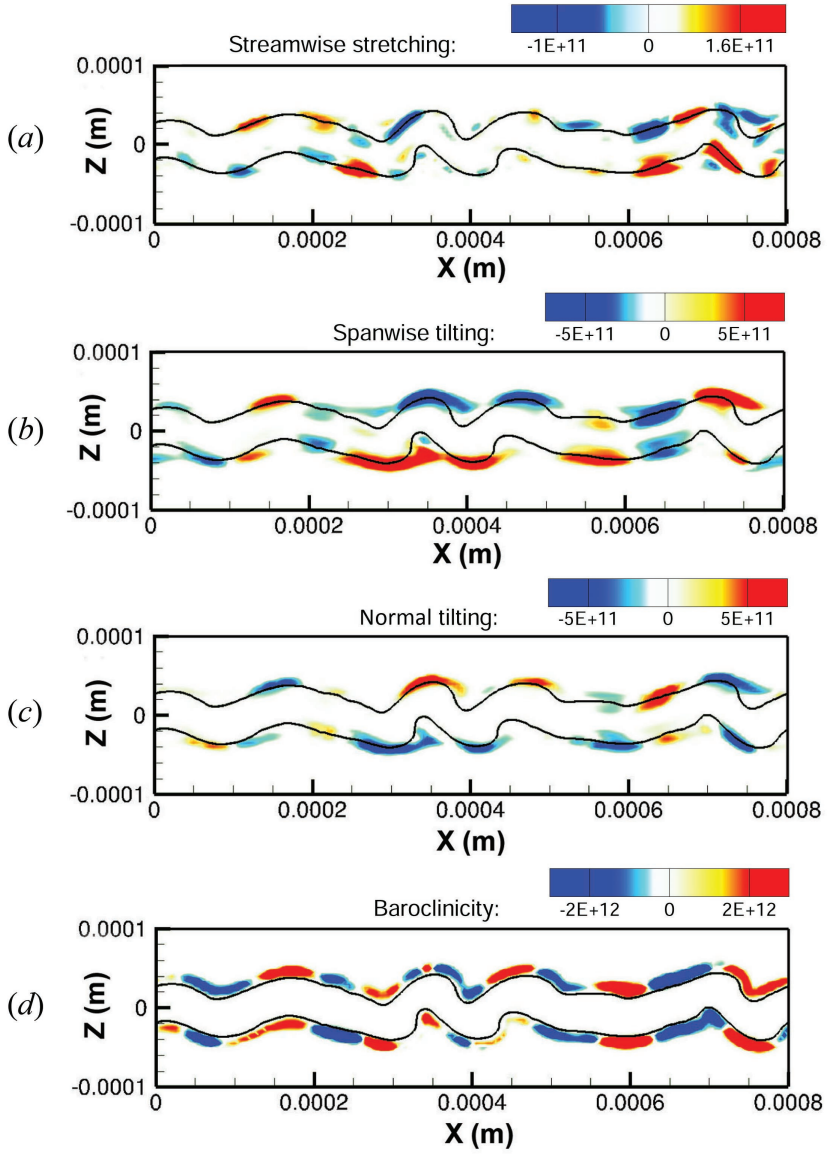

Figure 4.39: Contours of streamwise vortex stretching (a), spanwise vortex tilting (b), normal vortex tilting (c), and baroclinic generation (d) on a y-plane at $t = 13$ μs for $\hat{\rho} = 0.05$; $Re_l = 2500$, $We_l = 14,400$, $\hat{\mu} = 0.0066$.

computations. Thus, the deviation of the vortex tilting terms from the boldface terms is very small, and the two terms nearly cancel each other early on. Based on this, our earlier conclusion (and also that of Jarrahbashi & Sirignano [33]) should be modified: the spanwise and normal vortex tilting terms, even though the largest among the ω_x generating terms, are not the most important in ω_x generation, since they nearly cancel each other. The streamwise vortex stretching and baroclinic effects (RT instability) are the most important

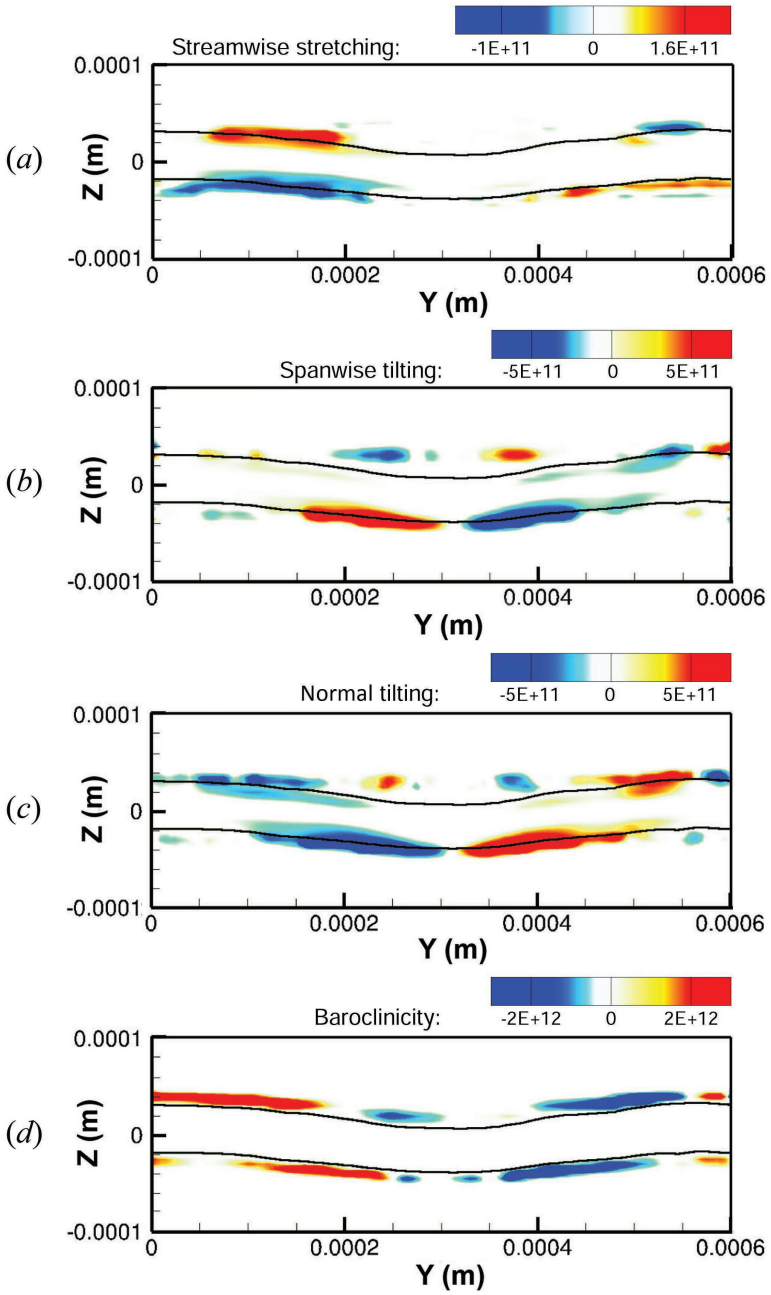

Figure 4.40: Contours of streamwise vortex stretching (a), spanwise vortex tilting (b), normal vortex tilting (c), and baroclinic generation (d) on a x-plane at $t = 13$ μs for $\hat{\rho} = 0.05$; $Re_l = 2500$, $We_l = 14,400$, $\hat{\mu} = 0.0066$.

in generation of ω_x, at high and low density ratios, respectively.

Figure 4.39(a) also confirms that the vortex stretching originates from the braids first, as the strain due to the adjacent primary vortical structures is highest at the saddle (braid)

and the ribs are aligned along the diverging separatrix [32]. Note that most of the colored spots in Figure 4.39(a) are on the braids and not the wave crests. This is consistent with the experimental observations of earlier researchers [4, 43, 49] for uniform-density flows. The location and direction of the stretch can also be seen in Figure 4.41, which shows the fluctuation velocity vectors relative to the average KH vortex velocity on a blown-up section of the liquid jet at 13 μs. It is evident that the saddles with the highest strain rate are on the braids between two adjacent vortices, where the fluctuation velocity vectors depart in the opposite directions. The stretch direction at the saddle point is shown by the green arrows in Figure 4.41. The saddle points are in the gas phase, close to the interface. The streamwise vortex stretching is highest at the saddle points (see Figure 4.39a), where the flow is primarily discrete ribs [32]. The fluid elements are stretched along the interface, i.e. along the diverging separatrix shown by the green arrows, and compressed normal to the interface at the saddle points. The center of the spanwise vortices (rolls) are at the

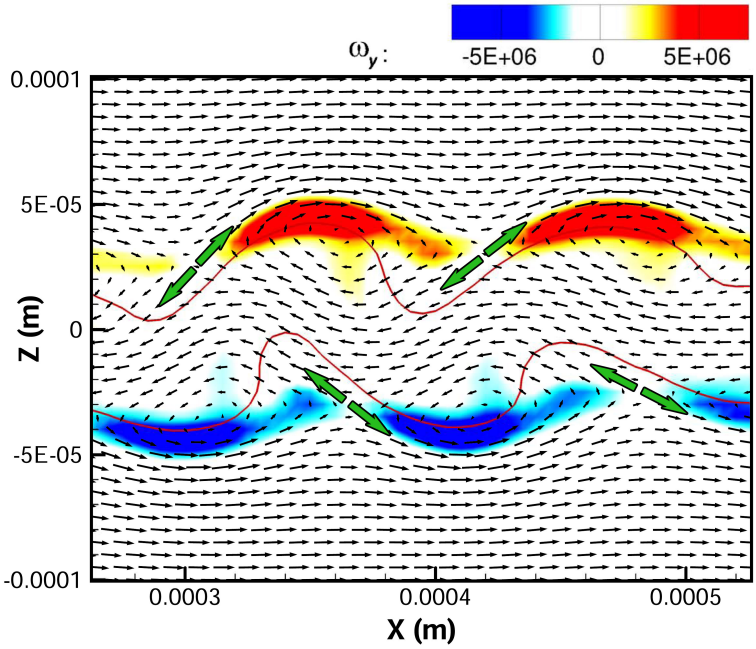

Figure 4.41: Perturbation velocity vectors superimposed on ω_y contours at $t = 13$ μs on a y-plane; $Re_l = 2500$, $We_l = 14,400$, $\hat{\rho} = 0.05$, and $\hat{\mu} = 0.0066$. Green arrows denote the maximum stretch along the diverging separatrix. The liquid-gas interface is indicated by the red line.

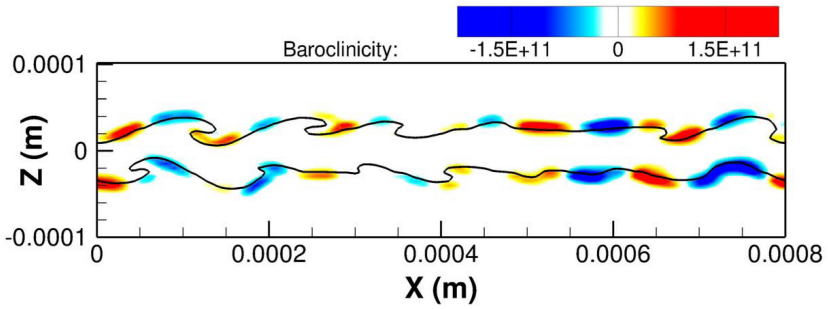

Figure 4.42: Contours of baroclinicity on a y-plane at $t = 13$ μs for $\hat{\rho} = 0.5$; $Re_l = 2500$, $We_l = 14,400$, $\hat{\mu} = 0.0066$.

crest of the interface waves, as denoted by the velocity vectors and the vorticity contours. Interestingly, the vorticity peak coincides with the interface at the crests, but not at the troughs, where the vorticity has migrated into the gas phase further away from the interface. Note that the vorticity contours look like crescents and not circular as the vorticity is not uniformly distributed as in a vortex column (like the typical Oseen vortex; see Ref. [67]); the non-centric vorticity distribution is due to the curved KH rollers.

The stretching and tilting terms are centered at the interface (see Figures 4.39*a*–*c* and 4.40*a*–*c*), but the baroclinic torque term $\frac{1}{\rho^2}\boldsymbol{\nabla}\rho \times \boldsymbol{\nabla}p$ is always larger in the gas phase (see Figures 4.39*d* and 4.40*d*). Baroclinic generation, being proportional to $1/\rho^2$, is two orders of magnitude larger in the gas phase compared to the liquid phase (for $\hat{\rho} = 0.05$). As $\hat{\rho}$ increases, the difference between the gas and liquid densities decreases; thus, the contours of baroclinicity get closer to the liquid interface. This is seen in the baroclinicity contours of $\hat{\rho} = 0.5$ in Figure 4.42. Since $\hat{\rho}$ is an order of magnitude higher than that of Figure 4.39(d), the local density in the gas zone is much higher, hence the baroclinicity in the gas is lower and closer to its value in the liquid. Thus, the contours are closer to the interface (compare Figures 4.42 and 4.39*d*). This contributes to the ω_x peak being closer to the interface and growing larger compared to the low density ratios, hence creating and stretching more lobes at higher density ratios. Also, the peak of baroclinic torque is an order of magnitude smaller in Figure 4.42 compared to Figure 4.39(d), since the density gradient normal to the interface

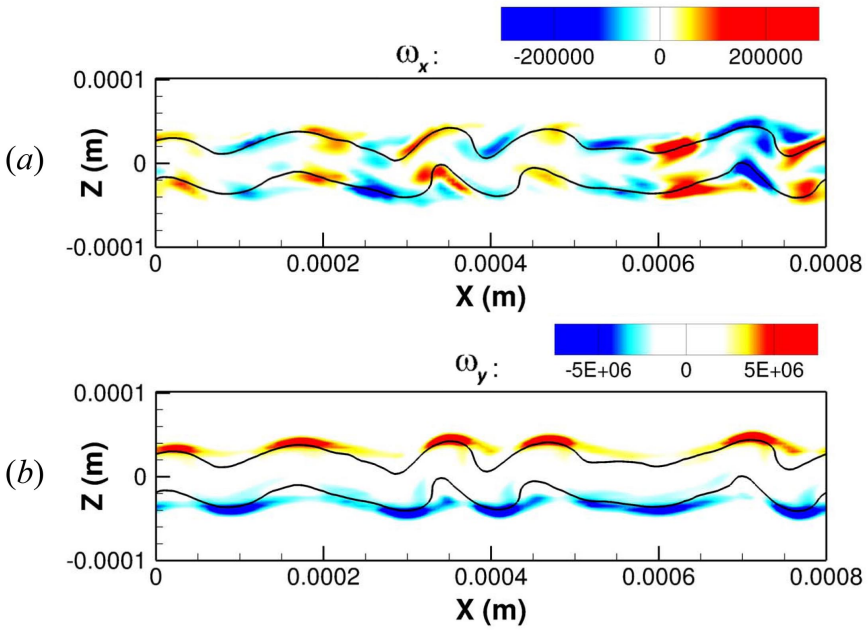

Figure 4.43: Contours of streamwise vorticity ω_x (a), and spanwise vorticity ω_y (b) at $t = 13$ μs for $\hat{\rho} = 0.05$; $Re_l = 2500$, $We_l = 14,400$, $\hat{\mu} = 0.0066$.

is lower at higher density ratios.

As shown in Figure 4.39(d), the baroclinicity contours change sign (i.e. color) continuously in x. This pattern is very similar to the hairpin pattern seen in the ω_x contours presented by Jarrahbashi & Sirignano [33]. The ω_x and ω_y contours for the current case are illustrated in Figure 4.43. Comparison of the contours of ω_x and baroclinicity (compare Figures 4.43a and 4.39d) shows that they follow a very similar pattern. Hence, we can conclude that baroclinicity is the most important factor in creation of the hairpin vortex structure at low $\hat{\rho}$. The role of the baroclinic torque in deformation of the surface waves in a stratified shear layer is studied in detail by Schowalter et al. [78], and is consistent with our results. The vector field of Figure 4.41 shows that ω_x and ω_y are highest at the braids and wave crests, respectively. This is also evident in the vorticity contours of Figure 4.43.

In order to understand how fast the liquid sheet deforms and manifests 3D instabilities, the magnitudes of the vorticity components are examined through time. The 3D instabilities are directly related to the magnitudes of ω_x and ω_z against ω_y, which exists from the begin-

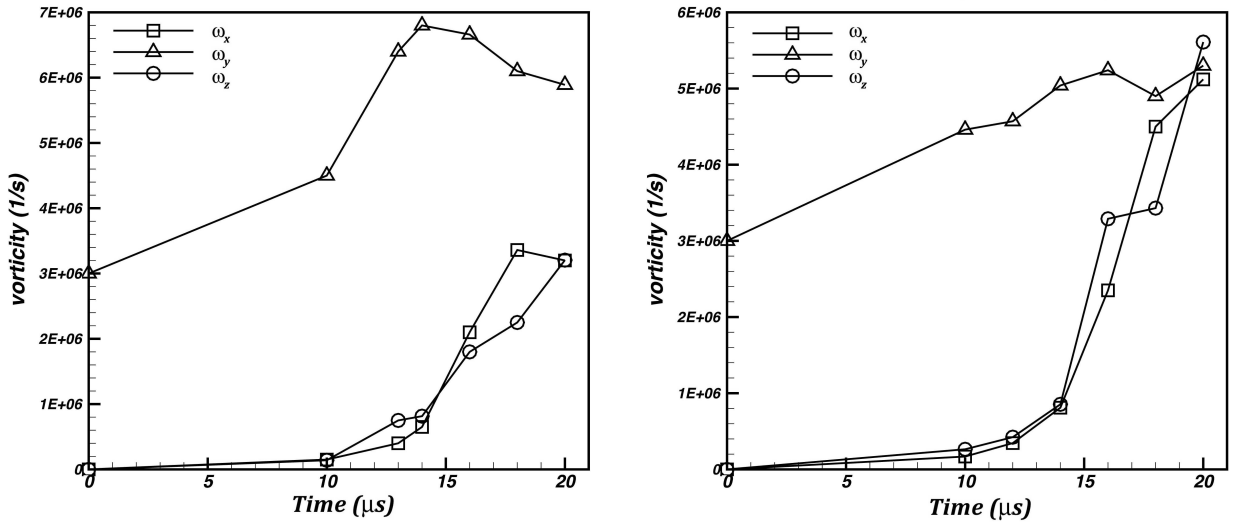

Figure 4.44: Temporal variation of the vorticity components for $Re_l = 2500$, $We_l = 14,400$, $\hat{\mu} = 0.0066$; $\hat{\rho} = 0.05$ (left), $\hat{\rho} = 0.5$ (right).

ning when the flow is still 2D. As mentioned earlier by Jarrahbashi & Sirignano [33], and Jarrahbashi et al. [34] the streamwise vorticity is the main cause of the 3D instabilities and interface distortion.

The absolute value of each vorticity component, averaged over the entire liquid-gas interface, is plotted in Figure 4.44 for low and high density ratios. The spanwise vorticity ω_y (KH vortex) is the only component that exists initially. In both cases, ω_y grows for a certain time, until about 15 μs, and then onward keeps more or less the same order of magnitude. The spanwise vorticity is larger for lower $\hat{\rho}$.

ω_x and ω_z grow very slowly up to 10 μs, after which, there is a sudden increase in their growth rate. In both cases, ω_x and ω_z are of the same order of magnitude, which indicates that initially spanwise vortex filaments are lifted in the normal direction and tilted in the streamwise direction at almost equal rates. The growth rate of ω_x is higher at higher $\hat{\rho}$. ω_x reaches the same order of magnitude as ω_y at $t = 20$ μs, for the high $\hat{\rho}$. For the lower $\hat{\rho}$, however, the growth is slower. Hence, three-dimensionality manifests sooner at higher gas densities. For $\hat{\rho} = 0.05$, the magnitude of ω_x and ω_z are still half of ω_y at 20 μs; notice that ω_y

always remains much higher. Thus, ω_y is still dominant and 2D deformations build up while the streamwise vorticity grows. ω_x growth has consequent impacts on the surface dynamics. In order to understand this, the liquid surface has been compared at two instances for both low and high density ratios in Figure 4.45. The boxes in this figure show the computational domain edges. The boundary remains far away from the liquid surface; hence the results are not influenced by the domain size.

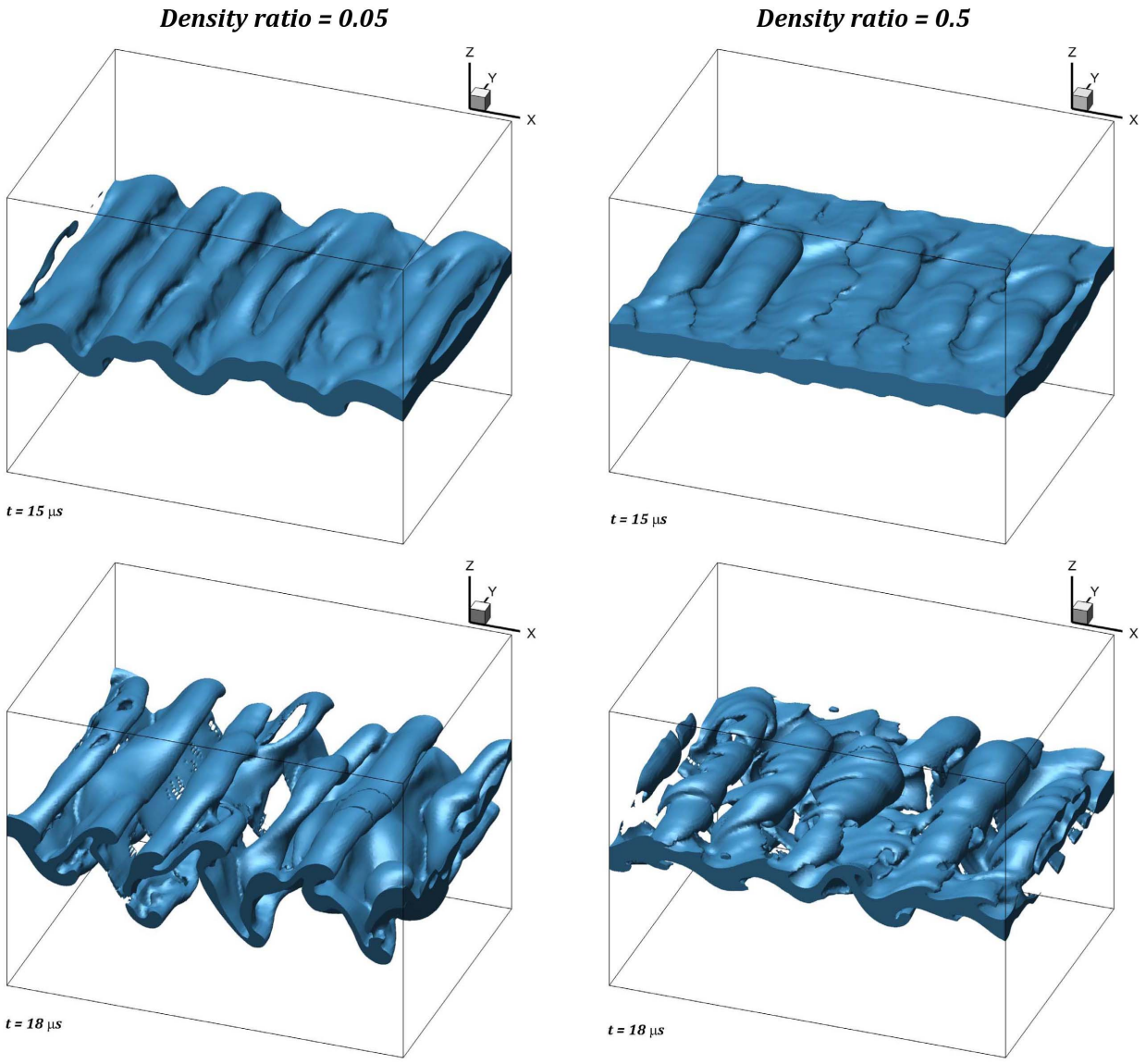

Figure 4.45: Liquid-gas interface at $t = 15$ μs (top) and 18 μs (bottom) for $Re_l = 2500$, $We_l = 14,400$, $\hat{\mu} = 0.0066$; $\hat{\rho} = 0.05$ (left), $\hat{\rho} = 0.5$ (right).

The higher ω_x growth rate at high $\hat{\rho}$ causes the liquid surface to undergo 3D instabilities faster, and there are more streamwise lobes seen at high $\hat{\rho}$ than at low $\hat{\rho}$. At 15 μs, the surface of the sheet with $\hat{\rho} = 0.05$ is still roughly 2D, while the high $\hat{\rho}$ case manifests more 3D deformations, and streamwise lobes are apparent on top of the primary KH waves. On the other hand, the higher ω_y compared to ω_x at low $\hat{\rho}$ causes the liquid sheet to become antisymmetric much faster (compare the top images of Figure 4.45). Recall that as explained in Section 4.2.2, transition towards antisymmetry expedites when the two vorticity layers – on top and bottom surfaces – become stronger, as ω_y grows.

The difference in the vorticity dynamics between the two cases has significant effects on the characteristics of the jet instabilities. As can be seen at $t = 18$ μs (Figure 4.45), the low $\hat{\rho}$ case can be characterized by roll-up of the KH waves, which creates more spanwise-aligned liquid structures and fewer stretched lobes; the entire sheet thins faster, and the liquid sheet breaks sooner. On the other hand, at high $\hat{\rho}$, the liquid structures orient streamwise more and manifest more lobes. The lobes are more stretched and thinned due to the larger ω_x of the KH vortex legs and are more prone to perforation. Hence, the hole-formation mechanism is expected to prevail over a larger area in the parameter space of We_l versus Re_l, at higher $\hat{\rho}$. This is consistent with the zones in Figure 3.2, and is in accordance with the density ratio effects discussed in Chapter 3 [97].

The top and bottom liquid surfaces tend towards an antisymmetric mode, whether we start with a flat surface or symmetric perturbations. The antisymmetric behavior is eventually favored since a planar jet is more unstable to the antisymmetric mode than the symmetric mode in the parameter range of interest. The transformation towards antisymmetry occurs sooner as density ratio is lowered.

Marmottant & Villermaux [55] "suggest" that, for a coaxial round jet, the transverse (azimuthal) deformation of the wave crests depends on surface tension (We_g), density ratio, and thickness of the vorticity layer. They propose the possibility that the transverse insta-

bility of the wave crest is the result of lobe and ligament formation due to opposing shear and surface tension. Unsteady motions at the sheet rim confer transient accelerations to the liquid perpendicular to the liquid-gas interface, which trigger a RT type of instability, producing indentations of the rim, which later result in ligaments.

In a physically different configuration for leading rim of a transient liquid sheet, Agbaglah et al. [2] also propose that the dynamics of a receding liquid sheet initiates a RT instability due to surface tension. They show that the growth rate of this transverse RT instability increases as the liquid sheet decelerates. Hence, they suggest that this instability is dominant at low We_g, where the deceleration is strong enough so that the retraction forces overcome the liquid/gas inertia. Our mechanisms for the lobe and ligament formation – via vortex interactions – would not be in effect for a configuration where the oppositely-oriented hairpin pairs do not exist – such as the leading rim of a liquid sheet studied by Agbaglah et al. [2]. Our results here do not indicate that capillary action plays a major role in the deformation of the crest rim to create 3D structures, e.g., lobes, corrugations and ligaments. Once ligaments are formed, capillary action becomes important.

4.2.6 Vortex dynamics of round jets

In this section, a qualitative comparison is made between the vortex dynamics of the planar jets (studied here) and round jets (from previous studies) to show that the causes of different liquid structures, e.g. lobes, holes, corrugations, and ligaments, are the same from the vortex dynamics perspective. For this purpose, the round liquid jet computational analysis of Jarrahbashi et al. [33, 34] are mainly incorporated, which are most pertinent to our vortex dynamics analysis. In a few cases, numerical results of Shinjo & Umemura [80] are also addressed.

Jarrahbashi & Sirignano [33] used the vorticity dynamics to explain the formation of lobes

and ligaments in their computations. They mainly used the vorticity contours and the vortex lines projection on the liquid surface in their analysis. Even though the explanation for the hole and corrugation formation was less detailed in their analysis, the vortex dynamics related to lobe formation and ligament elongation in their round jets is very similar to our findings. Similar to the planar jets, Jarrahbashi & Sirignano [33] and many researchers before them [5, 49, 56, 80] observed the origination of the streamwise vorticity in the braid region of the round jet first. Later, as the vortices stretch in the streamwise direction, counter-rotating streamwise vortex pairs are formed. These are shown to be 3D hairpin vortices that wrap around the KH rollers. The streamwise vorticity in the ring originates from the upstream braid adjacent to the ring. The hairpin vortex in the ring region is 180° (half wavelength) out of phase with respect to that of the braid region, similar to what we observed in our planar sheet. The lobe locations on the cone crests is correlated with locations of the hairpin vortices in the ring (crest) region.

A very similar mechanism involving hairpin vortices is proposed by Jarrahbashi & Sirignano [33] for the formation of ligaments. They show that the streamwise vorticity projection on the ligament surface changes sign inside the ligament. Therefore, counter-rotating vortex structures exist both near the lobes in the gas phase and inside the elongated ligament. The side-jet phenomenon in homogeneous jets is similar to the formation of the ligaments in two-phase jet flow based on these hairpin vortical structures. The effects of the pressure gradient on the ligament elongation and breakup is also addressed by Jarrahbashi & Sirignano [33]. The absolute value of the pressure decreases toward the center of the ligament at the smallest cross-sectional area; however, the pressure decreases radially outward at the tip of the ligament. Therefore, there is an oscillation of the pressure gradient inside a ligament that produces a waviness on its surface. According to Shinjo & Umemura [80], capillary waves in the short-wave mode propagate inside the ligament and decrease the diameter of the ligament locally. Surface tension pinches the ligament at minimum cross-sectional area. However, the large streamwise vorticity observed inside the ligament might produce

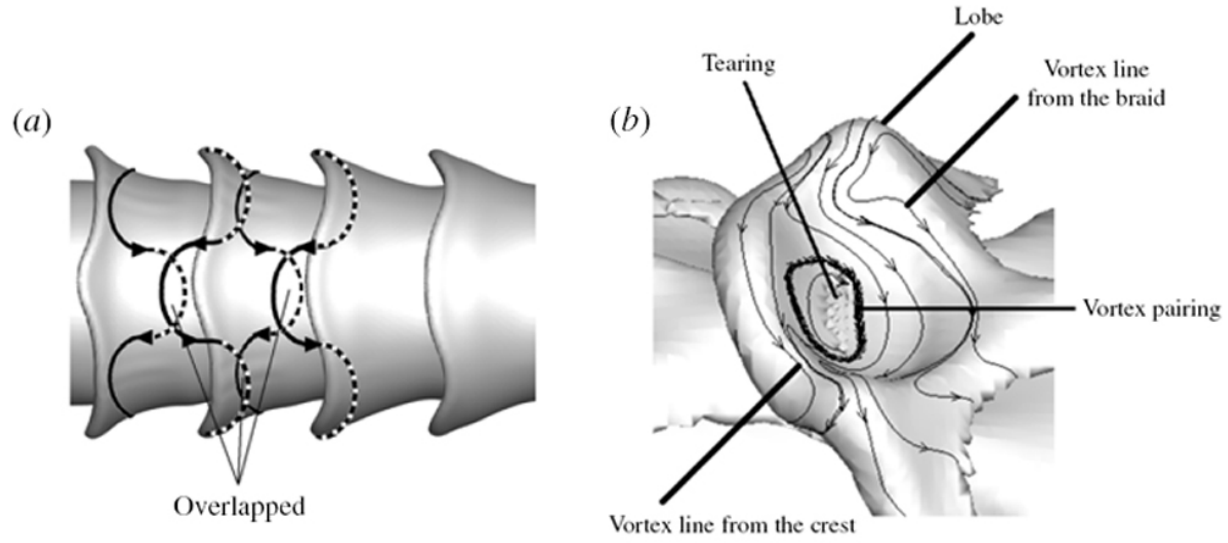

Figure 4.46: Isosurface of the liquid-gas interface accompanied by schematic of hairpin vortices on the ring and braid region (a); magnified lobe with projected vortex lines, showing two families of hairpin vortices from the braid and crest and their pairing at the center of the lobe leading to the lobe tearing and hole formation (b). $\hat{\rho} = 0.1$, $Re_l = 1600$, $We_g = 23,000$. The solid and dashed lines show hairpin portions stretching downstream and upstream, respectively. Gas flows from right to left. Recast from Jarrahbashi et al. [34].

a large angular momentum and compete with the capillary force. Jarrahbashi & Sirignano [33] define the competition between the vorticity effects and the capillary forces through a local Weber number, which is the ratio of the radial pressure gradient due to the transverse velocity difference caused by the streamwise vorticity inside the ligament and the radial pressure gradient due to surface tension, i.e. $We = \rho_l \omega_x^2 R^3/\sigma$; where R is the radius of the ligament. These two pressure gradients have different signs. If this We is much larger than one, the vorticity effects inside the ligament can be more important than the capillary force. In computations of Jarrahbashi & Sirignano [33] We is very close to unity, hence inertia can be as important as capillary forces in the ligament breakup.

In a later study, Jarrahbashi et al. [34] described the mechanism of hole and bridge formation in a round jet using the vorticity dynamics. They arrived at the same conclusion of hairpin overlapping for hole formation as described herein (Figure 4.46). However, the spanwise measure is replaced by the azimuthal angle for round liquid jets. At high Re_l of interest,

inertial effects dominate and vortex lines and material lines are almost identical. Thus, the hairpins are stretched around the braid and curled at the front of the crest following the fluid motion. In the vicinity of the lobe, the downstream stretching hairpin from the ring passes over the upstream stretching hairpin from the braid as the curling action continues, causing the phase variation sketched in Figure 4.46(a). Jarrahbashi et al. [34] also observed that the hairpin vortices approach each other and form a diamond-shaped region of the type shown by Comte et al. [11], very similar to the vortex lattice observed experimentally for single-phase planar mixing layers (see figures 3 and 4 of Comte et al. [11]). The hole formation process relates to the increase in circulation originated from the hairpin vortices that envelope the lobe and make it thinner with time, as was explained earlier. Hole formation begins on a lobe sheet where the We, based on lobe thickness and relative gas-liquid velocity, is too large for capillary action to be the initiating mechanism. As discussed earlier (Figure 4.5), where two hairpin vortices with same-sign circulation overlap, the liquid sheet between them becomes thinner because their mutual induction moves the material lines closer to the same radial position and a hole can form (Figure 4.46b).

Jarrahbashi et al. [34] express that, although the hole location can be predicted by hairpin overlap, other flow parameters, e.g. density ratio, viscosity ratio and surface tension, play a role in changing the flow details and the hole formation process. For example, when the surface area of the lobe increases and its edge curvature decreases, the locations of the holes in neighboring lobes will be closer to each other, and the holes merge to create larger holes.

The hole formation and ligament creation from the extension of the holes and tearing of the rim were observed in the computations of Shinjo & Umemura [80] for the same range of Re and We as Jarrahbashi et al. [34]. However, the lobe puncture was stated to be due to the impact of the droplets that formed earlier from the breakup of the mushroom-shaped cap on the jet core. Hence, their hole formation was inertially driven not vortically. Our temporal study produces no cap but better represents the behavior of spatial development after the

cap has moved far downstream.

Jarrahbashi et al. [34] relate the formation of small-scale corrugations to the smaller and less orderly alternating streamwise vorticity regions near the lobes for lower Re_l. However, they do not present a detailed explanation of the corrugation formation and stretching, nor do they explain the reason for such less orderly vortical structures near the ring region. Hence, even though our corrugation formation for planar jets is also related to smaller scales of the hairpin filaments (at high Re_l), this mechanism cannot be directly compared with their observations.

4.3 Conclusions

The present study has focused mainly on the vortex dynamics of planar liquid jets. A vortex has been defined using the λ_2 criterion. The relation between the surface dynamics and the vortex dynamics is sought to explain the physics of different breakup mechanisms that occur in primary atomization, by conducting DNS with LS and VoF surface tracking methods.

Vortex dynamics is able to explain the hairpins formation. The interaction between the hairpin vortices and the KH vortex explains the perforation of the lobes at moderate Re_l and high We_g, which is attributed to the overlapping of a pair of oppositely-oriented hairpin vortices on top and bottom of the lobe. The formation of corrugations on the lobe front edge at high Re_l and low We_g is also explained by the structure that hairpins gain due to the induction of the split KH vortices. At low Re_l and low We_g, on the other hand, the lobe perforation and corrugation formation are inhibited due to the high surface tension and viscous forces, which damp the small scale corrugations and resist hole formation. The hairpin vortices stretch in the normal direction while wrapping around the KH vortex. The induced gas flow squeezes the lobe from the sides and forms a thick and long ligament. In

summary, the vortex dynamics analysis helps explain the three major atomization cascades at different flow conditions. The atomization mechanisms for the planar jet are qualitatively identical to the round-jet mechanisms.

Baroclinicity is the most important factor in generation of the streamwise vortices and manifestation of 3D instabilities at low density ratios. At higher density ratios, the streamwise vortices are mostly rendered by streamwise vortex stretching. The streamwise vorticity growth is higher at higher density ratios, resulting in a faster appearance of three-dimensional instabilities. As density ratio is reduced, fewer lobes with less undulation form; hence, hole formation prevails more at higher density ratios. The relation between vortex dynamics and surface dynamics aids prediction of liquid-structure formations at different flow conditions and different stages of the primary atomization. This is very important in prediction and control of the droplet size distribution in liquid-jet primary atomization.

Chapter 5

Length-scale cascade rate and jet spread rate

As discussed in Chapter 1, the main focus of the literature has been on the final droplet-size distribution and the spatial growth of the spray (spray angle), but little emphasis has been placed on the temporal cascade of the surface length scales – growth of Kelvin-Helmholtz (KH) waves and their cascade into smaller structures leading to final breakup into ligaments and then droplets – and the spread rate of the spray (spray angle) in primary atomization. In order to better control and optimize the atomization efficiency, the transient process from the point of injection to the fully-developed state needs to be better understood. Hence the spray angle and the rate at which the length scales cascade at different flow conditions must be analyzed. This is the main focus of this chapter. The data presented herein will be crucial in the analysis and design of atomizers.

5.1 Problem description

In recent years, more computational studies have addressed the liquid-jet breakup length scales and spray width. Most of these, however, have qualitatively investigated the effects of fluid properties and flow parameters on the final droplet size distribution or the spray angle – as were introduced in Chapter 1. Only a few studies quantified the spatial variation of the droplet/ligament size along or across the spray axis. However, there are no detailed studies of the temporal variation of the liquid-structure size distribution and the spray width (spray angle) during primary atomization. Most recent computational studies [1, 22, 57, 61] analyze the spatially developing instability leading to breakup of liquid streams; however, all of them are at relatively low values of the Weber number ($We < 2000$). That is, although some of those works are described as "atomization" studies, they all fit better under the classical "wind-induced capillary instabilities" defined by Ohnesorge [59] and Reitz & Bracco [71]. Most of these studies are linear [61], 2D inviscid [57], two-dimensional [1, 22], or 3D large-eddy simulations [1]. Of course, these did not resolve the smaller structures that form during the cascade process of the breakup. An analysis with spatial development offers some advantage with practical realism over temporal analysis. At the same time, the additional constraints imposed by the boundary conditions remove generality in the delineation of the important relevant physics. For these reasons, we follow the path of temporal-instability analysis in the classical atomization (high We range) as was introduced in Chapters 3 and 4. The goal is to reveal and interpret the physics in the cascade process known as atomization. Note that some spatial development is provided when the temporal analysis covers a domain that is several wavelengths in size.

Jarrahbashi et al. [34] studied wide ranges of density ratio (0.05–0.5), Re ($320 < Re < 8000$), and We of $O(10^4$–$10^5)$ in round liquid jet breakup. They defined the radial scale of the two-phase mixture as the outermost radial location of the continuous liquid and showed that the radial spray growth increases with increasing gas-to-liquid density ratio ($\hat{\rho}$). They showed

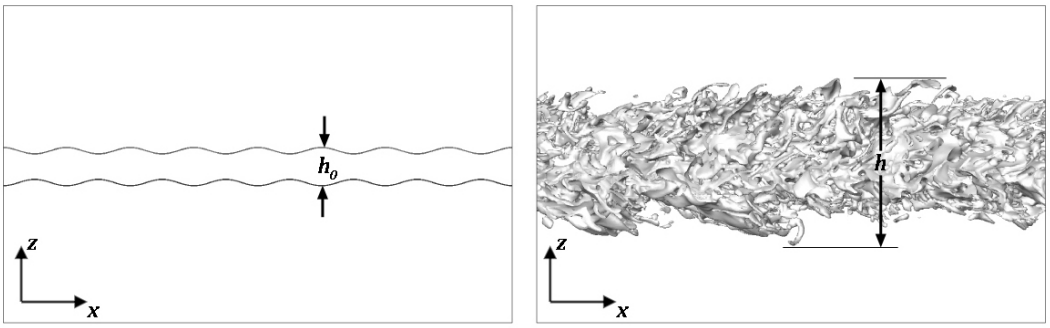

Figure 5.1: Schematic showing the spray width basis as defined by [96].

that droplets are larger for higher gas densities and lower We values, and form at earlier times for higher $\hat{\rho}$. However, the effects of Re and We were not fully studied there.

In a similar study, Zandian et al. [96] explored the effects of We on the droplet size as well as the liquid sheet expansion rate. They also showed the variation in the size and number density of droplets for We in the range 3000–72,000; however, both these quantities were obtained from visual post-processing, which incur non-negligible errors. Their qualitative comparison showed that droplet and ligament sizes decrease with increasing We, while the number of droplets increases. Their results applied for a limited time after the injection and did not show how fast the length scales cascade. Zandian et al. [96] in similar fashion to Jarrahbashi et al. [34] defined the distance of the farthest point on the continuous liquid sheet surface from the jet centerplane as the cross-flow width of the spray, as schematically depicted in Figure 5.1. Even though this definition provides a simple description of the spray growth, it lacks statistical information about the number density of liquid structures at different cross-flow distances from the jet centerplane. Thus, this definition is not optimal for the spray width analysis and failed to show the effects of We on the spray expansion rate.

Desjardins & Pitsch [16] defined the half-width of the planar jets as the distance from the jet centerline to the point at which the mean streamwise velocity excess is half of the centerline velocity. They showed that high We jets grow faster, which suggests that surface tension

stabilizes the jets. They also demonstrated that, regardless of We, droplets are generated through the creation and stretching of liquid ligaments (pertinent to Domain I in Figure 3.2 of Chapter 3). Ligaments are longer, thinner, and more numerous as We is increased. The corrugation length scales appear larger for lower Re_l – attributed to lesser energy contained in small eddies at lower Re_l. Consequently, earlier deformation on the smaller scales of the interface is more likely to take place on relatively larger length scales as Re_l is reduced. Their work was limited to We of $O(10^2$–$10^3)$, which were low compared to our range of interest for common liquid fuels and high-pressure operations. The effects of density ratio were also not studied in their work.

The scarcity of studies in Domain II – i.e. high We_g and moderate Re_l, refer to Figure 3.2 – is especially notable since the trend towards much higher operating pressures has started in engine designs. The studies introduced above (and also in Chapter 1) indicate that there is no proper method in the literature for quantification of the cascade rate and spray spread rate at early liquid-jet breakup. Therefore, implementation of a new methodology – as will be introduced here – is essential for evaluation of these quantities. Quantification of these parameters is very important for understanding and identifying the most significant causes, which are helpful in controlling the atomization process.

Our objectives are to (i) study the effects of the key non-dimensional parameters, i.e. Re_l, We_g, gas-to-liquid density ratio and viscosity ratio, and also the wavelength-to-sheet-thickness ratio, on the temporal variation of the spray width and the liquid-structures length scale; (ii) establish a new model and definition for measurement of the liquid surface length-scale distribution and spray width for the early period of spray formation; and (iii) explain the roles different breakup regimes play in the cascade of length scales and spray development during the early atomization period. The results are separated by atomization domains to clarify the effects of each atomization mechanism on the cascade process and spray expansion. Moreover, the time portions of the behaviors are related to the various structures

formed during the primary atomization period.

To address these objectives, two probability density functions (PDFs) are obtained from the numerical results, for a wide range of liquid-structure size and transverse location of the liquid-gas interface at different times to give a broader understanding of the temporal variation of the length-scale distribution and the spray width. The temporal evolution of the distribution functions is given rather than just showing the fully-developed asymptotic length scales, as is well explored and examined in the literature. The first PDF indicates the size of the small liquid structures through the local radius of curvature of the gas-liquid interface. The novelty of this model is that we do not address only the droplets that are formed, nor present only the size of the droplets as the length scale of the atomization problem – as what the SMD presents. Instead, the length-scale distribution here comprises the size of all the liquid structures – from the initial surface waves, to the lobes, bridges, ligaments, and finally droplets. Thus, this analysis reveals the change in the overall length scale of the jet surface even before the droplets are formed – not examined or quantified before. The second PDF indicates the location of the liquid-gas interface, giving more than just the outermost displacement of the spray, as was typically measured in most past computational studies. Rather, we present the "density" of the liquid surface at any transverse location, which provides a more meaningful and realistic presentation of the spray width. "Density" here means the relative liquid surface area at a given control volume at any distance from the jet midplane.

5.1.1 Data analysis

Twice the inverse of the liquid surface curvature ($\kappa = 1/R_1 + 1/R_2$, where R_1 and R_2 are the two radii of curvature of the surface in a 3D domain) has been defined as the local length scale in this study. This length scale represents the local radius of curvature of the interface, and

is a proper quantity enabling us to monitor the overall size of the surface structures. It would eventually asymptote to the droplet radius after the entire jet is broken into approximate spherical droplets. Based on this definition, a length scale is obtained at each computational cell in the fuzzy zone at the interface. The curvature of each cell containing the interface is computed at every time step; then, the structure length scale (L) is defined as

$$L_{ijk} = \frac{2}{|\kappa_{ijk}|}, \tag{5.1}$$

where κ is the curvature, and the ijk indices denote the coordinates of the cell in a 3D mesh. The length scale L_{ijk} of each cell is used to create a PDF of the length scales. The κ_{ijk} value is measured per computational cell and weighted by the interface area in that cell to obtain the PDFs. Only cells containing the interface are included in this analysis. The bin size used for the length-scale analysis is $\mathrm{d}L = \Delta = 2.5$ μm. The probability of the length scale in the interval $(L, L + \mathrm{d}L)$ is obtained by multiplying the PDF value at that length scale, $f(L)$, by the bin size:

$$prob(L \leq L' \leq L + \mathrm{d}L) \equiv P(L) = f(L)\mathrm{d}L. \tag{5.2}$$

This is an operational definition of the PDF. Since the probability is unitless, $f(L)$ has units of the inverse of the length scale; i.e. m^{-1}. However, in our study, the length scale is nondimensionalized by the initial wavelength. Thus, $f(L/\lambda_0)$ becomes unitless. The relation between the length-scale PDF and its probability could be derived from Equation (5.2);

$$f(L/\lambda_0) = \frac{P(L/\lambda_0)}{\mathrm{d}L/\lambda_0} = 40P(L/\lambda_0), \tag{5.3}$$

where $\mathrm{d}L$ is the bin size and $\lambda_0 = 100$ μm is the initial KH wavelength. The probability of having the length scale in the finite interval $[a, b]$ can be determined by integrating the PDF;

$$prob(a \leq \frac{L}{\lambda_0} \leq b) \equiv P(a \leq \frac{L}{\lambda_0} \leq b) = \int_a^b f(\frac{L'}{\lambda_0})\frac{\mathrm{d}L'}{\lambda_0}.$$

In order to obtain the average length scale at each time step, the length scales are integrated along the liquid-gas interface and divided by the total interface area. The average length scale δ is nondimensionalized using the initial perturbation wavelength, λ_0. The average length scale is defined as

$$\delta = \frac{1}{\lambda_0}\frac{\int L\mathrm{d}s}{S} \approx \frac{1}{\lambda_0}\frac{\sum L_i s_i}{\sum s_i}, \tag{5.4}$$

where S is the total surface area of the interface, s_i is the interface area in cell i and L_i is the length scale of that particular cell.

Since the length scale L has a wide range from a few microns to infinity (if the curvature is zero at a cell), we neglect the length scales that are very large, i.e. $L > 4\lambda_0$, so that the average length scale would not be biased towards large scales due to those off values. The mean length scale can show the overall change in the size of the structures on the liquid surface; therefore, one can track the stretching of the surface – if the mean length scale grows – or its cascade into smaller structures and appearance of subharmonic instabilities – as the mean decays.

Similar to the length scale, a PDF is obtained for the transverse distance of the interface from the centerplane. This is related to the interface density model introduced by Chesnel et al. [8], where the interface density was defined as the ratio of the interface area within the considered control volume. In our study, however, the interface density is measured at different transverse locations to form the PDFs. This PDF also has units of m^{-1}, as discussed before; however, it is normalized by the initial sheet thickness (h_0). This gives a better

statistical data about the distribution of the transverse location of the spray interface rather than just presenting the outermost location of the liquid surface. Thereby, the concentration, or density, of the liquid surface at any transverse plane is measured. This quantity also shows the breakup of surface structures and demonstrates how uniformly the spray spreads; i.e. the quality of spray development. In fact, this PDF is a more generalized version of the average liquid volume fraction distribution. To account for both sides of the liquid sheet in this analysis, the cross-flow distance h of each local point at the interface is defined as the absolute value of its z-coordinate ($z = 0$ at the centerplane);

$$h_{ijk} = |z_{ijk}|. \tag{5.5}$$

The probability of the spray width is obtained from an equation similar to Equation (5.2), where L is replaced by h. The relation between the spray-width PDF, $f(h/h_0)$, and its probability, $P(h/h_0)$, is

$$f(h/h_0) = \frac{P(h/h_0)}{\mathrm{d}h/h_0}, \tag{5.6}$$

where $\mathrm{d}h$ is the bin size for the spray-width PDF, taken to be equal to the mesh size, i.e. $\mathrm{d}h = \Delta = 2.5$ μm, and h_0 is the initial sheet thickness; $h_0 = 50$ μm for the thin sheet, and 200 μm for the thick sheet.

The average spray width (sheet thickness) ζ is also obtained by integrating h along the interface, and dividing it by the total interface area. The mean spray width is nondimensionalized by the initial sheet thickness h_0;

$$\zeta = \frac{1}{h_0}\frac{\int h\mathrm{d}s}{S} \approx \frac{1}{h_0}\frac{\sum h_i s_i}{\sum s_i}, \tag{5.7}$$

where h_i is the cross-flow distance of the interface in cell i from the midplane. This definition

represents how dense the surface is at any distance from the jet centerplane. Therefore, it gives a more realistic representation of the jet growth in a way that is more useful for many applications such as combustion and coating.

5.2 Results and discussion

5.2.1 Data analysis verification

The choice of bin size and the sensitivity of the measurements against the mesh resolution and computational-domain size are tested and verified in this section. The results of these tests are given in Figures 5.2 and 5.3. Figure 5.2(a) compares the temporal variation of the average length scale δ with two different bin sizes used for measurement of this parameter. The solid line is the result obtained by the actual bin size used in our analysis ($\mathrm{d}L = \Delta = 2.5$ μm), and the dashed line denotes the variation of δ with time using a bin size twice as big; i.e. $\mathrm{d}L = 2\Delta = 5$ μm. Both cases converge at about 40 μs and are in good agreement

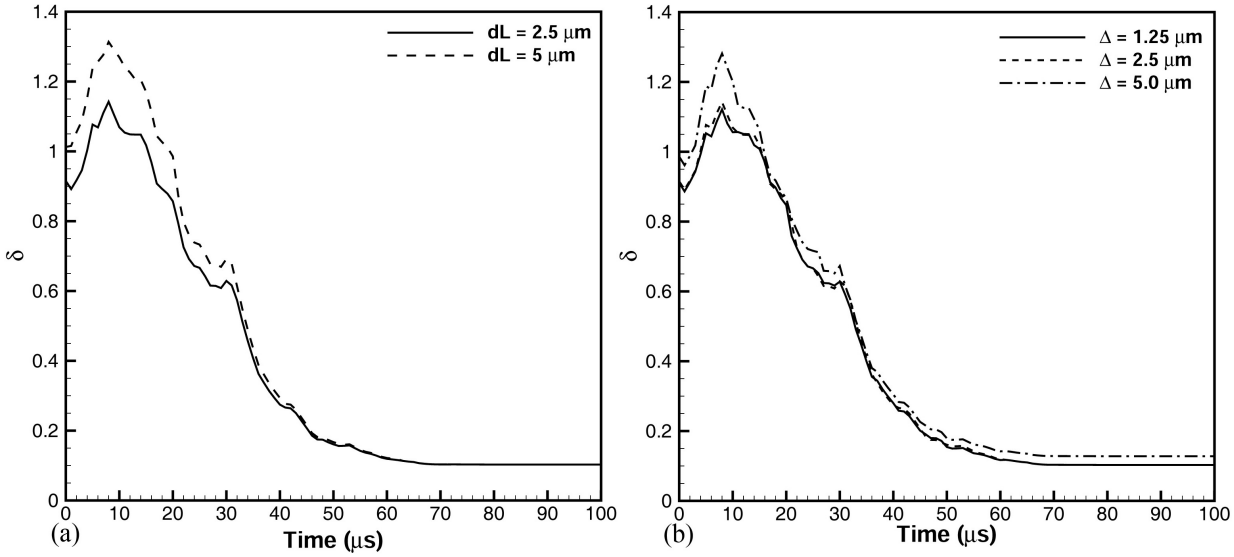

Figure 5.2: Effect of bin size (a) and mesh resolution (b) on the temporal evolution of the mean length scale; $Re_l = 2500$, $We_g = 7250$, $\hat{\rho} = 0.5$, $\hat{\mu} = 0.0066$, and $\Lambda = 2.0$.

thereafter. Both test cases result in the same asymptotic length scale at the end of the computation; however, in the early stages, the larger bin size produces slightly larger scales, especially around the maximum point ($t \approx 10$ μs). The maximum error in the larger bin size is around 13%. The error gradually decreases after 10 μs and becomes less than 1% at 40 μs. The temporal trend of the length scales, i.e. when the scales are growing or declining, predicted by both test cases, match very well. The only difference is that the larger bin overpredicts the length scales at early stages. Since the magnitude in the early stage of the length scale growth (around the time when the maximum errors occur) is not the main goal of our research, it can be concluded that choosing $\mathrm{d}L = 2.5$ μm as the bin size is acceptable for the purposes of this study.

Figure 5.2(b) shows the same length scale evolution in time for three different grid resolutions. The result for the grid size used in this study ($\Delta = 2.5$ μm) is denoted by dashed line in this plot. Two other grid resolutions – one twice as big ($\Delta = 5$ μm) and the other one half of the current grid size ($\Delta = 1.25$ μm) – are also plotted in dash-dotted and solid lines, respectively. The larger grid is unable to predict the asymptotic length scale and has about 5% error near the asymptote. The maximum error of this large grid is about 10% and occurs near the maximum scale. The result of the finest grid however, matches perfectly with the current grid after 15 μs. The maximum difference between the results of the two finer grids is less than 1%. Therefore, this comparison verifies that the 2.5 μm grid resolution is justified for our study.

The size of the computational domain (especially in the transverse direction) has a major influence on the evaluation of the mean spray width. Figure 5.3 compares the temporal growth of the mean spray width for three domain sizes – the original domain used in this study (1X), a domain half the original size (0.5X), and another 1.5 times larger (1.5X). The largest domain predicts a very similar result compared to the original case, with very slight difference in ζ after 70 μs. However, the difference in the results of the two larger

domains never exceeds 1.5%, which verifies the appropriateness of our chosen domain size. However, a larger domain is definitely required if one wants to study the process further in time. The predicted spray width of the 0.5X Domain is acceptable until 55 μs, but it departs from the correct trend henceforth and becomes noticeably underpredicted. The error of the smallest domain reaches about 14% by the end of the simulation. This clearly shows that the boundary conditions have a major impact on the predicted results for the small domain.

5.2.2 Weber number effects

The temporal variation of the average length scale for low, medium, and high We_g and moderate Re_l are illustrated in Figure 5.4. The density ratio is kept the same (0.5) among all these cases; hence, We_g is only changed through the surface tension. The effects of $\hat{\rho}$ are analyzed in Section 5.2.4, and the combined effects of $\hat{\rho}$ and We are revealed there. The symbols on the plot denote the first instant at which different liquid structures form during the atomization process. The definition of each symbol is introduced above the plot in Figure 5.4 and will be used hereafter in the proceeding plots. The symbols help us compare

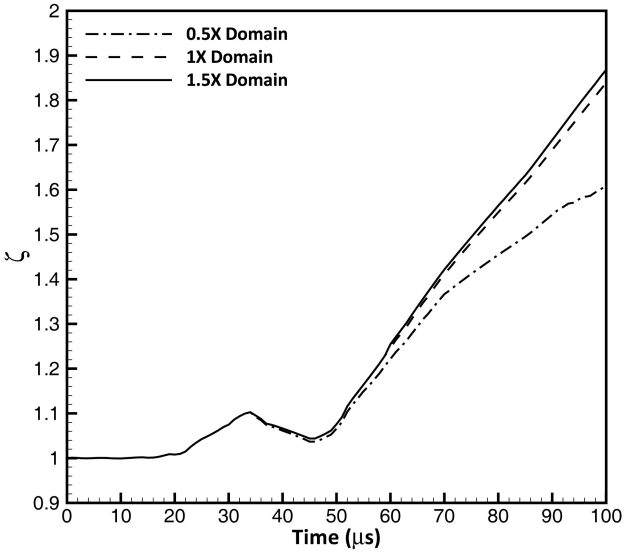

Figure 5.3: Effect of computational domain size on the temporal evolution of the mean spray width; $Re_l = 2500$, $We_g = 7250$, $\hat{\rho} = 0.5$, $\hat{\mu} = 0.0066$, and $\Lambda = 2.0$.

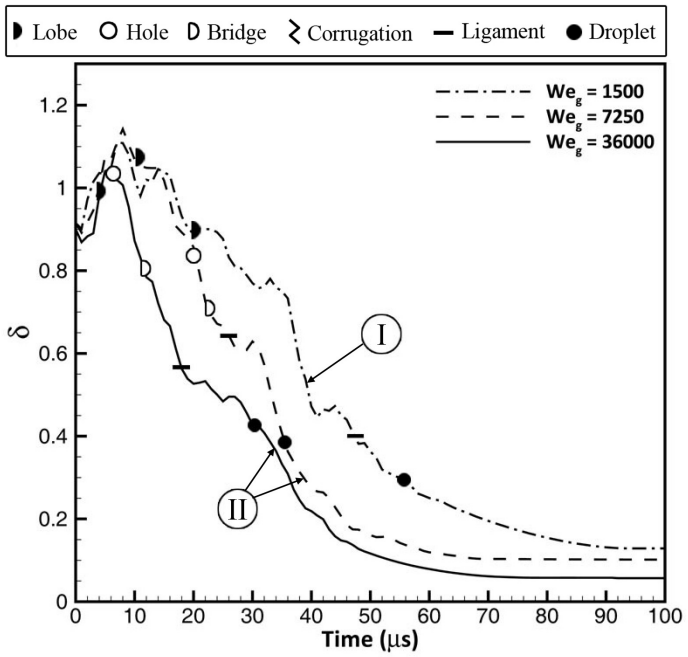

Figure 5.4: Effect of We_g on the temporal variation of the average dimensionless length scale δ; $Re_l = 2500$, $\hat{\rho} = 0.5$, $\hat{\mu} = 0.0066$, and $\Lambda = 2.0$. The symbols indicate the first time when different liquid structures form. The definition of each symbol is introduced above the plot.

the rate of formation of each structure, say ligament or droplet, at different flow conditions. The relation between the formation of each structure and the behavior of the length scale or spray width can also be better understood using these symbols. The atomization domain for each process is also denoted on the plot. Note that the zigzag symbol denoting the "corrugation" formation does not appear in Figure 5.4 because this structure forms only in Domain III (a Domain III result will be discussed in the next sub-section). All computations are stopped at 100 μs, which is sufficient for the quantities of interest to reach a steady state. It will be shown later that further continuation of the computations is not justified because the interface gets too close to the top and bottom computational boundaries, so that the length scale and sheet width get affected by the boundary conditions.

The lowest We_g falls in the ligament stretching ($LoLiD$) category in Atomization Domain I, while the two higher We_g cases follow the hole-formation mechanism ($LoHBrLiD$) in Domain II; see Figure 3.2. The average length scale decreases with time for all cases, to be

expected for the cascade of structures presented in Figure 3.1 – lobes to holes and bridges, to ligaments and then to droplets. δ becomes smaller as We_g increases, and its cascade is hastened by increasing We_g. At 40 μs, the average length scale for $We_g = 36,000$ is almost $0.22\lambda_0 = 22$ μm, while it increases to $0.3\lambda_0$ for $We_g = 7250$, and to $0.5\lambda_0$ at the lowest We_g. This shows the clear influence of surface tension on the length-scale cascade and on the size of the ligaments and droplets. An increase in surface tension suppresses the instabilities and increases the structure size. This trend is consistent with both analytical [58] and numerical [16] results. The droplets and ligaments formed in Domain II are generally smaller than in Domain I.

The length scale starts from $0.9\lambda_0$ in all three cases due to the initial perturbations, and the average scale increases for the first 10 μs, until it reaches a maximum. We_g, and hence surface tension, does not notably affect the initial length scale growth. This growth involves the initial stretching of the waves, which creates flat regions near the braids – they have low curvatures, hence large length scales. As lobes and ligaments form later, the length scale decreases because (i) the radius of curvature of these structures is much smaller than the initial waves, and (ii) the total interface area increases by the formation of lobes, bridges, ligaments, and droplets, smearing out the influence of the large length scales. Figure 5.4 also shows that all the structures – especially ligaments and droplets – form sooner with increasing We_g. Moreover, ligaments and droplets form slower in Domain I than in Domain II; that is, the $LoHBrLiD$ mechanism is more efficient than the $LoLiD$ process in terms of cascade rate at the same Re_l range.

As discussed in Chapter 3, two distinct characteristic times exist for the formation of holes and the stretching of lobes and ligaments. At a given Re_l, as surface tension increases (i.e. decreasing We_g), the characteristic time for hole formation increases, thereby delaying the hole formation. Thus, for lower We_g, most of the earlier ligaments are formed by direct stretching of the lobes and/or corrugations, while the hole formation is inhibited. On the

other hand, at relatively large Re_l (> 3000), as liquid viscosity is increased (i.e. decreasing Re_l), at the same We_g, the ligament-stretching time gets larger. In this case, hole formation prevails over the ligament stretching mechanism, resulting in more holes on the lobes. As We_g increases, the time at which the first hole forms decreases. This indicates that the hole formation time should be inversely proportional to We_g.

At low Re_l (< 3000), the liquid viscosity has an opposite effect on the hole formation and ligament stretching. As shown in Figure 3.2, near the left transitional boundary, the time scale of the stretching becomes relatively smaller than the hole-formation time scale as Re_l is reduced at a constant We_g. Therefore, there is a reversal to ligament stretching as Re_l is decreased at a fixed We_g. Keeping all these effects in mind, the following two nondimensional characteristic times were proposed (Chapter 3);

$$\frac{U\tau_h}{h_0} \propto \frac{1}{We_g}\left(1+\frac{k}{Re_l}\right), \tag{5.8}$$

$$\frac{U\tau_s}{h_0} \propto \frac{1}{Re_l}\ ; \tag{5.9}$$

where τ_h and τ_s are the dimensional characteristic times for hole formation and ligament stretching, respectively, and k is a dimensionless constant. The results in Figure 5.4 are consistent with Equation (5.8), which suggests the hole formation time scale to be inversely proportional to We_g. Therefore, the hole formation time for $We_g = 36,000$ should be nearly 5 times smaller than for $We_g = 7250$ since Re_l is the same for both cases. From Figure 5.4, the first instant when a hole is formed is 22 μs for $We_g = 36,000$ (solid line), and almost 5 μs for $We_g = 7250$ (dashed line). Thus, the ratio of τ_h for these two cases is about 4.4, in good agreement with the result obtained from Equation (5.8).

Even though the average length scale gives a good insight into the temporal variation of the

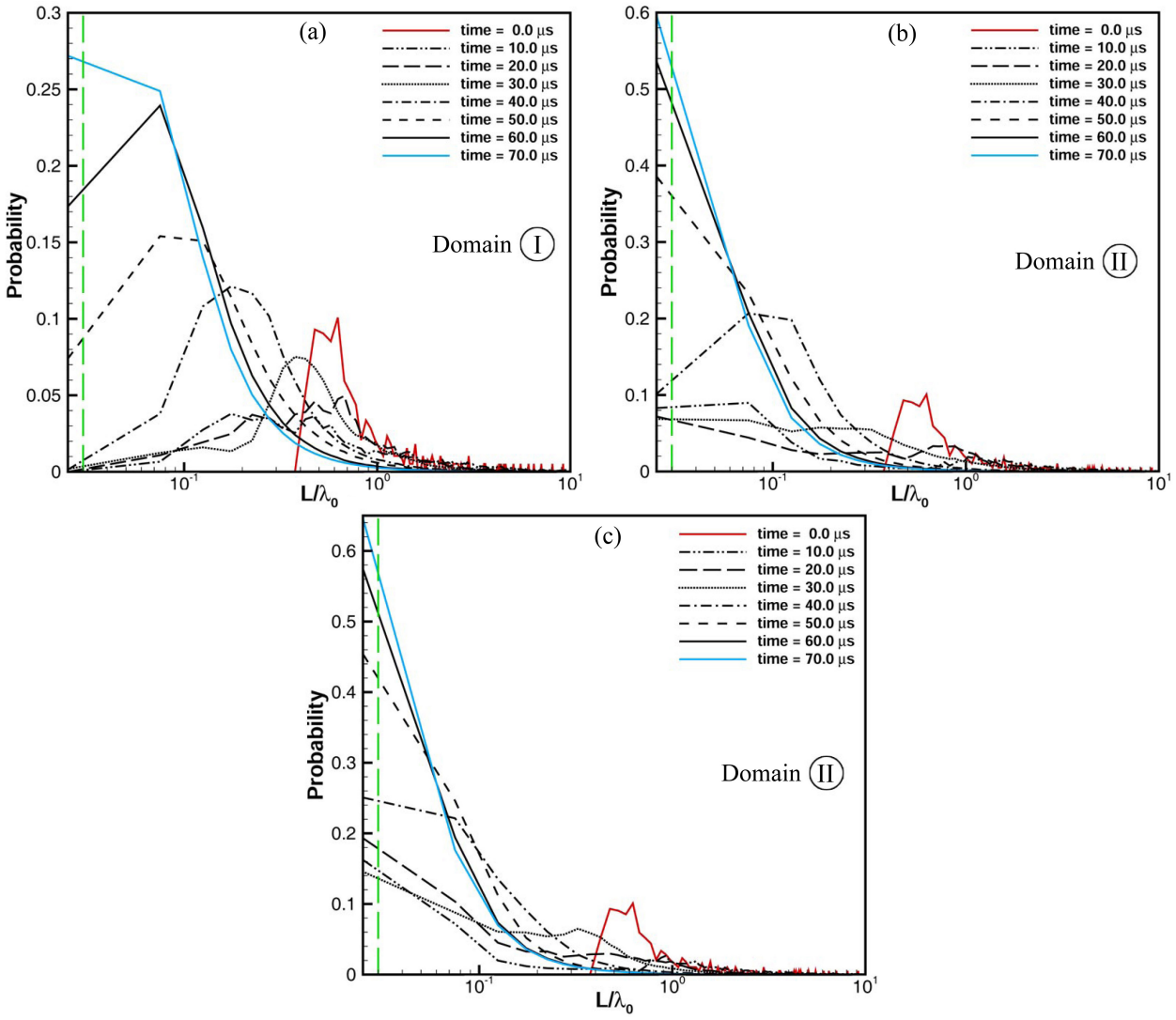

Figure 5.5: Probability distribution of the normalized length scales at different times for $We_g = 1500$ (a), $We_g = 7250$ (b), and $We_g = 36,000$ (c); $Re_l = 2500$, $\hat{\rho} = 0.5$, $\hat{\mu} = 0.0066$, and $\Lambda = 2.0$. The broken green lines indicate the cell size.

overall scale of the liquid structures, it does not show the distribution of the scales, for which the length-scale PDFs are needed. Figure 5.5 compares the probability distribution of the length scales of the three We_g cases at different times on a log-scale.

All cases start from the same initial distribution indicated by the red line. The length scales in the range $0.5\lambda_0$–$0.6\lambda_0$ have the maximum probability of approximately 10%. Later, the most probable length scale becomes smaller, while the probability of the dominant scale increases. The transition towards smaller scales is faster as We_g increases since lowering

surface tension reduces the resistance of the liquid surface against deformations. At 50 μs, the most probable length scale becomes $0.1\lambda_0$ for $We_g = 1500$ (dashed-line in Figure 5.5a). Higher We_g cases reach the same most probable length scale at 40 μs (dash-dotted line in Figure 5.5b) for $We_g = 7250$, and at less than 10 μs (not shown) for $We_g = 36,000$.

The PDFs also show an increase in the probability of smallest scales at higher We_g. At $t = 70$ μs, for example, the lowest We_g has a probability of about 27% for the smallest computed length scale of 2.5 μm; see where the blue curve intersects the vertical axis in Figure 5.5(a). That probability at the same time increases to 59% as We_g increases to 7250. At even higher $We_g = 36,000$, the probability of 2.5 μm or lower is slightly more than 64% at 70 μs. Since the smaller length scale also implies smaller volume, the conclusion is that the number density of the small droplets also increases with We_g. The green broken lines in Figure 5.5 indicate the normalized cell size. In all cases and at all times, more than 98% of the computed length scales lie to the right of this line and are larger than the mesh size, which justifies the sufficient resolution of the current grid. The effects of grid resolution on the liquid structures scale was demonstrated in detail in Chapter 2, and it was shown that the grid resolution used for the current analysis is fine enough to capture the smaller radii of curvature.

Figure 5.6 shows the liquid surface for the moderate $We_g = 7250$ case at 70μs. As shown in the magnified image, at this time the liquid surface is mainly comprised of ligaments (either broken or still attached) and droplets, while little or almost no lobes with very large scales are present. Therefore, the evolution of the surface is summarized mainly in stretching and breakup of the ligaments henceforth.

As shown in Figure 5.7, there are two radii of curvature in a typical perturbed ligament. R_1 is the smaller azimuthal radius which is initially equal to the radius of the cylindrical ligament. R_2, the radius of curvature of the streamwise arc of the ligament after it undergoes Rayleigh-Plateau (RP) instability, is much larger than R_1. Theoretical analyses of Rayleigh

[69] show that for a cylindrical liquid segment of radius R_1, unstable components are only those where the product of the wave number with the initial radius is less than unity; i.e. $kR_1 < 1$. Thus, the minimum unstable RP wavelength for a ligament of radius R_1 is $\lambda_{RP} = 2\pi R_1$. The volume of a cylinder of radius R_1 and length λ_{RP} is $V = 2\pi^2 R_1^3$. If this segment of the cylinder (ligament) breaks into a droplet, a simple mass balance shows that the resulting droplet radius (R_d in Figure 5.7b) would be $R_d \approx 1.67R_1$. R_2 is never smaller than R_1; $R_2 \approx R_1$ based on an approximate sinusoidal surface shape at the instant of ligament breakup, and $R_2 = \infty$ in case of unperturbed ligament; i.e. $R_1 \leq R_2 < \infty$. Considering these limits and using the relation between R_1 and R_d, the extents of ligament length scale $L_l = 2/(1/R_1 + 1/R_2)$ as a function of R_d follow

$$\text{if } R_2 = \infty \rightarrow L_l = \frac{2}{1/R_1} = 2R_1 \approx 1.2R_d, \tag{5.10a}$$

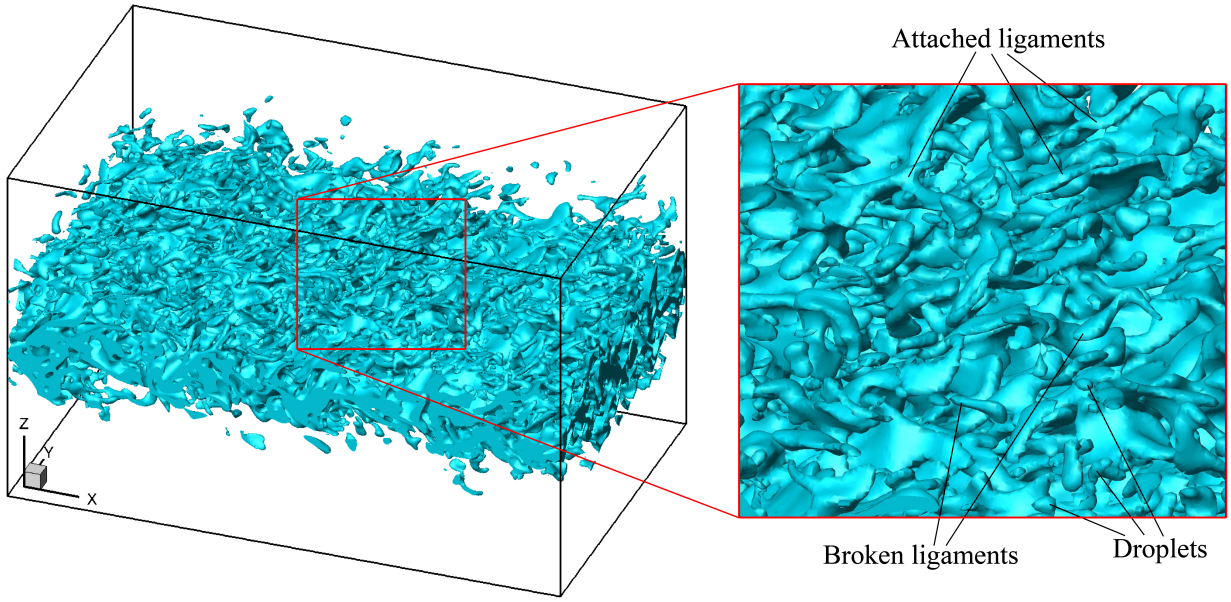

Figure 5.6: Liquid-jet surface at 70 μs for $We_g = 7250$; $Re_l = 2500$, $\hat{\rho} = 0.5$, $\hat{\mu} = 0.0066$, and $\Lambda = 2.0$.

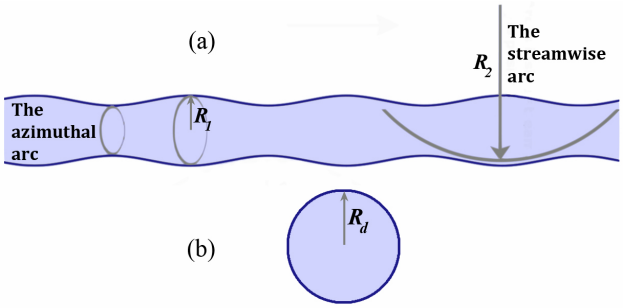

Figure 5.7: Schematic of the radii of curvatures on a typical ligament (a), and its resulting droplet (b).

$$\text{if } R_2 = R_1 \rightarrow L_l = \frac{2}{1/R_1 + 1/R_1} = R_1 \approx 0.6R_d; \tag{5.10b}$$

thus, $0.6R_d < L_l < 1.2R_d$. The droplet length scale is $L_d = R_d$. Therefore, the time-averaged ligament length scale is approximately equal to the droplet length scale during the short period of RP instability growth and ligament breakup. This simple analysis explains why the average length scale becomes almost constant after 70μs (see Figure 5.4) while the ligament breakup is still occurring and the number of droplets is increasing. Since the ligament formation is delayed (about 30 μs) at lower We_g, the asymptotic length scale is also expected to occur later for $We_g = 1500$. This is consistent with Figure 5.4, where the length scale asymptotes about 27 μs later for $We_g = 1500$ compared to $We_g = 7250$.

The standard deviation of the PDFs of Figure 5.5, illustrated in Figure 5.8, provides a more accurate quantitative measure of the length-scale distribution. The length scales range from a few microns, i.e. a small fraction of the initial wavelength, to several hundred microns, e.g. four times the initial wavelength. Therefore, the standard deviation of δ is very large, even in the beginning. δ is about $0.9\lambda_0 = 90$ μm at the start of the computations (see Figure 5.4), but the standard deviation of the length scales (σ_δ) is about $0.85\lambda_0 = 85$ μm at this time.

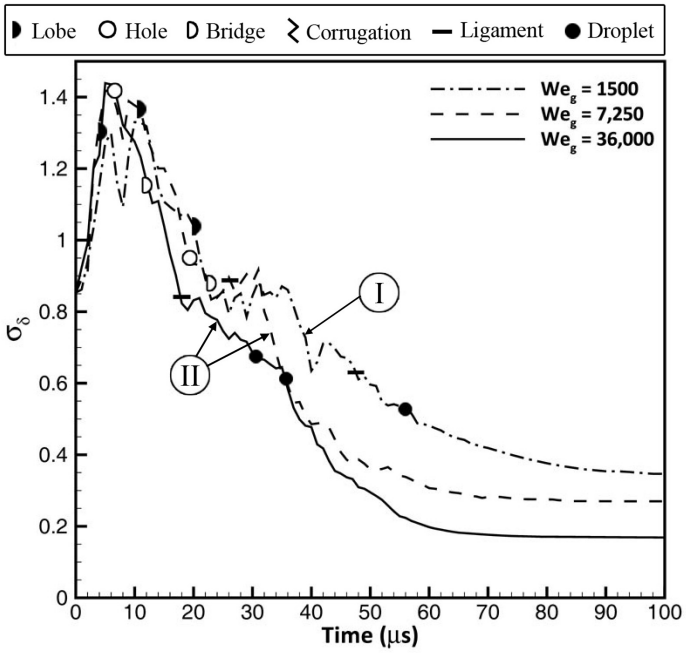

Figure 5.8: Temporal variation of the standard deviation of the dimensionless length-scale PDFs of Figure 5.5 for $We_g = 1500$, 7250, and $36,000$; $Re_l = 2500$, $\hat{\rho} = 0.5$, $\hat{\mu} = 0.0066$, and $\Lambda = 2.0$.

At the early stage, the standard deviation increases as larger scales become more probable following the flattening and stretching of the waves. Later, the flow field gets filled with more small ligaments and droplets and more curved surfaces, which reduce both the mean and the standard deviation. However, even at the end of the process, the standard deviation is still around 0.2–$0.4\lambda_0 = 20$–40 μm; so, a wide range of length scales is still present in the flow. The standard deviation decreases with increasing We_g, as the smaller capillary force allows the larger scales to deform easily and cascade more quickly into smaller scales with higher curvatures; this reduces the deviation of the scales. The standard deviation becomes almost constant when δ asymptotes to its ultimate value.

The length-scale PDFs show that: (i) the asymptotic length scale (ligament and droplet size) decreases with increasing We_g; (ii) the number of small droplets increases with increasing We_g; and (iii) the cascade of length scales occurs faster at higher We_g. The last item is also implied by the temporal evolution of the mean length scale. The first two items are

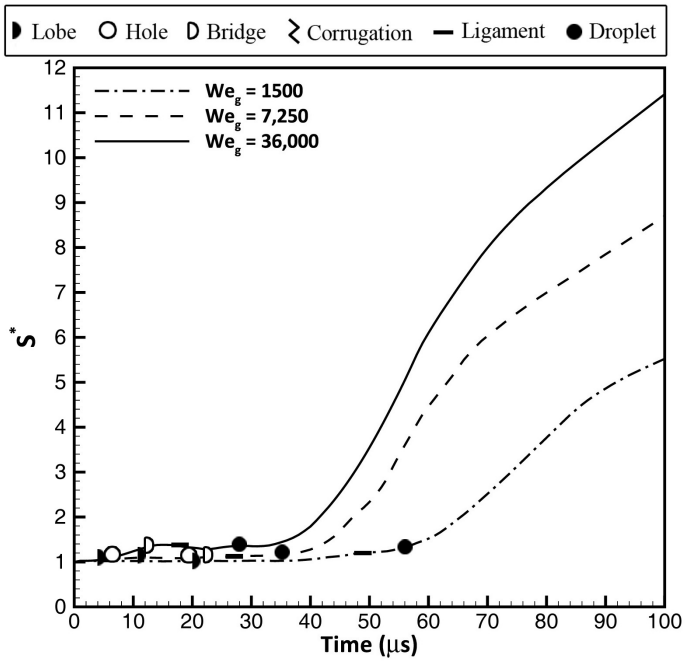

Figure 5.9: Temporal growth of the non-dimensional liquid surface area (S^*) for $We_g = 1500$, 7250, and $36,000$; $Re_l = 2500$, $\hat{\rho} = 0.5$, $\hat{\mu} = 0.0066$, and $\Lambda = 2.0$.

consistent with the literature, but the third item is a new finding.

Temporal growth of the non-dimensional liquid surface area (S^*) for the three We_g cases is plotted in Figure 5.9. The surface area (S) is non-dimensionalized by the initial liquid surface area; i.e. $S^* = S/S_0$. Therefore, S^* grows monotonically in time from 1 at $t = 0$; $S_0 \approx 0.8$ mm^2.

As expected, the surface area growth rate is higher for higher We_g, where the surface deformations occur and grow faster and ligaments and droplets form earlier. S^* grows very gradually in the first 30 μs, but experiences a sudden increase in the growth rate after the formation of first ligaments and droplets. This abrupt growth in surface area occurs sooner and at a higher rate for higher We_g following the earlier formation of ligaments in those cases. The S^* growth rate decreases slightly towards the end of the computations, while the area still keeps growing. The cause of this gradual decrease in growth rate is speculated to be mainly due to the breakup of ligaments into droplets. Surface tension minimizes the

surface area after ligament breakup. The surface deformation at later times mainly consists of formation of ligaments and their breakup into droplets. Following the simplified ligament and droplet radii model shown in Figure 5.7, a simple calculation reveals that the surface area of the resulting droplet is 10% smaller than the surface area of its mother ligament; i.e. $S_d = 0.9S_l$. Therefore, the ligament breakup decreases the S^* growth rate associated with mere stretching of the ligaments. Even though the mean length scale has reached an asymptote at the final stage ($t > 70$ μs), the increase in S^* indicates that the surface dynamics are still in progress and ligament and droplet formation still continues. The rate of growth of S^* becomes almost constant in the asymptotic phase. At 100 μs, the surface area has grown more than 11 times for $We_g = 36,000$, while for $We_g = 1500$, the surface has less than 6 times its initial area.

As mentioned earlier, defining the jet width (thickness) as the distance to the farthest liquid point from the centerplane might render results which are prone to misinterpretation. This definition does not take into account the interface location distribution and only considers the farthest liquid location. For this purpose, the PDFs of the transverse interface location are used to describe the expansion of the liquid sheet in a more meaningful form.

The effect of We_g on the temporal evolution of the average spray width is shown in Figure 5.10 along with the liquid-jet interface picture at 70 μs of each process. The spread rate of the liquid jet can be distinguished better with the new definition of the jet width (compare this plot with figure 40 of Zandian et al. [96]). The spray expands faster at higher We_g and results in a wider spray at the end – a result which is in agreement with numerical results of Desjardins & Pitsch [16]. The average spray width remains close to the initial sheet thickness for the first 50 microseconds for $We_g = 1500$ since the high surface tension suppresses instability waves, lobe stretching, and ligament breakup. The jet expands much sooner at higher We_g; for example, at about 20 μs for $We_g = 7250$, and at 7 μs for $We_g = 36,000$. The structures stretch much more quickly at higher We_g and are less suppressed by the

surface tension forces; thus, they can expand more freely and are carried around more easily by the gas flow, after breakup. The expansion of the jet at the lowest We_g (dash-dotted line in Figure 5.10) coincides with the formation of the first ligament (at 50 μs). Therefore, the lobes are much less amplified at such a low We_g, and the ligament formation and stretching are primarily in the normal direction in Domain I. Generally, the spray angle is larger in Domain II than in Domain I at a comparable Re_l range.

The spikes and oscillations in the average spray width ζ are caused by the detachment of a liquid structure, e.g. bridges, ligaments or droplets, from the jet core. The first decay in ζ coincides with the formation of the first droplets; i.e. the black circles in Figure 5.10. The spray-width PDFs, given in Figure 5.11, support this view.

All three cases in Figure 5.11 start from a bell-shaped distribution around $h = h_0$, denoted

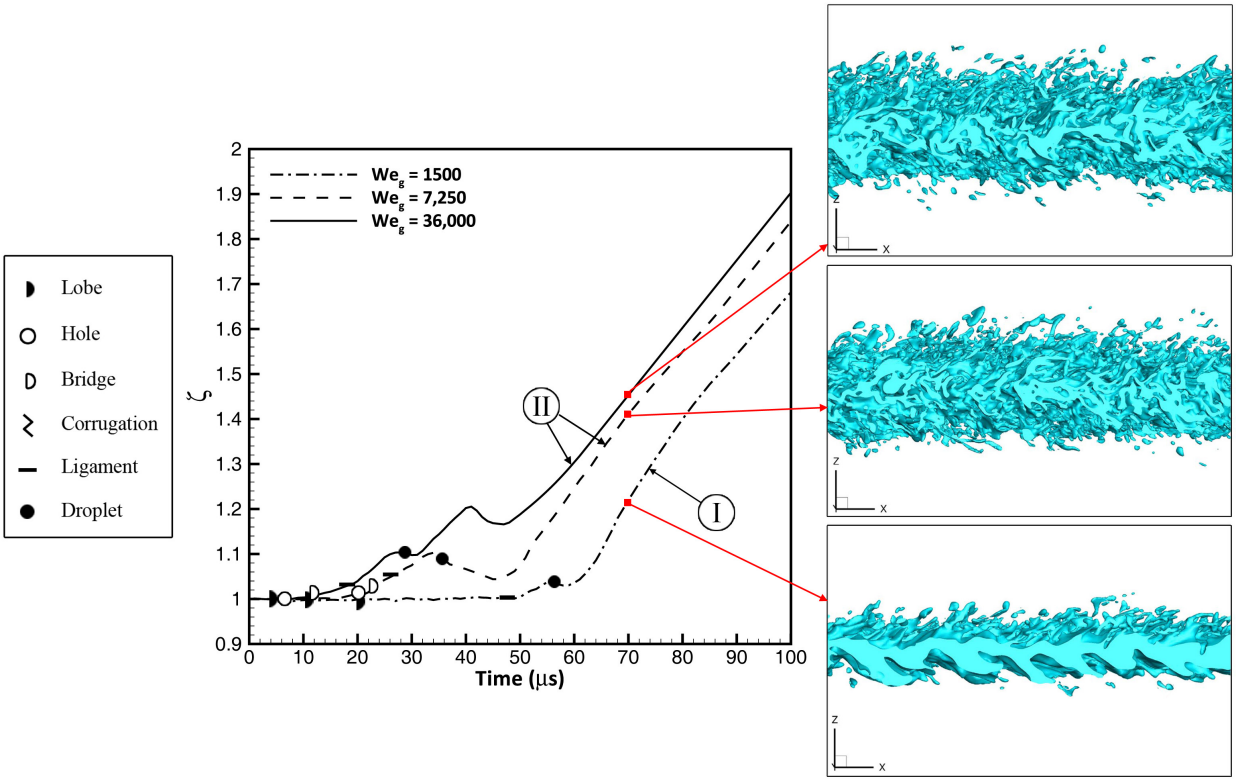

Figure 5.10: Effect of We_g on the temporal variation of the average dimensionless spray width ζ; $Re_l = 2500$, $\hat{\rho} = 0.5$, $\hat{\mu} = 0.0066$, and $\Lambda = 2.0$. The liquid jet surface at 70 μs is shown for each process.

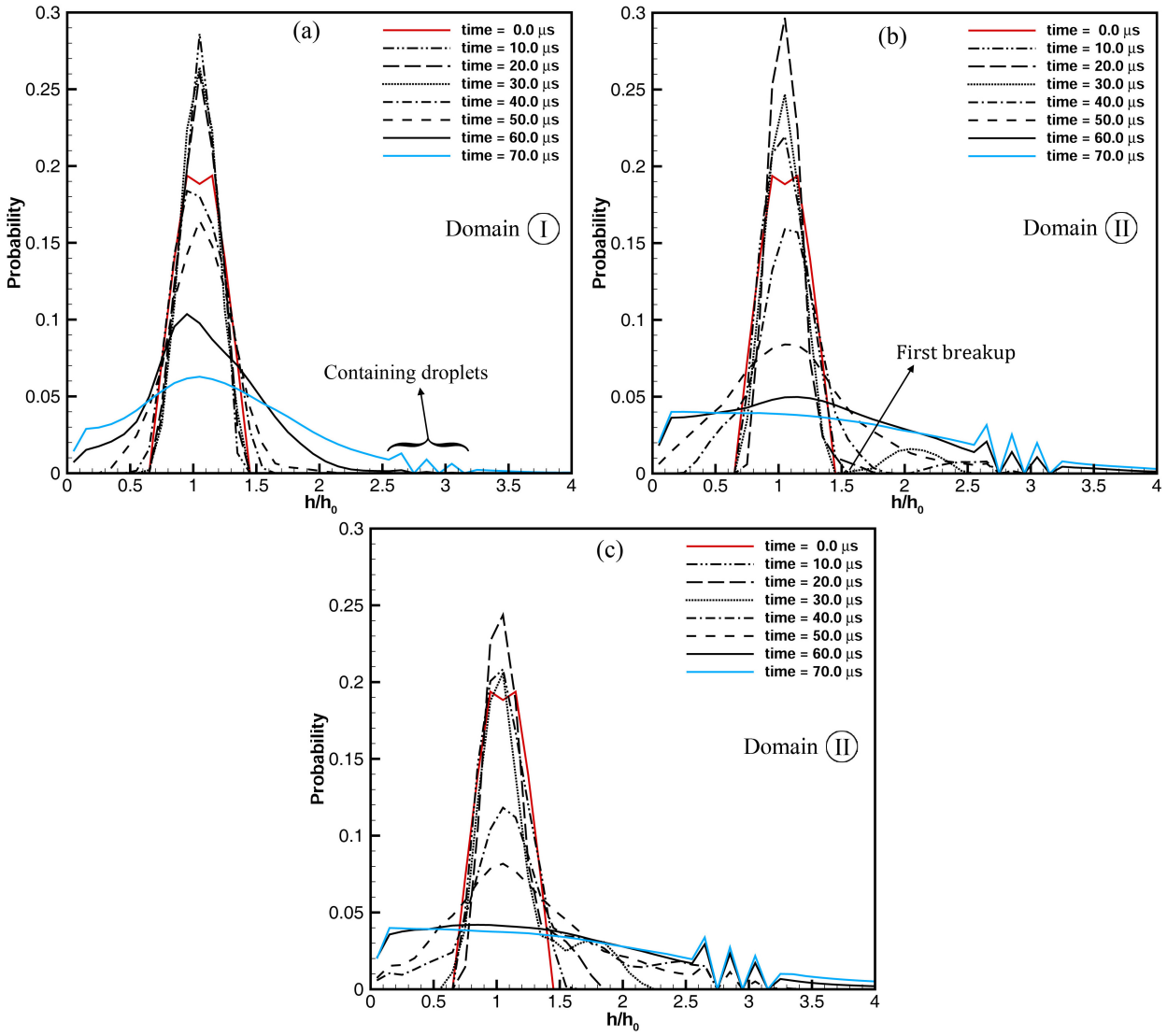

Figure 5.11: Nondimensional spray-width probability distribution at different times for $We_g = 1500$ (a), $We_g = 7250$ (b), and $We_g = 36,000$ (c); $Re_l = 2500$, $\hat{\rho} = 0.5$, $\hat{\mu} = 0.0066$, and $\Lambda = 2.0$.

by the red solid lines. The two peaks on the two sides of $h/h_0 = 1$ are due to the initial perturbations amplitude of 5 μm imposed on the surface of the sheet. Since there are more computational cells near the peak and trough of the perturbations compared to the neutral plane, i.e. $h/h_0 = 1$, the probability of those sizes are slightly higher. The probability of the initial thickness value increases in all cases during the first 20 μs since the wave amplitude decays as the waves get stretched in the flow direction, in the initial stage.

Later, when the waves start to grow due to the KH instability and roll-up of the lobes over the primary KH vortices, the jet width increases and the distribution becomes wider and skews towards larger values on the right. Meanwhile, smaller lengths are also observed. With time, the peak of the initial distribution curve decreases while the distribution broadens. This decline occurs faster at higher We_g, since the spray grows faster for lower surface tension. At $t = 50$ μs, only 8% of the surface, i.e. computational cells at the interface, lie near the initial thickness for $We_g = 36,000$ (dashed-line in Figure 5.11c), and the spray has grown upto three times the initial sheet thickness; i.e. $h/h_0 \approx 3$. At the same time, the farthest transverse distance reached by the liquid is about $2.8h_0$ from the centerplane for $We_g = 7250$; see where the dashed-line in Figure 5.11(b) meets the horizontal axis. At still lower We_g, the maximum spray width is just slightly more than $2h_0$ at 50 μs, and still more than 16% of the surface lies around the initial sheet thickness; see Figure 5.11(a).

Figure 5.11(b) shows a missing section (having zero probability) around $1.4 < h/h_0 < 1.8$ at $t = 30$ μs. The same missing section moves to the right (to $1.5 < h/h_0 < 2.0$) at $t = 40$ μs, and finally vanishes at 50 μs. These sections – marked as the "first breakup" – coincide with the places where the sudden decline in the average jet size was seen in Figure 5.10 for $We_g = 7250$, explaining the oscillations in the average spray width. The missing section appears since some part of the liquid jet (ligament, bridge or droplet) detaches from the jet core into the gas flow, leaving behind a vertical gap empty of any liquid surface at the breakup location, as shown in the sequential liquid surface images in Figure 5.12.

The lobes form and stretch until about 25 μs, resulting in an increase in the average sheet thickness. At 30 μs (Figure 5.12b), the bridge breaks from the lobe and creates a gap near the detachment location, where there are no liquid elements. Therefore, the average spray width suddenly drops at that instant, even though the distance of the farthest liquid element from the centerplane is still growing; i.e. the intersection of the PDF curves with the horizontal axis in Figure 5.11(b) moves to the right. While the detached liquid blob moves

away from the interface, the jet surface stretches outward again due to KH instability; the missing zone moves outward following this motion (Figure 5.12c). The average spray width grows again when the new lobes and ligaments stretch enough to compensate for the broken (missing) section. At this time, the lobes and ligaments fill in the missing gap while the broken liquid structures advect farther from the interface, as shown in Figure 5.12(d) at 50 μs. Figure 5.12 also shows that the instabilities start from a symmetric distribution but gradually move towards an antisymmetric mode (Figure 5.12d). The transition towards antisymmetry is seen in all cases studied here and was explained in detail in Chapter 4 via vortex dynamics analysis [98]. It was shown that transition towards antisymmetry is faster for thin liquid sheets due to the higher induction of the KH vortices on the opposite sides of the liquid surface. In practical atomization conditions, the antisymmetric mode has a higher growth rate and thus eventually dominates the symmetric mode.

The PDFs and the average spray-width plots indicate the first instance of ligament/bridge breakup, when the average spray width ζ starts to decline. Since the lower We_g has less stretching and fewer ligament detachments at early time – due to the high surface tension – its spike is less intense and also appears much later (about 55 μs). The higher We_g, however, breaks much sooner, at about 27 μs.

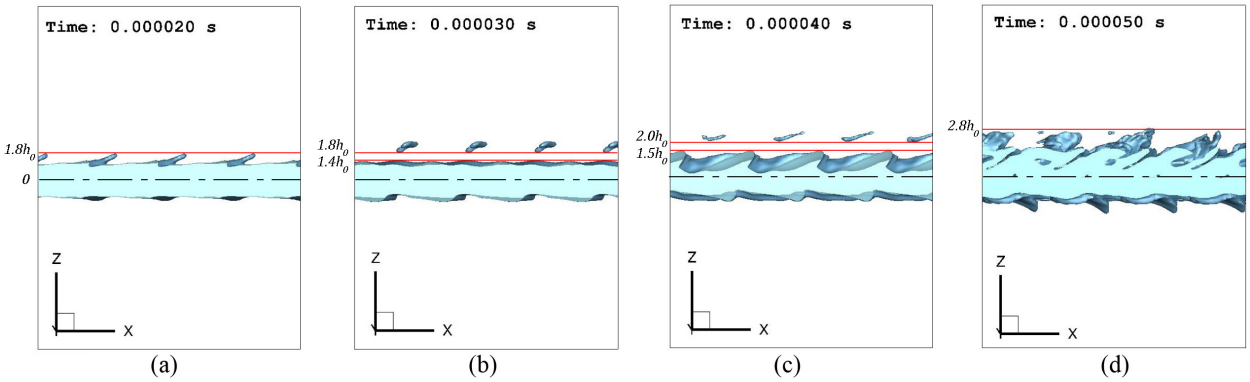

Figure 5.12: Side view of the liquid sheet surface at $t = 20$ μs (a), 30 μs (b), 40 μs (c), and 50 μs (d); $Re_l = 2500$, $We_g = 7250$, $\hat{\rho} = 0.5$, $\hat{\mu} = 0.0066$, and $\Lambda = 2.0$. Gas flows from left to right.

There are also some later oscillations near the maximum spray width of the PDF plots (see Figure 5.11), for all three cases. The reason for these spikes is explained using the liquid iso-surface at 70 μs for $We_g = 1500$, illustrated in Figure 5.13. The planes $2.5h_0$ and $3.0h_0$ away from the centerline are marked with the red lines. Undulations in the PDF curve occur in this range; see the blue line in Figure 5.11(a) marked as "containing droplets". This range is mostly empty of liquids, i.e. filled with gas, except for rare cells which contain the occasional droplets or detached ligaments. In the spray PDF plot, the empty spaces have zero or almost negligible probability, while other transverse heights containing liquid droplets and broken ligaments have greater probability. Thus, waviness is seen in the spray width probability distribution at later times and at greater distances from the centerplane. Those spikes represent the droplets that are thrown outward from the jet core, as the spray expands.

The reason for having non-zero probability for zero width in the PDF plots of Figure 5.11 can also be assessed in Figure 5.13. Since the antisymmetric mode is dominant in the considered range of Re_l and We_g, the trough of the surface wave reaches the centerplane (indicated by the broken black line in Figure 5.13) and even crosses it. Thus, after some time, non-zero probabilities occur for the surfaces that intersect the centerplane.

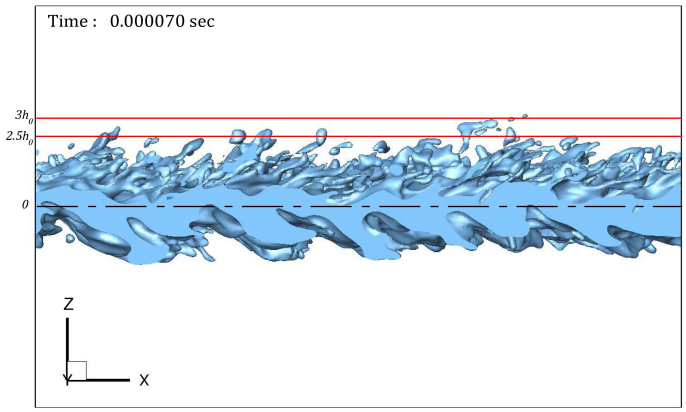

Figure 5.13: Side-view of the liquid surface at $t = 70$ μs; $We_g = 1500$, $Re_l = 2500$, $\hat{\rho} = 0.5$, $\hat{\mu} = 0.0066$, and $\Lambda = 2.0$. Gas flows from left to right.

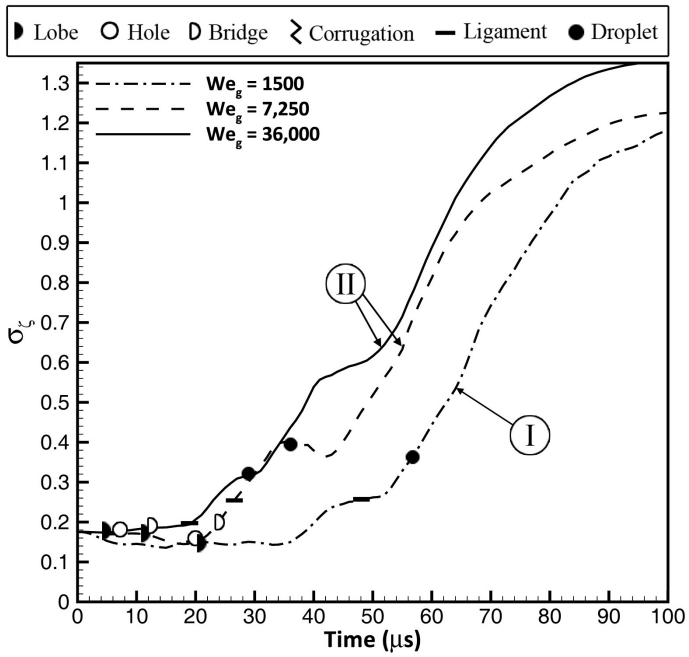

Figure 5.14: Temporal variation of the standard deviation of the dimensionless spray-width PDFs of Fig. 5.11 for $We_g = 1500$, 7250, and $36,000$; $Re_l = 2500$, $\hat{\rho} = 0.5$, $\hat{\mu} = 0.0066$, and $\Lambda = 2.0$.

Figure 5.14 shows the standard deviation of the spray-width PDFs of Figure 5.11. Initially, the standard deviation is slightly below $0.2h_0 = 10$ μm, which is exactly equal to the peak-to-peak amplitude of the initial perturbations. At early times, as the waves stretch in the streamwise direction, their amplitude decreases; hence, a larger portion of the interface gets closer to the initial sheet surface. This reduces the standard deviation of ζ. This reduction is greater for lower We_g because of the stabilizing role of surface tension. Later, as the spray expands, the distance between the outermost and the innermost liquid surface grows, and the spray-width PDF gets wider; see Figure 5.11. The standard deviation increases with increasing We_g. The rate of increase of standard deviation decreases at about 70 μs for the highest We_g and at 90 μs for the lowest one. The reason for this change in pace is that, beyond this point, some kind of saturation occurs in the computational box by the broken liquid blobs that get too close to the top and bottom boundaries; notice that the liquid particles cannot leave the box from the normal boundaries. This could clearly influence the dynamics of atomization. Thus, the computations are not continued beyond 100 μs. A larger

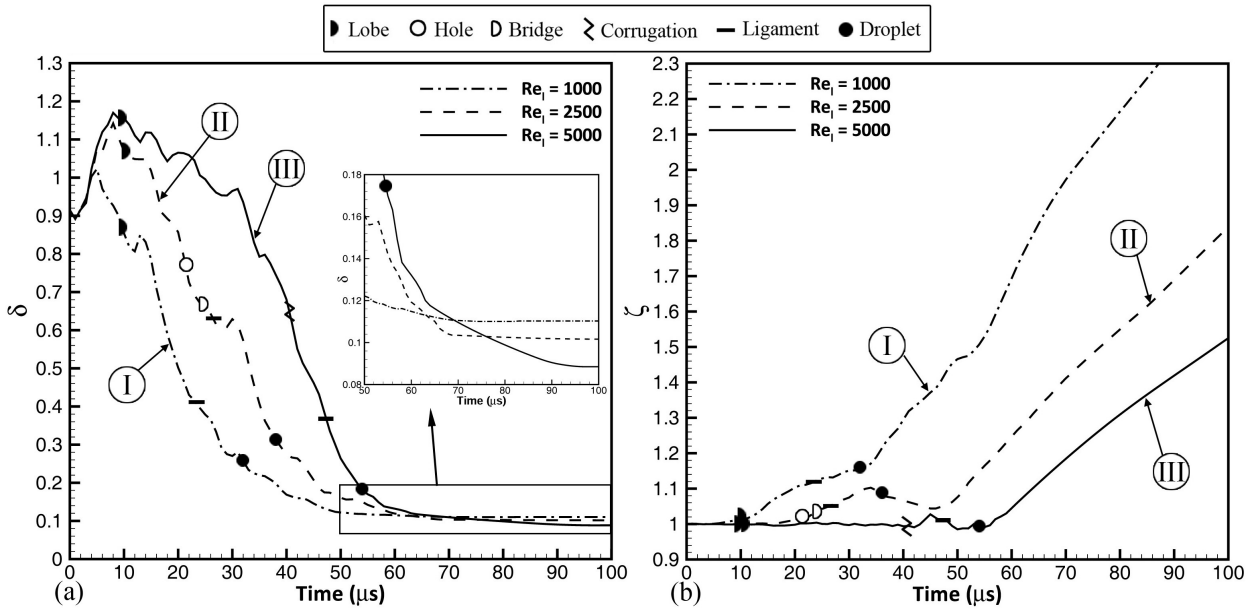

Figure 5.15: Effect of Re_l on the temporal variation of the average dimensionless length scale δ (a) and the average dimensionless spray width ζ (b); $We_g = 7250$, $\hat{\rho} = 0.5$, $\hat{\mu} = 0.0066$, and $\Lambda = 2.0$.

computational box is required if one would want to continue the analysis in time, but this is not plausible for this study due to its computational cost.

5.2.3 Reynolds number effects

Practically, Re_l should have a major effect on both the final droplet size and the spray angle as well as the rate of spray expansion or liquid structure cascade, since both the inertia and viscous effects are involved in these quantities. These effects are studied quantitatively here. Three different Re_l values are compared in this study; $Re_l = 1000$, 2500, and 5000 – each representing one of the domains in the We_g vs. Re_l plot with a particular breakup characteristic, as defined in Figures 3.2 and 3.1. $Re_l = 5000$ (in Domain III) and $Re_l = 1000$ (in Domain I) have the stretching characteristics during the primary breakup, with and without the corrugation formation, respectively. The $Re_l = 2500$ case follows the hole/bridge formation mechanism in Domain II.

Figure 5.15(a) demonstrates the effects of Re_l on the average length scale variation in time. As expected, the liquid surface is stretched more in the streamwise direction with increasing Re_l, creating flatter surfaces early on. Thus, as Re_l increases, relatively larger length scales occur at early times. For higher Re_l, the lobes stretch for a longer time before breakup, yielding maximum length scale at a later time. The actual breakup process and decrease of length scales occur later for higher Re_l.

After the early injection period, the rate of cascade of the large liquid structures, e.g. lobes and bridges, into smaller structures, e.g. corrugations, ligaments and droplets, is greater at higher Re_l, as observed from the mean slopes in Figure 5.15(a) in the downfall portion of the plot. By decreasing the liquid viscosity, i.e. increasing Re_l, with the other properties held constant, the breakup occurs faster and the rate of cascade of length scales grows. This can be attributed to the stabilizing effects of viscosity, which damps the small scale instabilities at low Re_l. Figure 5.15(a) also shows that Re_l affects the ultimate mean length scale. Even though the effect of Re_l on the final length scale is not as significant as We_g, the magnified subplot of Figure 5.15 shows that the asymptotic scale decreases from $0.11\lambda_0$ to $0.09\lambda_0$ as Re_l increases from 1000 to 5000. Even though the rate of cascade of length scales is larger at higher Re_l, the asymptotic length scale is achieved later for higher Re_l since the largest length scales are also larger for higher Re_l. The mean length scale of the highest Re_l case just becomes smaller than the two lower Re_l cases at about 75 μs. Negeed et al. [58] and Desjardins & Pitsch [16] also qualitatively showed that the final droplet size decreases with increasing Re_l; however, they did not quantify the droplet size nor its cascade rate.

Even though the formation of lobes is not affected much by Re_l, the ligaments and droplets form notably later as Re_l increases. This counter-intuitive fact is related to the process of ligament and droplet formation. At a constant We_g, the ligament formation in the $LoCLiD$ process (Domain III) is slower than in the $LoHBrLiD$ process (Domain II), and both are slower than that in the $LoLiD$ process (Domain I). All these cascade processes are explained

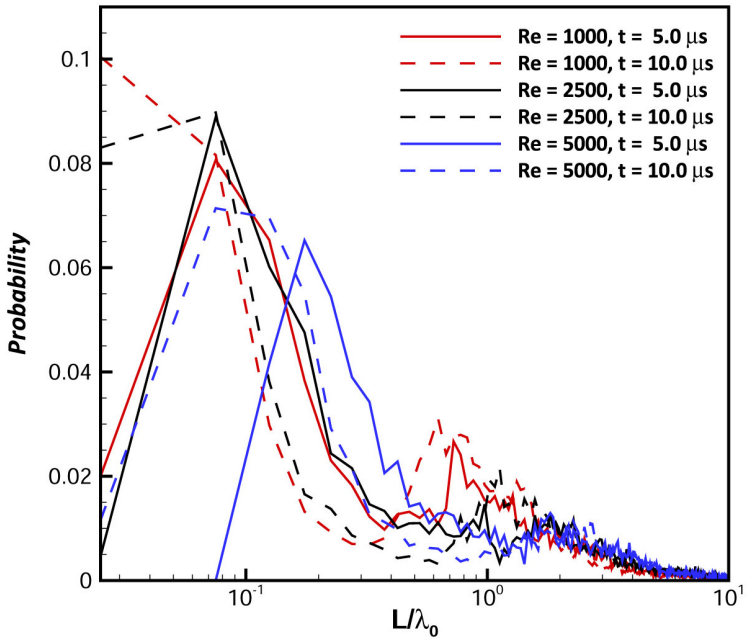

Figure 5.16: PDF of the normalized length scales at $t = 5$ μs (solid lines) and 10 μs (dashed-lines) for $Re_l = 1000$ (red line), $Re_l = 2500$ (black line), and $Re_l = 5000$ (blue line); $We_g = 7250$, $\hat{\rho} = 0.5$, $\hat{\mu} = 0.0066$, and $\Lambda = 2.0$.

via vortex dynamics in Chapter 4 [98]. It was shown that the formation of corrugations at higher Re_l takes longer and requires downstream advection of the split KH vortex by a distance of one wavelength (≈ 100 μm), until the hairpin vortices get undulated and induce the corrugations. The $LoHBrLiD$ process, on the other hand, requires only stretching and overlapping of the hairpins over the KH vortices, which occur faster. The $LoLiD$ mechanism involves cross-flow advection of the KH vortices, which occurs slightly more quickly. However, the droplets formed in the $LoCLiD$ process are smaller than in the other two processes, and the $LoLiD$ process results in the thickest ligaments and the largest droplets.

To better understand the difference in the mean length scale for the three Re_l cases at early injection stage, the length scale PDFs for these cases are plotted at 5 μs and 10 μs in Figure 5.16. Both times are within the initial injection period when the maximum length scale occurs; see Figure 5.15(a). The $Re_l = 1000$, 2500, and 5000 cases are shown by red, black, and blue lines in Figure 5.16, respectively. The PDFs are denoted by solid lines at

5 μs and by dashed lines at 10 μs.

The highest Re_l (blue line) has the highest probability of larger length scales ($L/\lambda_0 > 2.0$) at both 5 μs and 10 μs, confirming the earlier claim that higher Re_l causes more stretched surfaces and larger scales (less curved surfaces) early on. Even though the maximum distribution of the length scales moves to smaller scales from 5 μs to 10 μs for $Re_l = 5000$, the average scale still grows, as shown in Figure 5.15(a). In particular, a large population of the cells contains surfaces with very large length scales. As Re_l decreases, transition towards smaller scales occurs faster at these early times. Therefore, the mean length scale decreases sooner for lower Re_l. Clearly, there are two factors in determining the mean length scale: the sizes of the smallest and largest length scales, and the population of those scales. At an early stage, i.e. $t < 10$ μs, the smallest as well as the largest length scales are the same for all cases; however, it is the population of those small scales compared to the large ones that determines the mean scale. Since there are more large scales at higher Re_l, more time is needed for those structures to cascade to smaller scales; thereby, the mean length scale keeps growing for a longer period at higher Re_l. After this initial period, however, the cascade is faster for the higher Re_l because of the lower viscous resistance against surface deformation; therefore, the smallest bin gets populated at a higher rate.

There are two distinct spikes in the length-scale PDFs of Figure 5.16 at 5 μs – one at a low

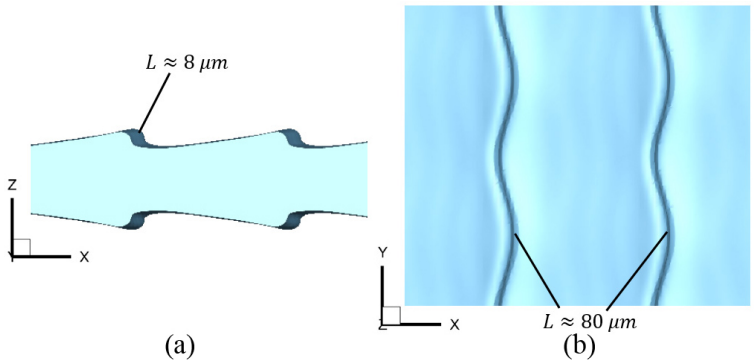

Figure 5.17: Liquid surface at $t = 5$ μs from a side view (a), and top view (b); $Re_l = 1000$, $We_g = 7250$, $\hat{\rho} = 0.5$, $\hat{\mu} = 0.0066$, and $\Lambda = 2.0$.

scale of approximately $L = 0.08\lambda_0 = 8$ μm, and another with lower probability but larger scale of $L = 0.8\lambda_0 = 80$ μm for $Re_l = 1000$. Similar two spikes are seen for other Re_l cases at an early time. The cause of the two spikes is shown in Figure 5.17. The smaller scale represents the radius of curvature of the streamwise KH wave crest, which has the largest probability because this length scale exists for many cells along the spanwise direction on the front edge of the waves. This is shown in the side-view of Figure 5.17(a). The other spike with the larger length scale but smaller probability applies to the radius of curvature of the spanwise waves. These points are indicated on the top-view of Figure 5.17(b). This length scale occurs for all the cells near the tip of the protruded liquid lobe.

The conclusion from the above results is that there are two stages in the liquid-sheet distortion: (i) the initial stage of distortion when the lengths grow, and (ii) the final asymptote in time. Viscosity but not surface tension is dominant in the first stage, which is inertially driven, while surface tension more than viscosity affects the mean scale at the latter stage.

Figure 5.15(b) shows the effects of liquid viscosity on the jet width. Since liquid inertia dominates the viscous effects at higher Re_l, the spray is oriented more in the streamwise direction, and the mean spray width and accordingly the spray angle are smaller at higher Re_l. This is consistent with both numerical simulations [34] and experimental results [7, 54]. Mansour & Chigier [54] and Carvalho et al. [7] showed that the spray angle is reduced by increasing the liquid velocity (or mass flowrate); i.e. increasing Re_l. However, they only reported the final spray angle, but did not address its temporal growth. We show here that the growth rate of the spray angle (width) is lower at higher Re_l. The expansion of the spray starts much sooner in Domain I than in Domains II and III, and the asymptotic spray growth rate, indicated by the slopes in Figure 5.15(b), is lower for higher Re_l.

Even though both the lowest and the highest Re_l cases produce similar lobe stretching mechanisms, there is a significant difference in their spray expansion. At high Re_l, the corrugations on the lobes stretch into streamwise ligaments, resulting in thinner and hence

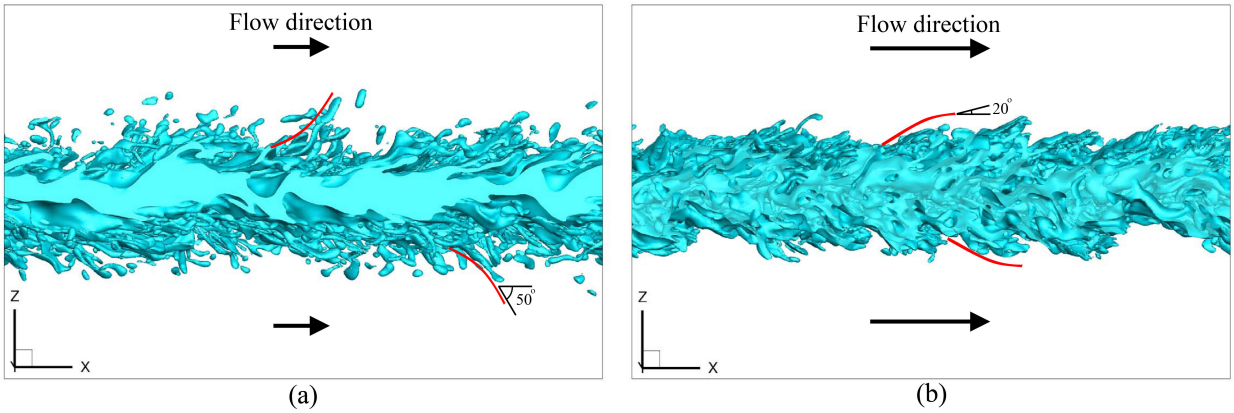

Figure 5.18: Liquid surface at $t = 70$ μs from a side view for $Re_l = 1000$ (a), and $Re_l = 5000$ (b); $We_g = 7250$, $\hat{\rho} = 0.5$, $\hat{\mu} = 0.0066$, and $\Lambda = 2.0$. The red lines indicate the qualitative form and angle of the ligaments.

shorter ligaments. The time lapse between ligament formation and ligament breakup is much shorter in Domain III since the ligaments are generally shorter and need less time to thin and break. At low Re_l, on the other hand, the lobes directly stretch into ligaments, and the stretching is oriented in the transverse (normal) direction as the viscous forces resist streamwise stretching caused by the inertia. It takes more time for the ligaments to break up into droplets. The ligaments are generally thicker and longer, as also shown for low Re_l by Marmottant & Villermaux [55]. This difference originates from the difference in the vortex structures of these two regimes, and shows that these two mechanisms have different causes from vortex dynamics perspective. As explained in Chapter 4, streamwise vortex stretching is stronger at higher Re_l, resulting in streamwise oriented ligaments.

The difference in the jet expansion rate at low and high Re_l manifests in the angle of ligaments that grow out of the liquid surface. This is clearly illustrated in Figure 5.18, where the liquid surface at a low Re_l (Figure 5.18a) and high Re_l (Figure 5.18b) are shown at 70 μs. The overall shape of ligaments is denoted by the red lines in this figure, and the average angle of the ligament tips (measured from the streamwise direction) are also indicated. At high Re_l, the lower viscous forces on the ligaments are not able to overcome the relatively high gas momentum, and the ligament angle decreases as it penetrates further into the gas. Thus, the

transverse velocity is much smaller than the streamwise velocity and the angle is small (about 20^o). On the other hand, the higher liquid viscosity at lower Re_l balances the gas inertia and opposes the streamwise stretching of the ligaments. Consequently, the ligament angle increases as it penetrates further into the gas, resulting in a 50^o angle at the ligament tip. The ligament shapes can be attributed to the velocity profile – the boundary layer becomes thinner and the velocity gradient in the z-direction becomes steeper as Re_l increases. These results are consistent with the temporal variation of ζ shown in Figure 5.15(b). Our results correctly predict that the asymptotic jet expansion rate ($\mathrm{d}\zeta/\mathrm{d}t$) is higher at lower Re_l. This was not the case for jet expansion rate versus We_g. This confirms that the reason for faster growth of jet width at higher We_g was mainly due to the fact that the droplets breakup faster and can be carried away by the vortices near the interface, which is completely different from the cause-and-effect of Re_l.

5.2.4 Density-ratio effects

The effect of density ratio ($\hat{\rho}$) on the average liquid-jet length scale is shown in Figure 5.19(a). Three density ratios are studied in a range of 0.05 (low gas pressure) to 0.9 (high pressure gas). The liquid Weber number, and thereby the surface tension coefficient, is kept the same for all three cases; thus, We_g is also different for these three cases through gas density. The lowest $\hat{\rho}$ falls in Domain I, where lobes stretch directly into ligaments, and the other two higher density ratios belong to Domain II, and involve hole and bridge formation in their breakup.

$\hat{\rho}$ has only a slight effect on the final length scale. All cases asymptotically reach a nearly similar average length scale of about $0.1\lambda_0$, with the final length scale being slightly smaller ($\approx 0.09\lambda_0$) for the lowest $\hat{\rho}$ (dash-dotted line in Figure 5.19a). Besides, $\hat{\rho}$ clearly affects the rate at which the ultimate length scale is achieved. The rate of length-scale cascade is higher

at lower gas densities. As $\hat{\rho}$ increases, the cascade of length scales becomes slower. The asymptotic length scale is achieved at 64 μs for $\hat{\rho} = 0.05$, but at about 68 μs for $\hat{\rho} = 0.5$, and at 70 μs for $\hat{\rho} = 0.9$. As denoted by the symbols in Figure 5.19(a), the rate of ligament and droplet formation is notably affected by $\hat{\rho}$. As $\hat{\rho}$ grows, so that the Domain changes from I to II, the ligament and droplet formation rates undergo a large jump. As $\hat{\rho}$ keeps increasing in the same Domain (II), the ligaments and droplets form faster, but the difference is not as notable as the jump during the domain transition. Jarrahbashi et al. [34] also showed that the drops form earlier at higher $\hat{\rho}$; however, they did not address the relation between this trend and the change in the breakup process. As gas density increases, the higher gas inertia intensifies the hole formation, therefore expediting the formation of ligaments and droplets.

$\hat{\rho}$ does not alter the initial length-scale growth rate significantly – the maximum scale occurs at nearly the same time – which proves it to be correlated with the liquid inertia and not the gas inertia. The asymptotic stage is also driven by the liquid inertia and is almost independent of the gas density in the $\hat{\rho}$ range considered here. As shown in Section 5.2.2,

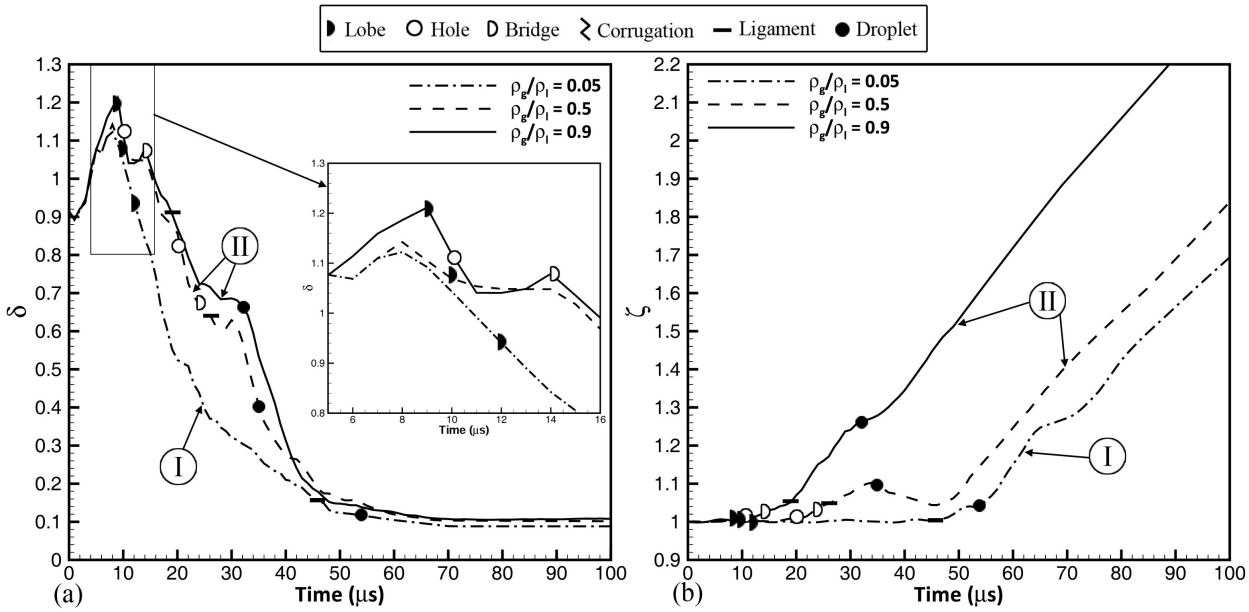

Figure 5.19: Effect of density ratio on the temporal variation of the average dimensionless length scale δ (a), and the average dimensionless spray width ζ (b); $Re_l = 2500$, $We_l = 14,500$, $\hat{\mu} = 0.0066$, and $\Lambda = 2.0$.

this stage is also correlated with surface tension. Therefore, the liquid Weber number (We_l) and not the gas Weber number (We_g) is the key parameter in determining the asymptotic droplet size – discussed more in this section.

Figure 5.19(b) shows the temporal variation of the average spray width for low, medium, and high density ratios. ζ increases with increasing $\hat{\rho}$, similar to the findings of Jarrahbashi et al. [34] for round jets. The jet with the highest $\hat{\rho}$ (solid line in Figure 5.19b), which approximates a homogeneous liquid jet, expands much more rapidly than the case with smaller $\hat{\rho}$ (dash-dotted line). The spray width grows from its initial thickness at 10 μs for the highest $\hat{\rho}$, while the expansion is postponed to 46 μs for the lowest $\hat{\rho}$. Some researchers have reported growth of the spray angle with increasing $\hat{\rho}$ or gas-to-liquid momentum ratio [7, 34] – based on the final stage of the fully-developed jet – but none has shown the temporal growth of the spray to be correlated with $\hat{\rho}$. Our results show that the jet expansion rate is also higher at higher $\hat{\rho}$.

Even though the average spray expansion rate is lower for lower gas densities, the asymptotic expansion rate is nearly the same after a long time from the start of the injection, regardless of $\hat{\rho}$. This is seen from the slopes of the curves in Figure 5.19(b), which become approximately equal near the end of the computations; i.e. the asymptotic slopes appear to be independent of the gas density. Jarrahbashi et al. [34] also found that the spray expansion rate is higher at higher $\hat{\rho}$ for circular jets. However, they used the traditional definition for the jet size, i.e. distance of the farthest continuous liquid structure from the centerline, which would be ambiguous in some cases, as discussed.

The lower spread rate for low $\hat{\rho}$ is directly related to the vortex dynamics near the interface. The main cause of the lower expansion is the baroclinic effects which are drastically different amongst the range of density ratios considered here. Due to the larger density gradient, the baroclinic torque is higher at low gas densities. Thus, the vortex cores locate farther from the interface [98]. The induced flow of the vortices away from the interface entrains more

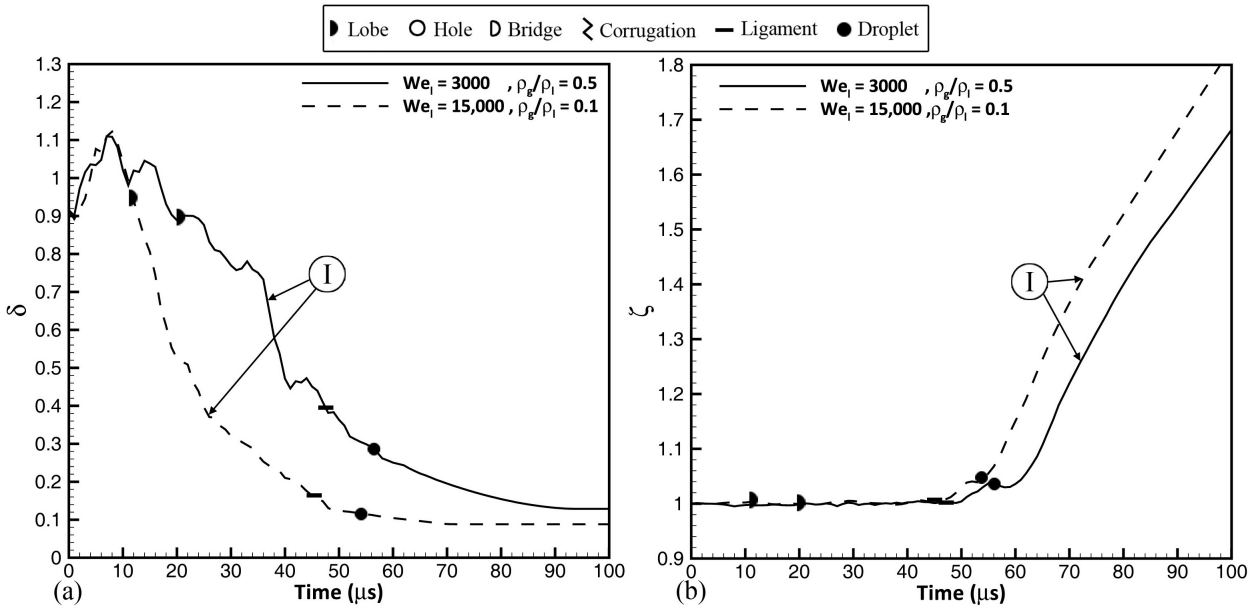

Figure 5.20: Effects of density ratio and We_l on the temporal variation of the average dimensionless length scale δ (a), and the average dimensionless spray width ζ (b); $Re_l = 2500$, $We_g = 1500$, $\hat{\mu} = 0.0066$, and $\Lambda = 2.0$.

gas into the mixing layer and expedites the two-phase mixing [34]. However, if the vortices remain closer to the interface, as in higher gas densities, KH roll-up occurs more vigorously, causing a higher growth rate of the instabilities and a faster transverse expansion of the jet. The detailed analysis of vortex dynamics and its connection with surface dynamics was provided in Chapter 4.

Since an increase in $\hat{\rho}$ increases the spray width and expansion rate, and the sheet expansion is also directly proportional to the liquid We (shown in Section 5.2.2), both We_l and $\hat{\rho}$ affect similarly the jet expansion. It is interesting now to examine the effects of We and $\hat{\rho}$ combined with the gas-phase Weber number (We_g). This is delineated in Figure 5.20(b), where the temporal evolution of the spray width for two cases that overlap at the same point in the We_g–Re_l map of Figure 3.2 are compared; both cases have the same $We_g = 1500$, but different $\hat{\rho}$ and We_l. Since $We_g = \hat{\rho} We_l$, $\hat{\rho}$ and We_l should change in opposite directions to keep We_g constant; i.e. as $\hat{\rho}$ increases (increasing the jet expansion), We_l should decrease (decreasing the jet expansion). Figure 5.20(b) shows that the two cases behave very

similarly in temporal expansion; both sprays expand at almost the same time and at the same asymptotic rate. The rate of ligament and droplet formation is also comparable in these two cases – consistent with Equation (5.8) – where the ligament stretching time scale τ_s is inversely proportional to Re_l, but independent of the Weber number. Since both cases in Figure 5.20 have equal Re_l, their ligament stretching rates are also nearly equal. Therefore, the two parameters, We_l and $\hat{\rho}$, could be combined into a single parameter We_g for jet expansion analysis. The gas inertia – and not the liquid inertia – and liquid surface tension are the key parameters in determining the spray width. This confirms We_g to be the proper choice for categorizing the liquid-jet breakup characteristics, as used in Chapter 3.

In Section 5.2.2, it was shown that a decrease in surface tension reduces the asymptotic droplet size and the average liquid-structures length scale. $\hat{\rho}$, however, has negligible effect on the average length scale. Thus, We_l is expected to be the key factor in determining the final droplet size. Figure 5.20(a) confirms this notion and shows that even though the two cases have the same We_g, they manifest a significant difference in the cascade process and the asymptotic length scale. Since the case with higher $\hat{\rho}$ has a lower We_l – keeping We_g constant – it produces larger average length scales and has a slower cascade. Thus, the liquid inertia is also important for the liquid structure cascade. Even though two jets at the same Re_l and We_g exhibit the same atomization mechanism (both from Domain I), the length scales of the resulting liquid structures depend on the density ratio. The lower gas density would result in finer structures. In other words, the atomization domain only determines the breakup quality (the type of process during the cascade), but other factors need to be considered to control the quantitative characteristics of the atomization; e.g. droplet size and structure length scales.

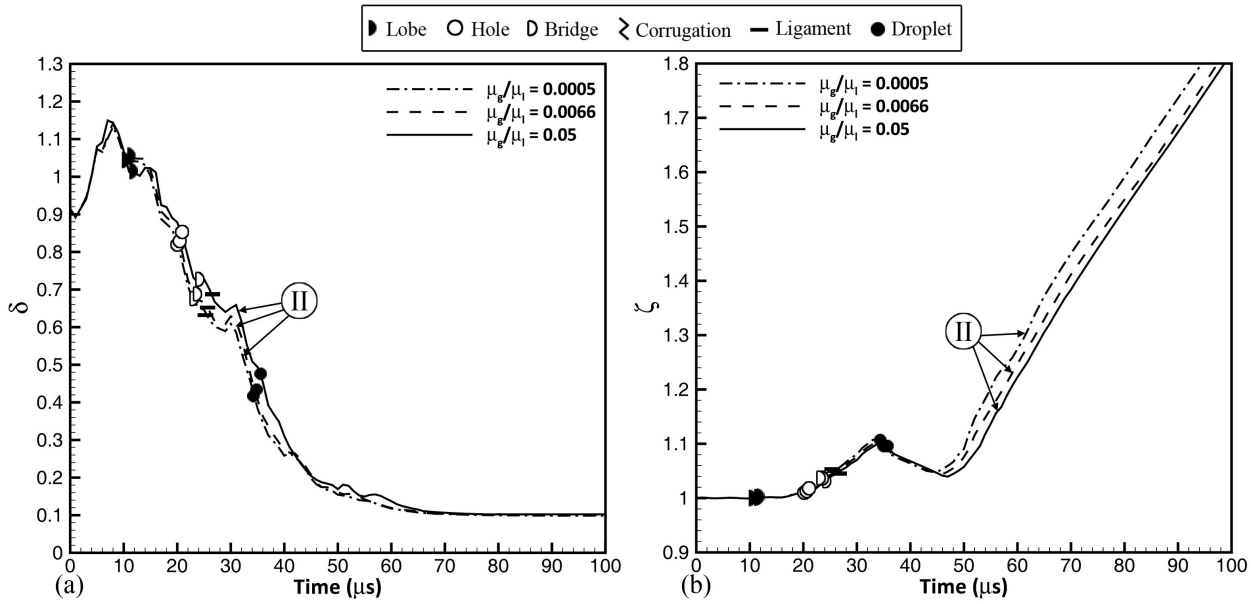

Figure 5.21: Effect of viscosity ratio on the temporal variation of the average dimensionless length scale δ (a), and the average dimensionless spray width ζ (b); $Re_l = 2500$, $We_g = 7250$, $\hat{\rho} = 0.5$, and $\Lambda = 2.0$.

5.2.5 Viscosity ratio effects

Stapper et al. [83] showed that viscosity ratio ($\hat{\mu}$) has little or no effect on the final droplet size (i.e. Sauter mean diameter) of liquid jets. Here, the same conclusion is reached, as shown in Figure 5.21(a). A wide range of viscosity ratios $0.0005 < \hat{\mu} < 0.05$ covering three orders of magnitude are compared here. All cases follow the same cascade with an almost identical rate. The cascade is delayed less than a few microseconds in the period 10–40 μs for higher $\hat{\mu}$, but the small difference vanishes at later times. The asymptotic length scale is the same for all viscosity ratios, i.e. about $0.1\lambda_0 = 10$ μm, and the rate of droplet formation also remains the same regardless of $\hat{\mu}$. The gas viscosity is the least important factor in determining the droplet size and has no effect on the structure stretching and length scale growth in the initial stage; i.e. at $t = 0$–10 μs.

Moreover, $\hat{\mu}$ does not have a notable influence on the expansion rate of the sheet either. As plotted in Figure 5.21(b), the sheet expands at the same time regardless of the gas viscosity.

The growth rate of the sprays, i.e. the slopes of the curves in Figure 5.21(b), is also the same at the end of the process for all viscosity ratios. The only minor difference is that the spray growth gets delayed a few microseconds as gas viscosity increases. This minor variation over three orders of magnitude $\hat{\mu}$ variation is insignificant. Therefore, the gas viscosity is not important in determining the spray angle and its growth rate, as it was not also for the mean droplet size. The importance of viscosity only manifests through Re_l, where an increase in the liquid viscosity, i.e. lowering Re_l, increases the size of droplets and increases the spray angle, as discussed in Section 5.2.3.

5.2.6 Sheet thickness effects

Senecal et al. [79] showed that ligament diameter is directly proportional to the initial sheet thickness. Our results, illustrated in Figure 5.22(a), confirm their findings; the length scales grow as the sheet thickens. For this comparison, two sheets of different widths have been analyzed – a thin sheet of 50 μm thickness with $\Lambda = 2.0$ and a thicker sheet of 200 μm thickness with $\Lambda = 0.5$. The initial perturbation wavelength is the same for both cases – i.e. $\lambda_0 = 100$ μm.

The cascade occurs much slower and the mean length scale oscillates more in its cascade process for the thicker sheet; see Figure 5.22(a). The extra oscillations found in the thicker sheet occur because the initial KH waves take more time to stretch and break into smaller structures as sheet thickness increases. This is explained via vortex dynamics of the interface deformation, where the two vortex layers on top and bottom of the sheet become farther apart and more independent as the sheet becomes thicker. The interaction between the two vortex layers is more intense for the thinner sheets – a simple consequence of Biot-Savart mutual induction between the vortices in the two layers – and consequently the cascade occurs faster under the local induction of these two vortex layers [98]. As the initial sinusoidal KH wave

stretches in the streamwise direction, the curvature of the interface decreases and the mean length scale grows; as the waves roll over the vortices and the lobes form, the mean length scale decreases. If the waves dampen again, the length scale temporarily increases until the next waves start to grow. The process of wave stretching and curling occurs continuously until the lobes stretch enough to cascade into smaller structures; e.g. ligaments and droplets. Because of the higher local induction of the KH vortex layers on top and bottom surfaces, the transition towards antisymetry is also faster for thinner sheets, which helps bringing down the length scales more quickly. The length scale keeps on decreasing until the asymptotic length scale is achieved. Increasing sheet thickness also significantly delays the structure formations on the sheet surfaces. The lobes and ligaments form respectively 40 μs and 60 μs later on the thick sheet than on the thin sheet.

The asymptotic length scales for the thin and thick sheets are $0.1\lambda_0$ and $0.46\lambda_0$, respectively – agreeing with the findings of Senecal et al. [79]. Based on their analytical study, the ligament size should be directly proportional to the initial sheet thickness; thus, as the sheet

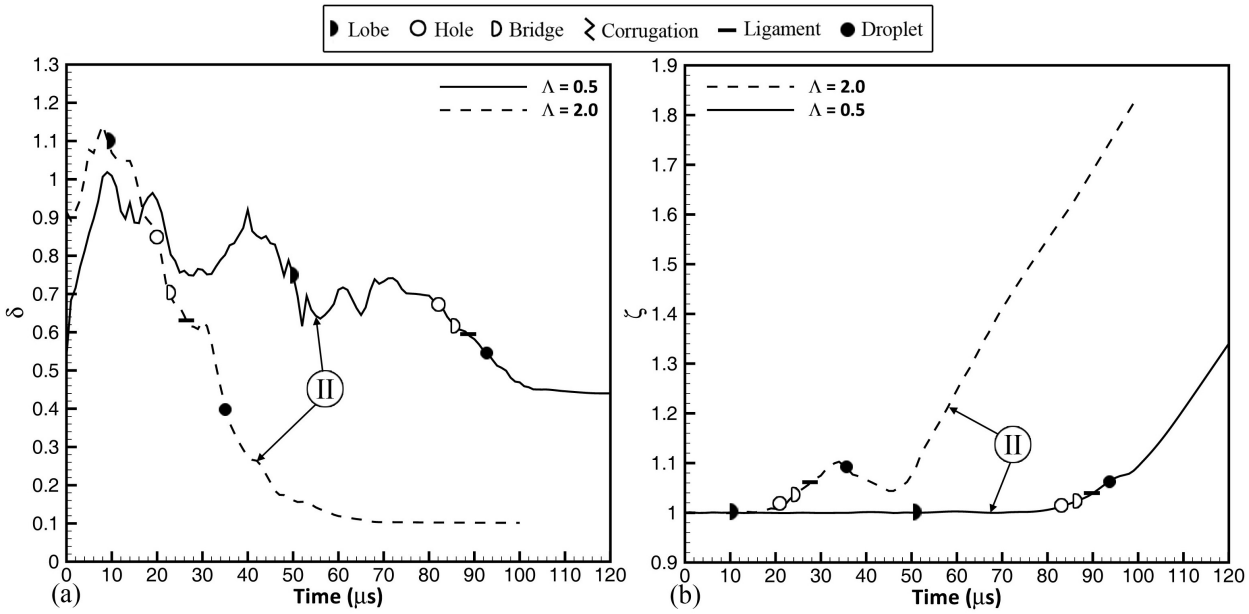

Figure 5.22: Effect of sheet thickness on the temporal variation of the average dimensionless length scale δ (a), and the average dimensionless spray width ζ (b); $Re_l = 2500$, $We_g = 7250$, $\hat{\rho} = 0.5$, and $\hat{\mu} = 0.0066$.

becomes four times thicker, the mean ligaments size should increase by a factor of four. Since the larger length scales caused by the curvature of the waves are also included in our mean length scale calculation, the ratio of the mean length scale for the thick-to-thin sheets in our case is about 4.6 – in fairly good agreement.

The spray expansion is significantly delayed as the sheet thickness increases; see Figure 5.22(b). While the thin sheet expands at 20 μs, the expansion of the thicker jet does not start until 80 μs. Even though a thin sheet has higher growth rate at the early stages of spray formation, the thicker sheet achieves a comparable growth rate at its final stage. This is seen from the slopes of the solid and dashed-lines in Figure 5.22(b) at the end of the processes, where the slopes are quite equal. This major difference in the jet width is caused by the reduced influence of the vortex layers in the thicker sheet, resulting in a slower shift towards antisymmetry as the vortex layers get farther apart. Since the mean spray width is normalized by the initial sheet thickness, the absolute growth rate of the thicker sheet in the final phase is much higher than the thin sheet. The instantaneous growth rates become the same after the vortices have grown sufficiently and both sheets have become totally antisymmetric. At this final stage, the vortices in the two layers are equally effective in influencing each other via mutual induction and thus the effect is independent of the sheet thickness.

5.2.7 L_{32} calculation

In liquid-jet atomization, the injector designer is usually interested in the average size based on mass distribution. Sauter mean diameter (SMD, d_{32}) is an average of particle size, defined as the diameter of a sphere that has the same volume/surface-area ratio as a particle of interest, normally used in the literature for this purpose. SMD is calculated using the

following equation;

$$\text{SMD} = \frac{\Sigma_i N_i d_i^3}{\Sigma_i N_i d_i^2}, \tag{5.11}$$

where N_i is the number of droplets per unit volume in size class i, and d_i is the droplet diameter.

The main assumption in SMD calculation is that all the liquid particles are in form of spherical droplets. For the early atomization period considered here, however, a combination of droplets, ligaments and unbroken surfaces exist at the end of computations (see Figure 5.6). Therefore, more than just the droplet diameter is considered for the measurement of the mean length scale of the spray. Specifically, the Sauter mean diameter is generalized by considering the scales (radius of curvature) of all the droplets, ligaments, waves, and any other liquid structures either broken or still attached to the jet core. In this respect, we present the mean length scale weighted on both spherical droplets (L_{32}) and cylindrical ligaments (L_{21}).

Similar to SMD (Equation 5.11), we calculate a mean based on the length scale L_i and its probability $P(L_i)$. This parameter, called L_{32}, is defined as

$$L_{32} = 2\frac{\Sigma_i P(L_i) L_i^3}{\Sigma_i P(L_i) L_i^2}. \tag{5.12}$$

Since L_i asymptotes to the droplet radius after all of the jet has broken into droplets, a coefficient of 2 is multiplied in Equation (5.12) in order to make it comparable to the mean diameter rather than radius. All the length scales greater than 100 μm are neglected in this analysis since those length scales are much larger than even the largest droplet diameters and instability wavelengths in our computations, and do not represent liquid structures but rather some flat surface on the interface. Consequently, L_{32} is expected to be much larger than SMD in such a parameter range. L_{32} is calculated after the length scales reach a constant

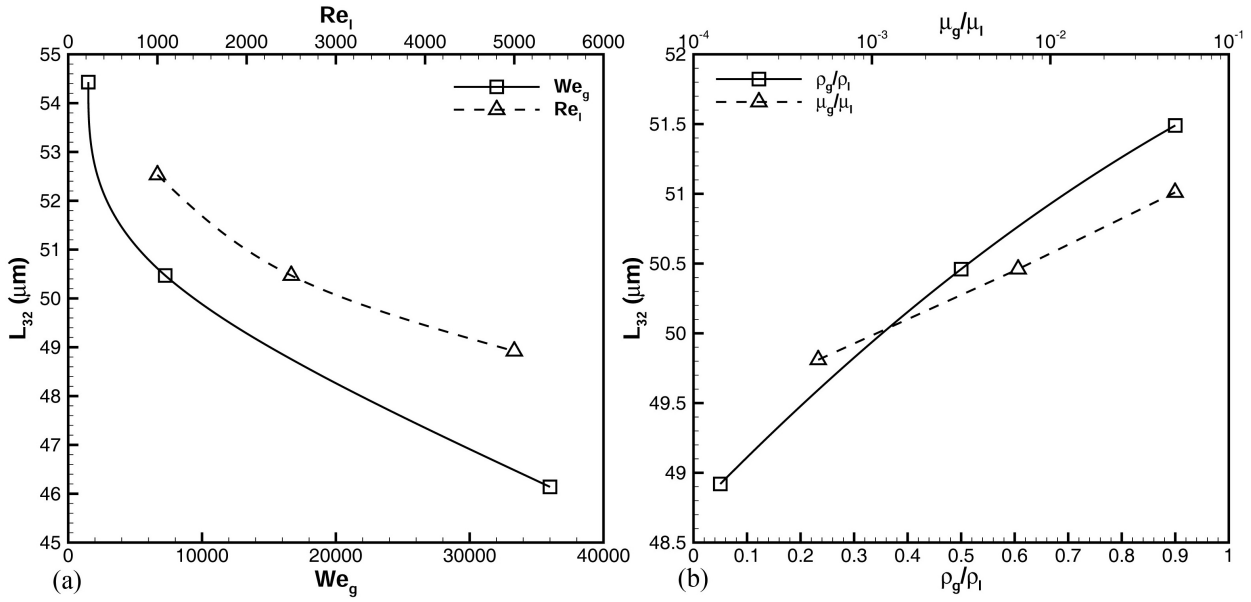

Figure 5.23: Effects of We_g and Re_l (a), and $\hat{\rho}$ and $\hat{\mu}$ (b) on L_{32}; $Re_l = 2500$, $We_g = 7250$, $\hat{\rho} = 0.5$, and $\hat{\mu} = 0.0066$.

value at the end of the computations, and it is expected to reach SMD asymptotically at later time.

The effects of We_g and Re_l on L_{32} are shown in Figure 5.23(a). As expected, We_g has the most significant influence on L_{32}, where it decreases from 54.5 μm to less than 46 μm as We_g is increased from 1500 to $36,000$. Even though this decrease is not as huge as was predicted by Varga et al. [88] for SMD – since all the length scales are not attributed to droplets only – its influence is more significant than of the other parameters. The dependence of SMD on We_g as given by Varga et al. [88] is limited to a much smaller We_g range than considered in our study. Our study shows that, at the higher range of We_g, the effect of We_g is not as pronounced as at lower ranges, though certainly not negligible.

Increasing Re_l also reduces L_{32}, as shown in Figure 5.23(a). The difference in L_{32} is slightly over three microns over the range of Re_l considered in this study; i.e. $1000 < Re_l < 5000$. However, Re_l clearly influences L_{32} and the final droplet size, as was discussed in Section 5.2.3. Both the range of L_{32} and its behavior with respect to Re_l are in fair agreement

with results of Lozano et al. [52]. The decrease in L_{32} becomes more gradual at high Re_l.

Figure 5.23(b) shows the effects of $\hat{\rho}$ and $\hat{\mu}$ on L_{32}. Both parameters have very minor influence on L_{32} compared to Re_l and We_g; even though $\hat{\mu}$ changes over three orders of magnitude and $\hat{\rho}$ ranges from 0.05 to 0.9, the difference in L_{32} is only slightly over 1 μm. L_{32} slightly increases with increasing $\hat{\rho}$ and $\hat{\mu}$, where the rate of increase is higher at lower $\hat{\rho}$ ranges. In the ranges covered here, the dependence on $\hat{\rho}$ becomes almost linear at high density ratios ($\hat{\rho} > 0.5$), while the dependence on $\hat{\mu}$ is completely linear on the log-scale.

The results presented in Figure 5.23 identify the trend in length scale growth or decline for the most important parameters; however, the differences are not very large compared to SMD measurements available in the literature. The reason behind this observation is that there are still many unbroken liquid structures with large scales in the flow field, which have higher influence on the L_{32} and increase its value; thus, the L_{32} measurements end up much closer to each other.

L_{32} is based on the assumption that the disintegrated elements are spherical droplets, and it gives a volume-to-surface weighting. In the primary atomization period considered here, however, much of the mass will be closer to cylinders (ligaments) rather than spheres. Thus, a comparison between L_{21} (Equation 5.13) might be more suitable, as it gives the volume-to-surface area weighting for a cylinder;

$$L_{21} = 2\frac{\Sigma_i P(L_i) L_i^2}{\Sigma_i P(L_i) L_i}. \tag{5.13}$$

Figure 5.24 shows that (as expected) L_{21} magnifies the difference between the non-dimensional parameter values. Even though the trends of L_{21} and L_{32} are very similar, more than 12 μm and 9 μm difference in the value of L_{21} is observed over the range of We_g and Re_l considered here, respectively. This indicates that the diameter of ligaments decreases significantly as

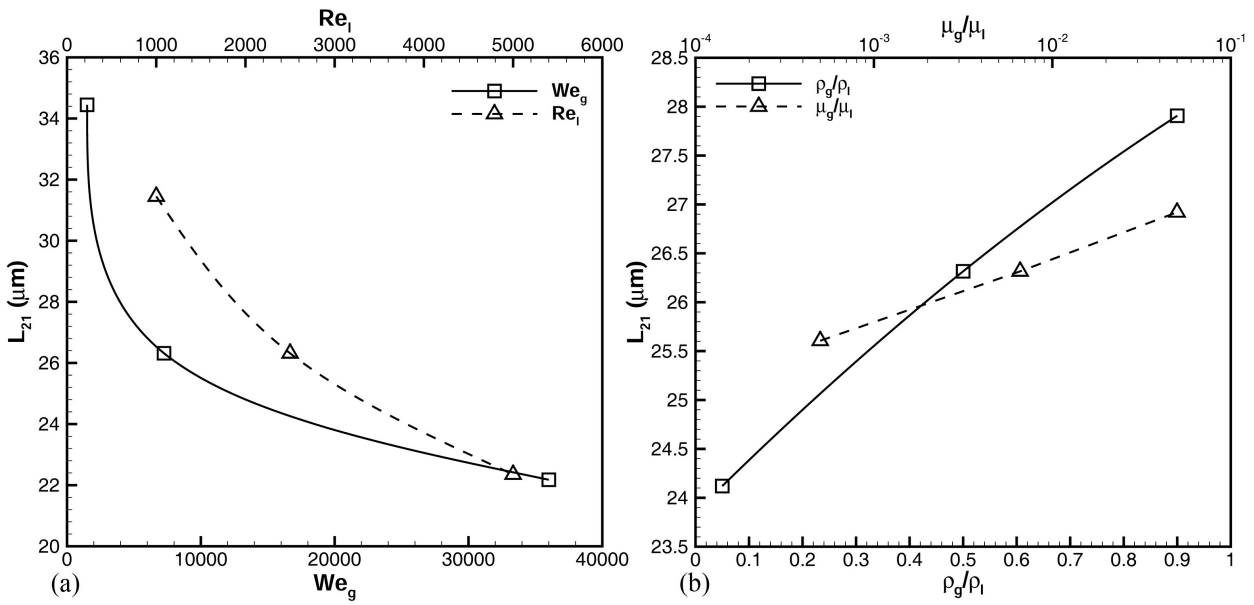

Figure 5.24: Effects of We_g and Re_l (a), and $\hat{\rho}$ and $\hat{\mu}$ (b) on L_{21}; $Re_l = 2500$, $We_g = 7250$, $\hat{\rho} = 0.5$, and $\hat{\mu} = 0.0066$.

the atomization domain is moved from Domain I to Domain III, following an increase in Re_l, or as the atomization moves from Domain I to Domain II, due to an increase in We_g. Both of these behaviors are in accordance with the characteristics of the atomization domains and the form of ligaments introduced in these three domains; see Figure 3.1. Figure 5.24(b) shows that in Domain II ($Re_l = 2500$, $We_g = 7250$), lowering $\hat{\rho}$ reduces the size of ligaments. This is consistent with the influence of $\hat{\rho}$ on the KH vortex structures downstream of the waves, as was indicated in Chapter 4. The lobe rims become thicker as $\hat{\rho}$ increases, resulting in thicker liquid bridges and consequently thicker ligaments after bridge breakup. The effects of viscosity ratio on the size of ligaments can be neglected compared to the other parameters. Viscosity ratio was also shown to have no effect on the atomization mechanisms and the vortex dynamics near the interface (Chapters 3 and 4).

The use of the approximation $R_d \approx 1.67R_1$ (introduced earlier) yields a new $L_{32} \approx 1.67L_{21}$ for droplets formed from these ligaments. This new L_{32} is notably smaller than the values in Figure 5.23.

5.2.8 Spray angle

Even though it is not possible to directly measure the spray angle in temporal studies like ours, we have calculated the spray angle using the spray width and length in this section. The spray angle α is twice the half-angle θ, as shown in Figure 5.25. The spray width (h_{max}) can be measured at any time from the simulations. The distance that the liquid jet has traveled (penetration length, l), however, needs further analysis, since it cannot be measured directly. The penetration length of the jet at any instance can be obtained by integrating the jet convective velocity (U_c) from the beginning of the simulation; i.e. $l = \int_0^t U_c \mathrm{d}t$. U_c is the liquid-jet convective velocity, also known as Dimotakis velocity [17], $U_c = (U_l + \sqrt{\hat{\rho}} U_g)/(1 + \sqrt{\hat{\rho}})$. The convective velocity represents the velocity of the interface at the base of KH waves. Since the liquid velocity U_l grows with time, U_c is not constant and needs to be measured at every time step. The spray angle can then be calculated from the following relation;

$$\alpha = 2\theta = 2\tan^{-1}\left(\frac{h_{max} - h_0}{2l}\right). \tag{5.14}$$

Using Equation (5.14), the spray angle is measured in time and is presented in Figure 5.26. In these plots, the values are for the converged value of the spray angle, after which the angle remains almost constant in time.

As shown in Figure 5.26(a), Re_l has the most significant impact on the spray angle, which

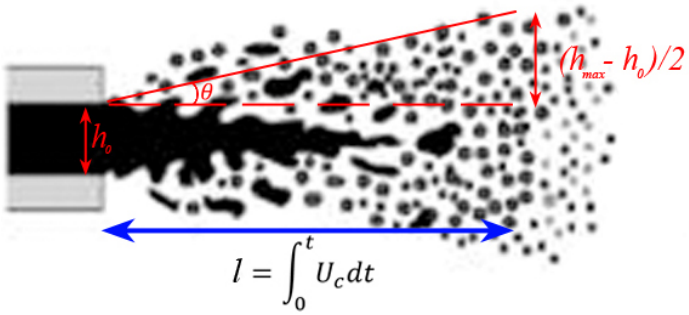

Figure 5.25: Definition of the spray angle, penetration length, and expanded width.

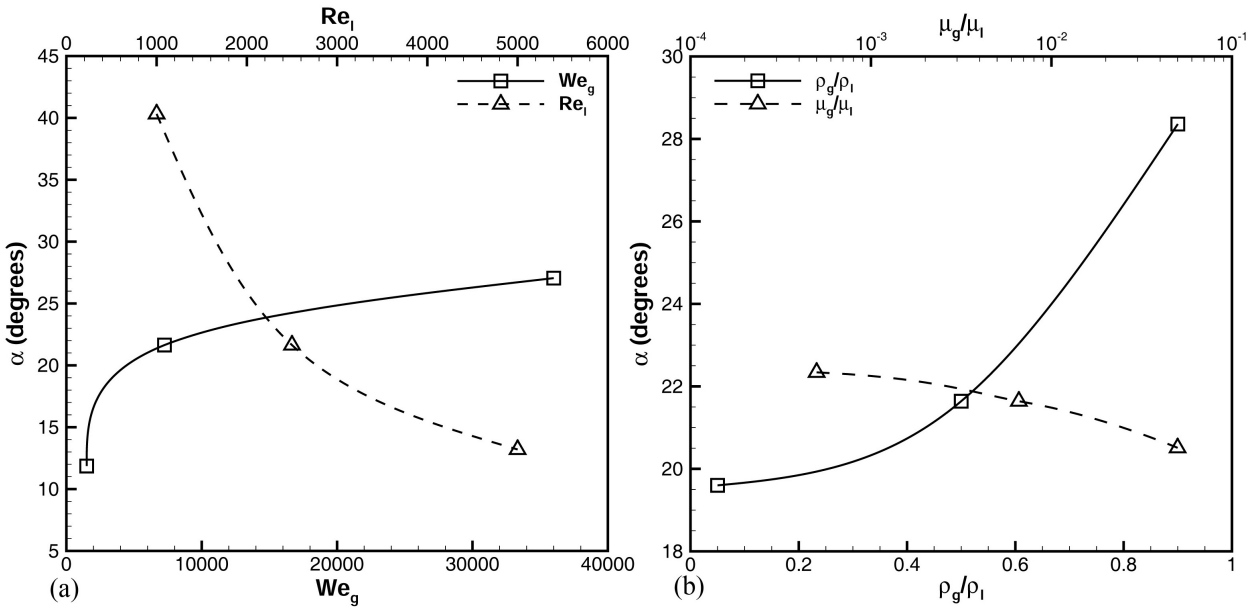

Figure 5.26: Spray angle α as a function of We_g and Re_l (a), and $\hat{\rho}$ and $\hat{\mu}$ (b); $Re_l = 2500$, $We_g = 7250$, $\hat{\rho} = 0.5$, and $\hat{\mu} = 0.0066$.

decreases with increasing Re_l, but less so at higher Re_l. Both the range of spray angle and its trend are in good agreement with the experimental results of Mansour & Chigier [54] and Carvalho et al. [7] at high liquid mass flow rate. Both of these studies show that α becomes almost independent of the mass flow rate (or Re_l) at very high liquid velocity (or Re_l). In our results, α decreases from 41° to about 13° as Re_l increases from 1000 to 5000, because of the reasons that were detailed in discussion of Figure 5.18. As was shown for low Re_l, the ligaments bend and grow normally away from the surface, thus increasing the transverse expansion of the spray and the spray angle. It was shown in Chapter 4 that the KH vortices convect away from the interface faster in domain I (low Re_l) compared to domains II and III. Thus, as Re_l increases and the breakup regime moves from domain I to domains II and III, the vortices remain closer to the interface and the transverse growth is hindered.

We_g has an opposite effect on the spray angle compared to Re_l (Figure 5.26a). The increase in We_g increases the spray angle, but this variation becomes less effective at higher We_g. At very low We_g, the surface tension is very large and prevents the transverse growth of the instabilities, which results in small α. As We_g increases, the instability growth rate increases

– due to the smaller surface tension resistance – and the spray angle increases. Since the breakup of ligaments occurs faster at high We_g, the broken ligaments and droplets can be easily carried in the transverse direction by the gas flow; this increases the spray angle. The far-field gas stream bounds the transverse growth of the spray, and prevents the spray angle from growing indefinitely with increasing We_g; thus, the spray angle grows very gradually at very large We_g. Also, as We_g increases, the breakup regime of the liquid jet moves from Domains I/III to Domain II (Figure 3.2), where the movement of vortical structures are mostly in the normal direction [98]. This contributes to increase of α.

Figure 5.26(b) shows that $\hat{\rho}$ also has a significant effect on the spray angle, but $\hat{\mu}$ effects are almost negligible. The effect of density ratio on the growth of instabilities and spray angle is consistent with vortex dynamics analyses of Hoepffner et al. [29] and Zandian et al. [98]. Both theses studies show that at higher density ratios, the KH vortex remains closely downstream of the KH waves and rolls up the KH waves and increases the growth of instabilities. At low $\hat{\rho}$ on the other hand, the downstream KH vortex fails to roll gas and liquid together, but takes the form of a gas vortex sheltered from the main stream by the liquid body of the wave [29]. The wave grows a tongue which undergoes flapping. Liquid drops are torn from the wave through this flapping motion, and sent partly off to the gas stream and partly into the vortex core. The droplets are mostly convected in the streamwise direction; thus, the spray width and the spray angle become smaller than in the higher $\hat{\rho}$ cases. As $\hat{\rho}$ decreases further, the vortices become smaller and α decreases. Since the vortices cannot decrease indefinitely, the change in α becomes almost negligible at very low $\hat{\rho}$. The effect of $\hat{\rho}$ on spray angle, as given in Figure 5.26(b), agrees with experimental results of Mansour & Chigier [54], where they showed that increasing the gas pressure (gas density) for a fixed liquid flow rate increased the spray angle.

Table 5.1: Summarized effects of non-dimensional parameters on quantities of interest.

Quantity	L_{32} & L_{21}	Cascade rate	Spray angle
$We_g \uparrow$	$\Downarrow$	$\Uparrow$	$\uparrow$
$Re_l \uparrow$	$\downarrow$	$\uparrow$	$\Downarrow$
$\hat{\rho} \uparrow$	$\uparrow$	$\downarrow$	$\uparrow$
$\hat{\mu} \uparrow$	$\uparrow$	–	–
$\Lambda \uparrow$	$\Downarrow$	$\Uparrow$	$\uparrow$

5.3 Conclusions

Two PDFs were formed for the liquid-structure length scale and the spray width from the numerical data that was obtained from a transient 3D DNS on a liquid-sheet segment. The PDFs provided statistical information about the length-scale distribution and the qualitative number density of ligaments/droplets during early liquid-jet atomization. The temporal variation of the mean of the PDFs gave the rate of cascade of liquid structures in different atomization domains. The mean and PDF of the spray width also showed the first instance of lobe and ligament breakup. The effects of gas Weber number (We_g), liquid Reynolds number (Re_l), density ratio ($\hat{\rho}$), viscosity ratio ($\hat{\mu}$), and wavelength-to-sheet-thickness ratio (Λ) on the mean length scale, the cascade rate, and the spray angle are quantified and summarized in Table 5.1. The size of arrows in this table indicate the relative significance of the change.

As the resistance of surface tension forces against surface deformation decreases by increasing We_g, the droplet size decreases, the cascade of structures and ligament breakup occur faster, and the spray width as well as the liquid surface area grow at higher rates. The initial growth of the length scales due to the stretching of the waves and lobes is affected by liquid inertia more than by the surface tension, as higher inertia results in a more vigorous and prolonged

Table 5.2: Summarized effects of Domain change on quantities of interest.

Domains	L_{32} & L_{21}	Cascade rate	Spray angle
I → II	↓	↑	↑
II → III	↓	↑	↓
I → III	↓	↑	↓

stretching and more flat surfaces. The asymptotic stage of length scale cascade, on the other hand, is affected mostly by surface tension and liquid inertia, but less by liquid viscosity.

The liquid-structure cascade rate is significantly increased by increasing Re_l as the viscous resistance against surface deformation decreases. The spray width is larger at lower Re_l, and the spray angle and the spray spread rate decreases as Re_l increases – attributed to the change in the angle of ligaments that stretch out of the sheet surface. Gas-to-liquid density ratio has minor influence on the final length scale, but the cascade occurs slower as density ratio increases. Gas inertia and liquid surface tension are the key parameters affecting the spray width, where it grows significantly with increasing gas density. Viscosity ratio has negligible effect on both the spray width and the final droplet size. Increasing the sheet thickness, however, decreases both the normalized spray width and its growth rate, while decreasing the structure cascade rate and producing larger droplets.

The cascade process and the spray expansion rate are decoupled for different atomization domains, and the trend of these quantities following the transition between the atomization domains is summarized in Table 5.2. Differences were notable for the length-scale distribution and spray expansion, which were correlated with the vortex structures at each domain. The times of length-scale cascade and sheet expansion were related to the formation of various liquid structures, showing that the ligament and droplet formation occurs faster at higher density ratios.

Chapter 6

Spatially developing coaxial jet

When a liquid jet discharges into a gaseous medium, it becomes unstable and breaks into droplets due to the growth of instabilities. In combustion and jet propulsion applications, the common purpose of breaking a liquid stream into spray is to increase the liquid surface area so that subsequent heat and mass transfer can be increased. Even though the liquid jet breakup has been studied theoretically, experimentally and numerically for more than half a century, the liquid surface deformation mechanisms and its causes are still not satisfactorily understood and categorized at different flow conditions. In this chapter, a spatially developing round liquid jet with slower coaxial gas flow is analyzed numerically. The main objective here is to examine the interaction of the vortices near the liquid-gas interface, and to see how those interactions vary with gas-to-liquid velocity ratio, and their consequent effects on the surface deformation and growth of instabilities.

6.1 Problem description

Lasheras and Hopfinger [43] in their review of the liquid-jet atomization in a coaxial gas stream, categorized the regimes of liquid-jet breakup and showed the effects of gas-to-liquid momentum ratio on those regimes (Figure 1.10). However, they did not relate those regimes to the dynamics of vortices generated prior to atomization. Shinjo and Umemura [80] briefly touched upon the axial and radial vortices generated in a round liquid-jet atomization process (without coaxial flow) and showed that the orientation of vortices determines the orientation of ligaments created during the primary breakup; however, they mainly focused on the vortices near the jet tip and claimed that the primary breakup is mainly affected by the vortices that are convected upstream from the jet tip, without detailing the vortex interactions. More recently, Jarrahbashi & Sirignano [33] and Jarrahbashi et al. [34] studied the details of vortex dynamics in a temporal study of a round liquid jet segment, and showed that the vortices can also form far upstream of the jet cap, independent of the vortices shed behind the cap region. They were able to relate the vortex interactions to the surface deformation, lobe formation and perforation. In Chapter 4, we extended the vortex dynamics analysis to the atomization of planar liquid sheets. Three main atomization regimes were identified in Chapter 3 with different characteristic length and time scales and unique breakup mechanisms based only on the liquid Reynolds number (Re_l) and gas Weber number (We_g). It was shown that one can understand each breakup mechanism by following the vortex interactions near the gas-liquid interface. Ling et al. [50] also observed the hairpin vortex structures emphasized by us (Chapter 4) at the surface of a spatial liquid jet, but failed to explain the details of those vortex interactions.

Here, we perform an analysis similar to what was presented in Chapter 4, but with inclusion of a slow coaxial gas flow and for a spatially developing jet. This study also shows the validity of the prior temporal studies and their relevance to a real atomization application.

6.1.1 Flow Configuration

The 3D computational domain forms a rectangular box, which is discretized into uniform-sized cells. The domain is initially filled with quiescent gas. The liquid jet of diameter $D = 200$ μm is injected from the left boundary at time zero with a constant velocity of $U_l = 50$ m/s. The domain size is $15D \times 6D \times 6D$, in the x (axial), y and z (radial) directions, respectively. The coaxial gas stream fills the rest of the inlet boundary with a constant velocity of $U_g = 5$, 10, and 25 m/s resulting in velocity ratios of $\hat{U} = 0.1$, 0.2 and 0.5, respectively. The other sides are outlet boundaries, where the Lagrangian derivatives of the velocity components are set to zero. A similar axisymmetric (2D) domain is also considered and solved for comparison, where necessary.

The most important dimensionless groupings in this study are the liquid Reynolds number (Re_l), the gas Weber number (We_g), and gas-to-liquid density ratio ($\hat{\rho}$), viscosity ratio ($\hat{\mu}$), and velocity ratio ($\hat{U}$), as defined below.

$$Re_l = \frac{\rho_l U R}{\mu_l}, \quad We_g = \frac{\rho_g U^2 R}{\sigma}, \quad \hat{\rho} = \frac{\rho_g}{\rho_l}, \quad \hat{\mu} = \frac{\mu_g}{\mu_l}, \quad \hat{U} = \frac{U_g}{U_l}. \tag{6.1}$$

The jet radius R is the characteristic length, and for the characteristic velocity the liquid jet velocity U_l is mainly used in the literature. However, our results show that the more relevant characteristic velocity in this problem is the relative velocity of the liquid with respect to gas; i.e. $U_r = U_l - U_g$. The subscripts l and g refer to the liquid and gas, respectively. In this study we mainly focus on $\hat{U}$ effects and for this purpose the three values indicated above are considered. For the other four parameters, the chosen values are kept constant: $Re_l = 2000$, $We_g = 420$, $\hat{\rho} = 0.05$, and $\hat{\mu} = 0.01$.

Our goal is to study the vortex dynamics and its influence on the liquid surface dynamics in order to understand breakup mechanisms at different coaxial flow conditions. To this end,

the λ_2 criterion introduced by Jeong & Hussain [36] is used to define a vortex.

6.2 Results and Discussion

6.2.1 Surface deformation regions

Two types of surface perturbations are distinguished when a liquid jet is injected in a gaseous medium. These two surface deformations and their regions of occurrence are shown schematically in Figure 6.1 and the 3D simulation result shown in Figure 6.2. The detached droplets and ligaments have been removed in Figure 6.2 to better display the surface waves on the liquid-jet core. The first region is right behind the jet start-up cap, to the right of the broken red line in Figure 6.1, and is called the Behind the Cap Region (BCR). In this region, the gas phase velocity is faster compared to the liquid jet and thus, the relative local velocity of the gas stream points downstream. The gas shear creates negative azimuthal vorticity (ω_z) near the interface, which generates KH vortices and consequently downstream facing KH waves, as shown in Figure 6.3. The vortices in this region are encapsulated inside the recirculation

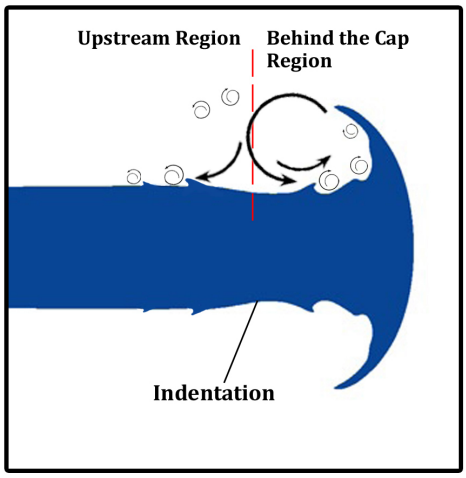

Figure 6.1: Schematic of Vortex regions and wave transmission paths.

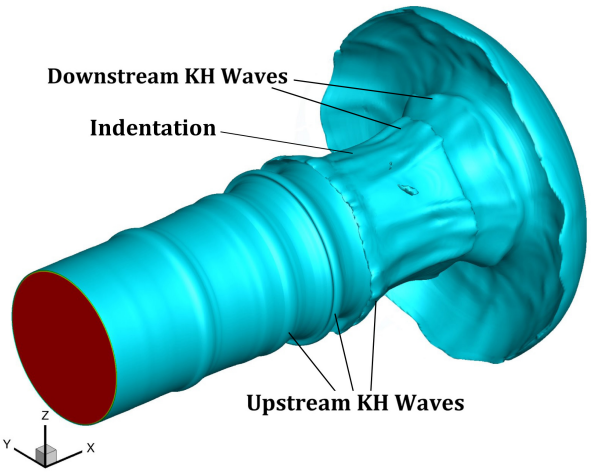

Figure 6.2: Liquid jet surface showing different instability types and their propagation directions; $\hat{U} = 0.1$.

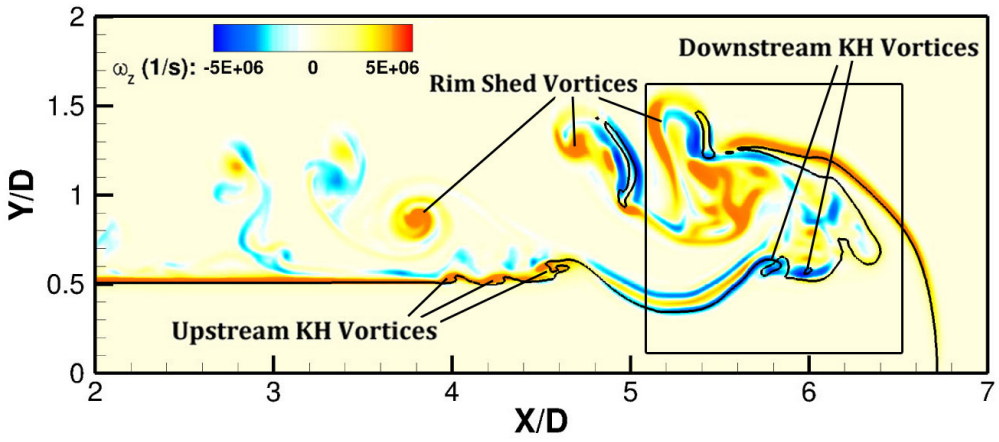

Figure 6.3: Azimuthal vorticity (ω_z) contours and the various vortices generated near the interface in the axisymmetric jet; $\hat{U} = 0.1$.

zone behind the cap – the region inside the box in Figure 6.3 – and the surface deformations are directly related to the dynamics of the growing cap and can be explained by the vortex interactions in that region. Shinjo & Umemura [80] briefly discussed this region in their 3D simulation of a round liquid jet with no coaxial flow, and while describing that the vortex dynamics in this region are very complex, they showed that the vortex orientation determines the orientation of the ligaments that are broken from the cap. The surface pattern is not periodic in BCR. Even though this region is not the main focus of our study, kinematics of the cap and the BCR waves are analyzed in a later section.

The second kind of surface deformations occurs farther upstream of the cap, to the left of the broken red line in Figure 6.1, and is called the Upstream Region (UR). In this region, the liquid-phase velocity is faster than the gas, and the relative gas velocity points upstream. The gas shear creates positive azimuthal vorticity which creates KH vortices that roll-up the liquid surface and generate upstream facing KH wave pattern. As also mentioned by Shinjo and Umemura [80], relatively periodic wave patterns can be observed in this region. They claim that the UR dynamics are highly affected by the BCR dynamics since the shed vortices and the broken droplets are transmitted upstream from the jet cap. However, our analysis shows that the vortices shed from the cap rim mainly affect the droplet propagation

in the downstream region and are far from the interface and have minor interactions with the UR KH waves (see Figure 6.3); thus, the surface dynamics in UR can be studied separately from the BCR in a temporal analysis with periodic boundary conditions similar to studies presented in Chapters 3–5.

As shown in Figures 6.1–6.3, a large indentation exists between the UR and BCR regions. This indentation is caused by the radially inward gas flow which impinges on the jet stem upstream of the cap. The gas stream then branches into two opposite streams, one flowing downstream and the other upstream in the frame of reference of the jet. The same indentation was also observed in results of Shinjo and Umemura [80] (see their Fig. 15a), although not emphasized by them. We draw the line between the two regions at the center of this indentation. Shinjo and Umemura [80] however, did not identify an exact criterion for the borderline between these two regions, and their BCR and UR regions overlapped at some places and also stretched beyond our proposed segmentation line.

6.2.2 Waves kinematics

Figure 6.4 shows the time and length of the first KH perturbation occurrence at different velocity ratios. Time has been non-dimensionalized by the injection velocity and jet diameter ($t^* = U_l t/D$), and the length is normalized by the jet diameter. Both jet smooth length and time increase substantially by increasing the coaxial gas velocity. The increase in the length seems to be almost linear, which means that the perturbations are transmitted downstream according to the gas stream velocity. However, the time at which the first perturbation occurs gets delayed exponentially by increasing the velocity ratio.

Figure 6.5 compares the average length of surface waves in the axial direction for different $\hat{U}$ values. By increasing $\hat{U}$ from 0.1 to 0.5, the average wavelength increases from 80 to 100 μm. The effect of coaxial gas velocity on axial wavelength becomes less significant as $\hat{U}$ increases.

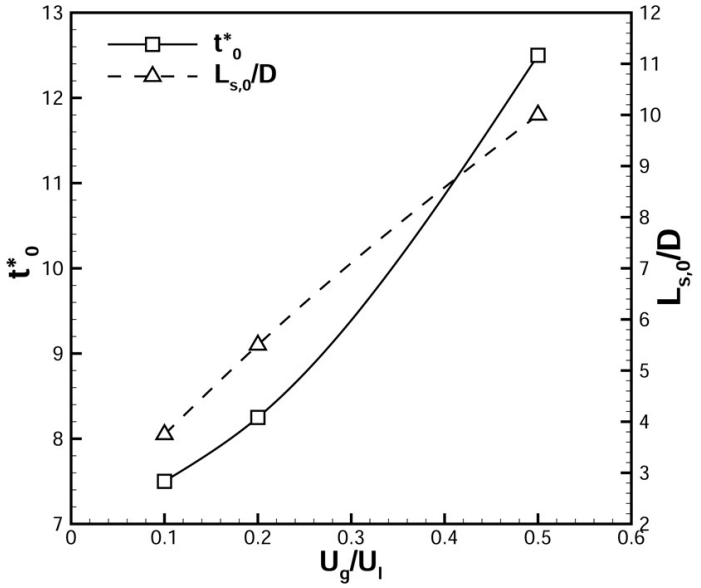

Figure 6.4: Non-dimensional time and distance of the first perturbation at different velocity ratios.

Results of Figures 6.4 and 6.5 clearly indicate that the most relevant characteristic velocity in coaxial injection problems is the relative velocity between the liquid and gas streams; i.e. U_r. Thus, since obviously Re_l is the same for all three cases, the most pertinent Reynolds number

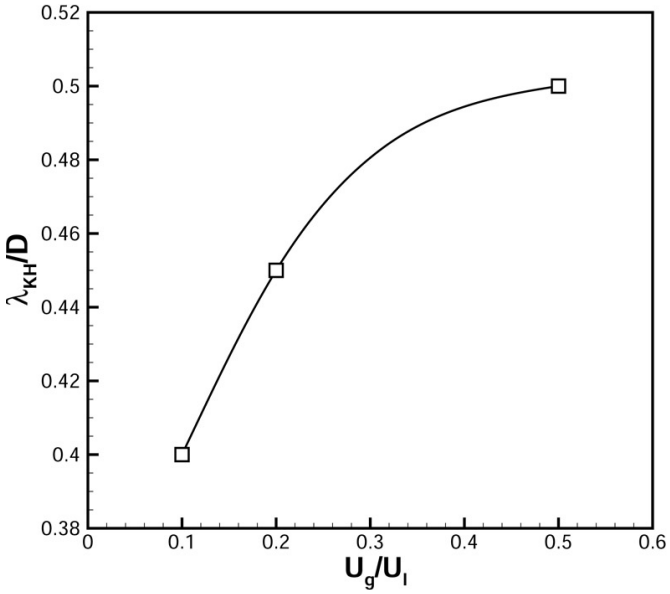

Figure 6.5: Non-dimensional average KH wavelength for different velocity ratios.

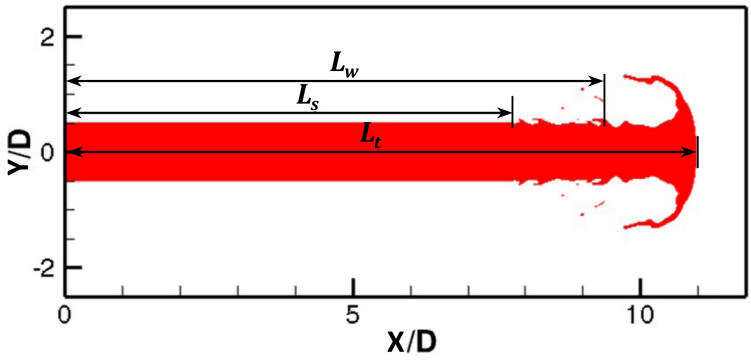

Figure 6.6: Definition of the tip length (L_t), the smooth region length (L_s), and the first UR-KH-wave length (L_w).

should also be based on U_r and not the injection velocity as is used in many studies in the literature. As $\hat{U}$ decreases, hence $Re_{l,r}$ increases, axial wavelength decreases, as intuitively expected.

Figure 6.6 schematically defines the length of the jet tip (L_t), the jet smooth length (L_s), and the length of the first surface wave in the UR region (L_w), which are measured for three $\hat{U}$ cases in time in Figure 6.7. All of the lengths are measured from the injection plane and all are normalized by the jet diameter. The average velocity of each length (in terms of the fraction of U_l), measured from the slope of each trend, is also computed and presented on the plots. The solid lines indicate the simple convection of the first perturbation with the Dimotakis velocity $U_d = (U_l + \sqrt{\hat{\rho}}U_g)/(1 + \sqrt{\hat{\rho}})$.

In all cases, the wave speed follows the Dimotakis speed at early times after its appearance, but it diverges and becomes slightly larger at later times. This divergence is more apparent at lower $\hat{U}$. The smooth length also grows in time for all cases, but it is always below L_w. Shinjo and Umemura [80] also observed a similar difference in the rate of smooth region growth and the injection speed. They concluded that this difference means that the size of the region of influence of the tip is spreading toward upstream as time passes. However, we do not see a direct connection between these perturbations and the vortices generated in the

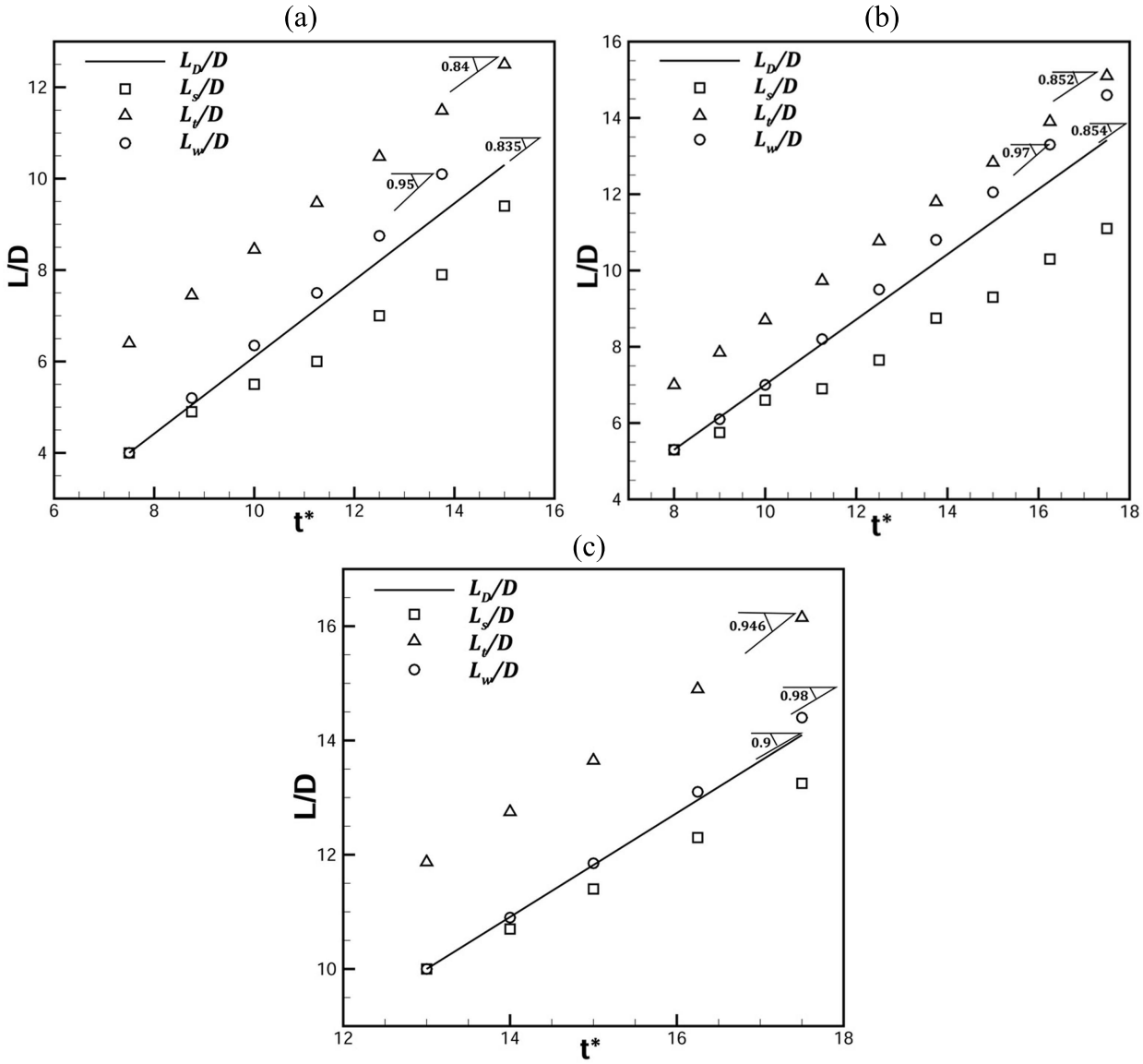

Figure 6.7: Temporal plot of L_s/D, L_t/D, and L_w/D for $\hat{U} = 0.1$ (a), $\hat{U} = 0.2$ (b), and $\hat{U} = 0.5$ (c). The solid line indicates simple convection with Dimotakis velocity.

BCR, and the only conclusion that can be drawn here is that new instabilities keep forming upstream of the initial perturbation, resulting in growth of the UR. We showed earlier that UR is not much affected by the BCR and thus, the only reason for the upstream spreading of the instabilities is concluded to be the increase in the strain rate on the surface after the growth of the former KH waves. This triggers new KH vortices, which result in new waves upstream. The rate of growth of the smooth length increases as $\hat{U}$ increases.

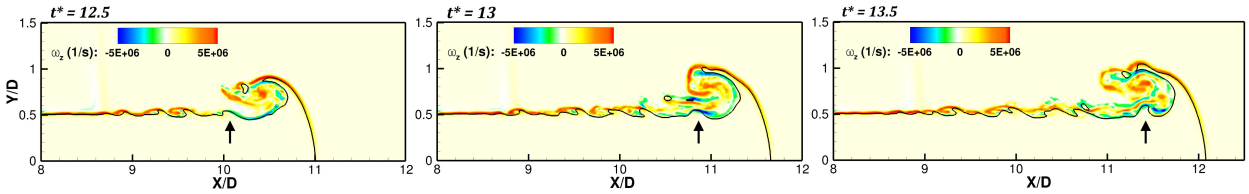

Figure 6.8: Change in roll-up direction of the KH wave as it moves from UR to BCR region; $\hat{U} = 0.2$.

The tip velocity is always smaller than the wave speed. This means that the KH waves that form in UR, finally enter BCR and catch up with the tip. The rate at which the KH waves reach the tip is directly proportional to the difference between the tip speed and the wave speed. This velocity difference becomes smaller at higher $\hat{U}$ and thus, it takes more time for the UR waves to merge with the cap and disappear. This happens at $t^* = 15$ for $\hat{U} = 0.1$, and at $t^* = 17.5$ for $\hat{U} = 0.2$. For $\hat{U} = 0.5$, this catchup is so slow that the cap moves out of the domain before the KH wave has enough time to reach it. When the UR waves get into BCR, their roll-up direction changes since the relative gas stream direction changes. This phenomenon is clearly shown in Figure 6.8, where the KH wave indicated by the black arrow faces upstream at $t^* = 12.5$ while it is in UR, becomes neutral as it enters BCR boundary at $t^* = 13$, and faces downstream while it is in BCR at $t^* = 13.5$. Notice the formation of a negative KH vortex just as the wave enters the BCR region.

6.2.3 Vortex dynamics of the coaxial jet

The liquid jet at a few time steps before the start of perturbations is shown in Figure 6.9. The vortex structures indicated by the λ_2 isosurface are also shown in the same figure at the same time step. The vortices that are attached to the jet tip include the vortex structure that covers the front of the jet cap (Tip Vortex), which is caused by the gas flow that goes around the mushroom-shaped cap, and a vortex ring that is shed from the rim of the cap (Rim Vortex), due to flapping of the rim. As discussed earlier, on the stem of the jet, there

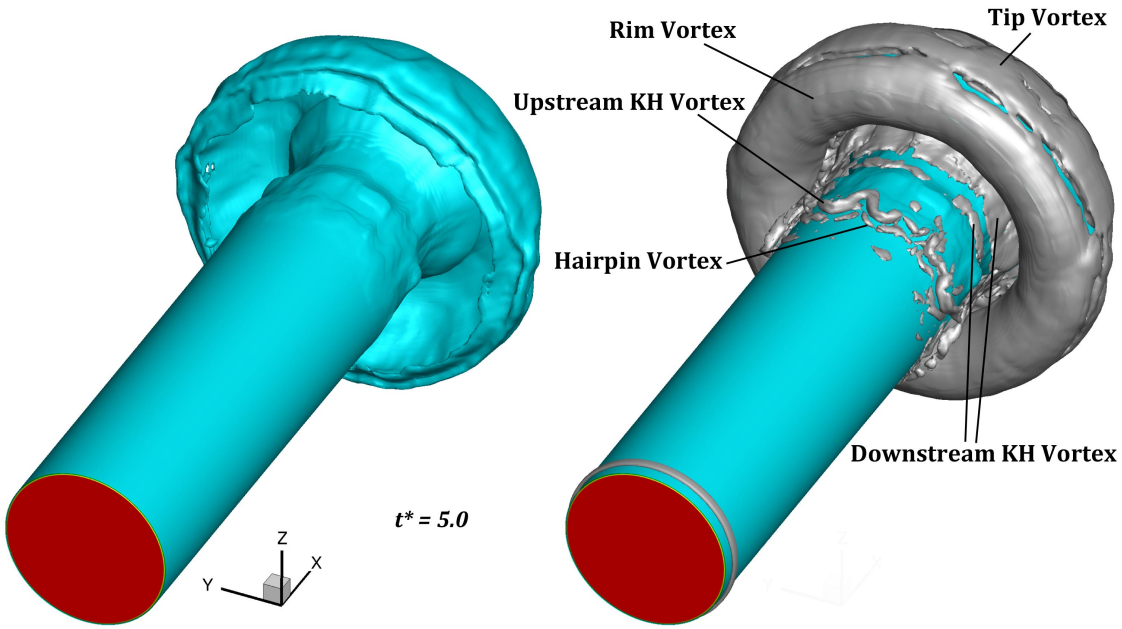

Figure 6.9: Liquid-jet surface on the left and vortices indicated by $\lambda_2 = -10^{11}$ s^{-2} isosurface on the right at $t^* = 5$; $\hat{U} = 0.2$.

are two sets of oppositely oriented KH vortex rings which are formed due to the shear caused by the entrained gas in the downstream and upstream directions. As seen in Figure 6.9, the KH vortices deform and take a hairpin structure before the surface of the jet is deformed. Figure 6.10, shows that the first liquid lobes are formed at the exact same location where the KH vortices are turned streamwise and create a hairpin structure, at a later time. This conveys that the vortex dynamics drives the surface dynamics, as was first identified by Jarrahbashi et al. [34] and shown in Chapter 4. Even though these studies were temporal with periodic conditions on a liquid segment, our spatial results show that the temporal study of vortex dynamics can capture well the mechanisms in the UR region, where fairly similar physical behaviors occur.

Figure 6.11 shows the liquid jet and its vortices at $t^* = 11.5$ for $\hat{U} = 0.1$. The KH vortex rings start from an axisymmetric form and grow and deform as they move downstream. Following this change in the KH vortex structure, we can see that the initially axisymmetric KH waves (closer to the nozzle) also become more corrugated as they move downstream. The mode

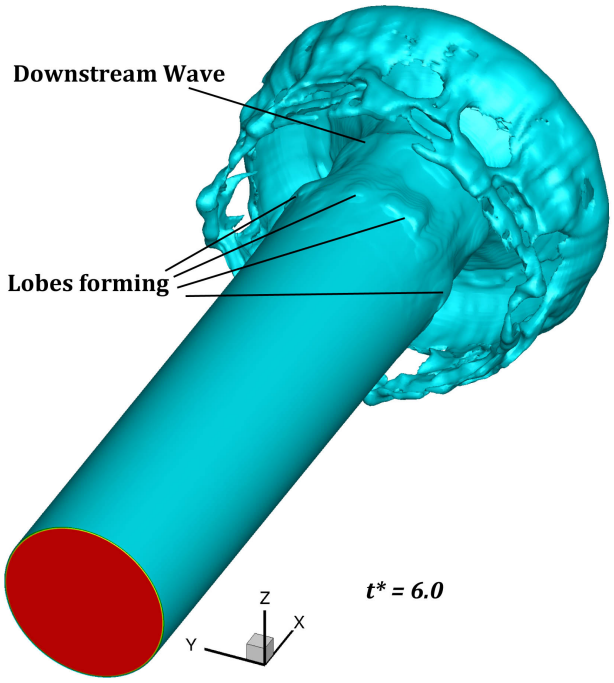

Figure 6.10: Liquid jet surface at $t^* = 6$; $\hat{U} = 0.2$.

number (azimuthal wavelength) of the lobes is directly related to the number of counter-rotating streamwise vortex pairs that form as the KH vortices become streamwise oriented. Thus, a detailed analysis of the causes of streamwise vortex generation and its growth rate (similar to analyses of Jarrahbashi & Sirignano [33] for round jets and our analysis for planar sheets in Chapter 4) can explain a lot regarding the future behavior of the lobes and their

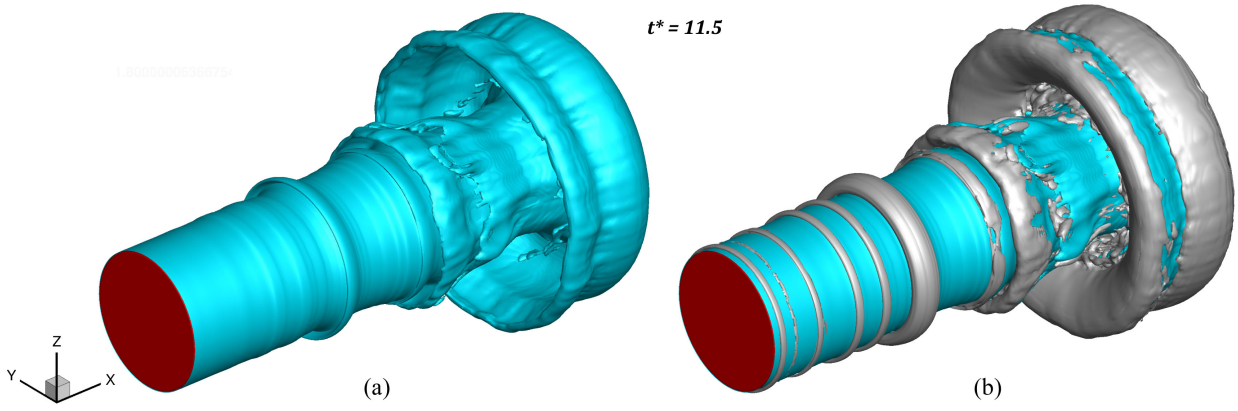

Figure 6.11: Liquid-jet surface (a), and vortex structures indicated by $\lambda_2 = -10^{11}$ s^{-2} isosurface (b) at $t^* = 11.5$; $\hat{U} = 0.1$.

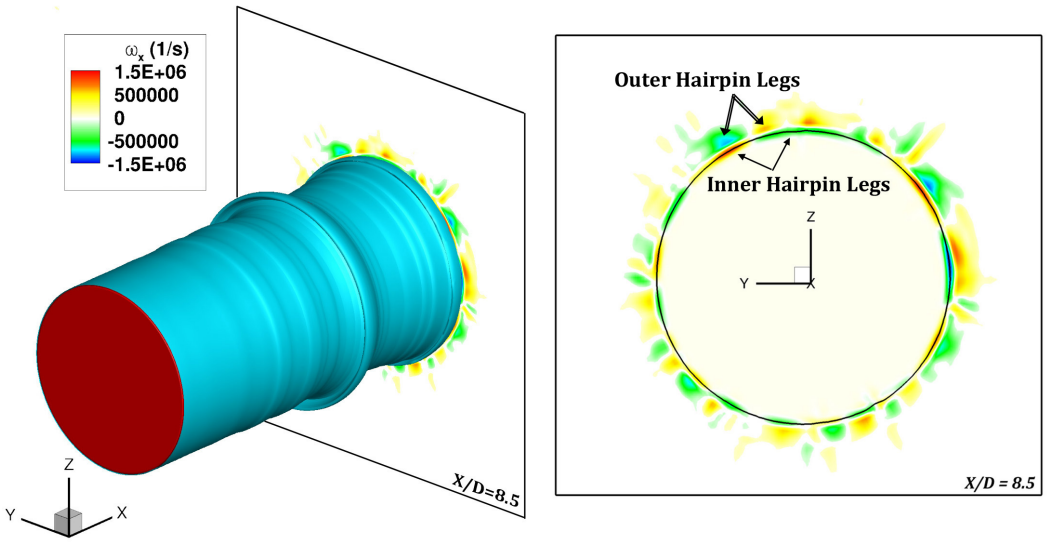

Figure 6.12: Liquid-jet surface and the axial vorticity (ω_x) contours on the plane intersecting the jet at $x/D = 8.5$ at $t^* = 11.5$; $\hat{U} = 0.1$.

breakup mechanism and size of ligaments and droplets. This analysis will not be quantified here, but the effects of velocity ratio on the mode number will be discussed qualitatively here.

The axial vorticity (ω_x) contours on a spanwise plane intersecting with the liquid jet stem at $x/D = 8.5$ and $x/D = 8.75$ at $t^* = 11.5$ (same time as Figure 6.11) are shown in Figures 6.12 and 6.13, respectively. The plane in Figure 6.12 cuts the jet at the braid of one of the newer KH waves slightly upstream of the former wave that is located at $x/D = 8.75$ and is the subject of Figure 6.13. Two layers of counter-rotating streamwise vorticity are seen in Figure 6.12. The inner layer closer to the liquid surface is the hairpin vortex ring with several counter-rotating axial vortices, a pair of which is indicated by the simple arrows. This hairpin stretches upstream and over the next consecutive KH wave upstream of the current wave. Right on the outer side of this vorticity layer is another layer of counter-rotating vorticity, shown by double-lined arrows. Since these counter-rotating vortex pairs are 180° out of phase with respect to the inner layer, it is concluded that this layer belongs to another hairpin vortex layer with opposite direction. This layer is called the outer hairpin layer and is

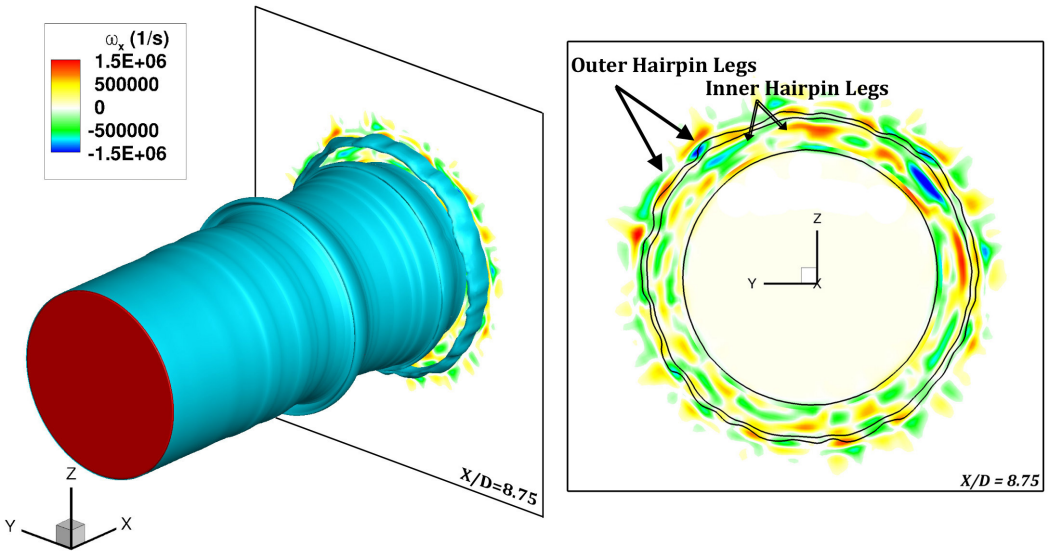

Figure 6.13: Liquid-jet surface and the axial vorticity (ω_x) contours on the plane intersecting the jet at $x/D = 8.75$ at $t^* = 11.5$; $\hat{U} = 0.1$.

stretched downstream and underneath the next downstream KH wave, shown in Figure 6.13. The reason why much axial deflection is still not seen in this vortex ring in Figure 6.11 is that the ω_x magnitude is an order of magnitude smaller than the azimuthal vorticity (ω_θ) magnitude at this time. Even though the vorticity layers are not very neat and organized at all azimuthal locations of this picture, seven counter-rotating vortex pairs are distinguished in Figure 6.12, which indicates that seven lobes are expected to form on this KH wave later.

In the downstream cross-sectional plane shown in Figure 6.13, three counter-rotating axial vortex layers are observed. The outer layer – indicated by thick arrows – is the outer hairpin vortex layer for this new wave which stretches downstream. This hairpin layer is right on the outer surface of the KH wave. Right on the inner side of this wave, there is another layer of counter-rotating hairpin vortex, indicated as inner hairpin layer. This layer is the same outer hairpin layer seen in Figure 6.12 and is stretched underneath the wave shown in Figure 6.13. A comparison between the counter-rotating vortex pairs of these two layers shows that they both belong to the same hairpin structure that wraps over the upstream wave and under the next downstream wave. There is another vortex ring on the inner side

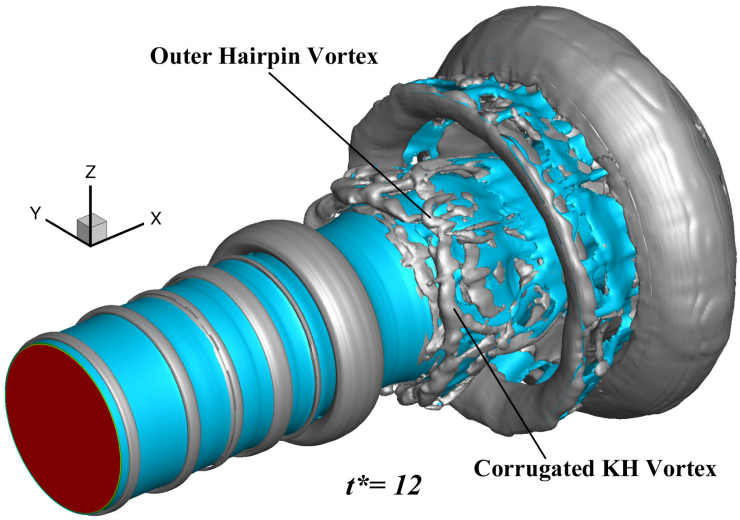

Figure 6.14: Liquid-jet surface (blue) and vortex structures (gray) at $t^* = 12$; $\hat{U} = 0.1$.

of this hairpin, which is less organized and more chaotic, but with smaller axial vorticity component. This layer is part of the KH vortex located underneath the wave and slightly deflected.

The effects of the counter-rotating axial vortex pairs shown in Figures 6.12 and 6.13 are more clear at a later time ($t^* = 12$) shown in Figure 6.14. When ω_x grows enough to become comparable to ω_θ, 3D instabilities occur and the vortices lose their axisymmetry. This phenomenon creates corrugations in the KH vortex ring and also larger axial stretch on the hairpin vortices that are also stretched by the KH vortex. The corrugated KH vortex and the hairpin vortex that stretches over it are shown in Figure 6.14. The inner hairpin vortex is not clearly seen in this figure since the KH vortex and the liquid lobes on the outer side of this hairpin block those hairpins from the view. As was shown in Chapter 4 [98], overlapping of these oppositely oriented counter-rotating hairpins that are on the outer and inner sides of the lobe, thins the lobe at its center and creates holes on the lobes. Thinning of the lobes (wave) can be clearly seen in the cross-sectional view of the plane illustrated in Figure 6.13.

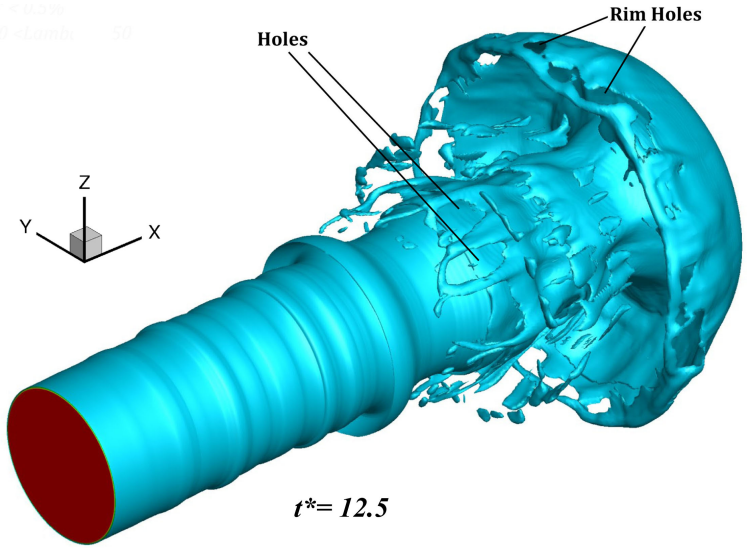

Figure 6.15: Liquid-jet surface at $t^* = 12.5$; $\hat{U} = 0.1$.

Following the same wave at a later time ($t^* = 12.5$), shown in Figure 6.15, it is seen that holes form on the lobes and they expand as the lobes get stretched in the axial direction. The liquid bridges that are formed around the lobe rim finally break and create the first ligaments, which then break into droplets or detach from the jet core. Figure 6.15 also shows that there are in fact seven liquid lobes on each KH wave, as was inferred earlier by the number of counter-rotating axial vorticity pairs. Four of these lobes are already seen in this figure, and the other three are on the hidden side of the jet stem, which are blocked in this view. As we follow the jet structure at much later time ($t^* = 15.5$ shown in Figure 6.16), we see that the same hole formation and breakup mechanism repeats for other waves as well. This confirms that the breakup mechanism on the jet stem in UR is periodic and occurs for all the waves formed in that range until they reach the BCR region and break into droplets and/or coalesce with the cap. This validates the temporal studies of Jarrahbashi et al. [33, 34] and our own studies presented in Chapters 3–5. The formation of holes on the rim of the jet cap (see Figure 6.15) is also conjectured to follow the same vortex overlapping mechanism, where the overlapping vortices in that case are the tip vortex and the downstream KH vortex (see Figure 6.9) as it runs along the inner side of the mushroom-shaped cap; however, these

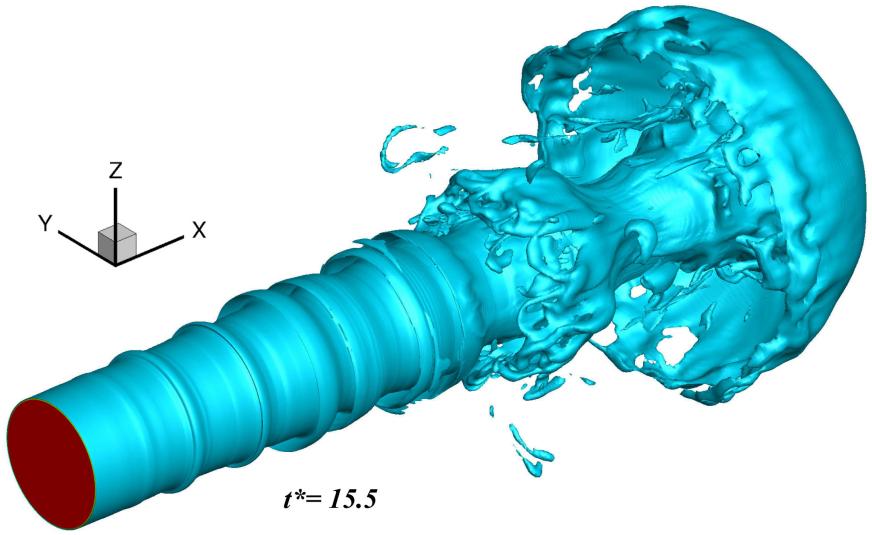

Figure 6.16: Liquid-jet surface at $t^* = 15.5$; $\hat{U} = 0.1$.

vortex structures are much harder to follow and are not analyzed in this Chapter.

Based on Re_l and We_g values of the current study, this jet (without coaxial gas flow) should belong to Domain I as indicated in Chapter 3 (Figure 3.2). In Domain I, lobes stretch directly into ligaments without formation of holes. The hole formation mechanism occurs in Domain II, at higher ranges of Re_l and We_g. Thus, we can conclude from this study that addition of coaxial gas flow shifts the breakup mechanism, as this jet now belongs to Domain II, which is consistent with the use of relative velocity for defining We_g and Re_l.

The same jet with a higher velocity ratio is simulated and the results are depicted in Figure 6.17 for $t^* = 15$ and 17. A few main differences are observed at a first glance between these results and the lower $\hat{U}$ cases. First, the azimuthal mode number has significantly decreased from seven (for $\hat{U} = 0.1$) to four. Four liquid lobes are seen in this figure – one in the front view, one on top, one on bottom, and one on the hind view which cannot be seen here, following the four axial pairs of KH vortices shown in Figure 6.17(b,d). The next main change is that the lobes, ligaments and cap rim seem much thicker compared to lower $\hat{U}$. Because of this thickening in the lobe structures, the lobes do not thin easily and they are stretched directly into thick ligaments. This means that the breakup mechanism has moved

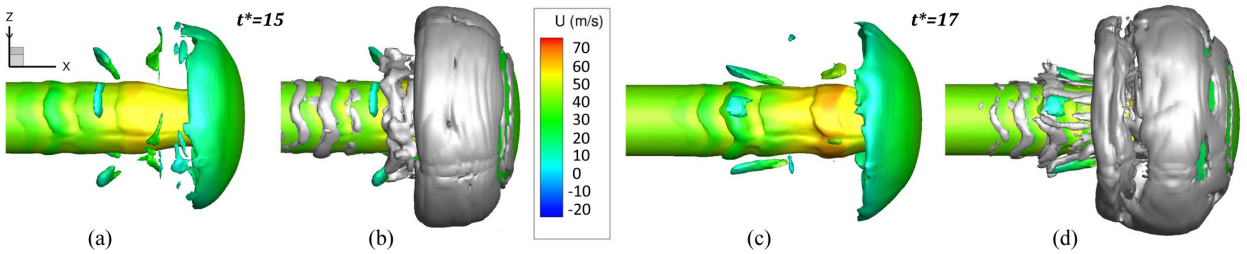

Figure 6.17: Liquid jet surface (a,c) and vortex structures (b,d) at $t^* = 15$ (a,b) and $t^* = 17$ (c,d); $\hat{U} = 0.5$. The surface of liquid jet is colored by the axial velocity contours.

from Domain II towards Domain I by increasing $\hat{U}$. This clearly shows that the Reynolds and Weber numbers in such coaxial flow should be based on the relative gas-liquid velocity rather than just liquid jet velocity. By increasing $\hat{U}$, the relative velocity U_r decreases, and thus, $Re_{l,r}$ and $We_{g,r}$ decrease too. This decrease in the Reynolds and Weber numbers is consistent with shifting from the hole formation breakup (Domain II) to lobe stretching mechanism (Domain I), as predicted by our analysis in Chapter 3. Therefore, a more thorough analysis of the effects of velocity ratio is required to generalize the breakup mechanisms formerly developed for non-coaxial jet flows. This is left for a prospective study.

6.3 Conclusions

A three-dimensional round liquid jet with coaxial, outer gas flow is numerically analyzed. The evolution of instabilities on the liquid-gas interface were observed to be correlated with the vortex interactions around the liquid-gas interface using a λ_2 analysis. Two main regions were identified on the liquid jet separated by a large indentation on the jet stem with distinguished surface deformations. The Behind the Cap Region (BCR) is encapsulated inside the recirculation zone behind the mushroom-shaped cap. The KH waves formed on the jet core roll downstream in BCR and flow downstream until they coalesce with the cap. The vortices and surface deformations in BCR are not periodic and are controlled by the dynamics of vortices in the recirculation zone. The second region (Upstream Region, UR) is farther

upstream of the cap. The gas speed is lower than the liquid jet in UR, and the shear caused by this upstream flowing gas stream relative to the liquid triggers a KH instability. The 3D deformation of the initially axisymmetric KH vortices leads to several liquid lobes. The lobes either thin and form holes at lower velocity ratios or stretch directly into elongated ligaments at higher velocity ratios, which could be explained by the vortex interactions in the UR region. The deformations developed in UR can be portrayed better in a frame moving with the convective velocity of the liquid jet with periodic conditions. The azimuthal and axial wavelengths of the instabilities and the breakup mechanism in UR can be well defined using a Reynolds and Weber number based on the relative gas-liquid velocity. The temporal study of the stem region (presented in Chapters 3–5) is legitamized by this study.

Chapter 7

Summary and conclusions

The Navier-Stokes equations combined with level-set and volume-of-fluid surface tracking methods were used to simulate the temporal behavior of a three-dimensional planar liquid jet segment during primary atomization. The spatially developing full-jet calculations revealed two regions on the liquid jet – a behind the cap region, where the surface deformation and vortex dynamics are irregular, and an upstream region, where a periodic behavior is witnessed in both surface dynamics and vortex dynamics near the interface. The spatial calculations legitamized the temporal analysis on the liquid segment in the upstream region.

Three main atomization cascades were identified on the liquid sheet. The atomization characteristics were well categorized on a parameter space of gas Weber number (We_g) versus liquid Reynolds number (Re_l). The gas-to-liquid density ratio affects the breakup process, thereby making We based on liquid density less important as a correlation factor. The atomization regime is now separated as three sub-domains. Atomization Domain I has a lobe-ligament-droplet ($LoLiD$) cascade; Domain II involves a lobe-hole-bridge-ligament-droplet ($LoHBrLiD$) cascade; and Domain III shows a lobe-corrugation-ligament-droplet ($LoCLiD$) cascade.

At high Re_l, the breakup characteristics change based on a modified Ohnersorge number ($Oh_m = \sqrt{We_g}/Re_l$). At high Oh_m, the lobes thin and perforate to form bridges, which eventually break into one or two ligaments. At lower Oh_m, the hole formation is hindered and instead, the lobe rims corrugate and stretch into small ligaments. There is also a transitional region, where both mechanisms co-exist. The transition region at high Re_l follows a constant Oh_m line.

At low Re_l, the transitional region follows a hyperbolic function in the We_g–Re_l plot. At low We_g and low Re_l, the lobes stretch directly into ligaments. The ligaments created in this domain are fairly thick and long, and result in larger droplets. As We_g is increased while keeping Re_l low, the hole formation process prevails. Thus, the hole formation process dominates over a wide range of low and high Re_l, but only over moderate to high We_g. Below a critical We_g, hole formation is completely hindered at all Re_l. These atomization cascades are independent of the jet geometry (planar or round). Furthermore, a very similar correlation describes the boundaries between different atomization domains for the planar and round jets.

Different characteristic time scales were introduced for the hole formation and lobe stretching – mainly related to the surface tension and liquid viscosity, respectively. At any flow condition, the mechanism having a smaller characteristic time is the dominant process. In the transitional region, both characteristic times are of the same order; thus, both mechanisms occur simultaneously and the cascade of liquid structures varies locally. The two characteristic times are related to each other by Oh_m, which involves the We_g and Re_l.

The vortex dynamics of the planar liquid jet was analyzed and the relation between the surface dynamics and the vortex dynamics is sought to explain the physics of different breakup mechanisms that occur during primary atomization. A vortex has been defined using the λ_2 criterion.

Vortex dynamics is able to explain the hairpins formation. The interaction between the hairpin vortices and the KH vortex explains the perforation of the lobes at moderate Re_l and high We_g, which is attributed to the overlapping of a pair of oppositely-oriented hairpin vortices on top and bottom of the lobe. The formation of corrugations on the lobe front edge at high Re_l and low We_g is also explained by the structure that hairpins gain due to the induction of the split KH vortices. At low Re_l and low We_g, on the other hand, the lobe perforation and corrugation formation are inhibited due to the high surface tension and viscous forces, which damp the small scale corrugations and resist hole formation. The hairpin vortices stretch in the normal direction while wrapping around the KH vortex. The induced gas flow squeezes the lobe from the sides and forms a thick and long ligament. In summary, the vortex dynamics analysis helps explain the three major atomization cascades at different flow conditions. The atomization mechanisms for the planar jet are qualitatively identical to the round-jet mechanisms.

Baroclinicity is the most important factor in generation of the streamwise vortices and manifestation of 3D instabilities at low density ratios. At higher density ratios, the streamwise vortices are mostly rendered by streamwise vortex stretching. The streamwise vorticity growth is higher at higher density ratios, resulting in a faster appearance of 3D instabilities. As density ratio is reduced, fewer lobes with less undulation form; hence, hole formation prevails more at higher density ratios. The relation between vortex dynamics and surface dynamics aids prediction of liquid-structure formations at different flow conditions and different stages of the primary atomization. This is very important in prediction and control of the droplet size distribution in liquid-jet primary atomization.

The liquid-structure length scale cascade rate and jet spread rate were quantified during primary atomization using two PDFs. The PDFs provided statistical information about the length-scale distribution and the qualitative number density of ligaments/droplets during early liquid-jet atomization. The temporal variation of the mean of the PDFs gave the rate

of cascade of liquid structures in different atomization domains. The effects of gas Weber number (We_g), liquid Reynolds number (Re_l), density ratio ($\hat{\rho}$), viscosity ratio ($\hat{\mu}$), and wavelength-to-sheet-thickness ratio (Λ) on the mean length scale, the cascade rate, and the spray angle were quantified.

As the resistance of surface tension forces against surface deformation decreases by increasing We_g, the droplet size decreases, the cascade of structures and ligament breakup occur faster, and the spray width as well as the liquid surface area grow at higher rates. The initial growth of the length scales due to the stretching of the waves and lobes is affected by liquid inertia more than by the surface tension, as higher inertia results in a more vigorous and prolonged stretching and more flat surfaces. The asymptotic stage of length scale cascade, on the other hand, is affected mostly by surface tension and liquid inertia, but less by liquid viscosity.

The liquid-structure cascade rate is significantly increased by increasing Re_l as the viscous resistance against surface deformation decreases. The spray width is larger at lower Re_l, and the spray angle and the spray spread rate decreases as Re_l increases – attributed to the change in the angle of ligaments that stretch out of the sheet surface. Gas-to-liquid density ratio has minor influence on the final length scale, but the cascade occurs slower as density ratio increases. Gas inertia and liquid surface tension are the key parameters affecting the spray width, where it grows significantly with increasing gas density. Viscosity ratio has negligible effect on both the spray width and the final droplet size. Increasing the sheet thickness, however, decreases both the normalized spray width and its growth rate, while decreasing the structure cascade rate and producing larger droplets.

The cascade process and the spray expansion rate are decoupled for different atomization domains. Differences were notable for the length-scale distribution and spray expansion, which were correlated with the vortex structures at each domain. The times of length-scale cascade and sheet expansion were related to the formation of various liquid structures, showing that the ligament and droplet formation occurs faster at higher density ratios.

Bibliography

[1] G. Agbaglah, R. Chiodi, and O. Desjardins. Numerical simulation of the initial destabilization of an air-blasted liquid layer. *Journal of Fluid Mechanics*, 812:1024–1038, 2017.

[2] G. Agbaglah, C. Josserand, and S. Zaleski. Longitudinal instability of a liquid rim. *Physics of Fluids*, 25(2):022103, 2013.

[3] W. T. Ashurst and E. Meiburg. Three-dimensional shear layers via vortex dynamics. *Journal of Fluid Mechanics*, 189:87–116, 1988.

[4] L. P. Bernal and A. Roshko. Streamwise vortex structure in plane mixing layers. *Journal of Fluid Mechanics*, 170:499–525, 1986.

[5] P. Brancher, J. M. Chomaz, and P. Huerre. Direct numerical simulations of round jets: vortex induction and side jets. *Physics of Fluids*, 6(5):1768–1774, 1994.

[6] R. Breidenthal. Structure in turbulent mixing layers and wakes using a chemical reaction. *Journal of Fluid Mechanics*, 109:1–24, 1981.

[7] I. S. Carvalho, M. V. Heitor, and D. Santos. Liquid film disintegration regimes and proposed correlations. *International Journal of Multiphase Flow*, 28(5):773–789, 2002.

[8] J. Chesnel, J. Reveillon, T. Menard, and F.-X. Demoulin. Large eddy simulation of liquid jet atomization. *Atomization and Sprays*, 21(9), 2011.

[9] C. J. Clark and N. Dombrowski. Aerodynamic instability and disintegration of inviscid liquid sheets. *Proc. R. Soc. Lond. A*, 329(1579):467–478, 1972.

[10] S. S. Collis, S. K. Lele, R. D. Moser, and M. M. Rogers. The evolution of a plane mixing layer with spanwise nonuniform forcing. *Physics of Fluids*, 6(1):381–396, 1994.

[11] P. Comte, M. Lesieur, and E. Lamballais. Large-and small-scale stirring of vorticity and a passive scalar in a 3-D temporal mixing layer. *Physics of Fluids A: Fluid Dynamics*, 4(12):2761–2778, 1992.

[12] J. Crank and P. Nicolson. A practical method for numerical evaluation of solutions of partial differential equations of the heat-conduction type. *Adv. Comput. Math*, 6:207–226, 1947.

[13] G. D. Crapper, N. Dombrowski, W. P. Jepson, and G. A. D. Pyott. A note on the growth of Kelvin-Helmholtz waves on thin liquid sheets. *Journal of Fluid Mechanics*, 57(4):671–672, 1973.

[14] S. Dabiri, W. A. Sirignano, and D. D. Joseph. Cavitation in an orifice flow. *Physics of Fluids*, 19(7):072112, 2007.

[15] I. Danaila, J. Dušek, and F. Anselmet. Coherent structures in a round, spatially evolving, unforced, homogeneous jet at low Reynolds numbers. *Physics of Fluids*, 9(11):3323–3342, 1997.

[16] O. Desjardins and H. Pitsch. Detailed numerical investigation of turbulent atomization of liquid jets. *Atomization and Sprays*, 20(4):311–336, 2010.

[17] P. Dimotakis. Two-dimensional shear-layer entrainment. *AIAA Journal*, 24(11):1791–1796, 1986.

[18] N. Dombrowski and P. C. Hooper. The effect of ambient density on drop formation in sprays. *Chemical Engineering Science*, 17(4):291–305, 1962.

[19] N. Dombrowski and W. R. Johns. The aerodynamic instability and disintegration of viscous liquid sheets. *Chemical Engineering Science*, 18(3):203–214, 1963.

[20] Z. Farago and N. Chigier. Morphological classification of disintegration of round liquid jets in a coaxial air stream. *Atomization and Sprays*, 2(2), 1992.

[21] R. P. Fraser, P. Eisenklam, N. Dombrowski, and D. Hasson. Drop formation from rapidly moving liquid sheets. *AIChE Journal*, 8(5):672–680, 1962.

[22] D. Fuster, J.-P. Matas, S. Marty, S. Popinet, J. Hoepffner, A. Cartellier, and S. Zaleski. Instability regimes in the primary breakup region of planar coflowing sheets. *Journal of Fluid Mechanics*, 736:150–176, 2013.

[23] M. Gaster. A note on the relation between temporally-increasing and spatially-increasing disturbances in hydrodynamic stability. *Journal of Fluid Mechanics*, 14(2):222–224, 1962.

[24] J. Glimm, O. McBryan, R. Menikoff, and D. H. Sharp. Front tracking applied to Rayleigh–Taylor instability. *SIAM Journal on Scientific and Statistical Computing*, 7(1):230–251, 1986.

[25] W. Hagerty and J. F. Shea. A study of the stability of moving liquid film. *ASME Journal of Applied Mechanics*, 22:509–514, 1955.

[26] T. Hayase, J. A. C. Humphrey, and R. Greif. A consistently formulated QUICK scheme for fast and stable convergence using finite-volume iterative calculation procedures. *Journal of Computational Physics*, 98(1):108–118, 1992.

[27] M. Herrmann. On simulating primary atomization using the refined level set grid method. *Atomization and Sprays*, 21(4):283–301, 2011.

[28] C. W. Hirt and B. D. Nichols. Volume of fluid (VOF) method for the dynamics of free boundaries. *Journal of Computational Physics*, 39(1):201–225, 1981.

[29] J. Hoepffner, R. Blumenthal, and S. Zaleski. Self-similar wave produced by local perturbation of the Kelvin-Helmholtz shear-layer instability. *Physical Review Letters*, 106(10):104502, 2011.

[30] E. J. Hopfinger. Liquid jet instability and atomization in a coaxial gas stream. In *Advances in Turbulence VII*, pages 69–78. Springer, 1998.

[31] J. W. Hoyt and J. J. Taylor. Waves on water jets. *Journal of Fluid Mechanics*, 83(1):119–127, 1977.

[32] A. K. M. F. Hussain. Coherent structures and turbulence. *Journal of Fluid Mechanics*, 173:303–356, 1986.

[33] D. Jarrahbashi and W. A. Sirignano. Vorticity dynamics for transient high-pressure liquid injection a. *Physics of Fluids*, 26(10):73, 2014.

[34] D. Jarrahbashi, W. A. Sirignano, P. P. Popov, and F. Hussain. Early spray development at high gas density: hole, ligament and bridge formations. *Journal of Fluid Mechanics*, 792:186–231, 2016.

[35] S. A. Jazayeri and X. Li. Nonlinear instability of plane liquid sheets. *Journal of Fluid Mechanics*, 406:281–308, 2000.

[36] J. Jeong and F. Hussain. On the identification of a vortex. *Journal of fluid mechanics*, 285:69–94, 1995.

[37] G. Jiang and D. Peng. Weighted ENO schemes for Hamilton–Jacobi equations. *SIAM Journal on Scientific Computing*, 21(6):2126–2143, 2000.

[38] J. Jimenez. A spanwise structure in the plane shear layer. *Journal of Fluid Mechanics*, 132:319–336, 1983.

[39] D. Joseph, J. Wang, and T. Funada. *Potential flows of viscous and viscoelastic liquids*. Cambridge Univ. Press, 2007.

[40] M. Klein. Direct numerical simulation of a spatially developing water sheet at moderate Reynolds number. *International Journal of Heat and Fluid Flow*, 26(5):722–731, 2005.

[41] V. Kolář. Vortex identification: New requirements and limitations. *International journal of heat and fluid flow*, 28(4):638–652, 2007.

[42] J. C. Lasheras and H. Choi. Three-dimensional instability of a plane free shear layer: an experimental study of the formation and evolution of streamwise vortices. *Journal of Fluid Mechanics*, 189:53–86, 1988.

[43] J. C. Lasheras and E. J. Hopfinger. Liquid jet instability and atomization in a coaxial gas stream. *Annual Review of Fluid Mechanics*, 32(1):275–308, 2000.

[44] J. C. Lasheras, E. Villermaux, and E. J. Hopfinger. Break-up and atomization of a round water jet by a high-speed annular air jet. *Journal of Fluid Mechanics*, 357:351–379, 1998.

[45] A. H. Lefebvre. Atomization and sprays. *New York: Hemisphere Publishing Corp.*, 1989, 1989.

[46] B. P. Leonard. A stable and accurate convective modelling procedure based on quadratic upstream interpolation. *Computer Methods in Applied Mechanics and Engineering*, 19(1):59–98, 1979.

[47] X. Li. On the instability of plane liquid sheets in two gas streams of unequal velocities. *Acta Mechanica*, 106(3-4):137–156, 1994.

[48] X. Li and R. S. Tankin. On the temporal instability of a two-dimensional viscous liquid sheet. *Journal of Fluid Mechanics*, 226:425–443, 1991.

[49] D. Liepmann and M. Gharib. The role of streamwise vorticity in the near-field entrainment of round jets. *Journal of Fluid Mechanics*, 245:643–668, 1992.

[50] Y. Ling, D. Fuster, S. Zaleski, and G. Tryggvason. Spray formation in a quasiplanar gas-liquid mixing layer at moderate density ratios: A numerical closeup. *Physical Review Fluids*, 2(1):014005, 2017.

[51] A. Lozano and F. Barreras. Experimental study of the gas flow in an air-blasted liquid sheet. *Experiments in Fluids*, 31(4):367–376, 2001.

[52] A. Lozano, F. Barreras, G. Hauke, and C. Dopazo. Longitudinal instabilities in an air-blasted liquid sheet. *Journal of Fluid Mechanics*, 437:143–173, 2001.

[53] A. Lozano, A. Garcıa-Olivares, and C. Dopazo. The instability growth leading to a liquid sheet breakup. *Physics of Fluids*, 10(9):2188–2197, 1998.

[54] A. Mansour and N. Chigier. Disintegration of liquid sheets. *Physics of Fluids A: Fluid Dynamics*, 2(5):706–719, 1990.

[55] P. Marmottant and E. Villermaux. On spray formation. *Journal of Fluid Mechanics*, 498:73–111, 2004.

[56] J. E. Martin and E. Meiburg. Numerical investigation of three-dimensionally evolving jets subject to axisymmetric and azimuthal perturbations. *Journal of Fluid Mechanics*, 230:271–318, 1991.

[57] J.-P. Matas, S. Marty, and A. Cartellier. Experimental and analytical study of the shear instability of a gas-liquid mixing layer. *Physics of Fluids*, 23(9):094112, 2011.

[58] E.-S. R. Negeed, S. Hidaka, M. Kohno, and Y. Takata. Experimental and analytical investigation of liquid sheet breakup characteristics. *International Journal of Heat and Fluid Flow*, 32(1):95–106, 2011.

[59] W. V. Ohnesorge. Die bildung von tropfen an düsen und die auflösung flüssiger strahlen. *ZAMM-Journal of Applied Mathematics and Mechanics*, 16(6):355–358, 1936.

[60] S. Osher and R. P. Fedkiw. Level set methods: an overview and some recent results. *Journal of Computational Physics*, 169(2):463–502, 2001.

[61] T. Otto, M. Rossi, and T. Boeck. Viscous instability of a sheared liquid-gas interface: Dependence on fluid properties and basic velocity profile. *Physics of Fluids*, 25(3):032103, 2013.

[62] Y. Pan and K. Suga. A numerical study on the breakup process of laminar liquid jets into a gas. *Physics of Fluids*, 18(5):052101, 2006.

[63] J. Park, K. Y. Huh, X. Li, and M. Renksizbulut. Experimental investigation on cellular breakup of a planar liquid sheet from an air-blast nozzle. *Physics of Fluids*, 16(3):625–632, 2004.

[64] S. V. Patankar and D. B. Spalding. A calculation procedure for heat, mass and momentum transfer in three-dimensional parabolic flows. In *Numerical Prediction of Flow, Heat Transfer, Turbulence and Combustion*, pages 54–73. Elsevier, 1983.

[65] S. B. Pope. An explanation of the turbulent round-jet/plane-jet anomaly. *AIAA Journal*, 16(3):279–281, 1978.

[66] S. Popinet and S. Zaleski. A front-tracking algorithm for accurate representation of surface tension. *International Journal for Numerical Methods in Fluids*, 30(6):775–793, 1999.

[67] D. S. Pradeep and F. Hussain. Transient growth of perturbations in a vortex column. *Journal of Fluid Mechanics*, 550:251–288, 2006.

[68] R. H. Rangel and W. A. Sirignano. The linear and nonlinear shear instability of a fluid sheet. *Physics of Fluids A: Fluid Dynamics*, 3(10):2392–2400, 1991.

[69] L. Rayleigh. On the capillary phenomena of jets. *Proc. R. Soc. London*, 29(196-199):71–97, 1879.

[70] L. Raynal. *Instabilite et entrainement à l'interface d'une couche de melange liquide-gaz*. PhD thesis, 1997.

[71] R. D. Reitz and F. V. Bracco. Mechanisms of breakup of round liquid jets. *Encyclopedia of Fluid Mechanics*, 3:233–249, 1986.

[72] W. J. Rider and D. B. Kothe. Reconstructing volume tracking. *Journal of Computational Physics*, 141(2):112–152, 1998.

[73] J. H. Rupe. *On the dynamic characteristics of free-liquid jets and a partial correlation with orifice geometry*. Jet Propulsion Laboratory, California Institute of Technology, 1962.

[74] W. Sander and B. Weigand. Direct numerical simulation and analysis of instability enhancing parameters in liquid sheets at moderate Reynolds numbers. *Physics of Fluids*, 20(5):053301, 2008.

[75] W. Sander and B. Weigand. Direct numerical simulation on the influence of the nozzle design for water sheets emerged at moderate Reynolds numbers. In *High Performance Computing in Science and Engineering '07*, pages 277–291. Springer, 2008.

[76] R. Scardovelli and S. Zaleski. Direct numerical simulation of free-surface and interfacial flow. *Annual Review of Fluid Mechanics*, 31(1):567–603, 1999.

[77] W. Schoppa, F. Hussain, and R. W. Metcalfe. A new mechanism of small-scale transition in a plane mixing layer: core dynamics of spanwise vortices. *Journal of Fluid Mechanics*, 298:23–80, 1995.

[78] D. G. Schowalter, C. W. Van Atta, and J. C. Lasheras. Baroclinic generation of streamwise vorticity in a stratified shear layer. *Meccanica*, 29(4):361–371, 1994.

[79] P. K. Senecal, D. P. Schmidt, I. Nouar, C. J. Rutland, R. D. Reitz, and M. L. Corradini. Modeling high-speed viscous liquid sheet atomization. *International Journal of Multiphase Flow*, 25(6):1073–1097, 1999.

[80] J. Shinjo and A. Umemura. Simulation of liquid jet primary breakup: Dynamics of ligament and droplet formation. *International Journal of Multiphase Flow*, 36(7):513–532, 2010.

[81] W. A. Sirignano and C. Mehring. Review of theory of distortion and disintegration of liquid streams. *Progress in energy and combustion science*, 26(4-6):609–655, 2000.

[82] H. B. Squire. Investigation of the instability of a moving liquid film. *British Journal of Applied Physics*, 4(6):167, 1953.

[83] B. E. Stapper, W. A. Sowa, and G. S. Samuelsen. An experimental study of the effects of liquid properties on the breakup of a two-dimensional liquid sheet. *J. Eng. Gas Turbines Power*, 114(1):39–45, 1992.

[84] M. Sussman, E. Fatemi, P. Smereka, and S. Osher. An improved level set method for incompressible two-phase flows. *Computers & Fluids*, 27(5):663–680, 1998.

[85] G. Taylor. The instability of liquid surfaces when accelerated in a direction perpendicular to their planes. I. *Proceedings of the Royal Society of London. Series A. Mathematical and Physical Sciences*, 201(1065):192–196, 1950.

[86] T. J. Tharakan, K. Ramamurthi, and M. Balakrishnan. Nonlinear breakup of thin liquid sheets. *Acta Mechanica*, 156(1-2):29–46, 2002.

[87] G. Tryggvason and S. O. Unverdi. Computations of three-dimensional Rayleigh–Taylor instability. *Physics of Fluids A: Fluid Dynamics*, 2(5):656–659, 1990.

[88] C. M. Varga, J. C. Lasheras, and E. J. Hopfinger. Initial breakup of a small-diameter liquid jet by a high-speed gas stream. *Journal of Fluid Mechanics*, 497:405–434, 2003.

[89] H. K. Versteeg and W. Malalasekera. *An introduction to computational fluid dynamics: the finite volume method*. Pearson Education, 2007.

[90] C. Weber. *On the breakdown of a fluid jet*. 1948.

[91] S. E. Widnall, D. B. Bliss, and C. Y. Tsai. The instability of short waves on a vortex ring. *Journal of Fluid Mechanics*, 66(01):35–47, 1974.

[92] S. E. Widnall and J. P. Sullivan. On the stability of vortex rings. *Proceedings of the Royal Society of London A: Mathematical, Physical and Engineering Sciences*, 332(1590):335–353, 1973.

[93] P.-K. Wu, L.-K. Tseng, and G. M. Faeth. Primary breakup in gas/liquid mixing layers for turbulent liquids. *Atomization and Sprays*, 2(3), 1992.

[94] S. S. Yoon. Droplet distributions at the liquid core of a turbulent spray. *Physics of Fluids*, 17(3):035103, 2005.

[95] S. S. Yoon and S. D. Heister. A nonlinear atomization model based on a boundary layer instability mechanism. *Physics of Fluids*, 16(1):47–61, 2004.

[96] A. Zandian, W. A. Sirignano, and F. Hussain. Three-dimensional liquid sheet breakup: vorticity dynamics. *AIAA Paper 2016-1593*, 2016.

[97] A. Zandian, W. A. Sirignano, and F. Hussain. Planar liquid jet: Early deformation and atomization cascades. *Physics of Fluids*, 29(6):062109, 2017.

[98] A. Zandian, W. A. Sirignano, and F. Hussain. Understanding liquid-jet atomization cascades via vortex dynamics. *Journal of Fluid Mechanics*, 843:293–354, 2018.

[99] H. K. Zhao, T. Chan, B. Merriman, and S. Osher. A variational level set approach to multiphase motion. *Journal of Computational Physics*, 127(1):179–195, 1996.

[100] D. Zuzio, J.-L. Estivalèzes, and B. DiPierro. An improved multiscale Eulerian-Lagrangian method for simulation of atomization process. *Computers & Fluids*, 2016.